THE UNIVERSITY OF CHICAGO

# REDUCED DENSITY MATRIX APPROACHES FOR QUANTUM SENSING, COMPUTATION, AND SIMULATION

A DISSERTATION SUBMITTED TO
THE FACULTY OF THE DIVISION OF THE PHYSICAL SCIENCES
IN CANDIDACY FOR THE DEGREE OF
DOCTOR OF PHILOSOPHY

DEPARTMENT OF CHEMISTRY

BY

IRMA AVDIC

CHICAGO, ILLINOIS

JUNE 2026

Copyright © 2026 by Irma Avdic

All Rights Reserved

To my mom, dad, and brother, for their unwavering love and support. Volim vas.

# TABLE OF CONTENTS

LIST OF FIGURES . . . . . viii

LIST OF TABLES . . . . . xi

ACKNOWLEDGMENTS . . . . . xii

ABSTRACT . . . . . xv

PREFACE . . . . . xvi

**I PRELIMINARIES**

1 INTRODUCTION TO QUANTUM CHEMISTRY . . . . . 2
- 1.1 Many-Electron Problem . . . . . 3
- 1.2 Wavefunctions, Operators, and Second Quantization . . . . . 5
- 1.3 Hartree-Fock Theory . . . . . 7
- 1.4 Beyond the Hartree-Fock Approximation . . . . . 8
  - 1.4.1 Electron Correlation . . . . . 8
  - 1.4.2 Multi-Reference Methods . . . . . 9

2 REDUCED DENSITY MATRIX THEORY . . . . . 11
- 2.1 Reduced Density Matrices . . . . . 11
- 2.2 N-Representability . . . . . 13
  - 2.2.1 1-Positivity Constraints . . . . . 13
  - 2.2.2 2-Positivity Constraints . . . . . 14
- 2.3 Convex Analysis and Optimization . . . . . 16
  - 2.3.1 Convex Sets, Functions, and Duality . . . . . 16
  - 2.3.2 Semidefinite Programming . . . . . 17
- 2.4 Variational Two-Particle Reduced Density Matrix Method . . . . . 18

**II CHARACTERIZING OPEN QUANTUM SYSTEMS VIA SINGLE-PARTICLE GEOMETRY**

3 OPEN QUANTUM SYSTEM VIOLATES GENERALIZED PAULI CONSTRAINTS ON QUANTUM DEVICE . . . . . 21
- 3.1 Chapter Synopsis . . . . . 21
- 3.2 Introduction . . . . . 21
- 3.3 Theory and Methods . . . . . 23
  - 3.3.1 Theory . . . . . 23
  - 3.3.2 Methods . . . . . 27
- 3.4 Results . . . . . 30
- 3.5 Discussion and Conclusions . . . . . 35
- 3.6 Acknowledgments . . . . . 37

4 QUANTUM SENSING USING MULTI-QUBIT QUANTUM SYSTEMS AND THE PAULI POLYTOPE . . . 38
4.1 Chapter Synopsis . . . 38
4.2 Introduction . . . 39
4.3 Results . . . 41
4.4 Conclusions . . . 50
4.5 Acknowledgments . . . 51

**III QUANTUM STATE TOMOGRAPHY WITH FERMIONIC CONSTRAINTS**

5 QUANTUM COMPUTING FOR QUANTUM CHEMISTRY . . . 53
5.1 Introduction to Quantum Computation . . . 53
5.2 Quantum State Tomography . . . 55
5.3 Quantum Chemistry Applications . . . 56

6 FEWER MEASUREMENTS FROM SHADOW TOMOGRAPHY WITH $N$-REPRESENTABILITY CONDITIONS . . . 60
6.1 Chapter Synopsis . . . 60
6.2 Introduction . . . 60
6.3 Theory . . . 62
6.4 Results . . . 67
6.5 Discussion and Conclusions . . . 70
6.6 Acknowledgments . . . 72

7 ENHANCED SHADOW TOMOGRAPHY OF MOLECULAR EXCITED STATES FROM ENFORCING $N$-REPRESENTABILITY CONDITIONS BY SEMIDEFINITE PROGRAMMING . . . 73
7.1 Chapter Synopsis . . . 73
7.2 Introduction . . . 74
7.3 Theory . . . 76
7.4 Results . . . 79
7.4.1 Low-lying $H_4$ excited states . . . 80
7.4.2 The photoexcited conversion of *gauche*-1,3-butadiene to bicyclobutane 84
7.5 Discussion and Conclusions . . . 88
7.6 Acknowledgments . . . 92

8 CONSTRAINED SHADOW TOMOGRAPHY FOR MOLECULAR SIMULATION ON QUANTUM DEVICES . . . 93
8.1 Chapter Synopsis . . . 93
8.2 Introduction . . . 93
8.3 Theory . . . 96
8.3.1 Shadow tomography for fermionic systems . . . 96
8.3.2 Constrained shadow tomography of the 2-RDM . . . 98
8.4 Results . . . 103

8.5 Discussion and Conclusions . . . 113
8.6 Acknowledgments . . . 114

**IV MANY-BODY QUANTUM ORDER IN MIXED-PARTICLE SYSTEMS**

9 WITNESSING ENTANGLEMENT IN MIXED-PARTICLE QUANTUM SYSTEMS 116
9.1 Chapter Synopsis . . . 116
9.2 Introduction . . . 116
9.3 Theory . . . 118
9.4 Results . . . 120
9.5 Discussion and Conclusions . . . 127
9.6 Acknowledgments . . . 128

10 CONCLUSION . . . 129

A SUPPLEMENTAL MATERIAL: CHAPTER 3 . . . 133
A.1 State Preparation . . . 133
A.2 Quantum Tomography . . . 134
A.3 Quantum Device Specifications . . . 135
A.4 Additional Data . . . 136

B SUPPLEMENTAL MATERIAL: CHAPTER 4 . . . 175
B.1 Chemical Dynamics . . . 175
B.2 Derivation of the Initial Density Matrix from Experimental Data . . . 176
B.2.1 Construction of Excitonic Transition Dipoles . . . 176
B.2.2 Optical Pulse Interactions With Excitonic Transition Dipole Moments 177
B.3 Occupations of the Excited-State Orbitals Over Time . . . 180
B.4 Fenna-Matthews-Olson Complex Population Dynamics . . . 181
B.5 The Effect of Dephasing on the Pauli Polytope Dynamics . . . 182

C SUPPLEMENTAL MATERIAL: CHAPTER 6 . . . 184
C.1 Additional Data . . . 184

D SUPPLEMENTAL MATERIAL: CHAPTER 7 . . . 189
D.1 Haar Random Unitary Matrices . . . 189
D.2 Cartesian Coordinates of $S_0$ Optimized Geometries . . . 189

E SUPPLEMENTAL MATERIAL: CHAPTER 8 . . . 191
E.1 Numerical Simulation Details . . . 191
E.1.1 Shadow Variational Two-Particle Reduced Density Matrix (sv2RDM) Method . . . 191
E.1.2 Fermionic Classical Shadows (FCS) . . . 192
E.2 Quantum Hardware Details . . . 195
E.2.1 $H_4$ Rectangle-Square-Rectangle Transition . . . 195
E.2.2 Linear Hydrogen Chains . . . 195

E.2.3 2-RDM Reconstruction and Post-Processing . . . . . 196
E.3 Additional Data . . . . . 198

REFERENCES . . . . . 201

# LIST OF FIGURES


1.1 Cartoon illustrating a veterinarian confronting a man in the waiting room. Benjamin Schwartz, New Yorker, 2015. . . . . 3

2.1 Illustration of an $N$-representable set. . . . . 15

3.1 The Pauli polytope for three particles in six orbitals . . . . . 25
3.2 Quantum circuit used for the state preparation of a four-qubit system. . . . . 28
3.3 Polytopes showing the sets of three lowest natural occupations, ordered from highest to lowest, for the three-qubit system (a) and for the four-qubit system (b), measured on a quantum computer. . . . . 31
3.4 Residual distributions under Pauli and generalized Pauli constraints for a five-qubit system. . . . . 32
3.5 Generalized Pauli constraint residuals vs. von Neumann entropy for five-qubit system and subsystems . . . . . 35

4.1 The Pauli polytope. . . . . 40
4.2 Population dynamics of the FMO energy transfer process. . . . . 43
4.3 Pauli polytope showing the femtosecond trajectories of a 3-qubit subsystem from the experimentally derived density matrix of the FMO complex. . . . . 45
4.4 Temporal trajectories of different 3-qubit subsystems of the FMO complex for the first 2 ps of the energy transfer process from the experimentally derived density matrix. . . . . 46
4.5 Arbitrary quantum circuit model representing the open-system quantum sensing scheme for three qubits. . . . . 47
4.6 Trajectories of different three-qubit subsystems of the FMO complex for the first 2 ps of the energy transfer process. . . . . 49

6.1 Potential energy curves of $N_2$ from FCI, v2RDM (DQG), and sv2RDM (DQG). 68
6.2 Energy and 2-RDM errors for $N_2$ at 1.75 Å as functions of the number of measurements. . . . . 69
6.3 Total ground-state energy of $H_4$ is shown as a function of the number of shadows in the presence and absence of Gaussian noise. . . . . 71

7.1 Energies of the low-lying excited states of $H_4$ as a function of the number of shadows. . . . . 81
7.2 Absolute energy error of low-lying excited states of $H_4$ for the different positivity conditions as a function of the number of shadows. . . . . 82
7.3 Critical points on the potential energy surface of the photoexcited conversion of *gauche*-1,3-butadiene to bicyclobutane computed via sv2RDM (DQG). . . . . 86
7.4 Absolute energy error and normalized Frobenius norm of the 2-RDM between sv2RDM and CASCI as functions of the number of shadows for the ground and excited states of the conical intersection system. . . . . 89

8.1 Energy and 2-RDM errors across v2RDM, sv2RDM, and FCS methods at fixed shot budgets as functions of system size for a series of hydrogen chains. . . . . 104
8.2 Lowest 2-RDM eigenvalue as a function of total shot budget for sv2RDM and FCS methods for the $H_4$ system. . . . . 106
8.3 Absolute error matrices for the $H_4$ system from sv2RDM and FCS methods. . . 107
8.4 Potential energy curve of $N_2$ computed with sv2RDM, CASCI, and FCS methods. 109
8.5 Potential energy curve for the $H_4$ rectangle–square–rectangle transition computed using DFT, LUCJ ansatz, and sv2RDM using measurements collected on a quantum computer. . . . . 110

9.1 Illustration of entanglement witnessing in a mixed fermion-boson system. . . . . 118
9.2 Contour plots of the entanglement witness for fermionic and bosonic sectors as a function of interaction parameter. . . . . 123
9.3 Entanglement witnesses for fermions and bosons as functions of the interaction parameter with a non-interacting initial state. . . . . 124
9.4 Entanglement witnesses for the electron–phonon model system as functions of interaction parameter. . . . . 126

A.1 Quantum circuit used for the state preparation of a four-qubit system. . . . . 134
A.2 Quantum circuit used for the state preparation of a three-qubit system. . . . . 136
A.3 Quantum circuit used for the state preparation of a four-qubit system. . . . . 136
A.4 Quantum circuit used for the state preparation of a five-qubit system. . . . . 137
A.5 Quantum circuit used for the state preparation of a six-qubit system. . . . . 137
A.6 Quantum circuit used for the state preparation of a seven-qubit system. . . . . 138
A.7 Pauli polytope and residual distribution for three-qubit system (noiseless simulator). 139
A.8 Pauli polytope and residual distribution for four-qubit system (noiseless simulator). 140
A.9 Pauli polytope and residual distribution for five-qubit system (noiseless simulator). 142
A.10 Pauli polytope and residual distribution for six-qubit system (noiseless simulator). 144
A.11 Pauli polytope and residual distribution for seven-qubit system (noiseless simulator). . . . . 147
A.12 Pauli polytope and residual distribution for three-qubit system (fake noise simulator). . . . . 150
A.13 Pauli polytope and residual distribution for four-qubit system (fake noise simulator). 151
A.14 Pauli polytope and residual distribution for five-qubit system (fake noise simulator). 153
A.15 Pauli polytope and residual distribution for six-qubit system (fake noise simulator). 155
A.16 Pauli polytope and residual distribution for seven-qubit system (fake noise simulator). . . . . 158
A.17 Pauli polytope and residual distribution for three-qubit system (quantum computer). . . . . 161
A.18 Pauli polytope and residual distribution for four-qubit system (quantum computer). 162
A.19 Pauli polytope and residual distribution for five-qubit system (quantum computer). 163
A.20 Pauli polytope and residual distribution for six-qubit system (quantum computer). 164
A.21 Pauli polytope and residual distribution for seven-qubit system (quantum computer). . . . . 167

A.22 Generalized Pauli constraints inequality residual plotted as a function of the von Neumann entropy for the occupation measurements collected on (a) simulator and (b) quantum computer for the three-qubit system. . . . . 170
A.23 Generalized Pauli constraints inequality residual plotted as a function of the von Neumann entropy for the occupation measurements collected on (a) simulator and (b) quantum computer for the four-qubit system. . . . . 171
A.24 Generalized Pauli constraints inequality residual plotted as a function of the von Neumann entropy for the occupation measurements collected on (a) simulator and (b) quantum computer for the five-qubit system. . . . . 172
A.25 Generalized Pauli constraints inequality residual plotted as a function of the von Neumann entropy for the occupation measurements collected on (a) simulator and (b) quantum computer for the six-qubit system. . . . . 173
A.26 Generalized Pauli constraints inequality residual plotted as a function of the von Neumann entropy for the occupation measurements collected on (a) simulator and (b) quantum computer for the seven-qubit system. . . . . 174

B.1 Calculated excitonic transition dipole moment squared and the linear absorption spectrum of FMO's excitonic transitions. . . . . 177
B.2 Exciton populations of the FMO complex for the first 1 ps of the energy transfer process. . . . . 182
B.3 Temporal trajectories of different 3-qubit subsystems of the FMO complex for the first 2 ps of the energy transfer process from the experimentally derived density matrix with high dephasing. . . . . 183

C.1 Total ground state energies of hydrogen chains as functions of the number of shadows. . . . . 188

E.1 Potential energy curve of $N_2$ computed using the sv2RDM, CASCI, FCS, and v2RDM methods. . . . . 198
E.2 Potential energy curve for the $H_4$ rectangle–square–rectangle transition computed using DFT, LUCJ ansatz, v2RDM, and sv2RDM using measurements collected on a quantum computer. . . . . 199

# LIST OF TABLES


6.1 Frobenius norm of the 2-RDM as a function of the number of shadows and the number of $N$-representability conditions for $H_4$. . . . . 70

7.1 Normalized Frobenius norm of the 2-RDM as function of the number of shadows and $N$-representability conditions for low-lying $H_4$ excited states . . . . . 83
7.2 Total and relative energies of critical points along the *gauche*-1,3-butadiene to bicyclobutane reaction pathway. . . . . 85
7.3 Natural occupation numbers and von Neumann entropies of critical points along the *gauche*-1,3-butadiene to bicyclobutane reaction pathway. . . . . 87
7.4 Normalized Frobenius norm of the 2-RDM as a function of the number of shadows and $N$-representability conditions for the critical points along the *gauche*-1,3-butadiene to bicyclobutane reaction pathway. . . . . 90

8.1 Frobenius-norm differences for various H chain lengths with the given total shot budgets in the fully state-agnostic regime. . . . . 107
8.2 Comparison of correlation energies with respect to Hartree Fock for various H chain lengths. . . . . 111

A.1 Calibration data for the IBM quantum computer "Jakarta" . . . . . 136

B.1 Qubit 1 populations over time in the specified chromophore subsystems. . . . . 180
B.2 Qubit 2 populations over time in the specified chromophore subsystems. . . . . 181
B.3 Qubit 3 populations over time in the specified chromophore subsystems. . . . . 181

C.1 The total energy and the Euclidean norm of the absolute error of the 2-RDM for $H_5$ as a function of the number of shadows. . . . . 184
C.2 The total energy and the Euclidean norm of the absolute error of the 2-RDM for $H_6$ as a function of the number of shadows. . . . . 185
C.3 The total energy and the Euclidean norm of the absolute error of the 2-RDM for $H_7$ as a function of the number of shadows. . . . . 186
C.4 The total energy and the Euclidean norm of the absolute error of the 2-RDM for $H_8$ as a function of the number of shadows. . . . . 187

D.1 Optimized *gauche*-1,3-butadiene (GBUT) geometry . . . . . 189
D.2 Optimized bicyclobutane (BIBUT) geometry . . . . . 190
D.3 Optimized disrotatory transition state (TSD) geometry . . . . . 190
D.4 Optimized conical intersection (CI) geometry . . . . . 190

E.1 Comparison of electronic energies (in hartree) for various H chain lengths in the fully state-agnostic regime. . . . . 200

# ACKNOWLEDGMENTS

I would first like to express my sincere gratitude to my research advisor, Prof. David A. Mazziotti, for his invaluable guidance, mentorship, and constant support throughout my Ph.D. His patience, empathy, and passion for science made the completion of this work possible. I am particularly grateful to David for his constant encouragement and for inspiring me to strive beyond what I believed possible.

I would next like to sincerely thank my Ph.D. thesis committee members, Prof. Gregory S. Engel and Prof. Laura Gagliardi, for their time, expertise, and valuable insights over the past five years. I am grateful to Greg for his collaboration on research projects, his thoughtful guidance on scientific writing, research directions, and career development, and for the opportunity to help launch a student-led seminar series, together with Olivia C. Wedig, within the NSF Quantum Leap Challenge Institute for Quantum Sensing for Biophysics and Bioengineering (QuBBE). To Laura, I am thankful for the continuous encouragement, inspiration, and thoughtful support of my Ph.D. work. Moreover, I would like to acknowledge the McCormick, Freud, and NSF Graduate Research Fellowships for providing financial support throughout my graduate career, as well as the IBM-UChicago Quantum Collaboration.

Next, I would like to thank my wonderful collaborators: Olivia C. Wedig, Dr. Jacob S. Higgins, Indranil Ghosh, Dr. Yuchen Wang, Michael Rose, Lillian I. Payne, Dr. Anna O. Schouten, Dr. Kevin J. Sung, Dr. Nate Earnest-Noble, Cameron Cianci, Dr. Rishab Dutta, Dr. Samuel Warren, Brandon Allen, Nam P. Vu, Prof. Lea F. Santos, Prof. Victor S. Batista, Luis H. Delgado-Granados, Timothy J. Krogmeier, Prof. LeeAnn M. Sager-Smith, Dr. Zixuan Hu, Dr. Manas Sajjan, Dr. Maryam Abbasi, Dr. Scott E. Smart, Prof. Prineha Narang, Prof. Sabre Kais, Dr. Anthony W. Schlimgen, Prof. Kade Head-Marsden, Dr. Julia Liebert, and Prof. Christian Schilling.

Thank you to all the members of the Mazziotti group, past and present for making a fun and enjoyable work environment: Prof. Kade Head-Marsden, Dr. Anthony Schlimgen,

Dr. Scott E. Smart, Prof. Jan-Niklas Boyn, Dr. Simon A. Ewing, Prof. LeeAnn M. Sager-Smith, Dr. Daniel Gibney, Dr. Samuel Warren, Dr. Anna O. Schouten, Dr. Yuchen Wang, Dr. Madhubani Mukherjee, Dr. Leah Weisburn, Luis H. Delgado-Granados, Lillian I. Payne, Michael Rose, Serina Tressler, Noah Garrett, Whitney Short, Nathan Meier, Jordan Klevens, Ryan Choi, Julia Zhao, Nicholas Cipi, Pavlik Braverman, Khushi Pusnur, Vanessa Zhao, Yagmur Varol, Connor Lo, Ian Schmidt, Filippos Tsoukis, and Aoife Beswick. I am grateful to LeeAnn for guiding me in my first year and patiently answering my many questions. I deeply thank Anna, Luis, and Lily not only for their invaluable feedback, thoughtful discussions, and research collaborations, but also for their friendship and steadfast support throughout my Ph.D. I also appreciate Kade for her support and career advice.

I would certainly not be where I am today without my early research experiences at the University of Louisville, working first in Prof. Jinjun Liu's spectroscopy lab and then in Prof. Lee M. Thompson's research group, under the mentorship of Dr. Emily M. Kempfer. I am very grateful for their continued support and mentorship throughout my graduate career.

I am grateful to Prof. Bozhi Tian, Prof. Meishan Zhao, Prof. Norbert F. Scherer, and Dr. Samuel Harris for their support of my fellowship applications and their mentorship in my development as an educator. Furthermore, I am grateful to the many students with whom I have had the privilege to learn and grow over the years.

I would now like to thank Prof. Britni Ratliff for her continuous mentoring and support throughout my Ph.D, and to Prof. Vera Dragisich for always being there to listen and offer wisdom. Thank you to Maria Jimenez, Laura Luburich, Mónica Lugo, Dr. Christin Ahn, Dr. Bentley Wall, Dr. Karen Watters, and Prof. Jiwoong Park for their invaluable administrative and logistical support that keeps the Department and outreach activities running. I would also like to acknowledge Dr. Amy Hark and Dr. Elahe Ganji for their guidance as I explored my career path. I am also grateful to Carolyn Banner, whose student wellness programs helped me stay grounded, healthy, and fulfilled along the way. A big thank you to the entire

QuBBE community, especially Dr. Joseph R. Sachleben, for his support of the QuBBE Science Talks and his enthusiasm for quantum sensing.

Next, I would like to thank my incredible friends: Kinga Pajdzik, Rachel Leech, Vanessa Zhang, Anna O. Schouten, Luis H. Delgado-Granados, Sharba Bhattacharjee, Kristina Trifonova, Damir Agić, Nermina Ademović Mujčinović, Lilly Gullickson, Kwanghoon Jeong, Ian Bongalonta, Kuntal Ghosh, Shreya Verma, Olga Medrano Martin del Campo, Ophelia Dominguez, Qiaohong Wang, Lauren Weiss, Qijie Shen, Van Do, Amer Dzankovic, Stacia Konow, and so many others, who have offered listening ears, kept me laughing, encouraged me, and reminded me to take breaks during this challenging journey.

To my partner and my very best friend, Abhishek Mitra, thank you for your love, patience, and encouragement throughout this journey. Your support has meant more to me than I can express, and I am deeply grateful to have you by my side. I am also sincerely thankful to your parents for their kindness and support along the way.

I am grateful to my grandparents, Hamdija and Refija Kerla and Nusreta Avdić, for their encouragement and belief in my pursuits, and I hold close the memory of those we lost during this time: my uncle and grandpa Amir and Adem Avdić, who I know would be beyond proud.

Finally, I would like to thank my mom and dad, Zinaida and Mirza Avdić, and my brother Omar Avdić, for their unconditional love and countless sacrifices. Your patience, steady support, and unwavering belief in me have shaped who I am. Thank you for giving me opportunities you never had and for being there through every part of this journey. This accomplishment is as much yours as it is mine. I am here because you were brave enough to begin again, and I will always carry that courage with me.

This thesis would not have been possible without the support of all these individuals.

# ABSTRACT

Theoretical chemistry uses the laws of physics to provide explanations for chemical observations, including molecular structure, bonding, and reactivity, in close connection with experiment. Though many answers in chemistry and materials science have been elucidated by accurate first-principles quantum chemical calculations, their applicability is limited by high computational costs. This motivates the use of reduced descriptions of quantum many-body systems that retain core physical information at a lower computational cost. This thesis explores the development of reduced density matrix (RDM) techniques at the interface of chemistry, physics, and quantum information that address challenges in quantum technologies, including decoherence and scalability. The first part explores how minimal single-particle information can be used to detect environmental interactions in many-body quantum systems, aiding in the development of novel quantum sensing techniques and error mitigation strategies for quantum computation. The second part presents a framework for accelerating quantum state characterization for practical molecular simulation on quantum devices. The final part elucidates properties of entanglement in systems with mixed particle statistics, offering insight into quantum communication and the design of hybrid quantum platforms. Together, these results demonstrate how RDM-based approaches can improve the efficiency, interpretability, and robustness of quantum sensing, computation, and simulation.

# PREFACE

In the early twentieth century, quantum mechanics was born, fundamentally changing our understanding of matter and, therefore, our physical reality. This year marks the centenary of the Schrödinger equation, which, among a cascade of discoveries around the same time, marked the advent of modern physics. It became clear then that these findings would have a profound impact on chemistry and the broader community of material and molecular sciences, although not without challenges. The origins of the thesis before you, though significantly younger, stem from my own fascination with the quantum realm.

Relatively early in my undergraduate studies at the University of Louisville, I realized that my scientific interests revolved around understanding the fundamental properties of matter and the way in which these behaviors shape macroscopic phenomena. It should come as no surprise then that I decided to pursue graduate studies in electronic structure theory at the University of Chicago, where I could push the boundaries of my curiosity with simulations. One thing that people don't always mention about graduate school is that if an idea sounds straightforward, it will most likely take a 4-5 year journey to grasp it, and my advisor, Prof. David A. Mazziotti, and I had a lot of "easy" ideas. Yet, I am beyond grateful we got to explore them together.

As I was taking the leap to the forefront of theoretical chemistry in 2021, a new chapter of quantum-enabled technologies was being written with the first commercial quantum computers revealed in 2019, and quantum sensing rapidly moving toward promising commercialization in medical imaging and navigation systems. The work in this thesis lies at the intersection of chemistry, physics, and quantum information, primarily addressing challenges in quantum technologies. Chapters 1 and 2 define the language of quantum chemistry and reduced density matrix theory, which serves as the foundation to the theories and methods that follow. Chapters 3 and 4 discuss approaches based on single-particle information that allow for the characterization of open quantum systems. First, a technique is developed using

the one-particle reduced density matrix to detect when many-body quantum systems interact with their environment, which is then used to introduce a quantum sensing algorithm guided by ultrafast spectroscopy experiments. Chapter 5 offers a brief review of fundamentals of quantum computation with emphasis on applications in quantum chemistry. Chapters 6, 7, and 8 present methods for reducing the cost of quantum state tomography on quantum computers via physical constraints and semidefinite programming. The methodology presented in these chapters is applied to a range of chemical systems, including ground and excited states, and demonstrated on state-of-the-art quantum computers, with significant implications for molecular simulation on quantum devices. Finally, chapter 9 introduces a framework for characterizing entanglement as a resource in quantum communication, in systems with mixed particle statistics.

This thesis contains only the works for which I am the lead author, while references [1–12] list all collaborative contributions I was grateful to make during the course of my Ph.D. Needless to say, there is much left to discover, but I hope this document provides some significance in the rapidly growing field of theoretical chemistry and aids in its merger with quantum technologies, which may lead to the next revolution in science. Thank you for your attention to this thesis, and I sincerely hope you find it valuable to whatever extent.

Irma Avdic

Chicago, IL

June 2026

# Part I

# Preliminaries

# CHAPTER 1

# INTRODUCTION TO QUANTUM CHEMISTRY

Molecular simulation and modeling provide a framework for predicting how atoms and molecules behave based on the principles of quantum mechanics. However, accurately describing complex, disordered systems and realistic chemical environments requires substantial computational power, often beyond current capabilities. While exact solutions for many-electron systems are generally intractable, a range of approximate methods enables reliable predictions of energies, structures, and reaction pathways, making them essential tools across chemistry, materials science, and biology. Advancing these methods to better balance accuracy and computational cost would reduce reliance on expensive trial-and-error experiments and accelerate the discovery of new drugs and materials, driving more efficient innovation in medicine, energy, and industry.

This dissertation investigates how reduced density matrix (RDM) theory, a mathematical approach that describes a selected part of a quantum system (such as a few particles within many) by averaging over all other variables, can reduce the computational cost of molecular simulation. Furthermore, it provides a framework for applications of RDM theory in emerging quantum technologies, such as quantum sensing and computation. First, it is shown that information from only a few individual particles can capture how a many-particle system is influenced by its surroundings. Since these environmental effects carry measurable information about the environment itself, this insight is used to develop a computationally efficient quantum sensing scheme. Next, a new algorithm is introduced for describing quantum states in molecular simulations using fewer measurements than conventional methods, and is demonstrated on a quantum computer, improving the practicality and scalability of these simulations. Finally, a theory for describing how different types of quantum particles share information, i.e., exhibit entanglement, is presented, providing insight for future quantum communication platforms and hybrid quantum technology design. Together, these advances

help bridge the gap between quantum science and practical quantum technologies, enabling applications in chemistry, materials science, and beyond. This chapter provides background on quantum chemistry and the theoretical frameworks used to describe molecular systems, setting the stage for the methods and developments presented in this dissertation.




*"About your cat, Mr. Schrödinger—I have good news and bad news."*

Figure 1.1: Cartoon illustrating a veterinarian confronting a man in the waiting room. Benjamin Schwartz, New Yorker, 2015.

## 1.1 Many-Electron Problem

Quantum chemistry aims to understand, simulate, and predict properties of molecules and materials, which, alongside experimental results, underpins applications in chemical reactivity and catalysis, materials and drug design, energy storage, and a plethora of others. The behavior of quantum systems can be described by the full non-relativistic time-independent Schrödinger equation [13],

$$\hat{H}|\psi\rangle = E\,|\psi\rangle\,, \tag{1.1}$$

where $\hat{H}$ is the $N$-particle Hamiltonian operator, $|\psi\rangle$ is the system's wavefunction (in Dirac notation), and $E$ is the system's electronic energy. Solving this eigenvalue equation provides stationary states of the Hamiltonian, which are naturally ordered by the Hamiltonian eigen-

values, i.e., energies. This ordering reflects the tendency of a quantum system to relax to its most stable, ground-state configurations or easily accessible low-lying excited states.

The total energy of a molecular system consists of the kinetic energy and the electrostatic interactions of electrons and nuclei [14]. For an $N$-electron system with $n$ nuclei, the Hamiltonian can be expressed as

$$\hat{H} = \overbrace{-\sum_{i=1}^{N}\frac{1}{2}\nabla_i^2 - \sum_{A=1}^{n}\frac{1}{2M_A}\nabla_A^2}^{\text{kinetic energy operators}} \quad \underbrace{-\sum_{i=1}^{N}\sum_{A=1}^{n}\frac{Z_A}{r_{iA}}}_{\text{electron-nuclei potential}} \quad \overbrace{+\sum_{i=1}^{N}\sum_{i<j}^{N}\frac{1}{r_{ij}} + \sum_{A=1}^{n}\sum_{A<B}^{n}\frac{Z_A Z_B}{R_{AB}}}^{\text{Coulombic repulsion terms}}, \tag{1.2}$$

where $A$ and $B$ denote nuclei, $M$ is nuclear mass, $Z$ is the atomic number, $r_{ij}$ is the distance between electrons $i$ and $j$, $r_{iA}$ is the distance between electron $i$ and nucleus $A$, $R_{AB}$ is the distance between the nuclei, and $\nabla^2$ is the Laplacian,

$$\nabla^2 = \frac{d^2}{dx^2} + \frac{d^2}{dy^2} + \frac{d^2}{dz^2}. \tag{1.3}$$

Practically, finding the solution to this Hamiltonian is a very challenging task since the nuclei are significantly more massive than the electrons [15]. To aid in this, the Born-Oppenheimer approximation decouples nuclear and electronic degrees of freedom by assuming that nuclei move considerably slower than electrons [16]. This approximation results in the following electronic Hamiltonian,

$$\hat{H}_e = -\sum_{i=1}^{N}\frac{1}{2}\nabla^2 - \sum_{i=1}^{N}\sum_{A=1}^{n}\frac{Z_A}{r_{iA}} + \sum_{i=1}^{N}\sum_{i<j}^{N}\frac{1}{r_{ij}}. \tag{1.4}$$

In general, solving the electronic Schrödinger equation exactly is prohibitively costly for any system with more than a single electron due to the electron-electron interaction term [17]. However, accurate treatment of this interaction allows for a rigorous prediction of molecu-

lar properties, so significant efforts have been made toward the development of electronic structure theories that account for electron-electron interaction effects.

## 1.2 Wavefunctions, Operators, and Second Quantization

The simplest representation of an $N$-electron wavefunction is a Slater determinant in the basis of one-electron functions [14, 18],

$$\psi_{SD} = \frac{1}{\sqrt{N!}} \begin{vmatrix} \phi_1(1) & \phi_2(1) & \cdots & \phi_N(1) \\ \phi_1(2) & \phi_2(2) & \cdots & \phi_N(2) \\ \vdots & \vdots & \ddots & \vdots \\ \phi_1(N) & \phi_2(N) & \cdots & \phi_N(N) \end{vmatrix}, \tag{1.5}$$

with $\phi_i$ spin orbitals. Electrons have half-integer spin ($\frac{1}{2}$), making them fermions, and their wavefunction becomes antisymmetric when any two electrons are permuted, reflected in the wavefunction's sign change [19]. In the formalism of second quantization, the particles are treated as excitations or relaxation of quantum fields [20, 21]. Physically, a creation operator, $\hat{a}_i^\dagger$ creates a particle in orbital $i$ while the annihilation operator, $\hat{a}_i$, destroys it. Considering a vacuum state, $|0\rangle$, the Slater determinant can be expressed as a product of creation operators,

$$|\psi_{SD}\rangle = \hat{a}_N^\dagger \cdots \hat{a}_2^\dagger \hat{a}_1^\dagger |0\rangle . \tag{1.6}$$

In order not to conflict with the symmetry of the wavefunction, these operators obey the following commutation relations:

$$\hat{a}_i^\dagger \hat{a}_j + \hat{a}_j \hat{a}_i^\dagger = \delta_j^i \tag{1.7}$$

$$\hat{a}_i^\dagger \hat{a}_j^\dagger + \hat{a}_j^\dagger \hat{a}_i^\dagger = 0 \tag{1.8}$$

$$\hat{a}_i \hat{a}_j + \hat{a}_j \hat{a}_i = 0, \tag{1.9}$$

where $\delta^i_j$ is the Kronecker delta function.

The spin-free, non-relativistic molecular Hamiltonian [22] can then be expressed in second quantization as

$$\hat{H}_e = \sum_{ij} K^i_j \hat{a}^\dagger_i \hat{a}_j + \frac{1}{2} \sum_{ijkl} V^{ik}_{jl} \hat{a}^\dagger_i \hat{a}^\dagger_k \hat{a}_l \hat{a}_j, \tag{1.10}$$

where $K^i_j$ and $V^{ik}_{jl}$ are elements of the one- and two-electron integrals, respectively, defined as

$$K^i_j = \int \phi^*_i(1) \Big( -\frac{1}{2}\nabla^2 - \sum_l \frac{Z_l}{r_{1l}} \Big) \phi_j(1) d1 \tag{1.11}$$

$$V^{ik}_{jl} = \iint \phi^*_i(1) \phi^*_k(2) \Big( \frac{1}{r_{12}} \Big) \phi_j(1) \phi_l(2) d1 d2. \tag{1.12}$$

The energy is the expectation value of the Hamiltonian in Eq. 1.10,

$$E = \langle \psi | \hat{H}_e | \psi \rangle \tag{1.13}$$

$$= \sum_{ij} K^i_j \langle \psi | \hat{a}^\dagger_i \hat{a}_j | \psi \rangle + \frac{1}{2} \sum_{ijkl} V^{ik}_{jl} \langle \psi | \hat{a}^\dagger_i \hat{a}^\dagger_k \hat{a}_l \hat{a}_j | \psi \rangle \tag{1.14}$$

$$= \sum_{ij} K^{i1}_j D^i_j + \frac{1}{2} \sum_{ijkl} V^{ik}_{jl} \, {}^2D^{ik}_{jl}, \tag{1.15}$$

where ${}^1D^i_j$ and ${}^2D^{ik}_{jl}$ are elements of the one- and two-electron reduced density matrices, respectively. For the exact ground-state wave function $\Psi_0$, the variational principle [14] gives

$$\frac{\langle \Psi_0 | \hat{H}_e | \Psi_0 \rangle}{\langle \Psi_0 | \Psi_0 \rangle} \leq \frac{\langle \Psi | \hat{H}_e | \Psi \rangle}{\langle \Psi | \Psi \rangle}, \tag{1.16}$$

with equality if and only if $\Psi = \Psi_0$ up to a phase factor. This principle guarantees that the ground-state energy is obtained by minimizing the energy functional over all admissible antisymmetric $N$-electron wavefunctions. In practice, the wavefunction is often approximated as a linear combination of Slater determinants constructed from single-particle spin

orbitals. Next, we discuss a fundamental electronic structure method that approximates the many-electron wave function using a single Slater determinant.

## 1.3 Hartree-Fock Theory

The Slater determinant of molecular orbitals, which are linear combinations of atomic orbitals, is the Hartree-Fock (HF) wavefunction ($|\psi_{\text{HF}}\rangle$) [23]. Evaluating the electronic Hamiltonian (Eq. 1.10) against this determinant provides the Fock matrix:

$$F = {}^1H + 2J - K, \tag{1.17}$$

where ${}^1H$ is the one-electron integral matrix and $J$ and $K$ are Coulomb and exchange integrals, respectively. Solving the following characteristic equation,

$$(F - \epsilon I)\vec{c}_i = 0, \tag{1.18}$$

where $I$ is the identity matrix, $\vec{c}_i$ is a vector of orbital coefficients, and $\epsilon$ are molecular orbital energies. The Fock matrix cannot be constructed if the orbitals are not known, but the orbitals themselves are eigenfunctions of the Fock matrix, so the Hartree-Fock equations are nonlinear and must be solved self-consistently [24–26]. After each iteration of the self-consistent field (SCF) procedure, the minimized set of molecular orbital coefficients is used to construct a new initial guess of orbitals to be optimized again until the total energy of the system converges to a given threshold.

At self-consistency, the Fock matrix commutes with the one-electron reduced density matrix (1-RDM), that is, they can be simultaneously diagonalized. So, in the basis that solves the Hartree-Fock equations, the 1-RDM is diagonal, meaning its eigenvalues are either 1 for occupied orbitals or 0 for unoccupied (virtual) ones. From this binary eigenvalue structure, it follows that the 1-RDM is idempotent. This implies that the 2-RDM's eigenvalues, since

they depend on the 1-RDMs, will also be either 0 or 1. From this, it can be seen that the RDMs encode useful information on the number of electrons in the system, as well as the presence of electron correlation, which will be explored in the following section.

## 1.4 Beyond the Hartree-Fock Approximation

The Hartree-Fock (HF) method recovers approximately 99% of the absolute energy for a wide range of systems; however, it treats electrons in an averaged sense, as independent of each other. Therefore, HF by itself is unable to reach the absolute ground state energy, even in the infinite basis set limit. The missing 1% of the absolute energy can result in large errors in relative energy predictions, including binding and excitation energies, which can, in turn, significantly affect physical interpretations of chemical phenomena. Nevertheless, the HF wavefunction is often used as the initial guess, or a reference determinant in post-Hartree-Fock methodologies, which aim to recover all or part of the missing electron correlation.

### *1.4.1 Electron Correlation*

Electron correlation energy [27–33] is defined as the difference between the exact energy of the system and the HF energy in a given basis set,

$$E_{corr} = E_{exact} - E_{\mathrm{HF}}. \tag{1.19}$$

Though the definition of electron correlation is still a topic of debate in the field, the most widely agreed-upon categorization is that of static and dynamic correlation [34–37]. Dynamic correlation corresponds to instantaneous electron-electron repulsion, while static correlation accounts for the effects of degenerate or near-degenerate electronic states, which fail to be described by a single Slater determinant. Approaches in electronic structure theory primarily differ in how electron correlation is recovered. For instance, methods built around system-

atic Hamiltonian corrections (e.g., coupled cluster theory [28, 38–42], Kohn–Sham Density Functional Theory [43–45], Møller–Plesset perturbation theory [46], etc.) tend to efficiently describe dynamic correlation, while methods explicitly constructing the many-electron wavefunction (e.g., full configuration interaction and active-space methods) are better suited to capture static correlation. Accordingly, the former are often referred to as single-reference methods, and the latter as multi-reference methods.

### *1.4.2 Multi-Reference Methods*

The exact wavefunction in the HF spin-orbital basis can be defined as the following expansion,

$$|\psi\rangle = c_0 |\psi_{\mathrm{HF}}\rangle + \sum_{ia} c_a^i \hat{a}_i^\dagger \hat{a}_a |\psi_{\mathrm{HF}}\rangle + \sum_{ijab} c_{ab}^{ij} \hat{a}_i^\dagger \hat{a}_j^\dagger \hat{a}_b \hat{a}_a |\psi_{\mathrm{HF}}\rangle + \cdots, \tag{1.20}$$

where $c_0, c_a^i, c_{ab}^{ij}$ are coefficients corresponding to probability amplitudes of each configuration, indices $a, b, c, \ldots$ represent occupied spin orbitals, and indices $i, j, k, \ldots$ represent unoccupied (virtual) orbitals. To evaluate the contributions of all possible configurations of $N$ electrons, the Hamiltonian can be expressed in the basis of all possible Slater determinants and diagonalized. This method provides an exact solution to the Schrödinger equation in a given basis set, and is known as the Full Configuration Interaction (FCI) [47]. However, the number of determinants in the FCI wavefunction grows as $\binom{2r}{N}$, where $r$ is the number of orbitals, making it computationally intractable for anything but the smallest systems [48].

Due to the unfavorable computational cost of FCI, various approximations have been developed to include only the most relevant configurations for the system of interest. For example, in complete active space configuration interaction (CASCI) [49, 50], the fully occupied molecular orbitals outside the valence shell are treated as core orbitals, while the unoccupied ones at higher energies are treated as the virtual orbitals. The problem is then limited to a subset of orbitals that make the "active space," where the FCI calculation can

be performed. If the reduction of full configuration to an active space is paired with a self-consistent orbital optimization, the method is referred to as the complete active space self-consistent field (CASSCF) [51, 52]. Still, the factorial scaling with the active space size renders these methods applicable only to relatively small active spaces [48]. Other notable multi-reference approaches include multi-reference perturbation theories (CASPT2, NEVPT2) [53–56], multi-reference configuration interaction (MRCI) [57], density matrix renormalization group (DMRG) [58–60], multi-reference coupled cluster theory (MR-CC) [61], localized active space (LAS) approaches [62], multiconfiguration pair-density functional theory (MC-PDFT) [63], and reduced density matrix approaches discussed in the following chapter.

# CHAPTER 2

# REDUCED DENSITY MATRIX THEORY

## 2.1 Reduced Density Matrices

The $N$-electron density matrix, first introduced by Landau [64] and von Neumann in 1927 [65], can be expressed as

$$^{N}D(1,2,\ldots,N;1',2',\ldots,N') = \psi(1,2,\ldots,N)\psi^{*}(1',2',\ldots,N'), \tag{2.1}$$

where the integers represent electronic spin and spatial components. The electronic energy can then be written in terms of the $N$-electron density matrix as

$$E = \mathrm{Tr}(\hat{H}^{N}D), \tag{2.2}$$

where $\hat{H}$ is the electronic Hamiltonian matrix. A $k$-electron reduced density matrix ($k$-RDM) [19] can be obtained by integrating Eq. 2.1 over coordinates $k+1$ to $N$ to give

$$\begin{aligned} {}^{k}D(1,2,\ldots,k;\,1',2',\ldots,k') = \frac{N!}{(N-k)!}\int \psi(1,2,\ldots,k,\ldots,N)\,\psi^{*}(1',2',\ldots,k',\ldots,N) \\ \times\, d(k+1)\cdots dN. \end{aligned} \tag{2.3}$$

In second quantization, the elements of $^{k}D$ can be expressed as

$${}^{k}D^{i_1 i_2 \ldots i_k}_{j_1 j_2 \ldots j_k} = \langle\psi|\,\hat{a}^{\dagger}_{i_1}\hat{a}^{\dagger}_{i_2}\ldots\hat{a}^{\dagger}_{i_{(k-1)}}\hat{a}^{\dagger}_{i_k}\hat{a}_{j_k}\hat{a}_{j_{(k-1)}}\ldots\hat{a}_{j_2}\hat{a}_{j_1}\,|\psi\rangle\,. \tag{2.4}$$

Because electrons are indistinguishable with only pairwise interactions, measuring physical properties in molecular systems is often sufficiently done by considering the two-electron

RDM (2-RDM) [48, 66]:

$$ {}^2D^{ij}_{kl} = \langle\psi|\, \hat{a}^\dagger_i \hat{a}^\dagger_k \hat{a}_l \hat{a}_j \,|\psi\rangle\,, \tag{2.5} $$

with trace normalized to $N(N-1)$. Similarly, the one-electron RDM (1-RDM) is defined as:

$$ {}^1D^i_j = \langle\psi|\, \hat{a}^\dagger_i \hat{a}_j \,|\psi\rangle\,, \tag{2.6} $$

with trace equal to the number of electrons, $N$. Using only the 2-RDM, the electronic energy can be obtained as

$$ E = \mathrm{Tr}({}^2K\,{}^2D), \tag{2.7} $$

where ${}^2K$ is the reduced Hamiltonian matrix given by:

$$ {}^2K = \frac{1}{N-1}\Big( -\frac{1}{2}\nabla^2_1 - \sum_j \frac{Z_j}{r_{1j}}\Big) + \frac{1}{2r_{12}} \tag{2.8} $$

with indices referring to members of a spin-orbital basis set [48, 67, 68]. Reduced density matrix approaches use the 2-RDM in place of the many-electron wavefunction, enabling the treatment of strongly correlated systems at affordable computational cost [36, 69–82] and forming the basis of this dissertation.

In Section 1.3, we have alluded to the connection between natural orbitals (eigenfunctions of the 1-RDM) and Hartree-Fock, single-particle orbitals. For non-interacting electrons, the natural occupations (eigenvalues of the 1-RDM) are strictly 0 or 1, while for interacting electrons, some, if not all, occupation numbers are fractional. Strong (static) correlation manifests as fractional natural orbital occupations, most prominently when occupations approach one-half. Dynamic correlation is, generally, characterized by occupations close to 0 or 1 [83]. Even when the full $N$-electron wavefunction is a pure state, tracing out electrons leads to reduced density matrices with fractional eigenvalues, which can appear in the higher-order RDMs as well. Part II explores how much of a quantum system's correlated

behavior can be inferred from single-particle reduced descriptions, with connections to open quantum systems and quantum sensing applications. Prior to exploring these connections, we first introduce the $N$-representability problem, which constrains the physical validity of such reduced descriptions.

## 2.2 N-Representability

> "There is an instinctive feeling that matters such as electron correlation should show up in the two-particle density matrix. ... but we still do not know the conditions that must be satisfied by $\Gamma_2$(1,2; 1',2'). Until these conditions have been elucidated, it is going to be very difficult to make much progress along these lines ... "
>
> — Charles Coulson

A variational formulation of the ground-state energy is well-defined only when the 2-RDM is restricted to be $N$-representable, i.e., derivable by contraction from an $N$-electron density matrix [84, 85]. These necessary yet sufficient conditions are known as the $N$-representability conditions [36, 67, 71, 79, 80, 84]. However, determining the full set of $N$-representability constraints for 1- and 2-RDM has proven to be extremely challenging, though fundamental to many areas of science.

### *2.2.1 1-Positivity Constraints*

We begin by examining the one-positivity conditions, whose metric matrices are fully determined by the one-particle reduced density matrix (1-RDM). The Pauli exclusion principle restricts natural orbital occupations of the 1-RDM to lie in the interval $[0, 1]$ [86], leading to the following necessary constraint on the 1-RDM:

$$^1D \succeq 0, \tag{2.9}$$

where $\succeq 0$ denotes that the matrix is positive semidefinite. Mathematically, this constraint restricts the 1-RDM to be positive semidefinite, i.e., to have nonnegative eigenvalues [73]. Physically, this constraint ensures a nonnegative probability of finding an electron in any orbital. Similarly, the one-hole reduced density matrix, whose elements are defined as:

$$ {}^1Q_i^j = \langle\psi|\, \hat{a}_j \hat{a}_i^\dagger \,|\psi\rangle\,, \tag{2.10} $$

obeys the same constraint,

$$ {}^1Q \succeq 0, \tag{2.11} $$

which, physically, corresponds to a nonnegative probability of finding a hole (i.e., absence of a particle) in any orbital. Collectively, these constraints are known as the 1-positivity conditions.

The Pauli exclusion principle defines the *ensemble* $N$-representability conditions for a 1-RDM. The complete set of *pure* $N$-representability conditions is significantly more challenging to obtain, though active research efforts in this area continue [87–89]. Chapters 3 and 4 will detail applications of a specific case of pure $N$-representability constraints for a system of three fermions in six orbitals, known as generalized Pauli constraints.

### *2.2.2 2-Positivity Constraints*

As in the previous case, constraining the two-particle reduced density matrices (2-RDMs) to be positive semidefinite imposes 2-positivity conditions [68, 90, 91]. By varying the choice of 2-particle operators such that: (a) a particle is created in orbitals $i$ and $j$, i.e., $\hat{a}_i^\dagger \hat{a}_j^\dagger$; (b) a particle is annihilated in $j$ and $i$ orbitals (or a hole is created in each of these orbitals), i.e., $\hat{a}_i \hat{a}_j$; and (c) a particle is annihilated in orbital $j$ and created in orbital $i$, i.e., $\hat{a}_i^\dagger \hat{a}_j$, the

following 2-RDM matrices can be defined:

$$^2D^{ij}_{kl} = \langle\psi|\,\hat{a}^\dagger_i\hat{a}^\dagger_j\hat{a}_l\hat{a}_k\,|\psi\rangle \tag{2.12}$$

$$^2Q^{ij}_{kl} = \langle\psi|\,\hat{a}_i\hat{a}_j\hat{a}^\dagger_l\hat{a}^\dagger_k\,|\psi\rangle \tag{2.13}$$

$$^2G^{ij}_{kl} = \langle\psi|\,\hat{a}^\dagger_i\hat{a}_j\hat{a}^\dagger_l\hat{a}_k\,|\psi\rangle \tag{2.14}$$

Constraining these matrices to be positive semidefinite, $^2D$,$^2Q$,$^2G \succeq 0$, defines the 2-positivity conditions.

The 2-positivity conditions imply the 1-positivity conditions since, by contraction,

$$^1D^i_k = \frac{1}{N-1}\sum_j {}^2D^{ij}_{kj} \tag{2.15}$$

$$^1Q^i_k = \frac{1}{r-N-1}\sum_j {}^2Q^{ij}_{kj}, \tag{2.16}$$

which implies $^1D$,$^1Q \succeq 0$ from $^2D$,$^2Q \succeq 0$, where $r$ is the rank of the one-particle basis set. Although higher-order RDM positivity conditions exist for all RDM orders $p \leq N$, we restrict the following discussion to the $p = 1$ and $p = 2$ conditions, which have been shown to yield reasonable accuracy in property prediction relative to the FCI limit.

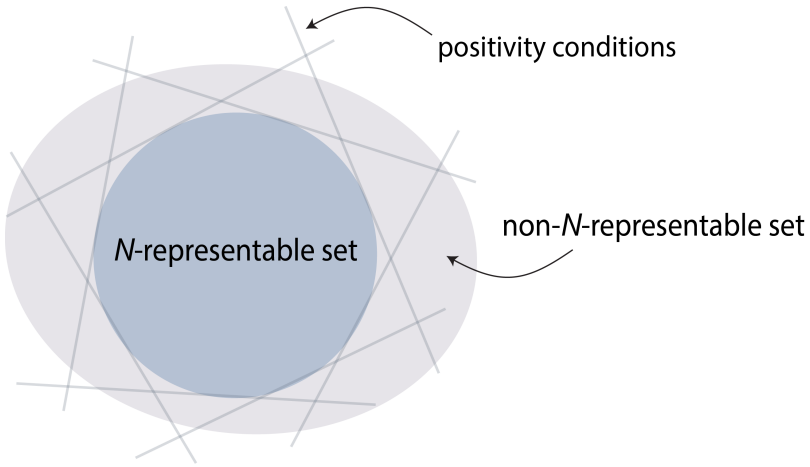


Figure 2.1: Illustration of a set (grey) being bounded by hyperplanes, i.e., positivity conditions, to create a smaller, $N$-representable set (blue).

## 2.3 Convex Analysis and Optimization

Convex analysis provides the foundation for many modern optimization techniques, including semidefinite programming, which will become one of the main themes of this thesis. For a convex problem, a locally optimal solution is also globally optimal, which is convenient for applications in quantum chemistry, where reliable bounds on ground-state energies are highly desirable within approximate methods. The main ingredients of convex analysis: convex sets, functions, and the notion of duality, will be explored in the next subsection.

### *2.3.1 Convex Sets, Functions, and Duality*

A set is convex if it contains the entire line segment connecting any two of its points, while a function is convex if averaging its inputs cannot produce a value larger than averaging its outputs. A set of matrices, $S$, is convex if, for any two matrices, $X$ and $Y$ in the set, every weighted average of those matrices also belongs to the set, that is

$$\lambda X + (1-\lambda)Y \in S, \tag{2.17}$$

where $\lambda \in [0,1]$. For example, a set of RDMs that satisfy given $N$-representability constraints forms a convex set, which physically implies that ensemble mixtures of physical states are themselves physical. From an optimization perspective, convexity enables the minimization of a linear function such that a unique global optimal solution is reached. Geometrically, convex sets can be described as regions bounded by hyperplanes, which are the higher-dimensional analogs of lines and planes (see Fig. 2.1 for illustration). When a convex set is defined by a finite number of linear constraints, it forms a polytope, which is a shape with flat faces and well-defined boundaries [92].

If primality is defined as the process of finding the best bound to the objective function from above, then duality can be interpreted as identifying the hyperplane that best bounds

the objective from below while remaining consistent with the constraints. This close relationship between the primal and dual formulations provides a practical way of identifying optimal solutions in convex problems. The development of efficient primal-dual algorithms [68, 74, 76] is of utmost importance to the polynomial-scaling semidefinite programs applied to quantum chemistry problems explored in this thesis.

### *2.3.2 Semidefinite Programming*

Semidefinite programming (SDP), a kind of convex optimization problem, emerged in the 1990s as a significant development in mathematical optimization, enabling various theoretical breakthroughs and practical applications [93, 94]. The development of efficient primal-dual interior-point algorithms for SDP in the mid-1990s [95] marked the beginning of a rapid expansion of the field, with results demonstrating the power of SDP in combinatorial optimization, control theory, and systems engineering [93, 96], culminating in the Fulkerson Prize recognition in 2000 [97, 98]. These developments positioned SDP as a powerful framework for solving a wide range of convex optimization problems and with practical relevance in various disciplines, including quantum chemistry [72, 75, 99]. As will be detailed in Sec. 2.4, a constrained optimization over the elements of the 2-RDM can also be cast as a SDP.

A semidefinite program can be written in primal and dual formulations. The primal formulation can be expressed as:

$$\begin{aligned} \min \quad & \mathrm{Tr}(CX) \\ \text{s.t.} \quad & \mathrm{Tr}(A_i X) = b_i, \\ & X \succeq 0 \end{aligned} \tag{2.18}$$

where $C, A$, and $X$ are symmetric matrices, $b$ is a real vector, and $X$ is held positive semidefinite. The conjugate dual formulation can be expressed as a maximization of the vector of

dual variables, $y$, within an inner minimization of the primal:

$$\begin{aligned} \max \quad & b^T y \\ \text{s.t.} \quad & S = C - \sum_i y_i A_i \\ & S \succeq 0, \end{aligned} \tag{2.19}$$

where $S$ is the dual slack matrix.

Feasible primal and dual solutions provide upper and lower bounds on the optimal value of the objective function. A solution is feasible if it satisfies the primal and dual constraints, respectively. The difference between the primal and dual objective values—the duality gap—vanishes if and only if the solution is a global optimum, a result first established by Erdahl in the context of 2-RDM theory [100].

## 2.4 Variational Two-Particle Reduced Density Matrix Method

In the context of solving the Schrödinger equation, Eq. 2.18 takes $C$ to be the Hamiltonian matrix, while $A$ and $b$ encode the $p$-positivity conditions. The optimization variable $X$ is a block-diagonal matrix composed of the particle-particle RDM ($^2D$), hole-hole RDM ($^2Q$), and particle-hole RDM ($^2G$),

$$X = \begin{bmatrix} {}^2D & 0 & 0 \\ 0 & {}^2Q & 0 \\ 0 & 0 & {}^2G \end{bmatrix}. \tag{2.20}$$

Minimizing the energy of a 2-RDM subject to the 2-positivity constraints via boundary-point semidefinite programming is known as the Variational 2-RDM Method (v2RDM) [68, 70, 72,

74–76, 80, 99]. The v2RDM algorithm can be expressed as:

$$\min_{^2D} \ \mathrm{Tr}(^2KX) \tag{2.21}$$

$$\text{s.t. } {}^2D \succeq 0 \tag{2.22}$$

$${}^2Q \succeq 0 \tag{2.23}$$

$${}^2G \succeq 0 \tag{2.24}$$

$$\mathrm{Tr}(^2D) = N(N-1) \tag{2.25}$$

$${}^2Q = f_Q(^2D) \tag{2.26}$$

$${}^2G = f_G(^2D). \tag{2.27}$$

Here, the 2-positivity conditions include positive semidefiniteness of the 2-RDMs, in addition to linear mappings among the ${}^2D$, ${}^2Q$, and ${}^2G$ matrices and a trace condition $N(N-1)$. The ${}^2D$ is further constrained to be Hermitian and antisymmetric with respect to particle exchange.

In variational 2-RDM methods, a zero duality gap guarantees that the optimal energy has been attained within the convex set defined by the positivity conditions. When only the necessary $N$-representability conditions are imposed, the resulting energy provides a lower bound to the FCI energy in the chosen basis. Implementing the 2-positivity conditions within the described SDP procedure results in a favorable computational scaling of $\mathcal{O}(r^6)$, where $r$ is the rank of the one-particle basis set. Within a CASSCF framework, v2RDM enables accurate treatment of multireference effects in active spaces far larger than those accessible to the traditional wavefunction-based complete active space self-consistent field method [78, 101–108].

# Part II

# Characterizing Open Quantum Systems via Single-Particle Geometry

# CHAPTER 3

# OPEN QUANTUM SYSTEM VIOLATES GENERALIZED PAULI CONSTRAINTS ON QUANTUM DEVICE

This chapter is reprinted (adapted) with permissions from *Commun. Phys.* **2023**, *6*, 180, 2399-3650

## 3.1 Chapter Synopsis

The Pauli exclusion principle governs the fundamental structure and function of fermionic systems from molecules to materials. Nonetheless, when such a fermionic system is in a pure state, it is subject to additional restrictions known as the generalized Pauli constraints (GPCs). Here, we verify experimentally the violation of the GPCs for an open quantum system using data from a superconducting-qubit quantum computer. We prepare states of systems with three-to-seven qubits directly on the quantum device and measure the one-fermion reduced density matrix (1-RDM) from which we can test the GPCs. We find that the GPCs of the 1-RDM are sufficiently sensitive to detect the openness of the 3-to-7 qubit systems in the presence of a single-qubit environment. Results confirm experimentally that the openness of a many-fermion quantum system can be decoded from only a knowledge of the 1-RDM, with potential applications from quantum computing and sensing to noise-assisted energy transfer.

## 3.2 Introduction

In 1925 Pauli postulated that two identical fermions cannot occupy the same quantum state [109], a principle that has wide-ranging implications for the qualitative behavior of fermionic systems, e.g., Aufbau principle. Shortly thereafter, Dirac and Heisenberg showed

that the Pauli exclusion principle is a consequence of the antisymmetry of the fermion wavefunction [19, 110]. As shown by Coleman in 1963 [84], when the exclusion principle is applied to the occupations of the natural orbitals (eigenfunctions) of the one-electron reduced density matrix (1-RDM), it provides necessary and sufficient constraints that the 1-RDM is representable by at least one ensemble $N$-electron density matrix, known as ensemble $N$-representability conditions. In 1971, using calculations on IBM computers, Borland and Dennis discovered additional restrictions on the natural-orbital occupations, known as the *generalized Pauli constraints* (GPCs) or pure-state $N$-representability conditions [87]. While the first constraint discovered by Borland and Dennis is specific to 3 electrons in 6 orbitals—the Borland-Dennis constraint, more recently, Klyachko and Altunbulak generalized the Borland-Dennis constraint using enumerative algebraic geometry to generate inequalities that include larger numbers of particles and orbitals [88, 89]. These constraints allow for a systematic interpretation of the 1-RDM behavior with applications in electronic structure theory [71, 111–121], open quantum systems [122–124], and the foundations of quantum theory [71, 111]. Additionally, GPCs can be used to assess the nature of electron correlation and entanglement, which may be exploited to address aspects of quantum simulation and error-mitigation on noisy intermediate-scale quantum (NISQ) devices.

Recently, Smart, Schuster, and Mazziotti randomly prepared correlated quantum many-fermion states on the quantum computer and measured their satisfaction of the GPCs [125]. This work experimentally verified the GPCs and highlighted restrictions imposed by the GPCs on many-qubit systems in pure states. Prior to this demonstration, Chakraborty and Mazziotti postulated the sufficient condition for openness of a many-fermion quantum system at the level of a single fermion by probing the 1-RDM's violation of GPCs [124]. These findings provided a geometric picture of a quantum system's interaction with its environment (quantum noise) based on the GPCs, and offered insight into the relationship between entanglement and openness of a quantum system. In this work, we experimentally verify the GPCs

as sufficient conditions for the openness of quantum systems using a superconducting-qubit quantum computer. Specifically, we prepare quantum states of systems with three-to-seven qubits and measure occupations of their natural orbitals on quantum devices, where each qubit is treated as a site with one fermion and two separate orbitals. Quantum computation allows us to measure experimentally the orbital occupations and provide a framework for probing GPCs in open quantum systems, opening new avenues for novel approaches to quantum sensing and simulation.

## 3.3 Theory and Methods

### *3.3.1 Theory*

Quantum computation allows for direct preparation of quantum states and is suitable for studying highly entangled systems [105, 126–137]. We systematically prepare quantum states of systems with three-to-seven qubits and measure eigenvalues of the one-fermion reduced density matrix (1-RDM) on the ibmq_jakarta quantum computer accessed through IBM Quantum [138]. The 1-RDM is defined by the integration of the $N$-fermion density matrix over the coordinates of all fermions except one

$$^1D(1;\bar{1}) = \int {}^N D(12\ldots N;\bar{1}2\ldots N)d2d3\ldots dN. \tag{3.1}$$

The eigenfunctions of the 1-RDM are known as the natural orbitals $\phi_i$, and the eigenvalues are known as the natural orbital occupation numbers $n_i$. The Borland-Dennis constraints on three fermions in six orbitals, also known as generalized Pauli constraints (GPCs) or pure-state $N$-representability conditions of the 1-RDM, can be expressed in terms of the natural

occupation numbers

$$n_5 + n_6 - n_4 \geq 0 \tag{3.2}$$

$$n_1 + n_6 = 1, \quad n_2 + n_5 = 1, \quad n_3 + n_4 = 1, \tag{3.3}$$

where $n_i \geq n_{i+1}$ [87]. If the GPCs are satisfied, there is at least one $N$-qubit state which is pure. However, not every $N$-qubit state that satisfies the GPCs is necessarily a pure state. Therefore, the violation of the GPCs provides only a sufficient condition for determining the ensemble character, i.e., openness of the quantum system. The physical relevance of GPCs to many-fermion systems is the most prominent in cases of complete saturation (pinning) and partial saturation (quasipinning) of the constraints [111, 112, 115, 116, 139] where pinning (or quasipinning) reveals fundamental one-body symmetries (or quasi-symmetries) of the system.

In the case of three fermions in six orbitals, the ordered set of the three smallest 1-RDM eigenvalues forms a polytope, a closed convex set with flat facets, known as the Pauli polytope, shown in Fig. 4.1. Both the yellow and blue regions of the polytope are allowed for occupation numbers from an ensemble (open) system, but only the yellow region of the polytope is allowed for a pure-state system. The facet separating the yellow and blue regions is the first-discovered GPC—the Borland-Dennis constraint. The following key states from quantum information are labeled in the polytope: $|W\rangle$ $(\frac{1}{3},\frac{1}{3},\frac{1}{3})$ [140], |EPR (Einstein–Podolsky–Rosen)$\rangle$ $(\frac{1}{2},\frac{1}{2},0)$ [141], and |GHZ (Greenberger-Horne-Zeilinger)$\rangle$ $(\frac{1}{2},\frac{1}{2},\frac{1}{2})$ [142], and an unentangled state |Slater$\rangle$ (0,0,0).

For four fermions in eight orbitals and five fermions in ten orbitals, there are 14 and 161 known inequalities, respectively, that define their necessary and sufficient pure-state $N$-representability conditions [89]. Violation of a single constraint demonstrates that the quantum system cannot be in a pure $N$-electron state. Here, we restrict the fermions and their orbitals to form qubits. The $2N$ orbitals are paired with the occupation of each pair

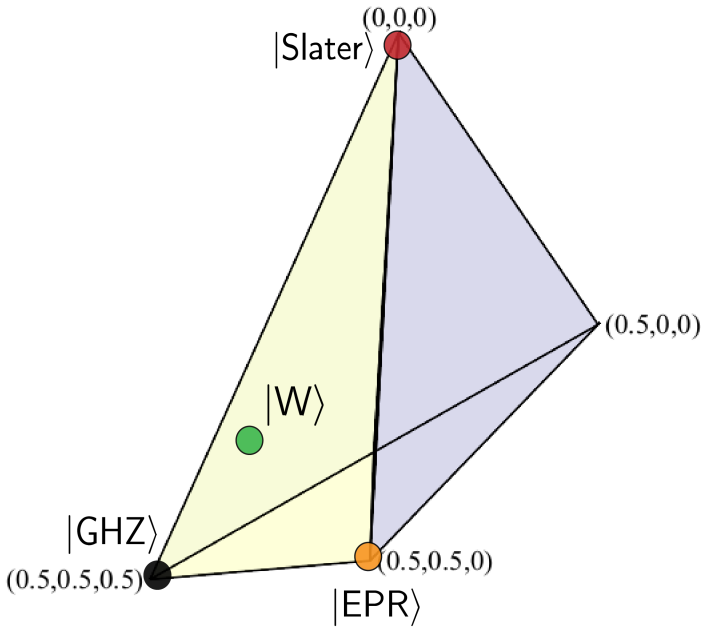


Figure 3.1: A convex set, known as the Pauli polytope, formed from the ordered natural occupations of the one-particle reduced density matrix (1-RDM) for three fermions in six orbitals. The sets of occupations lying inside the yellow region of the polytope, i.e., obeying the generalized Pauli constraints (GPCs), are compatible with at least one closed (pure-state) quantum system. Sets of natural occupations that lie in the blue region of the polytope, i.e., violating the GPCs, are only compatible with an open (ensemble) quantum system. The labeled points represent characteristic entangled states captured by the polytope, $|W\rangle$ $(\frac{1}{3},\frac{1}{3},\frac{1}{3})$, |EPR (Einstein–Podolsky–Rosen)⟩ $(\frac{1}{2},\frac{1}{2},0)$, and |GHZ (Greenberger-Horne-Zeilinger)⟩ $(\frac{1}{2},\frac{1}{2},\frac{1}{2})$, and an unentangled state |Slater⟩ (0,0,0) for this system.

of orbitals being restricted to one fermion. Importantly, in this case in which the fermions are also qubits, the GPCs for $N$ fermions in $2N$ orbitals reduce to a single inequality [143] defined as

$$\sum_{i=N+2}^{r} n_i - n_{N+1} \geq 0, \tag{3.4}$$

where $n_i$ are the smallest $N$ eigenvalues for the system and $r$ is the number of orbitals.

Each qubit on a quantum device is composed of a particle and a hole, and collectively these particles and holes obey fermion statistics. This is true even though the qubits, which are particle-hole quasi-particles, do not obey fermion statistics. Though our approach does not explicitly specify using a quantum device built from fermions, as recently proposed in [144], it allows for probing the GPCs on quantum systems that follow fermion statistics by directly measuring orbital occupations on quantum computers, as supported by our previous work [125, 129, 130, 137]. Since we are exploring a phenomenon produced as a consequence of the qubit particle-hole physics and not a transformation mapping, the presented framework allows for an experimental demonstration of the GPC behavior in open quantum systems. We emphasize that because the measurement is performed on a quantum system that obeys fermion statistics, the results provide experimental evidence that supports the GPC behavior for any quantum system obeying fermion statistics including systems that are composed of either composite or fundamental fermions.

A ladder-like state preparation with multiple variables and a 1-RDM tomography, described in the Methods, are employed to explore the 1-RDM set on the quantum computer. The variables in the state preparation are sampled randomly to cover the allowed set of 1-RDMs. While $m$ qubits are prepared in a state on the device, $n$ of the $m$ qubits are treated as part of the system with the remaining $m-n$ qubits representing the bath (environment). When $m = n$, the system is closed, and the GPCs of the system 1-RDM are satisfied by all randomly prepared states. When $m > n$, however, the $n$-qubit system is open, and the GPCs of the system 1-RDM may be violated by some of the prepared states. Demonstra-

tion of the GPC violation shows experimentally that the GPCs are only required for pure quantum states. The experiment probes one of the most fundamental relations in quantum mechanics—the Pauli exclusion principle and its generalization.

### *3.3.2 Methods*

#### Quantum State Preparation

The state preparation algorithm used in this work employs unitary rotations of control and target qubits with CNOT gates in between (Fig. A.1). For a four-qubit system, this can be expressed as

$$\begin{aligned}\mathbb{U}_a = U_3(\theta_{10},\phi_{10},\lambda_{10})U_2(\theta_9,\phi_9,\lambda_9)C_2^3\\ U_2(\theta_8,\phi_8,\lambda_8)U_1(\theta_7,\phi_7,\lambda_7)C_1^2\\ U_1(\theta_6,\phi_6,\lambda_6)U_0(\theta_5,\phi_5,\lambda_5)C_0^1\\ U_3(\theta_4,\phi_4,\lambda_4)U_2(\theta_3,\phi_3,\lambda_3)\\ U_1(\theta_2,\phi_2,\lambda_2)U_0(\theta_1,\phi_1,\lambda_1)\end{aligned}$$

where $U_i$ are unitary rotations around three Euler angles ($\theta_{i+1}$, $\phi_{i+1}$, $\lambda_{i+1}$) on qubit $i$. The $\mathrm{U}_3$ gates are defined as

$$U_3(\theta,\phi,\lambda) = \begin{bmatrix} \cos\left(\frac{\theta}{2}\right) & -\mathrm{e}^{i\lambda}\sin\left(\frac{\theta}{2}\right) \\ \mathrm{e}^{i\phi}\sin\left(\frac{\theta}{2}\right) & \mathrm{e}^{i\phi+i\lambda}\cos\left(\frac{\theta}{2}\right) \end{bmatrix}, \tag{3.5}$$

and the CNOT gates, $\mathrm{C}_i^j$ are standard with $i$ control and $j$ target qubits. The same algorithm is applied to all state preparations with additional rotations and CNOT gates added for each extra qubit in the system (see Appendix A Figs. A.1-A.5). The many unitary rotations allow

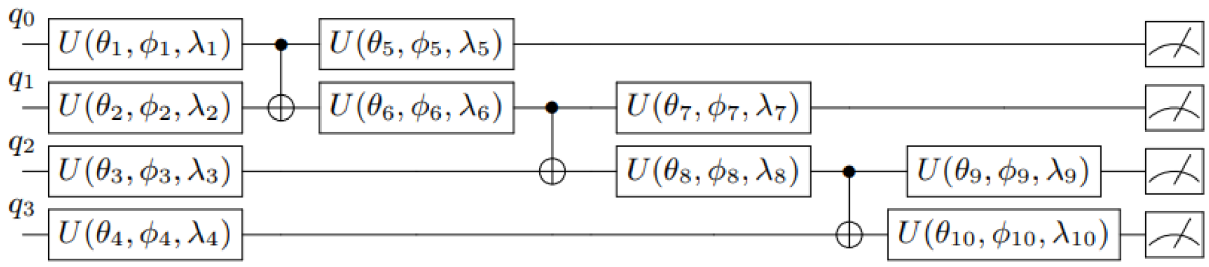


Figure 3.2: Quantum circuit used for the state preparation of a four-qubit system. The same logic was used for all state preparations (Appendix A Figures A.1-A.5).

for a wide range of parameter tuning to span the entirety of the Pauli polytope. Additionally, this algorithm includes some local degrees of freedom [145] and suggests that qubit-ordering dependence may be removed [125]. 2050 measurements of each prepared state were made to ensure statistical robustness of the collected data. The measurements were obtained by simulating each circuit over a range of random angles, $\theta$, $\phi$, and $\lambda$, from $-180°$ to $180°$ used for the single-qubit unitary rotations of qubits, as defined above.

## Quantum State Tomography

To directly measure the eigenvalues of the 1-RDM on a quantum device, we exploit the restriction of the $N$-fermions in $2N$-orbitals system to a system of $N$ qubits, where each qubit is a two-level system sharing an electron. In second quantization the elements of the 1-RDM are given by

$$ {}^1D^i_j = \langle\psi|\, \hat{a}^\dagger_i \hat{a}_j \,|\psi\rangle\,, \tag{3.6} $$

where $\hat{a}^\dagger_i$ creates a particle in the $i$-th orbital and $\hat{a}_j$ annihilates a particle in the $j$-th orbital, where $i$ and $j$ correspond to the same qubit [136]. A one-qubit 1-RDM can be constructed as follows,

| | $\hat{a}_{p,0}$ | $\hat{a}_{p,1}$ |
|---|---|---|
| $\hat{a}^\dagger_{p,0}$ | $\hat{a}^\dagger_{p,0}\hat{a}_{p,0}$ | $\hat{a}^\dagger_{p,0}\hat{a}_{p,1}$ |
| $\hat{a}^\dagger_{p,1}$ | $\hat{a}^\dagger_{p,1}\hat{a}_{p,0}$ | $\hat{a}^\dagger_{p,1}\hat{a}_{p,1}$ |

for some qubit $p$. In the Pauli basis, these elements can be written as,

$$\hat{a}^\dagger_{p,0}\hat{a}_{p,0} = \begin{pmatrix} 1 & 0 \\ 0 & 0 \end{pmatrix} = \frac{1}{2}(I + Z_p) \tag{3.7}$$

$$\hat{a}^\dagger_{p,0}\hat{a}_{p,1} = \begin{pmatrix} 0 & 1 \\ 0 & 0 \end{pmatrix} = \frac{1}{2}(X_p + iY_p) \tag{3.8}$$

$$\hat{a}^\dagger_{p,1}\hat{a}_{p,0} = \begin{pmatrix} 0 & 0 \\ 1 & 0 \end{pmatrix} = \frac{1}{2}(X_p - iY_p) \tag{3.9}$$

$$\hat{a}^\dagger_{p,1}\hat{a}_{p,1} = \begin{pmatrix} 0 & 0 \\ 0 & 1 \end{pmatrix} = \frac{1}{2}(I - Z_p) \tag{3.10}$$

Since the expectations of the single-qubit Pauli matrices can be directly obtained on a quantum device, it is straightforward to obtain the expectation values of the 1-RDM elements for each state preparation.

## Quantum Device Specifications

This work utilized superconducting-qubit IBM Quantum devices available online, ibmq_qasm_simulator, ibmq_jakarta, and a noise model qasm simulator of ibmq_jakarta (qasm_simulator(ibmq_jakarta)). ibmq_jakarta is one of the IBM Quantum Falcon Processors [138, 146]. The quantum computer is composed of fixed-frequency transmon qubits with co-planar waveguide resonators [147, 148]. For calibration details see Appendix A Table A.1.

## 3.4 Results

For three-qubit quantum states the 1-RDM natural occupations, obtained from measurement of the 1-RDM on the quantum computer, are shown in the Pauli polytope in Fig. 3.3 (a) (and also in Appendix A Figure A.16). The obtained result is in close agreement with the findings shown by Smart et al. [125], with the majority of measured occupation sets being inside the GPC-defined region of the polytope (yellow). The simulated results (Appendix A Figures A.6 and A.11) show no GPC violation, which indicate that the states in violation in Fig. 3.3 (a) are a consequence of the quantum noise. Therefore, we confirm that a closed three-qubit system obeys GPCs for three fermions in six orbitals.

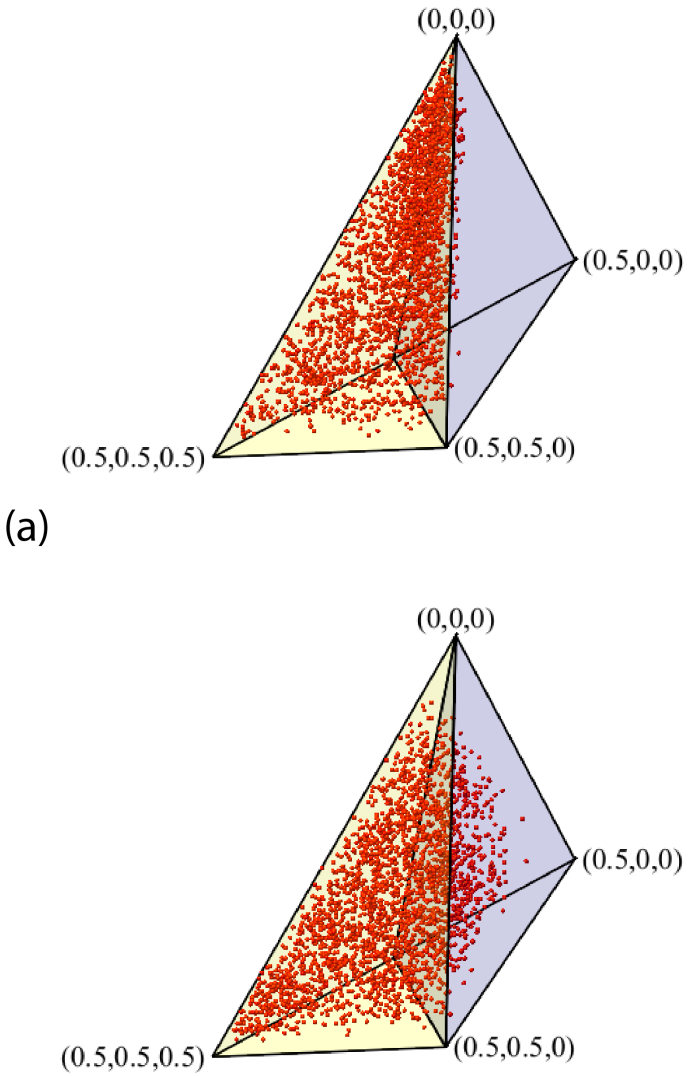


Figure 3.3: Polytopes showing the sets of three lowest natural occupations, ordered from highest to lowest, for the three-qubit system (a) and for the four-qubit system (b), measured on ibmq_jakarta. The sets of occupations lying inside the yellow region of the polytope are compatible with at least one closed (pure-state) quantum system. Sets of natural occupations that lie in the blue region of the polytope are only compatible with an open (ensemble) quantum system. Addition of a single environmental qubit to the closed three-qubit system results in the violation of the generalized Pauli constraints (GPCs) and allows the quantum system to reach openness.

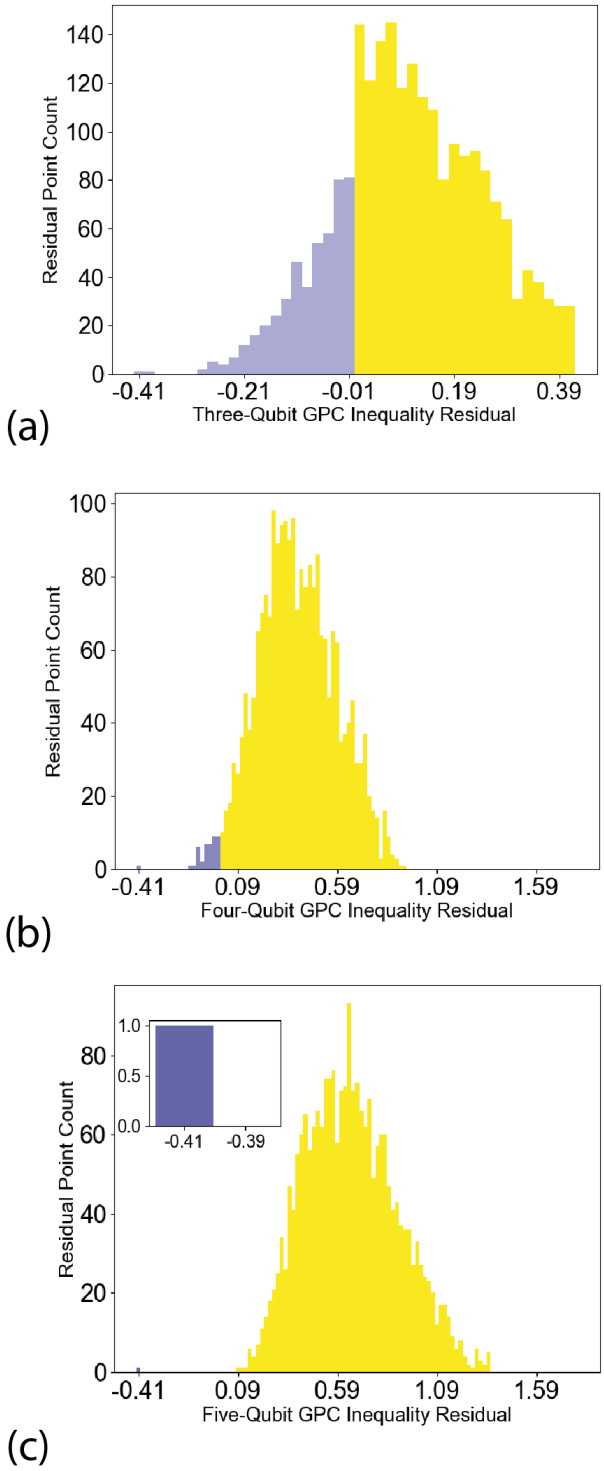


Figure 3.4: Bar graphs showing the distribution of higher-inequality residuals in the region defined by the generalized Pauli constraints (yellow only) and the region defined by ordinary Pauli constraints (blue and yellow) for the five-qubit system, collected on ibmq_jakarta; (a) three-qubit inequality, (b) four-qubit inequality, (c) five-qubit inequality.

To investigate the GPC behavior with an additional (environmental) qubit added to the three-qubit system, we prepared and measured four-qubit states on the quantum device. Here, the $N$-representability inequalities for both, a system of three fermions in six orbitals (three qubits), and a system of four fermions in eight orbitals (four qubits), were examined. When the ancillary qubit is treated as an environmental qubit, the GPCs for the three-qubit system are violated (Fig. 3.3 (b)), with a significant portion of the measured occupation sets being in the blue region of the polytope, defined solely by the ordinary Pauli constraints. When all four qubits are treated in the same conditions, there is no violation of the inequalities for the four-qubit system. These results, consistent in noiseless (Appendix A Figure A.7) and noisy environments (Appendix A Figures A.12 and A.17), experimentally verify the sufficient condition at the level of a single particle for openness of a many-particle quantum system, as proposed by Chakraborty and Mazziotti [124]. We show that to reach sets of occupation numbers that are only compatible with an open three-qubit quantum system, it is sufficient to add one environmental qubit to the closed three-qubit system. This demonstration of the expansion of accessible 1-RDMs provides a unique tool for determining the optimal size of the effective bath in open quantum system modeling on quantum devices.

The distributions captured for a five-qubit system in Fig. 3.4 (a)-(c) suggest that a single ancilla qubit may also be sufficient for there to be a violation of the four-qubit GPCs (constraints for 4 fermions in 8 orbitals) to indicate openness of the four-qubit system (Fig. 3.4 (b)). Though the number of states outside the GPC-defined region is low, the system still shows evidence for the sufficient condition for openness being at the level of a single particle, even in the presence of quantum noise. Furthermore, results simulated in the noiseless environment for all studied systems show that treating one of the m qubits as the environment generates an $(m-1)$-qubit open system whose openness is detectable by the $(m-1)$-qubit GPC (Appendix A Figures A.8, A.9, and A.10).

These findings support previous conclusions by Liebert et al. [149] on the hierarchy of

generalized exclusion principle constraints and are in line with the bounds of Borland-Dennis GPCs for a mixed state considered by Hackl et al. [144]. In particular, our results demonstrate how the flexibility of higher-order inequalities for some $n$-qubit system exposes the lower-order inequalities in the $(m-n)$-qubit environment, where $m > n$ (Appendix A Figures A.13-A.15, A.18-A.20). This generalization goes beyond the Borland-Dennis setting and provides a method for analyzing the mixed-state GPCs in qubit systems.

To assess the connection between the GPC inequalities and the degree of entanglement in the considered systems, we analyze the GPC inequality residual as a function of von Neumann entropy [150]. Fig. 3.5 and Appendix A Figures A.21-A.25 show the von Neumann entropy, generally, being minimized in the limit of high GPC violation. Additionally, the results demonstrate how states in the pure-state polytope regime (yellow points in Fig. 3.5) can exhibit a greater mixed character in the 1-RDM than the states in the ensemble-state polytope regime (light blue points with GPC inequality residual $< 0$ in Fig. 3.5). Finally, increasing entropy in the system shifts it away from the Borland-Dennis setting, which can be directly quantified in the comparison between an ideal simulation and a noisy quantum device, making this analysis a useful tool for error mitigation purposes.

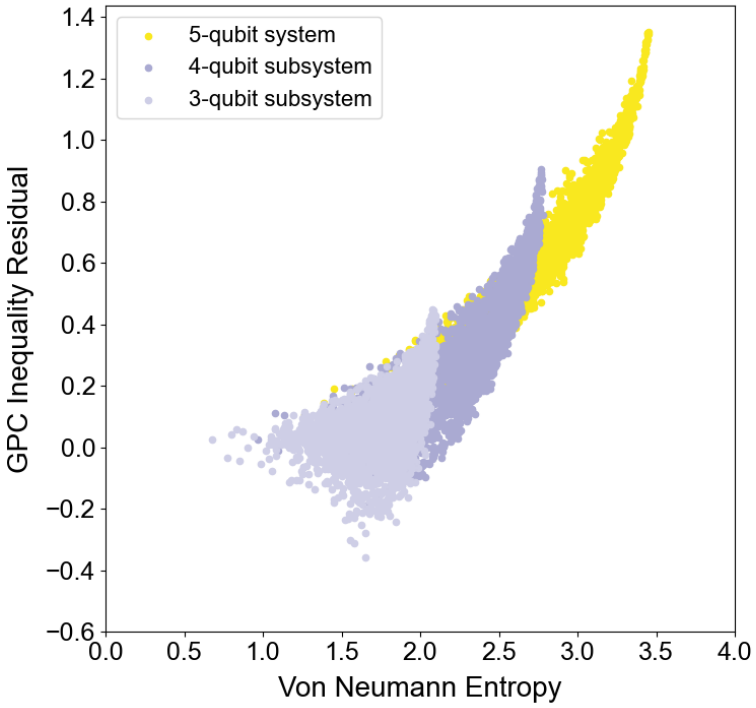


Figure 3.5: Generalized Pauli constraints (GPCs) inequality residual plotted as a function of von Neumann entropy for the 5-qubit system and its respective, 4- and 3-qubit subsystems from occupations measured on ibmq_jakarta. Light (dark) blue points represent the subsystem where there is some amount of violation of the respective, 3-qubit (4-qubit) GPC inequality for the prepared states. Yellow points represent the total system, where there is no violation of the respective 5-qubit GPC inequality for the prepared states.

## 3.5 Discussion and Conclusions

We have experimentally verified the violation of the GPCs in an open quantum system. Specifically, we showed that the GPCs of a $n$-qubit system with a $(m-n)$-qubit environment where $m > n$ are generally violated. The importance of the result is that it shows that evidence of the openness of a many-fermion quantum system can be decoded from only a knowledge of the 1-RDM. In the case of the 3-qubit systems we have an intuitive, geometric picture of the violation in terms of a violation of the Borland-Dennis facet of the GPC polytope. Similarly, for higher-qubit systems the degree of the GPC violation provides a

computational measure of the openness of the quantum system.

This experimental verification of the violation of GPCs due to environmental interactions has potentially important applications from quantum computing and sensing to noise-assisted energy transfer. First, they may be used for development of efficient quantum simulation algorithms for open quantum systems; for example, in combination with the density-matrix purification theory [151], they provide a framework for determining a practical size of the effective bath. Second, we observe that the 1-RDM eigenvalue sets measured on the quantum computer are consistently pulled away from the edge states, $|\text{EPR}\rangle$, $|\text{GHZ}\rangle$, and $|\text{Slater}\rangle$, toward the inside of the GPC-defined polytope, suggesting a signature behavior of quantum noise with respect to the Pauli polytope. Considering origins and nature of such 1-RDM behavior with respect to the GPCs has the potential to serve as a benchmarking tool for noise characterization on different quantum devices and development of novel noise-mitigation techniques. Third, the GPCs can be used in multi-qubit quantum sensors to enhance their sensitivity over 1- or 2-qubit quantum sensors. Finally, because the violation of the GPCs enlarges the set of physically accessible 1-RDMs, it can be used to understand and predict the role of noise in assisting energy transfer.

In summary, the demonstration of GPC violation in open quantum systems on quantum devices probes one of the most fundamental relations in quantum mechanics—the Pauli exclusion principle and its generalization. While many experiments have confirmed and reconfirmed that two fermions cannot occupy the same quantum state—the Pauli exclusion principle for fermions, the present work provides an experimental demonstration of the satisfaction and violation of the pure-state generalized Pauli exclusion principle in closed and open quantum systems, respectively. Albeit a fundamental result, the GPCs are central to many-fermion and many-qubit quantum systems with potential applications to building more error-tolerant quantum computers, designing more sensitive multi-qubit quantum sensors, and harnessing the environment to enhance energy transfer in materials.

## 3.6 Acknowledgments

D.A.M. gratefully acknowledges NSF QuBBE Quantum Leap Challenge Institute (NSF OMA-2121044), the U.S. National Science Foundation Grants No. CHE-2155082 and CHE-2035876, and the Department of Energy, Office of Basic Energy Sciences, Grant DE-SC0019215. L.M.S. acknowledges support from the NSF Graduate Research Fellowship Program, Grant DGE-1746045. We acknowledge the use of IBM Quantum services for this work. The views expressed are those of the authors, and do not reflect the official policy or position of IBM or the IBM Quantum team. The data supporting this Chapter can be found in Appendix A.

# CHAPTER 4

# QUANTUM SENSING USING MULTI-QUBIT QUANTUM SYSTEMS AND THE PAULI POLYTOPE

This chapter is reprinted (adapted) with permissions from *Phys. Rev. Research* **2023**, *5*, 4, 043097-043108

## 4.1 Chapter Synopsis

Quantum sensing has highly practical, potential applications in fields ranging from fundamental physics and quantum communication to biophysics and bioengineering. However, achieving high fidelity and control of entangled qubits that enable sensing beyond the quantum limit is still a challenging endeavor. In this study, we present a novel approach to quantum sensing, which we call open-system quantum sensing, where we exploit a generalization of the Pauli exclusion principle to sense the openness of a multi-qubit quantum system from only measurement of the qubit occupations. Qubit occupations of a pure state obey generalized Pauli exclusion constraints that define a convex set known as the Pauli polytope, and hence, violation of one of these constraints—a facet of the polytope—reveals a mixed state from the interaction of a quantum system with its environment without performing full-state tomography. We examine experimental ultrafast spectroscopic data from the photosynthetic light harvesting complex in green sulfur bacteria and show that we can sense and decode the relaxation of the complex due to environmental noise. More generally, we can apply open-system quantum sensing with any general multi-qubit quantum system where it provides a unique, visual approach that promises enhanced sensitivity and fidelity.

## 4.2 Introduction

Quantum sensors harness the high sensitivity of quantum systems to external disturbances to gain more information about the world around us. For example, technological applications of quantum sensing are found in precision timekeeping [152, 153], high-energy physics [154], diagnostic screenings, and single-molecule detection [155–160]. Diamond-based spin qubits, in particular, present a promising platform for high-sensitivity measurements [161]. Optical and magnetic properties of spin defects are studied extensively, providing detailed information on their energy level structures, coherence times, and spin properties [162–167]. Sensing with a single electron spin, such as that in a negatively charged nitrogen-vacancy (NV) center in diamond, relies on optimization of the two-level spin dynamics. The NV center spin state can be readily initialized via optical pumps, coherently manipulated using pulsed radiation, and measured with high fidelity. A greatly desired scientific goal has been realizing entangled networks of such spin qubits, which allow for sensitivity measurements that surpass the standard quantum limit. Though significant experimental progress in ensemble sensing has been made [155, 168–180], noise still presents a limitation in achieving greater coherence times of correlated sensors. To benefit from entanglement, it is necessary to understand the environmental fluctuations affecting the dynamics of the system of interest and the effect of internal degrees of freedom on the attainable sensitivity levels.

Fermionic systems naturally exhibit entanglement with a canonical example of a pair of indistinguishable fermions in an antisymmetric pure state [14, 181]. In 1925 Pauli recorded that no more than one fermion can occupy a spin orbital [109], requiring the occupations of that orbital to be between zero and one. Additional restrictions on three-electron systems, known as the *generalized Pauli constraints* (GPCs), were discovered by Borland and Dennis in 1971, paving the way for the development of entanglement polytopes [182], GPC-based electronic structure algorithms [121, 124, 183–187], studies on fundamental symmetries of systems [111, 112, 115, 116, 139], and even experimental demonstrations of the phenomenon

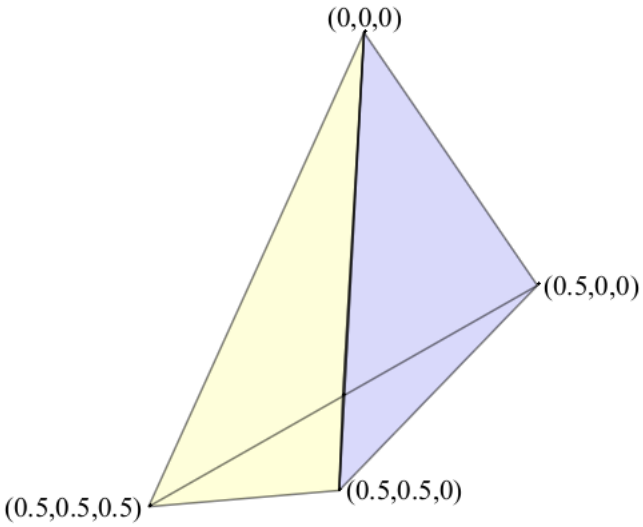


Figure 4.1: A convex set formed from the ordered natural occupations of the 1-RDM for three fermions in six orbitals. The sets of occupations lying inside the yellow region of the polytope, the pure-state Pauli polytope, are compatible with at least one closed (pure-state) quantum system. Sets of natural occupations that lie in the blue region of the polytope are only compatible with an open (ensemble) quantum system.

on quantum devices [125, 137]. The advantage of considering GPCs in terms of quantum sensing becomes apparent when going beyond the one-qubit sensing regime since the condition holds for $p$ qubits, where $p$ is arbitrary [87, 88, 143, 187]. In this work we present a scheme for open-system quantum sensing using a multi-qubit quantum system. We provide a theoretical framework in terms of the set of one-particle reduced density matrices (1-RDMs) for sensing openness of a 3-qubit system. The 1-RDM is defined by the integration of the $N$-fermion density matrix over the coordinates of all fermions except one

$$^1D(1;\bar{1}) = \int {}^N D(12\ldots N;\bar{1}2\ldots N)d2d3\ldots dN. \tag{4.1}$$

The eigenfunctions of the 1-RDM are known as the natural orbitals $\phi_i$, and the eigenvalues are natural orbital occupation numbers $n_i$. By applying our model to the data available

from an experimental study of the eight-chromophore Fenna-Matthews-Olson (FMO) complex [188, 189], we provide a practical analysis of a complex many-body environment and characterize the multi-qubit sensing ability under realistic conditions. We extract the desired sensing information on the noise-assisted relaxation process in the system by examining multiple 3-qubit subsystems and their geometric 1-RDM-based pictures in the Pauli polytope (Fig. 4.1).

## 4.3 Results

When the Pauli exclusion principle,

$$0 \leq n_i \leq 1 \tag{4.2}$$

is applied to the occupations of natural orbitals of the 1-RDM, $n_i$, it provides necessary and sufficient constraints that the 1-RDM is representable by at least one ensemble $N$-electron density matrix, also known as *ensemble $N$-representability conditions* [84]. In the presence of a third spin-$\frac{1}{2}$ particle, the *generalized Pauli constraints* (GPCs) for 3 fermions in 6 orbitals feature

$$n_5 + n_6 - n_4 \geq 0 \tag{4.3}$$

$$n_1 + n_6 = 1, \quad n_2 + n_5 = 1, \quad n_3 + n_4 = 1, \tag{4.4}$$

where $n_i \geq n_{i+1}$. They are also known as the *pure $N$-representability conditions* [87] since they only hold for pure states of 3 fermions. The sum rule for natural-orbital occupations in Eq. 4.4 is obeyed for all times, restricting the sum of the fermion population on each site to 1; therefore, the system of 3 fermions in 6 orbitals can be treated as a system of 3 qubits [143]. In the case where fermions are also qubits, the GPCs for $N$ fermions in $2N$

orbitals reduce to a single inequality [124, 143, 187] defined as,

$$\sum_{i=N+2}^{r} n_i - n_{N+1} \geq 0, \tag{4.5}$$

where $n_i$ are the smallest $N$ eigenvalues for the system and $r$ is the number of orbitals. Already for 3-qubit states there exist two physically distinct ways of entanglement represented by the Greenberger-Horne-Zeilinger $|GHZ\rangle$ [142] and $|W\rangle$ [140] states. The ordered set of the three smallest 1-RDM eigenvalues of a 3-qubit system forms a polytope, a closed convex set with flat facets shown in Fig. 4.1. The polytope serves as a visual tool for the detection of entanglement between particles, i.e., the deviation of points from the (0,0,0) point in the polytope, which is the Slater determinant. Both the yellow and blue regions of the polytope are allowed for occupation numbers from an ensemble (open) system, but only the yellow region of the polytope is allowed for a pure-state system. We refer to this part as the pure-state Pauli polytope.

To apply the GPCs to entanglement-enhanced sensing, we consider a sample of the eight-exciton FMO complex, previously studied by Higgins et al. [189] in view of photosynthetic light-harvesting, in particular, the variable steering of exciton energy transfer in reducing and oxidizing conditions. The FMO complex [188] is a well-characterized light-harvesting system present in green sulfur bacteria. It is comprised of three monomers, each containing eight bacteriochlorophyll-a (BChla) chromophores (sites), which serve as a molecular wire that facilitates energy transfer from the light-harvesting antennae to the reaction center. The Hamiltonian for this system is described as

$$\hat{H} = \sum_{j=1}^{8} \hbar\omega_j \sigma_j^+ \sigma_j^- + \sum_{j \neq l} \hbar\nu_{j,l} (\sigma_j^- \sigma_l^+ + \sigma_j^+ \sigma_l^-), \tag{4.6}$$

where $\hbar\omega_j$ is the site energy of each chromophore, $\hbar\nu_{j,l}$ is the coupling constant between the pair of chromophores $j$ and $l$, and $\sigma_j^+$ ($\sigma_j^-$) creates (annihilates) a single excitation on

chromophore $j$. In natural conditions, many light-harvesting complexes contain at most one excitation at a given time [190]; therefore, the representation of this system's density matrix can be restricted to an $M$-dimensional space of single excitations, where $M$ is the number of chromophore sites [112]. Each of the eight chromophores is generally treated as a single $\alpha$-spin fermion in a two-state model, where the two energy levels are separated by the excitation energy of the chromophore, so the terms *chromophore* and *qubit* are used interchangeably throughout this paper.

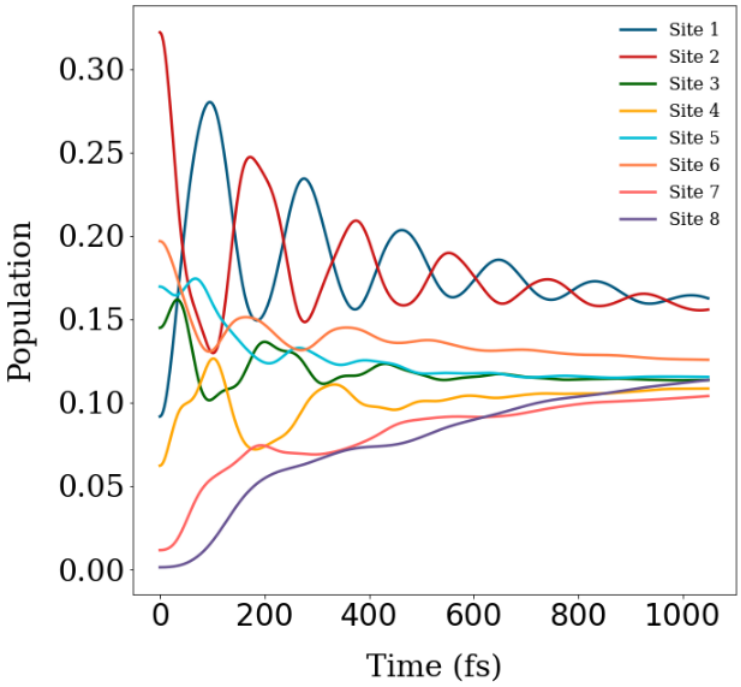


Figure 4.2: Population dynamics of the FMO energy transfer process at 77 K in the site basis. The initial excitation oscillates among the 8 sites but loses some of its population to environmental noise after 1 ps of the chromophore coherence lifetime.

The FMO complex is extensively used as a platform for studying quantum phenomena [191–196], and more recently, for machine learning and quantum information approaches to simulating energy transport processes in light-harvesting complexes [197–201]. This highly correlated exciton network features relaxation time on a timescale of femtoseconds and presents an ideal architecture for exploring the effects of entanglement on physical observables

of interest in quantum sensing. Figure 4.2 shows the site population in the FMO complex for the first 1 ps of the energy transfer process at 77 K. We employ the 8×8 Hamiltonian given in Ref. [202] and an 8-exciton density matrix, $D$, that was initialized following an optical excitation as employed in the ultrafast spectroscopy experiments described in Ref. [189] (see Appendix B.2). The population dynamics are generated by evolving the Lindblad equation,

$$\frac{d}{dt}D = -\frac{i}{\hbar}[\hat{H}, D] + \hat{L}(D), \tag{4.7}$$

where L is the Lindblad operator taken to be the sum of operators describing dephasing and dissipation of the system following the initial excitation [123]. The use of experimental values for dephasing and dissipation parameters, consistent with definitions in Ref. [203], along with the experimentally derived density matrix, provides a realistic treatment of the chromophore entanglement and its influence on the population dynamics. The initial excitation oscillates among the 8 sites, after which the system relaxes and loses some of its initial population to dissipation into the environment. The experimental FMO sample was not attached to a reaction center, so the population loss is primarily due to quantum noise experienced by the system from its interaction with the environment.

The generalized Pauli constraints (Eq. 4.3) allow us to model the relaxation process in the FMO complex by calculating the three smallest natural-orbital occupation numbers of the 3-qubit 1-RDMs obtained from the time evolution of the initial density matrix. The features of environmental noise and internal degrees of freedom on the time evolution trajectories are then inferred from the Pauli polytope. Figure 4.3 shows the trajectories of the natural occupation numbers of a 3-qubit FMO subsystem for 2 ps. The points colored black (red) show the spectrum outside (inside) the set of allowed 1-RDMs for pure quantum states. The FMO system is exposed to dephasing and dissipation noise; therefore, the initial 1-RDM is ensemble $N$-representable, sharply violating the GPCs. The system then enters the pure set periodically and eventually converges to a classical ensemble, $(\frac{1}{8}, \frac{1}{8}, \frac{1}{8})$, where the excitation

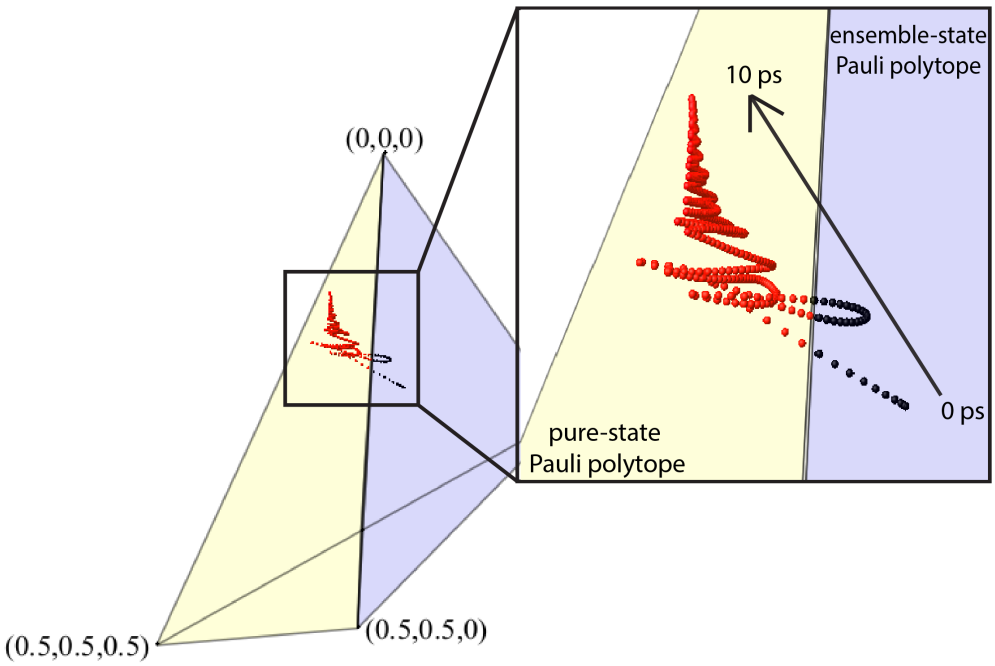


Figure 4.3: Pauli polytope showing the femtosecond trajectories of a 3-qubit subsystem (chromophores 1, 2, and 3) from the experimentally derived density matrix of the FMO complex. The blue (yellow) region of the polytope shows the spectrum outside (inside) the set of allowed $N$-electron pure states, also denoted using black (red) spheres. Due to the presence of dephasing and dissipation, the spectrum of this open quantum system originates in the blue region of the polytope, violating the GPCs, and converges to a classical ensemble, in the yellow region, at 10 ps, obeying the GPCs for the most part of the temporal evolution.

is spread equally among the eight sites. The equidistribution of energy over the degrees of freedom follows from the excitation reaching the classical limit over a sufficiently long period of time. In this scenario, the quantum noise, i.e., the environment, can be thought of as a quantum probe performing an indirect measurement on the 3 qubits in the system. Therefore, using the GPC framework, we are able to obtain geometric information about the openness of the 3-qubit system, i.e. its interaction with the environment, as a function of time from only a knowledge of its time-evolving 1-RDM. By measuring the temporal evolution of the openness of the system, we are able to sense the temporal evolution of the environment, providing us with an open-system quantum sensor. The use of a 3-qubit system

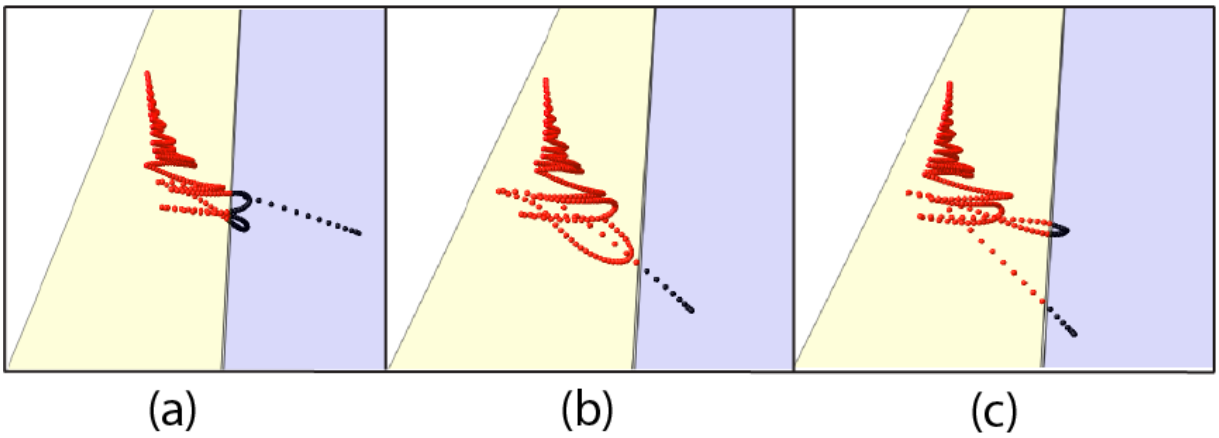


Figure 4.4: Temporal trajectories of different 3-qubit subsystems of the FMO complex for the first 2 ps of the energy transfer process from the experimentally derived density matrix. In each case, the time evolution produces an expanded set of 1-RDMs, violating the GPCs initially, and then converges to the classical limit at longer times. The three figures differ in the choice of one of the three qubits/chromophores in the subsystem: (a) 124, (b) 125, (c) 126 where, for example, 124 denotes chromophores 1, 2, and 4. Varying only one qubit shows enhanced measurements of the relaxation processes of the remaining qubits in the system.

is important because three is the smallest number of qubits whose 1-RDM can distinguish between an open (ensemble) and a closed (pure-state) quantum system [112]. Furthermore, the presence of three qubits supports an entangled multi-particle interaction that cannot be simulated by being broken into two-particle subsystems [182].

Our open-system quantum sensing approach can be represented using a generic quantum circuit model shown in Fig. 4.5. All three qubits are initially in the $|0\rangle$ state, which is flipped to $|1\rangle$ upon the excitation, as demonstrated with single-qubit X-gates. Following this excitation, the qubits can be manipulated via unitary operations to prepare different entangled states. Finally, the noise operator, $N$, is applied, representing the environment interacting with the 3-qubit system. In this example, $N$ may function as a well-defined Kraus operator that can be converted to unitary matrices in a dilation-based algorithm [198, 204]. The measurements provide single-qubit populations used for decoding the relaxation process of this multi-qubit system. If the prepared state is interacting with the environment, the pure-state Pauli polytope will be violated, demonstrating how the Pauli polytope can be

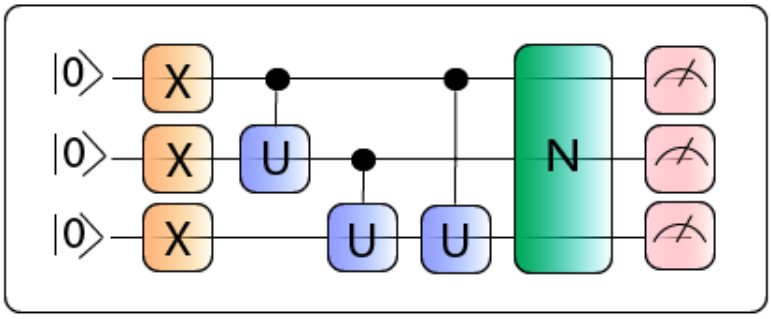


Figure 4.5: Arbitrary quantum circuit model representing the open-system quantum sensing scheme for three qubits. The X- and U-gates function as traditionally ascribed and the N-gate represents environmental noise. The circuit is generic and does not illustrate a lower bound of the unitary gates needed to prepare an entangled 3-qubit state.

used as a valuable tool for visualizing a quantum sensing process. The presented scheme provides a look at a general approach for embedding quantum computing and quantum sensing into a single platform for exploring ensemble and high-fidelity sensing regimes. Since the experimental data on the FMO complex only includes information on dephasing and dissipation in the system, the theory focuses on those sources of quantum noise, which are also of significance as idle qubit errors in quantum information science. The advantage of embedding few-qubit quantum "computers" within quantum sensors is that we can exploit additional state preparations, measurements, and pure-state requirements, such as the GPCs or more general $N$-representability conditions, to enhance the sensitivity and fidelity of the sensors and improve post-measurement analysis. Additionally, since we are considering a multi-qubit system, this allows for conducting entangling measurements across multiple quantum states, a process polynomial in $n$, where $n$ is the number of qubits, as opposed to measuring one state at a time.

To demonstrate the application of GPCs in quantum sensing, we highlight system-specific detection of the multi-qubit relaxation process. Figure 4.4 a, b, c demonstrates spatially distinct trajectories exhibiting differences only based on the selection of the three chromophores in the 3-qubit subsystem: (a) 124, (b) 125, (c) 126 where, for example, 124 denotes chro-

mophores 1, 2, and 4. We observe that, in each system, the degrees of freedom of a single qubit enhance the measurement of the relaxation process of two correlated qubits. This demonstration establishes a relationship between entanglement, coherence time, and the generalized Pauli constraints. The violation of the GPCs certifies the openness of the quantum system while the unique time evolution of the natural-orbital occupations, defining the GPCs and polytope, provides detailed information about the environment. This information can be mined visually, or by machine learning, to identify, assess, and understand variations that reflect (or sense) major or even nuanced changes in the environment. Such an open-system quantum sensor is able to enhance the measurement of energy relaxation processes by examining the effect of noise on the purity of the quantum state via the GPCs that define the facets of the pure-state Pauli polytope. Furthermore, we are able to distinguish unique features of the quantum mechanism exhibited by the subsystems, without having prior knowledge of their functionalities. For example, our previous work on the FMO complex showed that in the presence of quantum noise and a reaction center, the spectrum of 1-RDM occupations of the FMO system converges to the $(0, 0, 0)$ point, which corresponds to the Slater determinant of the ground state [187]. It is clear from our present model that the system of interest in this study converges to a classical ensemble instead due to the absence of the reaction center, showing the potential of the GPCs to be used for sensing the presence of an energy sink in similar light-harvesting complexes.

We can also observe two distinct types of 3-qubit interactions in the Pauli polytope. For example, Fig. 4.6 illustrates different helical behavior than noted in Fig. 4.4 a, b, c. The set of physically accessible 1-RDMs is expanded to a greater extent when chromophores 7 and 8 constitute the third qubit in the system. Moreover, the rate at which the subsystems reach the classical ensemble state varies across the given examples (see Appendix B.3). These results demonstrate the temporal evolution of entanglement in five different multi-qubit systems and illustrate how a single qubit can suppress or enhance the measured relaxation

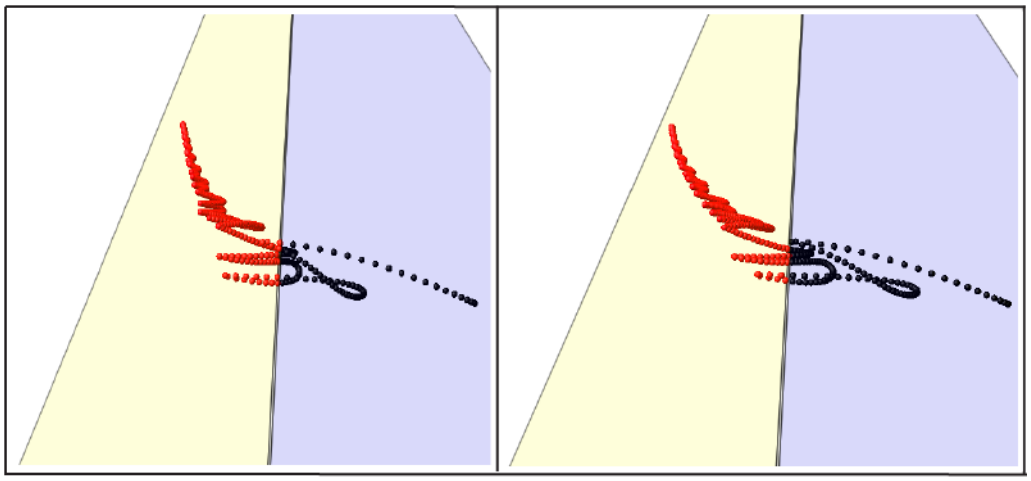


Figure 4.6: Trajectories of different three-qubit subsystems of the FMO complex for the first 2 ps of the energy transfer process. In each case, the time evolution produces an expanded set of 1-RDMs, violating the GPCs initially, and then converges to a classical ensemble at longer times. The two figures differ in the choice of one of the three qubits in the subsystem: (a) 127, (b) 128. The 128 subsystem relaxes to its classical ensemble state at a faster rate than any of the other subsystems considered.

process. It is important to note that the present model is not limited to sensing by the FMO complex, rather it is an illustration of a theoretical framework that may be applied to an arbitrary multi-qubit system exhibiting entanglement and that can be described using the GPC formalism in Eq. 4.3 and the Pauli polytope. We provide a scheme for designing a multi-qubit sensor with the ability to act as a simplified quantum "computer" by receiving external stimuli, performing a sequence of calculations through gate manipulation, and carrying an output to the measurement of the final state. In this study, the FMO complex converts quantum information to quantum memory, which is then processed and measured using the GPC framework. Practically, this proof of concept could be implemented in the design of solid-state probes, where, for example, NV centers are functionalized with antenna complexes [205, 206], which serve as mini quantum computers that may be used to distinguish environmental noise from the signal or to allow for initialization of the NV centers at different times.

Remarkably, not only do the GPCs behave as an indicator of entanglement in a multipartite system, but they also demonstrate that the essential features of such strong entanglement and correlation can be decoded from a knowledge of no more than the 1-RDM. Previous work has shown that GPCs of the 1-RDM contain important information about the many-fermion system and its wavefunction [111, 112, 114] and, recently, it has been demonstrated that a combination of machine learning and RDMs may provide a significant reduction in the computational cost of calculating highly correlated systems [207]. Here we establish that the GPCs and the 1-RDM provides a general platform for constructing a multi-qubit-driven class of quantum sensors that are capable of reporting on the environment by measuring and analyzing the openness of the quantum sensor.

## 4.4 Conclusions

Our results reveal that 3-qubit systems provide sufficient degrees of freedom for establishing an entanglement-enhanced interaction whose 1-RDM can discern between an open and a closed system. Therefore, we demonstrate how an entangled multi-qubit sensor of low computational cost for simulation can be harnessed for performing non-trivial computations, acting as an effective few-qubit quantum "computer." The final non-exponential measurement performed by the sensor uncovers whether the prepared state is interacting with the environment, in which case the pure-state Pauli polytope is violated. Here, the Pauli polytope is an important tool that visually highlights openness of the 3-qubit system as a function of time. The advantage of embedding multi-qubit quantum systems in quantum sensors is that it enables more sophisticated state preparation and measurement schemes by exploiting fundamental restrictions of a pure-state quantum space, such as the GPCs and pure $N$-representability conditions, to enhance the sensitivity and fidelity of the quantum sensor to the environment. The computational complexity of checking the GPCs is determined by the cost of computing the eigenvalues (natural occupations) of the 1-RDM. The measure-

ment and storage costs of the 1-RDM increase as $N^2$ while the computation of the 1-RDM's eigenvalues scales as $N^3$ where $N$ is the number of qubits. Therefore, learning how to extract information on the system-environment interactions using single-qubit populations could lead to enhanced quantum sensors that maximally utilize quantum computational advantage.

Though the implementation of entangled multi-qubit sensors would enable sensing beyond the standard limit, practical deployment of entanglement-enhanced quantum sensors, in part, relies on striking the correct balance between noise suppression and signal conservation. By acting on the border between quantum sensing and quantum computation, we present a scheme for the detection of environmental noise in a particular implementation of an entangled open quantum system by exploiting the Pauli polytope. Our open-system quantum sensing approach demonstrates how the constraints on fermionic correlation and entanglement can be used to extract enhanced sensing information on the noise-assisted relaxation process of a multi-qubit system. We show how multi-particle entanglement in sensors of three and more qubits can be used to exploit the GPCs or, more generally, the pure-state $N$-representability conditions to sense the openness of the quantum system. Hence, the use of GPCs in quantum sensors offers a novel paradigm for merging multi-qubit quantum systems with quantum sensors.

## 4.5 Acknowledgments

D.A.M. and G.S.E. gratefully acknowledge NSF QuBBE Quantum Leap Challenge Institute (NSF OMA-2121044). D.A.M further acknowledges the U.S. National Science Foundation Grants No. CHE-2155082 and CHE-2035876, and the Department of Energy, Office of Basic Energy Sciences, Grant DE-SC0019215. I.A., L.M.S., O.C.W., and J.S.H. acknowledge support from the NSF Graduate Research Fellowship Program, Grant DGE-1746045. J.S.H. further acknowledges support from the National Research Council postdoctoral fellowship. The data supporting this Chapter can be found in Appendix B.

# Part III

# Quantum State Tomography with Fermionic Constraints

# CHAPTER 5

# QUANTUM COMPUTING FOR QUANTUM CHEMISTRY

Over many decades, electronic structure theories have advanced the frontier of quantum mechanics; yet, many important challenges in molecular science, including strongly correlated materials and photochemical and charge-transfer reaction mechanisms, remain computationally intractable for classical computers. The motivation for quantum computing can be traced to the early 1980s, when Feynman and Manin independently observed that the classical simulation of general quantum systems becomes impractical as the dimension of the Hilbert space grows exponentially with system size [208, 209]. Quantum computing offers a new framework for tackling this limitation by leveraging qubits, entangling gates, and circuits to process quantum information. As hardware platforms mature and chemistry-oriented algorithms continue to develop, quantum computation is increasingly being viewed as an important tool for addressing challenges in quantum chemistry. The present chapter offers an overview of quantum computing fundamentals most pertinent to quantum chemistry.

## 5.1 Introduction to Quantum Computation

Classical computers encode information using bits, binary variables that take values of either 0 or 1, and process this information through sequences of deterministic logic gates such as AND, OR, and NOT. Quantum computers, on the other hand, store information in quantum bits, or qubits, which are physical realizations of two-level quantum systems with basis states conventionally labeled as $|0\rangle$ and $|1\rangle$ [210]. The state of a single qubit can be written as a linear combination of these basis states, $|q\rangle = \alpha\,|0\rangle + \beta\,|1\rangle$, where $\alpha, \beta \in \mathbb{C}$ and satisfy the normalization condition $|\alpha|^2+|\beta|^2= 1$. This superposition principle allows qubits to represent probability amplitudes rather than definite classical values, indicating the main difference between quantum and classical information processing. Measurement of the qubit projects

the state onto one of the basis states, yielding outcomes that are intrinsically probabilistic and governed by the squared magnitudes of the amplitudes.

Beyond superposition, quantum computation relies on the phenomenon of quantum entanglement, which arises in multi-qubit systems and leads to correlations that cannot be described by independent single-qubit states. Entanglement enables quantum computers to represent and manipulate complex, highly correlated states efficiently, a feature that, at least intuitively, parallels the role of electronic correlation in quantum chemistry. Many chemically relevant problems, such as the accurate determination of ground-state electronic energies, involve correlated wavefunctions that scale exponentially with system size when treated classically. In principle, quantum computers may offer exponential improvements for such tasks by operating directly within the underlying quantum Hilbert space. In practice, however, current state-of-the-art quantum devices are subject to significant noise and decoherence, resulting from unavoidable interactions between qubits and their surrounding environment. These effects, including coupling to electromagnetic fluctuations, material defects, and control imperfections, lead to the gradual degradation of quantum information and limit the depth and fidelity of feasible computations.

The current generation of quantum hardware is still limited to relatively small system sizes by the lack of fully scalable quantum error correction. As a result, computations on present-day devices inevitably accumulate errors, motivating the development of a growing suite of error mitigation techniques aimed at reducing the impact of noise without the substantial overhead required for fault-tolerant operation [183, 211–219]. Understanding, characterizing, and mitigating noise is currently, therefore, one of the main challenges in contemporary quantum computing research. In this context, accurately reconstructing and diagnosing quantum states produced by quantum hardware becomes significant for validating quantum algorithms and for guiding improvements in device performance. These considerations motivate the following discussion of quantum state tomography, which provides a

framework for characterizing quantum states and plays an important role in the remainder of this chapter.

## 5.2 Quantum State Tomography

Reconstructing an accurate representation of a quantum system based on measurement data is termed quantum state tomography (QST). There exist numerous mathematical representations of a quantum system, including the wavefunction, state vector, and the density matrix. In each case, QST aims to recover the given representation from experimentally available data. In this thesis, we are primarily concerned with the density matrix description.

QST relies on the property that any density matrix can be expanded in a complete operator basis. One such choice is the Pauli basis:

$$D = \frac{1}{2^n} \sum_{P \in \mathcal{P}_n} c_P P, \tag{5.1}$$

where $D$ is a general density matrix, and $\mathcal{P}_n = \{I, X, Y, Z\}^{\otimes n}$ is the set of $n$-qubit Pauli operators with coefficients (expectation values)

$$c_P = \mathrm{Tr}(DP). \tag{5.2}$$

Therefore, the QST task reduces to the task of estimating a complete set of Pauli expectation values through repeated measurements in different bases.

Since an $n$-qubit system spans a Hilbert space of dimension $2^n$, $D$ is a $2^n$ by $2^n$ matrix. Therefore, reconstructing the full $D$ requires exponentially many measurements, limiting full QST to small systems. Additionally, experimental noise and finite sampling budgets only further complicate this challenge. Given these limitations, a very active area of quantum technology research is dedicated to investigating scalable alternatives to full QST.

A broad range of scalable quantum state tomography techniques has emerged in recent years to address the impracticality of fully reconstructing arbitrary many-qubit states [220–229]. Rather than attempting complete density matrix reconstruction, many of these approaches aim to extract only physically relevant information (e.g., expectation values and correlations) using significantly fewer measurements. Among the most prominent developments is the framework of classical shadows, which leverages randomized measurement protocols to build a compact classical representation from which a large number of observables can be efficiently predicted [230–235, 235–260]. However, while classical shadows are powerful for observable estimation, they do not necessarily guarantee that the reconstructed outcomes correspond to a valid physical state, a limitation that becomes more pronounced on noisy hardware and in the treatment of excited states, where additional complications such as orthogonality constraints and strong correlation often arise. Chapters 6-8 will discuss improvements to shadow tomography that address these limitations via semidefinite programming and fermionic constraints, with applications in quantum chemistry.

Several other scalable QST approaches have been developed, including compressed sensing [261, 262], neural-network-based reconstruction [263, 264], direct fidelity estimation [265–267], and maximum-entropy-inspired approaches such as restricted Boltzmann machine methods [268]. Collectively, these techniques provide a growing toolbox for characterizing quantum states in practice, with applications ranging from entanglement diagnostics [269] and Hamiltonian learning [270–272] to reduced density matrix reconstruction in quantum chemistry [3–5, 9, 11, 236, 238].

## 5.3 Quantum Chemistry Applications

Quantum computing holds the most promise for addressing electronic structure problems that are difficult to treat with classical methods, particularly strongly correlated electronic structure problems, including catalytic sites such as FeMoco [273, 274], as well as open-

quantum-system dynamics [7, 275], photochemistry and materials science involving conical intersections and charge-transfer states [8, 276], and transition-state energetics and reaction barriers [277]. The role of quantum computation is not merely to improve upon classical solvers' time, but instead to enable the study of quantum mechanical phenomena that would otherwise remain out of reach for classical methods. Although the field is evolving rapidly, most progress is still anticipated to take place in conjunction with classical techniques, such as high-performance computing (HPC) and artificial intelligence. Comprehensive overviews of existing approaches to quantum computing algorithms for chemistry can be found in various reviews, including Refs. [7, 133, 134, 278–280]. In this section, we highlight only the most relevant and widely used algorithms for quantum chemistry applications.

A starting point to most algorithms is the encoding of a molecular electronic Hamiltonian into qubit representation. This can be done via fermion-qubit mappings such as the Jordan-Wigner [281] or Bravy-Kitaev [282], where the Hamiltonian is expressed as a sum of Pauli strings and, hence, amenable to gate-based computation. The fermion-qubit mapping is a nontrivial step in quantum algorithm development, and numerous mapping strategies and optimizations have been proposed to reduce nonlocality, lower Pauli operator weight, or exploit problem structure, including parity-based mappings, low-rank factorization techniques, and symmetry-preserving encodings [283–285].

The most accurate approach to estimating the molecular ground-state energies via quantum computation is the quantum phase estimation (QPE) algorithm [136, 286, 287]. QPE determines the eigenvalues and eigenvectors of a Hamiltonian in polynomial time and is actively being applied in quantum chemistry contexts [210, 288–292]. However, QPE requires deep coherent circuits and fault-tolerant error correction, which remain challenging for current platforms.

In contrast, variational quantum algorithms have dominated applications on near-term quantum devices, with the variational quantum eigensolver (VQE) [293] being the most

notable. VQE employs a hybrid quantum–classical loop in which a parameterized quantum circuit prepares trial states and a classical optimizer iteratively minimizes the measured energy expectation value. The success of VQE depends heavily on the choice of ansatz, with some of the most widely used being the chemistry-inspired unitary coupled cluster (UCC) [134, 294, 295], hardware-efficient [296], adaptive structure [297], and qubit coupled-cluster approaches [229, 298, 299]. Though variational methods have become the dominant paradigm for molecular simulations on current hardware, they face significant limitations including measurement overhead, optimization instability, and sensitivity to noise [134, 278].

Hamiltonian simulation, i.e., implementation of the time-evolution operator $e^{-i\hat{H}t}$, meanwhile, underlies both QPE and variational approaches, providing the basis for many advanced quantum algorithms. Approaches such as Trotterization [300], for example, have been widely used and studied in simulation of many-body dynamics on quantum computers or tensor networks [301–304]. In addition, qubitization has recently emerged as a promising approach with reduced scaling for chemistry applications in the fault-tolerant regimes [305].

In addition to ground states, algorithms for the treatment of excited states are rapidly being discovered due to their prevalence in applications for photochemical processes, spectroscopy, and reaction dynamics. A significant number of state-of-the-art approaches for accessing low-lying excited states draw their inspiration from variational techniques, with the most widely used examples being the quantum subspace expansion [211, 306] and the equation-of-motion techniques [307].

Besides advances in algorithmic development, practical applications in quantum chemistry rely on improvements in error mitigation and measurement cost reductions. Methods such as symmetry verification [217], zero-noise extrapolation [308], and probabilistic error cancellation [309] aim to suppress errors without requiring full fault tolerance. Similarly, randomized measurement strategies such as classical shadows [230, 231, 236] offer promising routes toward scalable estimation of chemical properties. The next three chapters develop

shadow-based methods that incorporate physical constraints and optimization techniques, and demonstrate their utility for chemically relevant observables and fermionic systems.

# CHAPTER 6

# FEWER MEASUREMENTS FROM SHADOW TOMOGRAPHY WITH $N$-REPRESENTABILITY CONDITIONS

This chapter is reprinted (adapted) with permissions from *Phys. Rev. Lett.* **2024**, *132*, 22, 220802–220809

## 6.1 Chapter Synopsis

Classical shadow tomography provides a randomized scheme for approximating the quantum state and its properties at reduced computational cost with applications in quantum computing. In this Letter we present an algorithm for realizing fewer measurements in the shadow tomography of many-body systems by imposing $N$-representability constraints. Accelerated tomography of the two-body reduced density matrix (2-RDM) is achieved by combining classical shadows with necessary constraints for the 2-RDM to represent an $N$-body system, known as $N$-representability conditions. We compute the ground-state energies and 2-RDMs of hydrogen chains and the $N_2$ dissociation curve. Results demonstrate a significant reduction in the number of measurements with important applications to quantum many-body simulations on near-term quantum devices.

## 6.2 Introduction

Shadow tomography [230–236, 245, 246, 249, 252, 253, 259, 310–315] has recently emerged as a critical technique in quantum information theory, offering an efficient implementation of random sampling for characterizing complicated quantum systems. Built around the principle of using minimal measurements to image a quantum state [238, 239], this approach stands at the forefront of recent advances in tomography [220–229, 316] that aim to address outstanding challenges in quantum computing [317] and quantum state verification [318].

Despite its promise and generality, however, shadow tomography has limitations, including its scalability for measuring large quantum states and its robustness with noisy data as generated by near-term intermediate-scale quantum (NISQ) devices. These limitations can be particularly challenging for many-body quantum systems whose complexity increases dramatically with system size [133, 134, 319, 320].

In this Letter, we present a substantial acceleration of the shadow tomography of two-particle reduced density matrices (2-RDM) of many-body systems by imposing $N$-representability constraints [67, 69, 84, 90, 91, 100, 321–324]. Conventional shadow tomography neglects the fact that a 2-RDM must obey significant, non-trivial constraints, known as $N$-representability conditions [67, 69], to ensure that it derives from the integration of at least one valid $N$-particle density matrix. Here, we introduce a classical algorithm that reconstructs the 2-RDM from a set of classical shadows while enforcing necessary $N$-representability conditions. In particular, we consider a hierarchy of $N$-representability conditions on the 2-RDM that arise from constraining $(p+1)$ $p$-particle metric matrices to be positive semidefinite, known as the $p$-positivity conditions [90, 322–324]. Both the positivity conditions and the shadow constraints can be imposed on the 2-RDM through a special family of convex optimization, known as semidefinite programming [72, 75, 325]. We can also view the approach as adding the shadow constraints obtained from measuring a wavefunction (e.g., a wavefunction prepared on a quantum computer) to the variational calculation of the 2-RDM subject to $N$-representability conditions [68, 74–79, 81, 326–332]—a classical-computing method that has been successfully applied to strongly correlated many-electron systems from spin systems to molecules and materials [82, 333–336].

After we develop the theory for $N$-representability-enhanced shadow tomography, we demonstrate its advantages by computing the ground-state energies and 2-RDMs of hydrogen chains and the $N_2$ dissociation curve. Results reveal a significant reduction in the number of measurements for 2-RDM tomography, even in the presence of noise, with applications to

many-body simulations on noisy intermediate-scale quantum devices.

## 6.3 Theory

We consider an $N$-electron system whose 2-RDM elements arise from the integration of the $N$-particle density matrix over all particles except two and can be expressed as

$$ {}^2D_{kl}^{ij} = \langle \Psi | \, \hat{a}_i^\dagger \hat{a}_j^\dagger \hat{a}_l \hat{a}_k \, | \Psi \rangle \, , \tag{6.1} $$

where $\hat{a}_i^\dagger$ creates a particle in orbital $i$ and $\hat{a}_i$ annihilates a particle in orbital $i$. The protocol developed by Huang et al. [231], previously introduced by Aaronson [230], illustrates a method for creating a classical shadow of a quantum state $|\Psi\rangle$ by first applying a unitary transformation on the state such that $|\Psi\rangle \mapsto \hat{U} \, |\Psi\rangle$ where $\hat{U}$ is a random matrix from an ensemble $\mathcal{U}$ and then measuring the state in the computational basis. After passing $|\Psi\rangle$ through a unitary transformation, i.e., a quantum circuit, the classical shadow description of the 2-RDM is expressible as

$$ S_n^{pq} = \langle \Psi | \, \hat{U}_n^\dagger \hat{a}_p^\dagger \hat{a}_q^\dagger \hat{a}_q \hat{a}_p \hat{U}_n \, | \Psi \rangle \, , \tag{6.2} $$

where $\hat{U}_n = \exp\Big\{ \big( \sum_{uv} A_n^{uv} \hat{a}_u^\dagger \hat{a}_v \big) \Big\}$ in which the indices denote spin orbitals, $A_n$ is a one-body anti-Hermitian matrix, and $n$ is the index for the shadow. The $n^{\text{th}}$ shadow corresponds to the measurement of all diagonal elements of the 2-RDM after application of the $n^{\text{th}}$ one-body unitary transformation $\hat{U}_n$ to the wavefunction. Each one-body unitary transformation, generated by random sampling with the Haar measure [337], has the effect of rotating the orbitals into a new basis. From Eq. (8.5), the collection of shadows can be written in terms

of the elements of the 2-RDM as

$$S_n^{pq} = \sum_{ijkl} U_n^{pi} U_n^{qj}\, {}^2D_{kl}^{ij}\, U_n^{ql} U_n^{pk}, \tag{6.3}$$

where $U_n = \exp\{(A_n)\}$. Because a sufficiently large set of the above shadows defines a system of equations that determines the 2-RDM, the technique can be used to predict the 2-RDM—or any one- or two-body expectation value—of the original state. Nonetheless, since the output state is constructed from the measurements of only classical parts of the 2-RDM, which are commutable and, hence, measurable in parallel, the tomography cost is significantly reduced.

Here, we use necessary $N$-representability conditions in combination with the linear constraints arising from the classical shadows to determine the 2-RDM. The $N$-representability conditions define a convex set ${}_2^N\tilde{P}$ of approximately $N$-representable 2-RDMs that contains the set ${}_2^N P$ of exactly $N$-representable 2-RDMs [323]. Likewise, a collection of $m$ classical shadow constraints define a convex set $\tilde{S}_m$ of 2-RDMs that approximate the 2-RDM of the quantum state. As the number $m$ of randomly sampled classical shadows increases, the set $\tilde{S}_m$ decreases until at some limiting $m^*$ the set contains only the state's 2-RDM. However, to maximize the efficiency of the tomography, we want to obtain a good approximation of the 2-RDM for $m \ll m^*$. Importantly, we can significantly accelerate the convergence of the classical shadows to the correct 2-RDM by considering the intersection of the $m$-shadow set of 2-RDMs $\tilde{S}_m$ with the set ${}_2^N\tilde{P}$ of approximately $N$-representable 2-RDMs. Because the intersection set $\tilde{S}_m^+$ is a convex subset of $\tilde{S}_m$

$$\tilde{S}_m^+ = \tilde{S}_m \cap {}_2^N\tilde{P} \subset \tilde{S}_m, \tag{6.4}$$

the approximations of the quantum state's 2-RDM in $\tilde{S}_m^+$ converges much faster with $m$ towards the correct 2-RDM than the 2-RDM approximations in the set $\tilde{S}_m$ using only conven-

tional shadow tomography. The difference in the sets and, hence, the degree of convergence acceleration is especially pronounced for our target range of $m \ll m^*$.

To obtain a unique 2-RDM for a finite value of $m$, we score the 2-RDMs in the convex set $\tilde{S}_m^+$ by a merit function. To obtain a convex optimization problem, we can select the merit function to be any convex function of the 2-RDM. Potential merit functions include the nuclear norm or the Frobenius norm, as in matrix completion theory [338, 339]. Here, we choose the merit function to be the expectation value of the energy, which, for a quantum many-body system with at most pairwise interactions, is expressible as a linear functional of the 2-RDM, $F[{}^2D]$. We have the following convex optimization problem

$$\min_{{}^2D \in {}^N_2\tilde{P}} \quad F[{}^2D] \tag{6.5}$$

$$\text{such that} \quad S^n_{pq} = ((U \otimes U)^2 D (U \otimes U)^T)^{pq}_{pq}, \tag{6.6}$$

for $n \in [0, m]$ where the 2-RDM is approximately $N$-representable. The optimization converges to the 2-RDM, subject to both the $N$-representability conditions and the shadow constraints, that minimizes the energy. The choice of the energy for the merit function is particularly attractive because, in the absence of the shadow constraints (i.e., $m = 0$), the optimization becomes a variational 2-RDM calculation in which the energy is minimized over the approximately $N$-representable set ${}^N_2\tilde{P}$ of 2-RDMs. From this perspective, the classical shadow constraints can be viewed as state-specific conditions that improve the performance of variational 2-RDM theory.

In practice, the set ${}^N_2\tilde{P}$ can be described by a systematic hierarchy of $N$-representability conditions known as the $p$-positivity conditions [90, 322–324]. The $p$-positivity conditions constrain $(p+1)$ metric matrices, which interrelate by linear mappings and contract to the 2-RDM, to be positive semidefinite. The convex optimization becomes a semidefinite program (SDP) [72, 75, 325]. If we consider only the 2-positivity conditions, we obtain the following

SDP

$$\min_{^2D} \; E[^2D] \tag{6.7}$$

$$\text{such that } {}^2D \succeq 0 \tag{6.8}$$

$${}^2Q \succeq 0 \tag{6.9}$$

$${}^2G \succeq 0 \tag{6.10}$$

$$\mathrm{Tr}({}^2D) = N(N-1) \tag{6.11}$$

$${}^2Q = f_Q({}^2D) \tag{6.12}$$

$${}^2G = f_G({}^2D) \tag{6.13}$$

$$S_n^{pq} = ((U \otimes U)^2 D (U \otimes U)^T)_{pq}^{pq} \tag{6.14}$$

where $E[^2D]$ is the energy-specific functional of the 2-RDM and ${}^2Q$ and ${}^2G$ are the hole-hole and particle-hole metric matrices whose elements are given by

$${}^2Q_{ij}^{kl} = \langle \Psi | \hat{a}_k \hat{a}_l \hat{a}_j^\dagger \hat{a}_i^\dagger | \Psi \rangle \tag{6.15}$$

$${}^2G_{kj}^{il} = \langle \Psi | \hat{a}_i^\dagger \hat{a}_l \hat{a}_j^\dagger \hat{a}_k | \Psi \rangle. \tag{6.16}$$

$M \succeq 0$ indicate that the matrix $M$ is constrained to be positive semidefinite, $\mathrm{Tr}({}^2D)$ denotes the trace of the 2-RDM that is set to $N(N-1)$, and the functions $f_Q$ and $f_G$ represent the linear mappings between ${}^2Q$ and ${}^2D$ and ${}^2G$ and ${}^2D$, respectively, that are obtained from rearranging the creation and annihilation operators in Eqs. (7.9) and (7.10). Physically, the D, Q, and G conditions [69, 84, 91] constrain the probability distributions of two electrons, two holes, and an electron-hole pair to be nonnegative.

Within the SDP protocol, we can replace the equality in Eq. (6.14) with inequalities to offer flexibility in handling statistical error in the 2-RDM, e.g., in the presence of quantum

noise on quantum devices

$$S_n^{pq} - \epsilon_n^{pq} \leq X_n^{pq} \leq S_n^{pq} + \epsilon_n^{pq} \tag{6.17}$$

where

$$X_n^{pq} = ((U_n \otimes U_n)\,^2 D\,(U_n \otimes U_n)^T)_n^{pq} \tag{6.18}$$

and each $\epsilon_n^{pq}$ is a nonnegative parameter that reflects the maximum error expected in an element of the $n^{\text{th}}$ shadow. In this formulation we observe that the $N$-representability conditions serve not only to accelerate the convergence of the shadow tomography but also to mitigate errors in the shadows that potentially arise from the noise on a quantum device. The use of $N$-representability conditions for error mitigation in shadow tomography extends and generalizes earlier work in which $N$-representability conditions are applied post-measurement for error mitigation [340–344].

In the described program, the 2-positivity (DQG) conditions have a computational scaling of $r^4$ and $r^6$ in memory and floating-point operations, respectively [72], where $r$ is the number of orbitals; therefore, the $N$-representability-enhanced tomography retains a polynomial scaling. Additionally, since the $N$-representability conditions are independent of a reference wavefunction, the described program applies to a wide range of strongly correlated systems. The number of measurements needed to perform the full 2-RDM tomography on a quantum device would be approximately $r^4$. The number of measurements with our technique would be approximately $n_s r^2$, where $n_s$ is the number of shadows with $n_s$ typically obeying $n_s \ll r^2$ for a targeted accuracy, $\epsilon$. The feasibility of performing these measurements on a NISQ device will depend on the circuit requirements of the quantum algorithm and the size of $\epsilon$. For example, some algorithms may not require measuring the full 2-RDM but just a part of it, in which case the scaling would be further reduced.

## 6.4 Results

To implement shadow tomography with $N$-representability conditions, we solve the SDP in Eqs. (7.2-6.14) by adding the shadow constraints to the variational 2-RDM method (v2RDM) [75, 345] in the Maple Quantum Chemistry Package [346, 347]. We refer to the resulting algorithm as the shadow v2RDM (sv2RDM) method. The SDP is solved using the boundary-point algorithm in Ref. [72]. We generate the classical shadows from full configuration interaction (FCI) wavefunctions. The enhanced shadow tomography is applied to the dissociation of the nitrogen dimer and the ground-state energies of strongly correlated hydrogen chains [348] with up to eight equally spaced atoms. The hydrogen atoms are represented in the minimal Slater-type-orbital (STO-3G) basis set [349] while nitrogen is represented in the correlation-consistent polarized valence double-zeta (cc-pVDZ) basis set in a 10 electrons-in-8 orbitals [10,8] active space [350].

Total energies for $N_2$ from the sv2RDM method with 2-positivity (DQG) conditions converge quickly with the number of shadows to those from FCI as shown in Fig. 6.1. Note that for the FCI of $N_2$, when symmetry is neglected, the total number of configuration state functions is 1176 [15]. With 18 shadows, the Frobenius norm of the difference between the sv2RDM and FCI 2-RDMs is on the order of $10^{-4}$. Hence, significantly fewer than $d^2$ shadows, where $d$ is the dimension of the 2-RDM describing the system, are needed for convergence to FCI energies and 2-RDMs, which is consistent with previous work on shadow tomography [231].

For $N_2$ at 1.75 Å, Fig. 6.2 demonstrates that the number of measurements required by the shadow tomography depends critically upon the number of $N$-representability conditions. The energy and 2-RDM errors with only 3 shadows and either the DQ or the DQG conditions are more accurate than those with as many as 14 shadows and just the D condition. Moreover, the addition of the D condition is still better than shadow tomography without any positivity conditions. For nearly all numbers of shadows in the range 0-17, the energy errors from

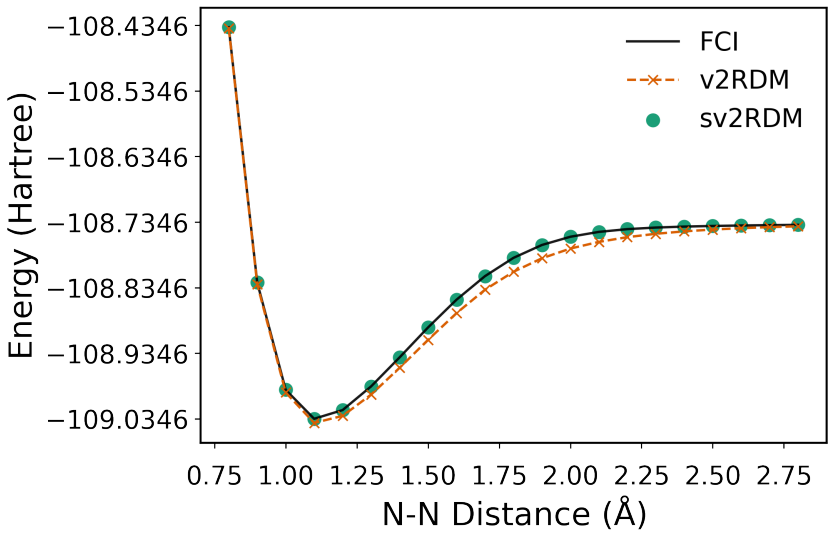


Figure 6.1: Potential energy curves of $N_2$ from FCI, v2RDM (DQG), and sv2RDM (DQG) are shown. Total energies of sv2RDM with 18 shadows are in exact agreement with those calculated using FCI.

DQG conditions are approximately two orders of magnitude better than those from just the D condition. Moreover, the 2-RDM errors from the DQG conditions are approximately three orders of magnitude better than those from the D condition.

While the D curve in both panels of Fig. 6.2 decreases gradually in most of its domain, the DQ curve shows a steeper convergence pattern with respect to the number of shadows measured. This behavior indicates a nontrivial synergistic relationship between the classical shadows and the 2-RDM $N$-representability conditions that enhances the accuracy of the sampling. Overall, the total energy significantly relies on the positivity conditions, but as the energies and 2-RDMs of DQ approach those of DQG, the convergence slows and becomes more reliant on the shadow behavior. Therefore, considering $N$-representability conditions is crucial to achieving accurate electronic structure results and reliable convergence with the fewest number of shadows.

The total energy as a function of the number of shadows for each hydrogen chain studied shows a logarithmic convergence pattern (Fig. 6.3), with the Q and G conditions significantly improving the accuracy of the calculated values compared to the D condition alone

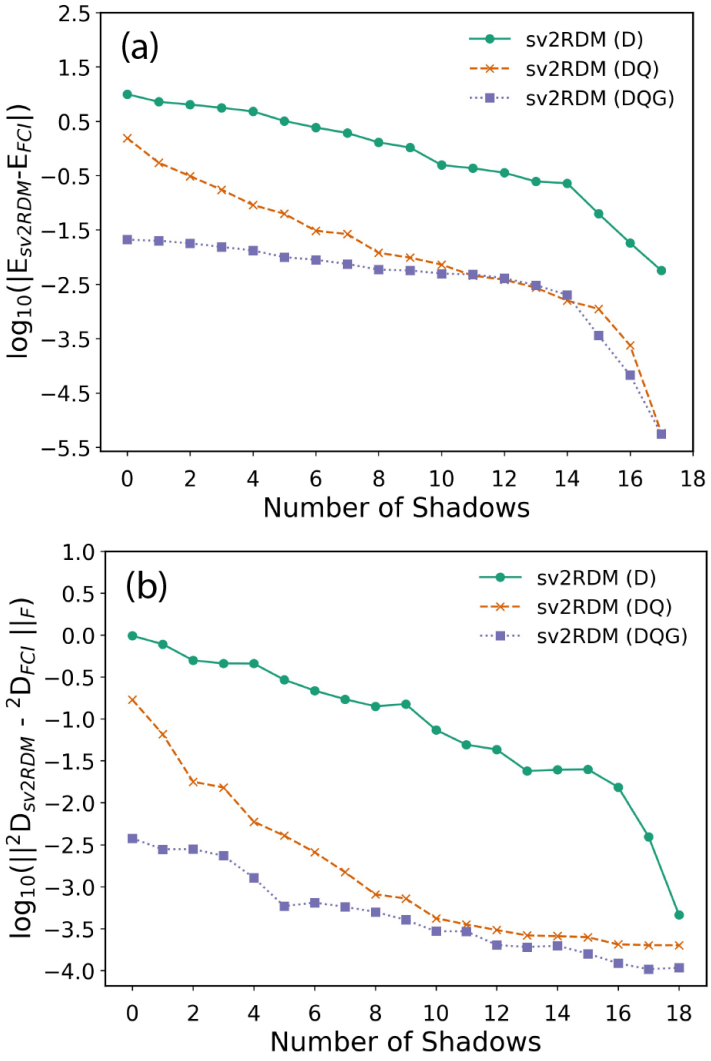


Figure 6.2: For $N_2$ at 1.75 Å, the number of measurements required by the shadow tomography depends critically upon the number of $N$-representability conditions. The energy and 2-RDM (normalized to one) errors with only 3 shadows and the DQ and the DQG conditions are more accurate than those with as many as 14 shadows and just the D condition.

Table 6.1: For $H_4$ with 1.00 Å H-H bonds the Frobenius norm of the 2-RDM (normalized to one) relative to FCI is presented as a function of the number of shadows and the number of $N$-representability conditions. The DQG conditions improve upon D by 1-3 orders of magnitude for all shadows.

| Shadow number | D | DQ | DQG |
|---|---|---|---|
| 1 | 0.21997267 | 0.02815293 | 0.00282400 |
| 3 | 0.21604040 | 0.00313894 | 0.00041823 |
| 5 | 0.01120927 | 0.00113098 | 0.00020163 |
| 7 | 0.00075773 | 0.00066025 | 0.00011213 |
| 9 | 0.00074105 | 0.00062567 | 0.00003492 |
| 11 | 0.00074105 | 0.00062914 | 0.00001140 |

(Table 7.1). With just 9 shadows, the sv2RDM total energy converges to the FCI energy of the $H_4$ chain in Fig. 6.3 (a). Additional numerical results on the hydrogen chains are available in Appendix C.

Finally, we consider the performance of sv2RDM in the noisy setting where the measured 2-RDM contains errors introduced by a Gaussian noise matrix. The shadow constraints are replaced by the inequalities in Eqs. (6.17- 6.18) that allow for errors $\epsilon_n^{pq}$. We choose $\epsilon_n^{pq} = \sigma$, where $\sigma$ is the standard deviation in the Gaussian noise model. Figure 6.3 (b) shows the sv2RDM convergence outcomes for various noise levels. Though the algorithmic performance is the best in low-noise environments, the example with even $\epsilon \leq 10^{-4}$ shows the energy approaching that of the FCI. This result indicates that the $N$-representability conditions can help mitigate the errors introduced by noise and thereby retain chemical accuracy at a reduced measurement cost even in the presence of noise, which has potentially important applications on NISQ devices.

## 6.5 Discussion and Conclusions

Shadow tomography has recently emerged as an important technique for characterizing quantum states, and yet despite its promise, it has potential limitations in its scalability for treat-

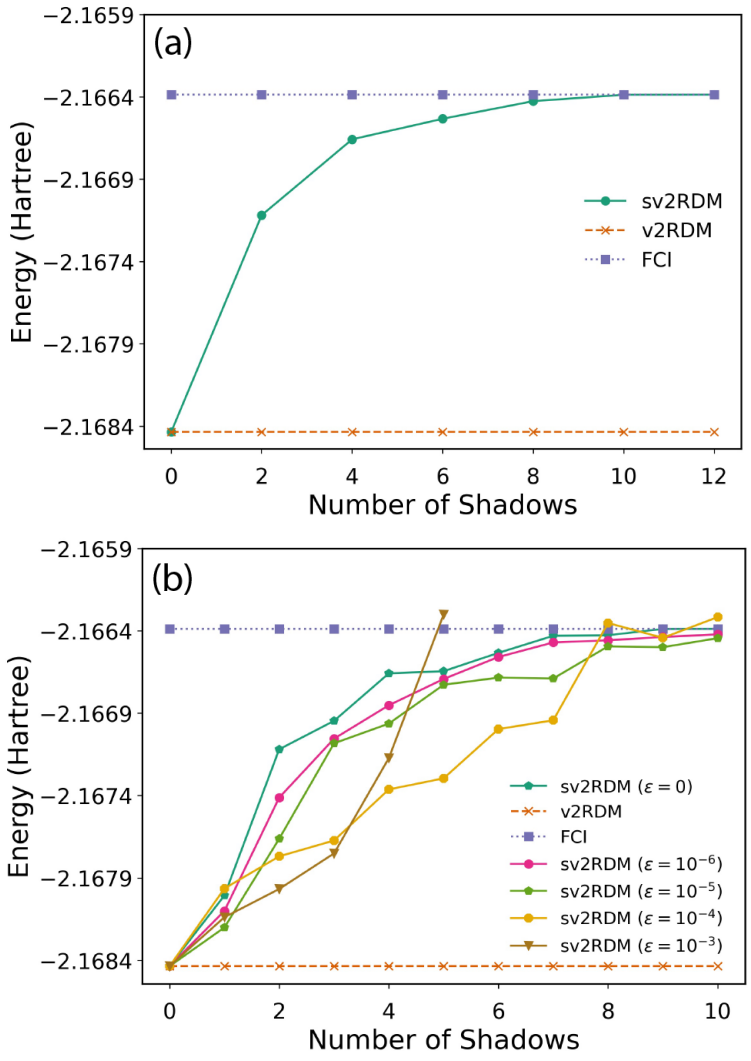


Figure 6.3: Total ground-state energy of $H_4$ with equally spaced H atoms is shown as a function of the number of shadows, (a) without and (b) with the presence of Gaussian noise. The sv2RDM energy converges *exactly* to the FCI energy within 10 shadows in the noiseless environment and *approximately* in the noisy environments.

ing large quantum states and its sensitivity for dealing with quantum noise. We have demonstrated a method based on the theory of classical shadows that utilizes $N$-representability conditions to achieve the accuracy of target observables from the 2-RDM with fewer measurements than possible without these constraints. Our enhanced shadow tomography addresses the issue of exponential scaling of full quantum tomography by combining classical shadows for a succinct description of quantum states with the 2-RDM $N$-representability conditions, which allow for even fewer measurements with reliable convergence. The $N$-representability conditions are shown to decrease significantly the number of measurements needed to converge the 2-RDM for strongly correlated many-electron systems in both ideal and noisy settings, promising future advancements in many-body quantum tomography from reduced information. While the numerical calculations demonstrate exact agreement with electronic FCI wavefunctions, the presented theory is general and applicable to performing tomography of any exact or approximate many-body wavefunction. Future work will explore the ability of the algorithm to deal with different types of noise and its application to the quantum simulation of many-body problems on current quantum platforms.

## 6.6 Acknowledgments

D.A.M. gratefully acknowledges the Department of Energy, Office of Basic Energy Sciences, Grant DE-SC0019215, the U.S. National Science Foundation Grant CHE-2155082 and DMR-2037783, and the NSF QuBBE Quantum Leap Challenge Institute (NSF OMA-2121044). I.A. gratefully acknowledges the NSF Graduate Research Fellowship Program under Grant No. 2140001. The data supporting this Chapter can be found in Appendix C.

# CHAPTER 7

# ENHANCED SHADOW TOMOGRAPHY OF MOLECULAR EXCITED STATES FROM ENFORCING $N$-REPRESENTABILITY CONDITIONS BY SEMIDEFINITE PROGRAMMING

This chapter is reprinted (adapted) with permissions from *Phys. Rev. A* **2024**, *110*, 5, 052407–052418

## 7.1 Chapter Synopsis

Excited-state properties of highly correlated systems are key to understanding photosynthesis, luminescence, and the development of novel optical materials, but accurately capturing their interactions is computationally costly. We present an algorithm that combines classical shadow tomography with physical constraints on the two-electron reduced density matrix (2-RDM) to treat excited states. The method reduces the number of measurements of the many-electron 2-RDM on quantum computers by (*i*) approximating the quantum state through a random sampling technique called shadow tomography and (*ii*) ensuring that the 2-RDM represents an $N$-electron system through imposing $N$-representability constraints by semidefinite programming. This generalizes recent work on the $N$-representability-enhanced shadow tomography of ground-state 2-RDMs. We compute excited-state energies and 2-RDMs of the $H_4$ chain and analyze the critical points along the photoexcited reaction pathway from *gauche*-1,3-butadiene to bicyclobutane via a conical intersection. The results show that the generalized shadow tomography retains critical multireference correlation effects while significantly reducing the number of required measurements, offering a promising avenue for the efficient treatment of electronically excited states on quantum devices.

## 7.2 Introduction

Most fundamental life processes rely on photochemistry. Electronically excited states play a central role in the mechanism of light-induced reactions driving many important phenomena such as photosynthesis [351, 352], vision [353], and the protection of DNA from damage [354–357]. However, excited-state computations are typically more difficult to compute than their ground-state counterparts. Ensuring orthogonality of the excited states to the lower-lying ones [14, 358–360] and accounting for the many determinants contributing to the excited-state wavefunction, i.e., the multireference character [361–364], represent just some of the challenges. Using quantum computers offers an efficient paradigm for treating excited states because their quantum states can be directly prepared as a superposition of qubits without explicit classical representation or storage of the wavefunction [133, 365]. Nonetheless, a significant part of realizing this potential depends upon achieving efficient, noise-resilient tomography of critically important observables (e.g., from the 1- and 2-electron reduced density matrices) with a minimal number of measurements.

While full quantum state tomography is possible, it is highly inefficient, requiring an exponential number of parameters to describe an $N$-particle state as well as an exponentially large amount of post-processing [316]. Various approaches to quantum state tomography of generic, complex quantum systems have been developed in recent years [220–229], including those based on the theory of classical shadows [230–237]. By focusing only on the physically relevant quantities "hidden" in the reduced-dimensional space of the system, the classical shadow theory allows for learning of many properties of an $N$-dimensional quantum system from partial information [235, 238–260]. While the classical shadow approach is able to predict many observables efficiently, it does not guarantee that the sampled outcomes will correspond to physical states, especially on noisy intermediate-scale quantum (NISQ) devices. This challenge is only amplified in the case of excited states where it is compounded by issues like state orthogonality and strong correlation, arising from the energetic degen-

eracies of the molecular orbitals.

Here, we combine the concept of shadow tomography and reduced density matrix theory to accelerate the convergence of classical shadow tomography for excited states. In reduced density matrix theory, the energy of a system is variationally minimized as a functional of the two-electron reduced density matrix (2-RDM). The energy of any stationary state is a linear functional of the 2-RDM [48, 66, 67, 84], but the 2-RDM must be restricted by additional, nontrivial constraints, known as $N$-representability conditions [75, 84, 90, 100, 321–324, 345, 366–369], to ensure that it is representable by at least one $N$-electron density matrix. In the context of tomography, the $N$-representability conditions provide a tremendous advantage because they significantly constrain the convex set of 2-RDMs, thereby decreasing the degrees of freedom to be sampled by shadow tomography. Here we impose the $N$-representability conditions through a novel post-processing algorithm on a classical device, in which the 2-RDM is extracted from a very small number of shadows by semidefinite programming (SDP) [72, 325, 370]. The fusion of SDP with minimal shadows on quantum devices provides the framework for more efficient and more accurate quantum molecular computations of excited states on quantum devices. This algorithm generalizes the previous work on ground-state shadow-enhanced tomography of the 2-RDM [3].

We first present the $N$-representability-enhanced shadow tomography and its generalization to excited states. We then demonstrate the approach by studying the first four low-lying singlet excited states of the $H_4$ chain and the photoexcited pathway from *gauche*-1,3-butadiene to bicyclobutane via a conical intersection. We show that the excited-state shadow tomography with $N$-representability conditions is able to capture single- and multireference correlation effects and achieve chemical accuracy ($\approx 1$ kcal/mol) with reasonable computational resources. Moreover, we illustrate how considering $N$-representability in the context of shadow tomography provides a significant advantage in reaching high accuracy from fewer measurements even in highly multireference systems such as conical intersections.

Although the presented tomography is demonstrated through classical calculations here, it has important applications to accelerating and enhancing the quantum tomography of excited states on quantum devices. Not only does the approach accelerate the convergence of the classical shadows towards the 2-RDM but it also provides a built-in error mitigation for correcting preparation and measurement errors in the 2-RDM with respect to known physical constraints—the $N$-representability conditions.

## 7.3 Theory

The two-electron reduced density matrix (2-RDM) is defined as,

$$ {}^2D^{ij}_{kl} = \langle \Psi | \, \hat{a}^\dagger_i \hat{a}^\dagger_j \hat{a}_l \hat{a}_k \, | \Psi \rangle \, , \tag{7.1} $$

where $\hat{a}^\dagger_i$ creates an electron in orbital $i$ and $\hat{a}_i$ annihilates an electron in orbital $i$. To minimize the energy as a functional of the 2-RDM, $E[{}^2D]$ while making sure the particle-particle (${}^2D$) particle-hole (${}^2G$) and the hole-hole (${}^2Q$) matrices are positive semidefinite and related through linear mappings, we use semidefinite programming (SDP). The following is a description of such a program for a variational 2-RDM calculation,

$$ \min_{{}^2D \in {}^N_2\tilde{P}} \; E[{}^2D] \tag{7.2} $$

$$ \text{such that } {}^2D \succeq 0 \tag{7.3} $$

$$ {}^2Q \succeq 0 \tag{7.4} $$

$$ {}^2G \succeq 0 \tag{7.5} $$

$$ \mathrm{Tr}({}^2D) = N(N-1) \tag{7.6} $$

$$ {}^2Q = f_Q({}^2D) \tag{7.7} $$

$$ {}^2G = f_G({}^2D). \tag{7.8} $$

Here, ${}^2Q$ and ${}^2G$ are the hole-hole and particle-hole matrices whose elements are given by

$$ {}^2Q_{ij}^{kl} = \langle \Psi | \hat{a}_k \hat{a}_l \hat{a}_j^\dagger \hat{a}_i^\dagger | \Psi \rangle \tag{7.9} $$

$$ {}^2G_{kj}^{il} = \langle \Psi | \hat{a}_i^\dagger \hat{a}_l \hat{a}_j^\dagger \hat{a}_k | \Psi \rangle. \tag{7.10} $$

The positivity constraint $M \succeq 0$ enforces the matrix $M$ to be positive semidefinite, and $\mathrm{Tr}({}^2D) = N(N-1)$ ensures the correct normalization. The functions $f_Q$ and $f_G$ represent the linear mappings between ${}^2Q$ and ${}^2D$ and ${}^2G$ and ${}^2D$, respectively, derived from the rearrangement of creation and annihilation operators in Eqs. (7.9) and (7.10) [69]. ${}_2^N\tilde{P}$ is a convex set of approximately $N$-representable 2-RDMs.

Building upon our previous work for ground states [3] as well as work by Huang et al. [231] and Aaronson [230], we introduce an excited-state shadow tomography that combines the reduced density matrix theory above with classical shadows. We create a collection of two-electron classical shadows $S_n$ of a quantum state $|\Psi\rangle$, indexed by the integer $n$, by applying a set of unitary transformations $\hat{U}_n$ and then measuring the resulting states in the computational basis

$$ S_n^{pq} = \langle \Psi | \, \hat{U}_n^\dagger \hat{a}_p^\dagger \hat{a}_q^\dagger \hat{a}_q \hat{a}_p \hat{U}_n \, | \Psi \rangle \,, \tag{7.11} $$

where $\hat{U}_n = \exp\Big\{ \big( \sum_{uv} A_n^{uv} \hat{a}_u^\dagger \hat{a}_v \big) \Big\}$, with $A_n$ being a one-body anti-Hermitian matrix, and $|\Psi\rangle$ a ground- or excited-state wavefunction. Each shadow $S_n^{pq}$ corresponds to the set of measured diagonal elements of the 2-RDM after the $n^{\text{th}}$ one-body unitary transformation. The transformations, which rotate the orbitals into randomly selected bases, are sampled using the Haar measure [337] (see Appendix D for more details). Unlike in quantum Monte Carlo [371], where random sampling is done over probability distributions or paths in high-dimensional spaces, the shadow tomography presented here is based on collecting measurements of the diagonal elements of the 2-RDM in randomly sampled measurement bases.

The collection of shadows forms a system of equations whose solution determines the

matrix elements of the 2-RDM

$$S_n^{pq} = \sum_{ijkl} U_n^{pi} U_n^{qj}\, {}^2D_{kl}^{ij}\, U_n^{ql} U_n^{pk}, \tag{7.12}$$

with $U_n = \exp\{(A_n)\}$. Rather than solving this system directly, however, we add this system of equations in Eq. (7.12) to the constraints of the semidefinite program in Eqs. (7.3-7.8). The solution of the shadow constraints by SDP allows us to find the solution of the underdetermined shadow constraints that minimizes the energy and satisfies the $N$-representability conditions [3]. From this perspective, the SDP and $N$-representability conditions serve to regularize the solution of the shadow tomography, accelerating its convergence towards an accurate, physically meaningful solution. Conversely, we can also view the shadow constraints as modifying the variational 2-RDM method to restrict its domain of the minimization to be consistent with the prior information obtained from the state measurements on the quantum device.

A sufficiently large set of shadows—each shadow defined by Eq. (7.12)—allows full prediction of the 2-RDM or any two-electron expectation value without full tomography of the $N$-electron density matrix or even the 2-RDM since only diagonal parts of the 2-RDM are being measured for each shadow. Moreover, because the diagonal parts of the 2-RDM commute, they can be measured simultaneously (i.e., in parallel) on the quantum device. The most efficient procedure constructs just enough shadows to approximate the 2-RDM, subject to an approximate set of necessary $N$-representability conditions, such that its properties (e.g., energy, dipole, or orbital occupations) are within a target range. Importantly, each of the linear equations in Eq. (7.12), relating the measured shadows to the underlying 2-RDM, can be relaxed to a pair of inequalities that account for noise in the shadows through error parameters, reflecting the level of noise (refer to Ref. [3] for more details).

While the above procedure for excited states is similar to that previously introduced for ground states [3], the excited states must obey orthogonality to the ground state and the

lower-lying excited states. Importantly, this orthogonality is not added to the variational 2-RDM calculation of the $N$-representability-enhanced shadow tomography but rather is enforced implicitly through the shadow constraints. The shadow constraints indirectly contain information about the orthogonality conditions through their description of the excited state. Consequently, the procedure is applicable to a single excited state without reference in the shadow tomography to the other states. Solution of the SDP of the $N$-representability-enhanced shadow tomography whose constraints are given by Eqs. (7.3-7.8) and Eq. (7.12) yields a lower-bound approximation to the excited-state energy. Adding more classical shadows of the 2-RDM as SDP constraints causes the energy to converge from below to the energy of the excited state.

The $N$-representable shadow tomography is compatible with any quantum algorithm for excited states and is robust to statistical error in the 2-RDM such as in the presence of noise on quantum devices, as demonstrated in [3]. For example, the presented tomography can be combined with variational approaches for excited states such as the variational quantum deflation (VQD) and variational subspace expansion (VSE) algorithms [372, 373] or non-variational approaches like the contracted quantum eigensolver (CQE) [319, 374, 375] algorithms that solve the contracted Schrödinger equation (CSE). In each case, the enhanced shadow tomography may be used for more efficient and more accurate measurements of excited-state 2-RDMs and their observables.

## 7.4 Results

To illustrate the effectiveness of the excited-state shadow variational 2-RDM (sv2RDM) method, we explore the algorithm's performance in two applications, the four lowest-lying singlet excited states of the strongly correlated linear $H_4$ chain [348] and the photoexcited reaction pathway from *gauche*-1,3-butadiene to bicyclobutane via a conical intersection [376–383]. For the $H_4$ chain we generate the classical shadows from the full configuration interac-

tion (FCI) [384] wavefunction with the minimal Slater-type-orbital (STO-3G) basis set [349] and for the *gauche*-1,3-butadiene to bicyclobutane pathway we use those from complete active space configuration interaction (CASCI) [385] with a 10 electrons-in-10 orbitals (10,10) active space and the split-valence double-zeta polarized (6-31G*) basis set [386]. Using multiple excited states showcases the applicability of the SDP framework for accurately describing multi-reference, excited-state energies. All computations are performed using the Quantum Chemistry Package [347] in Maple [346].

### *7.4.1 Low-lying $H_4$ excited states*

Figure 7.1 shows excited-state energies of $H_4$ from the sv2RDM method with 2-positivity (DQG) conditions converging quickly with the number of shadows to those from the FCI solution. For the first excited state, adding a single classical shadow with D, Q, and G conditions to a shadowless variational 2-RDM calculation increases the convergence accuracy to the target state by 16 times. Similarly, in the calculation of higher excited states, the difference between the energy without shadows and the energy with one shadow shows the largest change—larger than the change from any subsequent additions of a single shadow.

The $N$-representability in the ground-state shadow tomography enhances the accuracy of observables with fewer measurements. In this work, the combination of shadow and $N$-representability constraints not only decreases the number of measurements relative to conventional shadow tomography for the 2-RDM but also imposes orthogonality of the targeted excited state relative to the ground state and the lower-lying excited states. While we focus on applying the technique to computing singlet states, the algorithm can treat any spin symmetry.

The logarithm of the absolute energy error for sv2RDM with different $N$-representability conditions is shown in Fig. 7.2(a)-(d). The energy errors for results with a single shadow decrease notably faster when all three $N$-representability conditions, rather than just the D

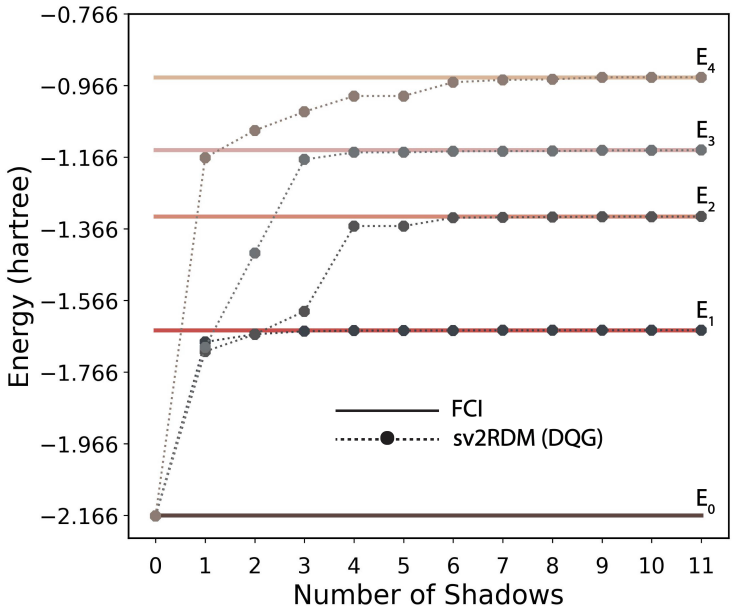


Figure 7.1: The energies (hartree) of the four lowest-lying singlet excited states of the $H_4$ chain with 1.00 Å H-H bonds are shown as a function of the number of shadows included in the sv2RDM. In each case, the exact convergence of energy to the FCI solution is reached within 11 shadows when all 2-positivity conditions (D, Q, and G) are included.

condition, are considered. The sv2RDM (DQ) and (DQG) energies converge to the exact FCI energy with 11 generated shadows, while both reach chemical accuracy ($\approx$ 1 kcal/mol) in 7 shadows. Using only the D condition, we find that the sv2RDM calculation is within 17 mhartree of the target excited state, which also holds for the higher excited states.

Table 7.1 illustrates the importance of including D, Q, and G conditions along with the shadow procedure for attaining the highest accuracy of the observables estimated from the 2-RDM. For example, with a single shadow and the DQG conditions, the Frobenius norm of the 2-RDM relative to FCI is approximately four times lower than that with only the D condition. With 9 shadows, the Frobenius norm of the difference between the sv2RDM (DQG) and FCI 2-RDMs is within the range of $10^{-3}$ - $10^{-6}$ for all studied excited states. Meanwhile, the excited-state energies computed with only the D condition show incomplete convergence to those from FCI with errors on the order of $10^{-2}$. The results emphasize the necessity of including $N$-representability in the 2-RDM tomography for achieving both the

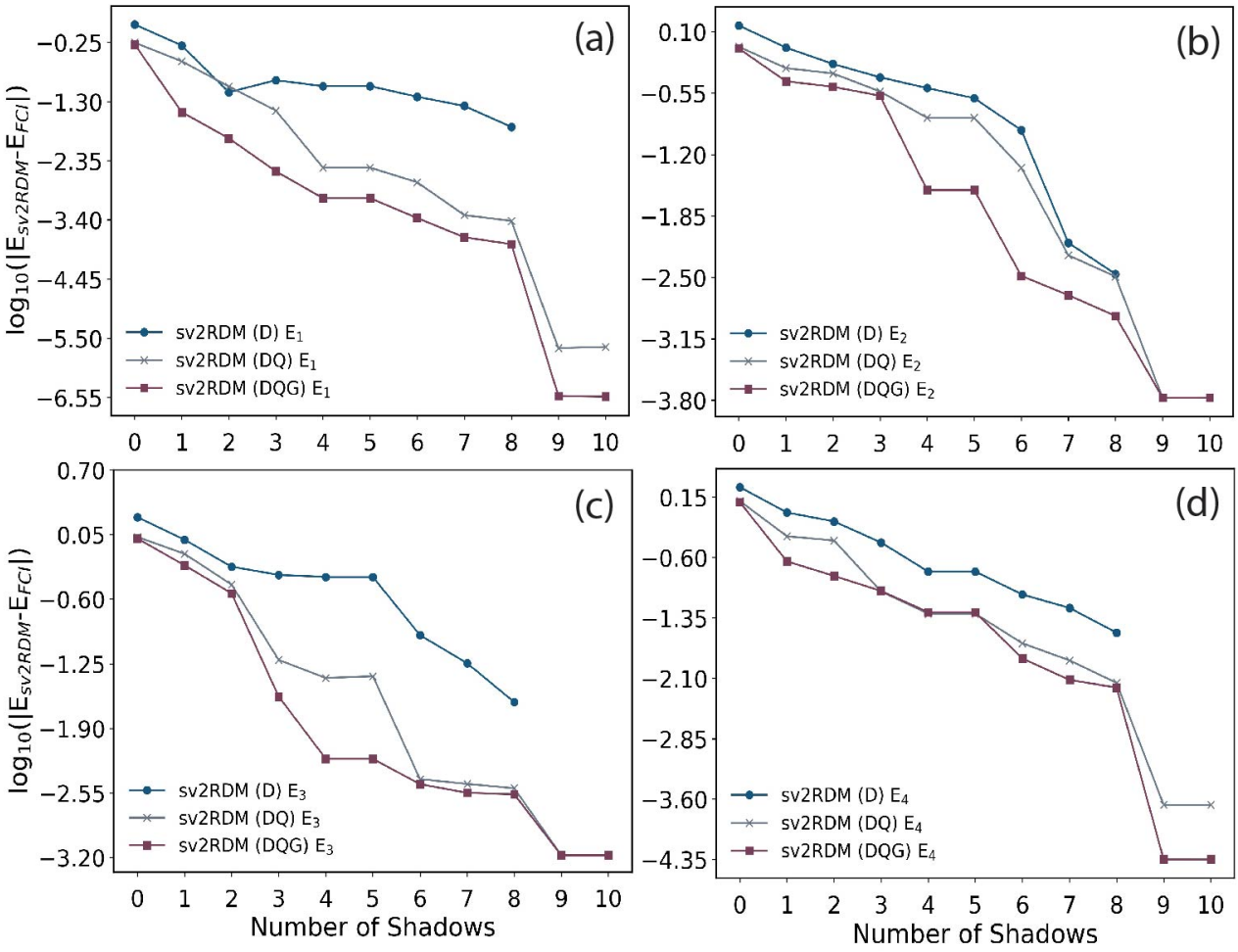


Figure 7.2: The absolute energy error of each of the four lowest-lying singlet excited states of $H_4$ for the different positivity conditions, plotted on the $\log_{10}$ scale as a function of the number of shadows. Here, the panels show (a) the first excited state, $E_1$, (b) the second excited state, $E_2$, (c) the third excited state, $E_3$, and (d) the fourth excited state, $E_4$. The collective DQG conditions significantly improve the accuracy of any given excited-state calculation compared to the D condition alone.

Table 7.1: The normalized Frobenius norm of the 2-RDM relative to FCI in the STO-3G basis set is presented as a function of the number of shadows and $N$-representability conditions for the first four excited states of $H_4$ with 1.00 Å H-H bonds. The DQG conditions significantly improve upon D for all shadows.

| State | Shadow(s) | D | DQ | DQG |
|---|---|---|---|---|
| $E_1$ | 1 | 0.37158371 | 0.28627519 | 0.09754087 |
| | 5 | 0.07565879 | 0.00713184 | 0.00180852 |
| | 9 | 0.03222087 | 0.00291267 | 0.00000549 |
| $E_2$ | 1 | 0.42849229 | 0.20740997 | 0.21358258 |
| | 5 | 0.14951900 | 0.12699556 | 0.02117810 |
| | 9 | - | 0.00122819 | 0.00037389 |
| $E_3$ | 1 | 0.33982215 | 0.30487523 | 0.29051657 |
| | 5 | 0.19731070 | 0.03114331 | 0.00379993 |
| | 9 | - | 0.00625127 | 0.00045033 |
| $E_4$ | 1 | 0.41517114 | 0.28399191 | 0.13804940 |
| | 5 | 0.08075783 | 0.03443228 | 0.03624089 |
| | 9 | - | 0.00418814 | 0.00178340 |

target accuracy and the reduction in computational scaling with the number of shadows. The latter is especially true at the point of greatest difference between the initial and target states, as in the case of excited-state calculation from a ground-state reference.

Though the convergence pattern of the DQ and DQG curves in all panels of Fig. 7.2 remains similar, it is important to note that in the higher excited states (panels (c) and (d)), including only the D and Q conditions may be enough for reaching chemical accuracy with the fewest computational resources. For example, in the case of the fourth excited state, 9 shadows are sufficient to reach convergence within chemical accuracy for both DQG and DQ conditions. Previously, we have demonstrated this interplay between the shadow behavior and $N$-representability conditions in the study of ground-state systems [3]. Here, we demonstrate the efficiency of including even a subset of the conditions in the treatment of excited states with high accuracy.

### *7.4.2 The photoexcited conversion of gauche-1,3-butadiene to bicyclobutane*

The electrocyclic conversion of *gauche* 1,3-butadiene (GBUT) to bicyclobutane (BIBUT) has been a subject of extensive study, with a special emphasis on the many conical intersections along its potential energy surface (PES) [376–378, 382, 383, 387–389]. The conical intersections in these reactions offer an efficient radiationless deactivation or chemical transformation pathway of the reacting system. Previously, it has been shown that the transition from the photoexcited GBUT to BIBUT occurs via a disrotatory pathway [377], which is a conversion of a conjugated molecule to a cyclic structure where the ring closing of the two end carbons occurs by rotation in opposite directions according to the Woodward-Hoffmann rules [390]. The disrotatory transition state (TSD) is a biradical with two approximately half-filled molecular orbitals and, as such, has a multireferenced wavefunction. We compute absolute energies of the critical points along the ground- and excited-state PES of GBUT and BIBUT via complete-active-space configuration-interaction (CASCI) [385] method in a basis of complete-active-space self-consistent-field (CASSCF) orbitals, with a 10 electrons-in-10 orbitals (10,10) active space and in the split-valence double-zeta polarized (6-31G*) basis set [386]. Molecular geometries of GBUT, BIBUT, and TSD are taken from Ref. [376] and the molecular geometry of the conical intersection (CI) is taken from Ref. [377]. All geometries are listed in Appendix D. All geometries were optimized using the CASSCF method in the 6-31G* basis set with a (10,10) active space for GBUT, BIBUT, and TSD, and a (4,4) active space for the CI and state averaging with a weight of [1, 1].

The total and relative energies of the stationary points of the ground- and excited-state PES calculated using CASCI and sv2RDM (DQG) are reported in Table 7.2. The results confirm the monotonically decreasing reaction pathway from the photoexcited state of *gauche*-1,3-butadiene (GBUT*) to BIBUT through the CI. The qualitative description of this pathway is presented in Fig. 7.3 with included geometries of the studied stationary points and their energies relative to GBUT in kcal/mol. Both CASCI and sv2RDM confirm the previ-

Table 7.2: Total energies (hartree) and relative energies (kcal/mol), with respect to the *gauche*-1,3-butadiene (GBUT) molecule, are reported for the ground and first excited states of GBUT, bicyclobutane (BIBUT), disrotatory transition state (TSD), and the conical intersection (CI) in the 6-31G* basis set. The reported sv2RDM values are computed with D, Q, and G conditions.

| Molecule | Total energies (hartree) | | | Relative energies (kcal/mol) | |
|---|---|---|---|---|---|
| | CASCI | sv2RDM | Shadows | CASCI | sv2RDM |
| GBUT | -155.021 | -155.022 | 100 | 0.00 | 0.00 |
| GBUT* | -154.776 | -154.777 | 110 | 154.08 | 153.72 |
| CI | -154.863 | -154.868 | 90 | 99.03 | 96.92 |
| CI* | -154.861 | -154.866 | 90 | 100.48 | 98.44 |
| TSD | -154.890 | -154.892 | 120 | 82.13 | 81.54 |
| TSD* | -154.795 | -154.797 | 120 | 142.02 | 141.17 |
| BIBUT | -154.954 | -154.956 | 80 | 42.17 | 41.45 |
| BIBUT* | -154.610 | -154.614 | 90 | 257.88 | 256.04 |

ously reported features of this relaxation [377, 378, 381, 382] with a monotonically decreasing energy pathway through the conical intersection, which is geometrically very similar to TSD. Remarkably, sv2RDM, a method fundamentally based on the ground-state 2-RDM, is able to predict the correct excitation energies of both ground- and excited-state systems to within 1 mhartree for GBUT/GBUT* and 5 mhartree for the CI/CI* structures. Most importantly, the energy gaps between the ground and excited states of each system are conserved with the sv2RDM method. This suggests that the classical shadow, when sampling from an accurate excited-state wavefunction, does not implicitly alter the degree of correlation present in the system and uniformly retains the correlation effects. Additionally, with sufficient shadows, exact convergence is possible, though the optimal choice of the $N$-representability conditions and the number of shadows used will depend on the target accuracy.

To assess the degree of electron correlation and, more generally, the amount of quantum information present in the studied systems, we compute the natural occupation numbers and

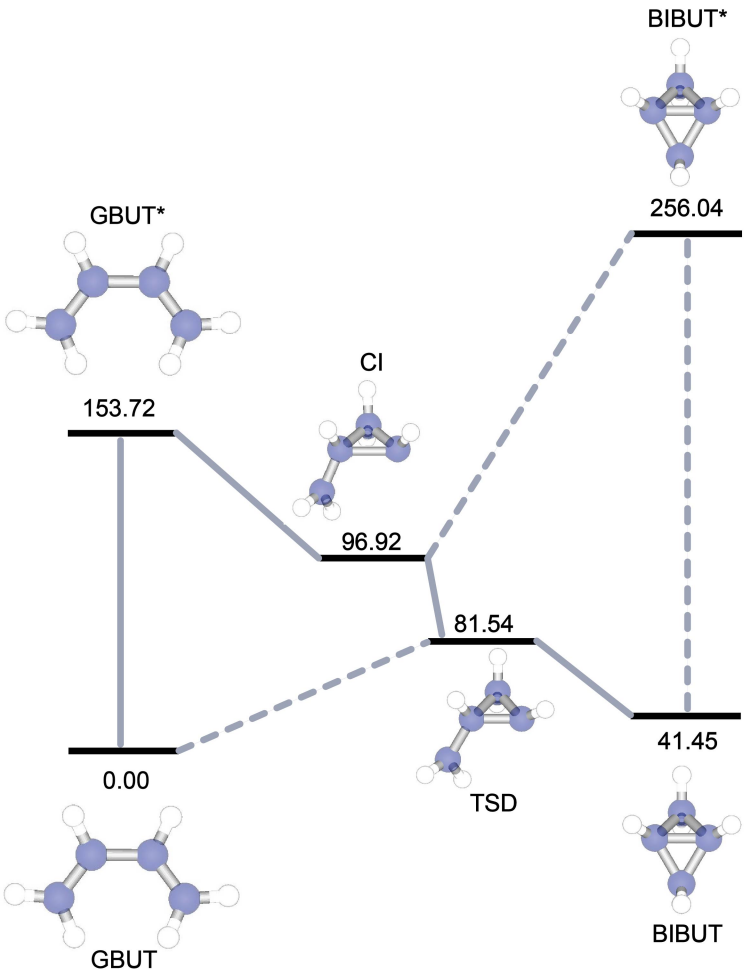


Figure 7.3: Critical points on the potential energy surface of the photoexcited conversion of *gauche*-1,3-butadiene (GBUT) to bicyclobutane (BIBUT) computed via sv2RDM (DQG) in the 6-31G* basis set. The solid lines represent a path for the conversion of the excited-state reactants to ground-state products. The dashed lines represent the reverse pathway. The disrotatory transition state is labeled as TSD and the conical intersection is labeled as CI. Energies relative to GBUT are computed in kcal/mol.

Table 7.3: Natural occupation numbers and von Neumann entropies (vNEs) are reported for the ground- and first-excited states of the *gauche*-1,3-butadiene (GBUT), bicyclobutane (BIBUT), disrotatory transition state (TSD), and the conical intersection (CI) in the 6-31G* basis set from the sv2RDM (DQG) method. The values agree exactly with those from the CASCI method in the same basis set.

| Orbital index | GBUT | GBUT* | BIBUT | BIBUT* | TSD | TSD* | CI | CI* |
|---|---|---|---|---|---|---|---|---|
| 14 | 0.9598 | 0.8004 | 0.9864 | 0.9852 | 0.9835 | 0.9798 | 0.9774 | 0.9726 |
| 15 | 0.9373 | 0.5267 | 0.9799 | 0.4995 | 0.5511 | 0.9333 | 0.7675 | 0.8441 |
| 16 | 0.0646 | 0.4976 | 0.0213 | 0.4939 | 0.4496 | 0.0682 | 0.2349 | 0.1577 |
| 17 | 0.0387 | 0.1750 | 0.0123 | 0.0158 | 0.0192 | 0.0166 | 0.0240 | 0.0271 |
| vNE | 0.4028 | 1.1685 | 0.1694 | 0.7753 | 0.7801 | 0.3355 | 0.6548 | 0.5592 |

von Neumann entropies (vNEs) in Table 7.3. The computed vNE is defined as,

$$\text{vNE} = -\sum_{i}^{r} n_i \ln(n_i), \tag{7.13}$$

where $n_i$ is the occupation number of the $i$-th active orbital and $r$ is the number of active orbitals. Natural orbitals are defined as the eigenfunctions of the one-electron RDM (1-RDM) and their eigenvalues are the natural occupations (NOs). The exact agreement in NOs between CASCI and sv2RDM is reported in Table 7.3. Without any electron correlation, the vNE is zero and increases with more fractional NOs between 0 and 1. The reported values correspond to a single spin block since all systems are studied in their singlet states, where the two spin blocks of the 1-RDM are identical. Nearly degenerate occupation of orbitals 15 and 16 in GIBUT* and BIBUT*, the highest- and lowest-occupied Hartree-Fock orbitals, respectively, reflects a significant amount of multireference (biradical) correlation in these systems, also depicted by vNE values significantly greater than zero. With respect to the number of shadows generated in the SDP, sv2RDM shows the highest agreement with the CASCI energy values for the GBUT* system. This demonstrates that the classical shadow procedure implemented with the DQG conditions has the ability to reconstruct a state of high multireference character, a result particularly relevant for chemically accurate

simulation of physically relevant systems with high correlation on quantum devices.

The conical intersection (CI) is a particularly interesting feature along this photoexcited conversion pathway, for it is a region where two potential energy surfaces intersect [387, 391]. It is also a point of energetic degeneracy in the crossing of electronic states and thus, exhibits a significant amount of multireference correlation. The ground and excited states of the CI calculated with sv2RDM maintain a very narrow energy gap with one or all three of the positivity conditions, as shown in Fig. 7.4. Importantly, the accuracy of the converged values at each shadow step is much higher when all three of the 2-positivity conditions are considered. Hence, including the positivity conditions in the semidefinite procedure along with the shadow constraints plays a key role in efficiently and accurately reconstructing the highly correlated states. This conclusion is further supported by the results in Table 7.4, where the normalized Frobenius norm of the 2-RDM from the sv2RDM method relative to that from CASCI is reported. Evidently, including the Q and G conditions in addition to D suffices to provide near-to or chemically accurate results with the error in terms of the Frobenius norm being on the order of $10^{-4}$ for all systems. Overall, the DQG conditions significantly improve upon D for any number of generated shadows.

## 7.5 Discussion and Conclusions

In this work, we generalize the previously demonstrated $N$-representable shadow tomography of the 2-RDM [3] to treat excited states. In the 2-RDM shadow tomography, the diagonal (classical) parts are measured with respect to randomly generated unitary transformations of the natural orbitals. The outputs of this procedure are classical shadows of an unknown quantum state that can be used to predict arbitrary expectation values. Our classical algorithm reconstructs the 2-RDM from a set of classical shadows while enforcing the necessary $N$-representability conditions to ensure the system of interest corresponds to an $N$-particle wavefunction. This procedure, we show here, can be generalized to treat excited states.

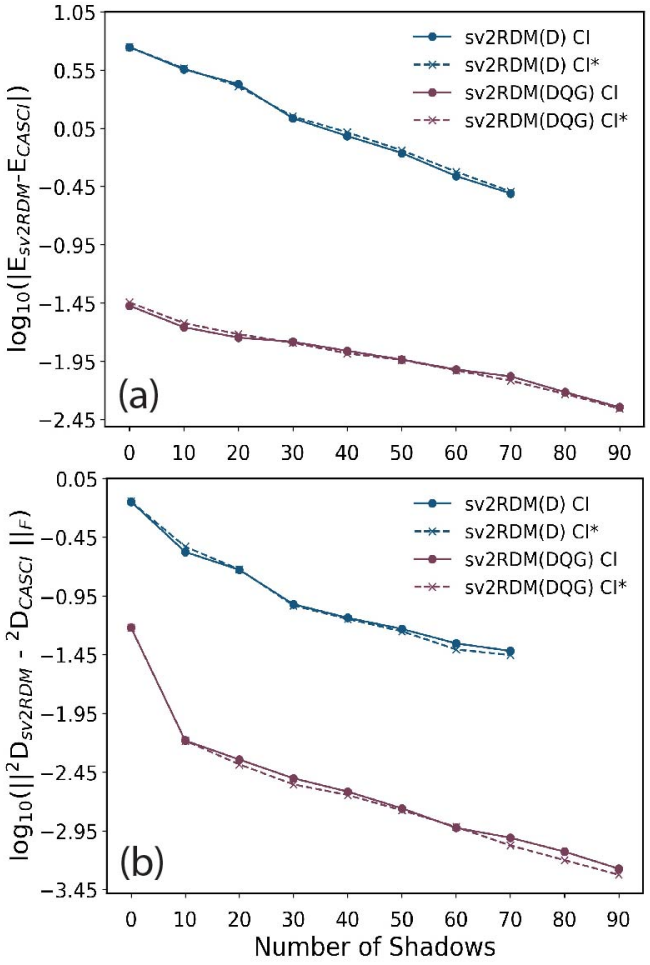


Figure 7.4: The absolute energy error between sv2RDM and CASCI (a) and the normalized Frobenius norm of the 2-RDM from sv2RDM relative to CASCI (b) are presented on the $\log_{10}$ scale as functions of the number of shadows for the ground and excited states of the conical intersection (CI/CI*) with a comparison of calculations including only the D condition (blue lines) with those including D, Q, and G conditions (purple lines). It can be noticed the sv2RDM retains the small energy gap between the ground and excited states of the CI regardless of the number of positivity conditions included in the calculation, though the accuracy is significantly enhanced when all of the D, Q, and G conditions are considered.

Table 7.4: The normalized Frobenius norm of the 2-RDM relative to CASCI is reported as a function of the number of shadows and $N$-representability conditions for the ground and first excited states of *gauche*-1,3-butadiene (GBUT), bicyclobutane (BIBUT), disrotatory transition state (TSD), and the conical intersection (CI) systems. In some cases, the sv2RDM with only the D condition was not able to converge beyond a certain number of shadows, which is illustrated by the absence of data in the table.

| Molecule | Shadows | D | DQG |
|---|---|---|---|
| GBUT | 0 | 0.70721306 | 0.00561919 |
| | 30 | 0.12277152 | 0.00198033 |
| | 60 | 0.06623763 | 0.00079912 |
| | 90 | - | 0.00033200 |
| GBUT* | 0 | 0.70721307 | 0.11905626 |
| | 30 | 0.12624018 | 0.00658575 |
| | 60 | 0.05740913 | 0.00233879 |
| | 90 | - | 0.00090734 |
| BIBUT | 0 | 0.71642749 | 0.00517725 |
| | 30 | 0.07324626 | 0.00108944 |
| | 60 | 0.03608055 | 0.00040568 |
| | 80 | - | 0.00020316 |
| BIBUT* | 0 | 0.70949264 | 0.10192894 |
| | 30 | 0.09922607 | 0.00278957 |
| | 60 | 0.04188981 | 0.00122781 |
| | 90 | - | 0.00047068 |
| TSD | 0 | 0.70776552 | 0.00816901 |
| | 30 | 0.10629265 | 0.00306653 |
| | 60 | 0.05140730 | 0.00137910 |
| | 90 | - | 0.00058986 |
| TSD* | 0 | 0.71332641 | 0.11034467 |
| | 30 | 0.08720601 | 0.00229741 |
| | 60 | 0.04024479 | 0.00098947 |
| | 90 | - | 0.00037923 |
| CI | 0 | 0.71359496 | 0.06047515 |
| | 30 | 0.09519725 | 0.00313828 |
| | 60 | 0.04425476 | 0.00118907 |
| | 90 | - | 0.00053367 |
| CI* | 0 | 0.71523441 | 0.06047524 |
| | 30 | 0.09311047 | 0.00278766 |
| | 60 | 0.03932743 | 0.00121062 |
| | 90 | - | 0.00047420 |

Significantly, the orthogonality of the excited states is implicitly contained in the classical shadows, allowing us to tomography various excited states without explicitly accounting for the orthogonality in the optimization. We can, therefore, apply the shadow tomography to any single excited state without knowledge of the ground state or the other excited states, making the algorithm applicable to any quantum algorithm for electronic excited states.

We demonstrated the effectiveness of $N$-representability conditions (DQG) in shadow tomography of the excited-state 2-RDM by calculating the four lowest-lying singlet excited states of the $H_4$ chain and the stationary points along the photoexcited conversion pathway of *gauche*-1,3-butadiene to bicyclobutane via a conical intersection. The results illustrated accurate ground- and excited-state properties computed efficiently with approximately $n_s r^2$ measurements, where $n_s$ is the number of shadows and $r$ is the number of orbitals, with $n_s \ll r^2$ for target accuracy. Moreover, at this reduced computational cost, the algorithm preserved essential multireference correlation effects, which is especially important in studying physically relevant systems on quantum hardware.

Including the $N$-representability constraints in the shadow tomography of the reduced density matrices of many-body systems has the benefits of a reduced number of measurements, the ability to treat strong electron correlation, and a framework generalizable to calculating properties of larger many-fermion quantum systems. Here, our results showcase the significant advantage of merging $N$-representability constraints with shadow tomography, especially for excited states. Additionally, we demonstrate that including only a subset of the $N$-representability conditions, such as the D and Q conditions, can be highly effective for reaching target accuracy.

The present work lays the foundation for the application of the $N$-representable shadow tomography to calculating excited states with various quantum algorithms, including those based on the variational quantum eigensolver (VQE) as well as the contracted quantum eigensolver (CQE), on quantum devices. On NISQ devices the addition of the $N$-representability

conditions to the classical post-processing of the shadows will be useful not only in decreasing the number of measurements but also in mitigating the errors in the shadows during the reconstruction of the 2-RDM. The benefits of the enhanced shadow tomography—reduction in measurements and enhancement in accuracy—may be especially useful for resolving nearly degenerate excited states such as those arising in the study of conical intersections and nonadiabatic dynamics. Additionally, the described shadow state tomography can readily be applied to process tomography [258, 392], which will be explored in future work. Combining shadow tomography with $N$-representability conditions via semidefinite programming provides an important step towards the more realistic simulation of molecular excited-state phenomena on quantum devices.

## 7.6 Acknowledgments

D.A.M. gratefully acknowledges the U.S. National Science Foundation Grant CHE-2155082 and the Department of Energy, Office of Basic Energy Sciences, Grant DE-SC0019215. I.A. gratefully acknowledges the NSF Graduate Research Fellowship Program under Grant No. 2140001. The data supporting this Chapter can be found in Appendix D.

# CHAPTER 8

# CONSTRAINED SHADOW TOMOGRAPHY FOR MOLECULAR SIMULATION ON QUANTUM DEVICES

This chapter is reprinted (adapted) with permissions from *Chem. Sci.* **2026**, Advance Article, DOI: 10.1039/D5SC09162D

## 8.1 Chapter Synopsis

Quantum state tomography is a fundamental task in quantum information science, enabling detailed characterization of correlations, entanglement, and electronic structure in quantum systems. However, its exponential measurement and computational demands limit scalability, motivating efficient alternatives such as classical shadows, which enable accurate prediction of many observables from randomized measurements. In this work, we introduce a bi-objective semidefinite programming approach for constrained shadow tomography, designed to reconstruct the two-particle reduced density matrix (2-RDM) from noisy or incomplete shadow data. By integrating $N$-representability constraints and nuclear-norm regularization into the optimization, the method builds an $N$-representable 2-RDM that balances fidelity to the shadow measurements with energy minimization. This unified framework mitigates noise and sampling errors while enforcing physical consistency in the reconstructed states. Numerical and hardware results demonstrate that the approach significantly improves accuracy, noise resilience, and scalability, providing a robust foundation for physically consistent fermionic state reconstruction in realistic quantum simulations.

## 8.2 Introduction

Reconstructing a system's quantum state from measurement data, a process known as quantum state tomography [393–396], is foundational to quantum information science, many-

body physics, and quantum chemistry. Accurate knowledge of a system's quantum state enables quantitative characterization of correlations, entanglement, and electronic structure properties, all of which are important for performing quantum simulations, benchmarking quantum hardware, and interpreting experimental outcomes. Quantum state tomography provides the most direct route to validating state preparation, certifying entanglement in quantum devices, and probing nonclassical correlations in condensed matter and chemical systems. However, conventional full-state tomography requires measurement and computational resources that scale exponentially with system size, rendering it infeasible for all but the smallest quantum systems [133, 134, 319, 320].

To overcome this limitation, a wide range of scalable tomographic approaches have been developed. These methods aim to infer only the most relevant or physically meaningful aspects of a quantum state rather than reconstructing the full wavefunction. Such approaches include compressed sensing [261, 262], neural-network-based tomography [263, 264], direct fidelity estimation [265–267], and maximum-entropy-inspired methods based on restricted Boltzmann machines [268], among others. A particularly powerful and widely adopted framework is that of classical shadows [230, 231], which enables efficient estimation of a large number of observables from randomized measurements. The shadow tomography protocol constructs a compact classical representation, termed a "shadow", from a set of randomized qubit or fermionic measurements, from which expectation values of many observables can be predicted with polynomial or even logarithmic scaling in system size. This paradigm has been successfully applied in a variety of contexts, including entanglement estimation [269], Hamiltonian learning [270–272], and reduced density matrix (RDM) reconstruction for quantum chemistry [236, 238].

When specialized to fermionic systems, shadow-based methods can leverage rich physical structure, such as antisymmetry [397], particle-number conservation [236], spin symmetries, and Gaussian unitary transformations [238, 398, 399], to further improve sampling efficiency

and reconstruction fidelity. These fermionic shadow protocols enable scalable characterization of electronic structure properties and correlation functions relevant to molecular and solid-state systems, potentially bridging the gap between quantum simulation and classical post-processing. However, despite their theoretical efficiency, existing fermionic shadow tomography approaches face significant practical challenges. In particular, the presence of sampling noise, gate infidelity, and finite measurement statistics on quantum devices can severely degrade reconstruction accuracy.

In this work, we introduce an improved and optimized *constrained shadow tomography* framework, building on prior work [3, 4], specifically tailored for the simulation of realistic fermionic systems on quantum devices. Our method formulates the reconstruction of the two-particle reduced density matrix (2-RDM) as a bi-objective semidefinite optimization, extending shadow-based tomography through a constrained formulation designed to improve robustness to noise and limited measurement data. By incorporating physical $N$-representability constraints directly into the optimization and adding a nuclear-norm regularization to the energy minimization, the method reconstructs a shadow-consistent 2-RDM that satisfies the $N$-representability conditions through an optimization that balances energy minimization against fidelity to the measured shadow data. This unified semidefinite program simultaneously mitigates errors arising from finite sampling and hardware noise while enforcing physical consistency in the resulting RDMs. Consequently, the framework can be viewed as a noise-aware, state-tailored extension of variational RDM theory [72, 74, 76–81, 90, 324, 326, 328, 330–332, 400–405], capable of producing physically valid density matrices under realistic quantum measurement conditions.

Through comprehensive numerical analysis, we explore how measurement requirements scale with system size, orbital basis dimension, and the choice of $N$-representability constraints, identifying practical regimes where constrained tomography yields superior performance over other approaches. Finally, we validate constrained shadow tomography through

computations performed on IBM's superconducting quantum device, confirming that the advantages of constraint-enforced shadow tomography persist under realistic experimental conditions involving gate noise, readout errors, and limited sampling depth. Our results highlight the importance of integrating physical priors and optimization-based constraints into quantum state reconstruction frameworks, paving the way for accurate and scalable molecular simulation on quantum hardware.

## 8.3 Theory

### *8.3.1 Shadow tomography for fermionic systems*

Characterizing the full state of a quantum system requires exponentially scaling resources, making it infeasible for practical applications. Tomography schemes based on random measurements have emerged as more computationally accessible alternatives [225, 406, 407], with classical shadow tomography being among the most widely used [230, 231]. Classical shadow tomography allows for the reconstruction of a quantum state from repeated measurements in different unitary bases, using resources that scale logarithmically with the system size in some cases [238]. By applying random unitary operations, $U$, to the quantum state, $|\psi\rangle$, followed by a computational basis measurement, $|b\rangle$, a "classical shadow" estimator can be constructed,

$$\hat{\rho}_i = \mathcal{M}^{-1}\left(U_i^\dagger |b_i\rangle\langle b_i| U_i\right), \tag{8.1}$$

where $\mathcal{M}$ is the measurement channel. The estimator can then be used to predict the expectation values of many observables with provable guarantees,

$$\langle O\rangle_{\text{shadow}} = \frac{1}{M}\sum_{i=1}^{M} \text{Tr}(O\hat{\rho}_i), \tag{8.2}$$

which converges to $\mathrm{Tr}(O\rho)$ as the number of measurements $M$ increases. For fermionic systems, the choice of measurement unitaries is key to an optimal protocol. For example, particle-number conserving transformations or fermionic Gaussian unitaries (FGUs) preserve antisymmetry and can be implemented efficiently on qubit hardware through linear optical or Majorana representations [238, 397, 399]. These structured unitaries significantly reduce circuit depth and improve measurement fidelity compared to fully random Clifford unitaries.

The statistical efficiency of classical shadow tomography is further characterized by the shadow norm, which quantifies the variance of observable estimators under random measurements [231]. For a given observable $O$, the estimation error scales as

$$\mathrm{Var}[\langle O\rangle_{\mathrm{shadow}}] \leq \frac{\|O\|_{\mathrm{sh}}^2}{M}, \tag{8.3}$$

where $\|O\|_{\mathrm{sh}}$ is the shadow norm determined by the chosen measurement ensemble. A smaller shadow norm implies that fewer measurement samples are required to achieve a target precision, emphasizing the importance of designing measurement schemes that minimize $\|O\|_{\mathrm{sh}}$ for low-rank or local fermionic operators.

In the context of electronic structure and many-fermion simulations, the goal is often not full state reconstruction but accurate estimation of low-order observables such as the 2-RDM. Classical shadow tomography provides an efficient statistical framework for directly estimating these quantities from measurement data, enabling integration with post-processing schemes and physical consistency.

Since fermionic wavefunctions prohibitively scale exponentially with particle number, their state tomography is often simplified to an estimation of $p$-particle reduced density matrices ($p$-RDMs). If represented in the qubit basis, estimating all $p$-RDMs on $n$ fermionic modes requires $\mathcal{O}((2n)^p/\epsilon^2)$ measurements [282, 408]. Using FGUs, the sample complexity can be reduced to $\mathcal{O}(\binom{\eta}{p}p^{3/2}\log(n)/\epsilon^2)$ [238]. Considering particle-number symmetry, the required number of samples can further be reduced to $\mathcal{O}(\eta^p/\epsilon^2)$ [236] with $\eta$ particles. Here, the

estimation error remains independent of the full Hilbert space dimension.

### *8.3.2 Constrained shadow tomography of the 2-RDM*

In fermionic shadow tomography, the conservation of parity and particle number symmetry ensures compatibility with the physically relevant symmetry sectors of many-body Hamiltonians, leading to reduced sample complexity. Similarly, ensuring the estimated $p$-RDMs correspond to $N$-particle wavefunctions, i.e., that they are $N$-representable [67, 69, 80, 84, 90, 91, 100, 321, 322, 324], allows for a reduction in measurement overhead as previously demonstrated by some of the authors [3]. Since the electronic Hamiltonian contains at most pairwise interactions, we restrict demonstration of the present work to 2-RDMs. The 2-RDM elements of an $N$-electron system arise from the integration of the $N$-particle density matrix over all particles except two and can be expressed as

$$ {}^2D_{kl}^{ij} = \langle \Psi | \, \hat{a}_i^\dagger \hat{a}_j^\dagger \hat{a}_l \hat{a}_k \, | \Psi \rangle \, , \tag{8.4} $$

where $\hat{a}_i^\dagger$ creates a particle in orbital $i$ and $\hat{a}_i$ annihilates a particle in orbital $i$. The classical shadow representation of the 2-RDM can be expressed as

$$ S_n^{pq} = \langle \Psi | \, \hat{U}_n^\dagger \hat{a}_p^\dagger \hat{a}_q^\dagger \hat{a}_q \hat{a}_p \hat{U}_n \, | \Psi \rangle \, , \tag{8.5} $$

where $\hat{U}_n = \exp\Big\{ \big( \sum_{uv} A_n^{uv} \hat{a}_u^\dagger \hat{a}_v \big) \Big\}$. Here, the indices denote spin orbitals, $A_n$ is a one-body anti-Hermitian matrix, and $n$ is the shadow index. Each shadow $n$ corresponds to measuring all diagonal elements of the 2-RDM after applying the one-body unitary transformation, $\hat{U}_n$, to the wavefunction. The one-body unitaries are generated by random sampling according to the Haar measure [337], effectively rotating the orbitals into a new basis. From Eq. (8.5),

the shadow measurements can be expressed in terms of the 2-RDM elements as

$$S_n^{pq} = \sum_{ijkl} U_n^{pi} U_n^{qj} \, {}^2D_{kl}^{ij} \, U_n^{ql} U_n^{pk}, \tag{8.6}$$

where $U_n = \exp\{(A_n)\}$. A sufficiently large collection of such shadows defines a system of equations that uniquely determines the 2-RDM. Consequently, this approach can be used to reconstruct the 2-RDM (or any one- or two-body expectation value) of the original quantum state. Importantly, since the measurements only involve the classical components of the 2-RDM, which commute and can therefore be measured simultaneously, the overall cost of the tomography is substantially reduced.

By defining an objective functional of the 2-RDM, $(J[{}^2D])$, such as the nuclear norm, Frobenius norm [131], or the energy expectation value [72, 338, 339], a convex optimization problem can be formulated with respect to the shadow constraints,

$$\begin{aligned} &\min_{{}^2D \in {}_2^N\tilde{P}} \quad J[{}^2D] \\ &\text{such that} \quad S_{pq}^n = ((U \otimes U)^2 D (U \otimes U)^T)_{pq}^{pq}, \end{aligned} \tag{8.7}$$

for $n \in [0, m]$, where ${}_2^N\tilde{P}$ denotes the convex set of approximately $N$-representable 2-RDMs. For a quantum many-body system with at most pairwise interactions, minimizing the energy functional $E[{}^2D]$ is particularly appealing due to its direct relevance to molecular simulation. The 2-RDM can further be used to estimate the energy gradients [409, 410] and multipole moments [411]. However, to enable practical implementation on current quantum devices, the formulation must be augmented to properly account for quantum measurement errors.

Motivated by the need to consider two complementary objectives: (1) to obtain an optimal solution to a general functional of the 2-RDM and (2) to minimize measurement errors (e.g., shot/gate noise, readout errors, limited sampling depth, etc.) affecting the 2-RDM, we cast Eq. 8.7 into the following bi-objective semidefinite-programming optimization problem [412,

413]:

$$\min_{^2D \in {}^2_2\tilde{P}} \quad J[^2D] + w \,\|^2D - {}^2\tilde{D}\|_* \tag{8.8}$$

$$\text{subject to} \quad \tilde{S}^n_{pq} = \left((U \otimes U)\, {}^2\tilde{D}\, (U \otimes U)^T\right)^{pq}_{pq}, \tag{8.9}$$

where

$${}^2\tilde{D} = {}^2D + \mathbf{E}_1 - \mathbf{E}_2. \tag{8.10}$$

Here, $w > 0$ is a penalty weight (i.e., regularization parameter), $\|\,\|_*$ denotes nuclear norm, and $\mathbf{E}_i \succeq 0$ are positive semidefinite slack "error" matrices. The penalty parameter $w$ controls the trade-off between energy minimization and physical deviations of the 2-RDM from the shadow measurements. A smaller $w$ allows for a lower energy value but with potentially larger shadow-constraint violations. A similar relaxation strategy was previously employed by some of the authors to infer time-dependent quantum states from measurement data using matrix completion techniques and a modified Frobenius norm within a multiobjective SDP [414]. Related approaches have since been investigated on quantum computers using purification of the 2-RDM [131] and the Quantum Approximate Optimization Algorithm [415].

The second objective function in Eq. 8.9 minimizes the nuclear norm, or the sum of the singular values of the slack matrix, over the constraint set including the shadow constraints. The nuclear norm serves as a convex and computationally tractable surrogate for matrix rank, and efficient first-order algorithms based on singular value thresholding have been developed to solve such problems at large scale [339]. Being convex and easy to optimize, the nuclear norm offers the best convex approximation of the rank function for matrices whose largest singular value is no greater than one [416]. When the matrix variable is symmetric and positive semidefinite, the method relaxes to the trace heuristic, i.e., $\|X\|_* = \mathrm{Tr}(X)$, frequently used in systems and control studies [417, 418].

For practical implementation, considering the energy functional of the 2-RDM and the case where $w_i = w$ for all $i$, we obtain the following bi-objective semidefinite program (SDP), which includes the relaxation for rank via the nuclear norm,

$$\begin{aligned}
\min_{^2D} \quad & E[^2D] + w\mathrm{Tr}(\mathbf{E}_1 + \mathbf{E}_2) \\
\text{such that} \quad & {}^2D \succeq 0 \\
& {}^2Q \succeq 0 \\
& {}^2G \succeq 0 \\
& \mathbf{E}_1 \succeq 0 \\
& \mathbf{E}_2 \succeq 0 \\
& w > 0 \\
& \mathrm{Tr}({}^2D) = N(N-1) \\
& {}^2Q = f_Q({}^2D) \\
& {}^2G = f_G({}^2D) \\
& {}^2\tilde{D} = {}^2D + \mathbf{E}_1 - \mathbf{E}_2 \\
& \tilde{S}^n_{pq} = ((U \otimes U)\, {}^2\tilde{D}\, (U \otimes U)^T)^{pq}_{pq}.
\end{aligned} \tag{8.11}$$

The two error matrices, $\mathbf{E}_1$ and $\mathbf{E}_2$, act as a "positive" and "negative" direction of error, respectively, increasing and decreasing the correction to the 2-RDM simultaneously. In the limit where $w \to 0$, the SDP reduces to the variational 2-RDM algorithm [72, 401], in which only the energy functional $E[^2D]$ is minimized subject to the $N$-representability conditions. In the limit $w \to \infty$, the SDP gains the ability to treat arbitrary quantum states, including excited and non-stationary electronic states, within the same variational framework [10, 419, 420]. In this work, we adopt equal weighting between the energy and measurement-consistency terms as a simple, minimally-biased default that avoids over-committing to either

objective in the presence of noise. More generally, the $w$ parameter may be guided by standard trade-off criteria (e.g., balancing energetic improvement against deviation from the measured shadow data). Additionally, a closely related study by the authors [419] shows that reconstruction performance is often robust across a fairly broad intermediate range of w, with clear improvement over a wide range of choices.

The present algorithm enforces a necessary subset of the $N$-representability conditions, known as the 2-positivity (DQG) conditions [69, 80, 84, 91, 115, 421]. The 2-positivity conditions restrict the particle-particle RDM (${}^2D$), the hole-hole RDM (${}^2Q$), and the particle-hole RDM (${}^2G$) to be positive semidefinite where $f_Q$ and $f_G$ are linear maps connecting ${}^2Q$ and ${}^2G$ to ${}^2D$, respectively. These semidefinite constraints correspond to keeping the particle-particle, hole-hole, and particle-hole probability distributions nonnegative. The 2-positivity conditions incur a computational scaling of $\mathcal{O}(r^4)$ in memory and $\mathcal{O}(r^6)$ in floating-point operations [72], where $r$ denotes the number of orbitals, and therefore, constrained shadow tomography maintains overall polynomial scaling. This scaling is consistent with variational 2-RDM SDP theory, where large-scale calculations have previously been demonstrated with millions of optimization variables (explicit timing data on standard hardware can be found in Ref [72]). Scalability can further be modified by exploiting symmetry and solver structure, and partial constraint hierarchies (e.g., D or DQ). Performing full 2-RDM tomography on a quantum device would nominally require $\mathcal{O}(r^4)$ distinct measurements, whereas our shadow-based technique reduces this requirement to approximately $n_s r^2$, where $n_s$ is the number of classical shadows and typically satisfies $n_s \ll r^2$ for a desired accuracy $\epsilon$ [3, 4].

From a practical standpoint, the error-mitigating formulation presented is particularly well-suited for application on quantum devices, where finite sampling noise and gate errors can corrupt 2-RDM estimates derived from shadow tomography or other measurement schemes. By incorporating error matrices directly into variational optimization, the method provides a mechanism to regularize noisy experimental data while maintaining physical con-

sistency through the $N$-representability constraints. Beyond molecular electronic structure, this framework is broadly applicable to quantum simulation tasks involving spin models, correlated materials, and quantum state tomography, where convex relaxation and data-driven corrections offer a scalable and physically grounded route to extracting reliable observables from imperfect measurements.

## 8.4 Results

To implement constrained shadow tomography, we solve the semidefinite program (SDP) in Eq. 8.11 by adding shadow constraints and nuclear norm relaxation to the variational 2-RDM (v2RDM) method [345, 401] in the Maple Quantum Chemistry Package [422, 423]. We refer to the resulting algorithm as the shadow v2RDM (sv2RDM) method. The SDP is solved using the boundary-point algorithm in Ref. [72]. To simulate measurement uncertainty, we generate noisy 2-RDMs by adding element-wise Gaussian perturbations to the full configuration interaction (FCI) 2-RDMs, corresponding to the Bernoulli shot noise expected from finite sampling (details can be found in Appendix E Sec. E.1). The Fermionic Classical Shadows (FCS) protocol is implemented as described in Ref. [236] (details can be found in Appendix E Sec. E.1). Constrained shadow tomography is applied to the dissociation of the nitrogen dimer, ground-state energies of strongly correlated hydrogen chains [348] with up to ten equally spaced atoms, and a rectangle-square-rectangle transition of $H_4$. The hydrogen atoms are represented in the minimal Slater-type orbital (STO-3G) basis set [349] while nitrogen is represented in the correlation-consistent polarized valence double-zeta (cc-pVDZ) basis set [350] in a 10 electrons-in-8 orbitals [10,8] active space. All quantum circuits used for data collection are implemented using the Qiskit package [146] and ffsim library [424] on IBM's 156-qubit superconducting processor ibm_fez (details can be found in Appendix E Section E.2).

We begin by assessing the accuracy and consistency of the sv2RDM approach against the

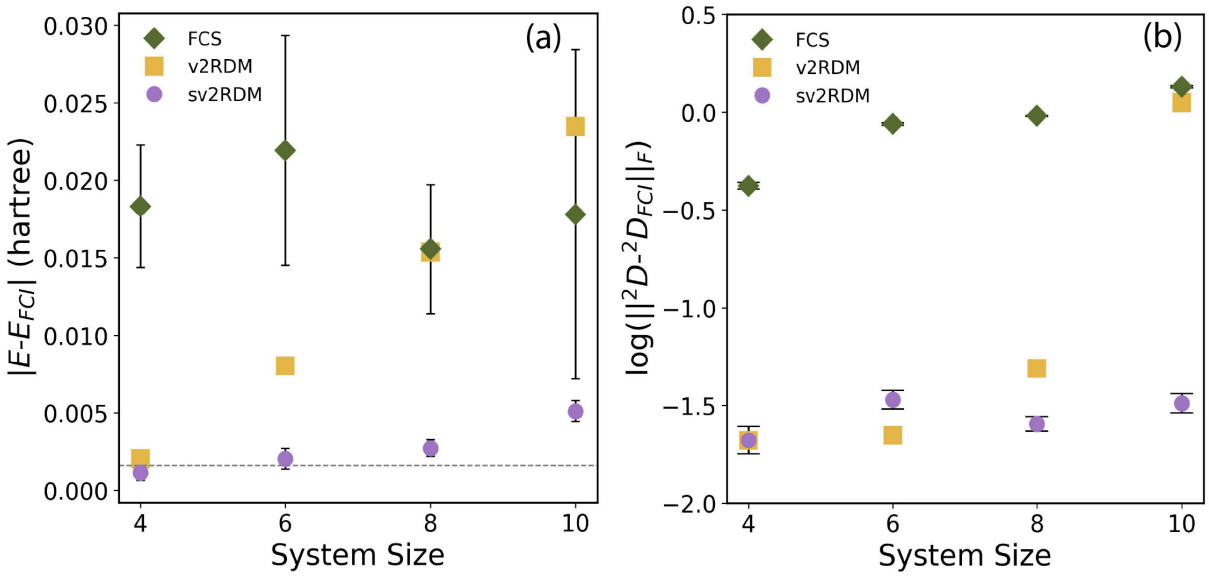


Figure 8.1: (a) Absolute energy error as a function of system size under a fixed total shot budget. (b) Absolute Frobenius norm of the 2-RDM error (relative to 2-RDM from FCI) plotted on a logarithmic scale. Shot budgets compared are: 16,000 unitaries $\times$ 1 shot vs. 16 unitaries $\times$ 1,000 shots for $H_4$; 36,000 unitaries $\times$ 1 shot vs. 36 unitaries $\times$ 1,000 shots for $H_6$; 160,000 unitaries $\times$ 1 shot vs. 160 unitaries $\times$ 1,000 shots for H8; and 300,000 unitaries $\times$ 1 shot vs. 300 unitaries $\times$ 1,000 shots for $H_{10}$. Each data point for the Fermionic Classical Shadows (FCS) and shadow variational 2-RDM (sv2RDM) methods represents the mean of 20 independent runs (10 for $H_{10}$). Error bars denote 95% confidence intervals (approximately $2\sigma$) computed from these measurements. All calculations are performed using the minimal basis set.

most-favorably scaling FCS tomography protocol [236]. Figure C.1 summarizes the dependence of absolute energy error, computed in the minimal basis set, and the Frobenius norm of the 2-RDM error (relative to the 2-RDM from full configuration interaction (FCI)) on system size under fixed total shot budgets for hydrogen chains of increasing length ($H_4$-$H_{10}$). Two sampling strategies were compared: the many-unitary/single-shot optimum for the FCS and the few-unitary/ multiple-shot protocol for the sv2RDM. Each data point represents an average over 20 independent runs (10 for $H_{10}$), with 95% confidence intervals indicated by the error bars. Both quantum tomography methods are compared with the classical v2RDM method. Across all systems, the overall trends reveal sv2RDM outperforming FCS in both total energy and 2-RDM reconstruction with respect to the FCI results, given the same total shot budget for the two protocols. Importantly, the circuits corresponding to the shot budgets used are up to two orders of magnitude lower in depth for sv2RDM, substantially improving the feasibility of constrained shadow tomography on quantum hardware. Moreover, the sv2RDM method provides greater accuracy than the classical v2RDM method with increasing system size.

Figure 8.2 shows the lowest eigenvalue of the 2-RDM as a function of the total shot budget for $H_4$ in the minimal basis, comparing the sv2RDM method with full 2-positivity conditions (DQG) to the FCS approach, which does not inherently produce $N$-representable matrices. As the total number of shots increases, both methods converge toward consistent eigenvalue estimates, indicating improved reconstruction of the underlying fermionic state. At low shot budgets, the FCS results exhibit larger fluctuations and unphysical negative eigenvalues, reflecting the stochastic nature of randomized measurement sampling. As expected from the scaling analysis in Ref. [236], the statistical fluctuations in the FCS protocol diminish approximately as $1/\sqrt{(N_{shots})}$, leading to a smooth convergence toward the physically valid spectrum at greater sampling depths. In contrast, the sv2RDM (DQG) results remain stable across all sampling regimes with the most “negative" eigenvalue being zero, demonstrating

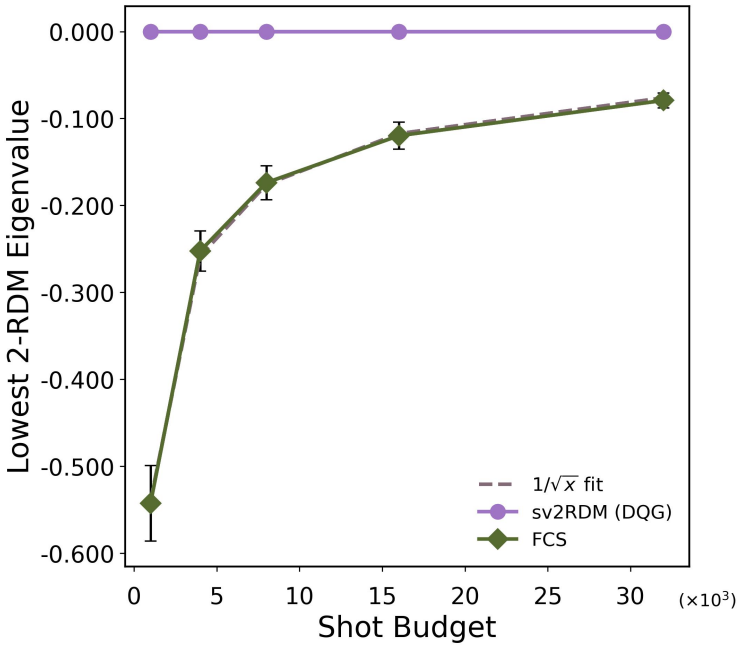


Figure 8.2: Lowest 2-RDM eigenvalue as a function of total shot budget for the shadow variational 2-RDM (sv2RDM) method with full 2-positivity (DQG) constraints and for the Fermionic Classical Shadows (FCS) approach applied to $H_4$ in the minimal basis set.

that explicit enforcement of $N$-representability constraints significantly mitigates noise sensitivity and maintains physically valid 2-RDM spectra.

To further address the physicality of the reconstructed RDMs, Fig. 8.3 compares the absolute error matrices of the 2-RDMs obtained from sv2RDM (DQG) (a) and FCS (b) for the $H_4$ system in the minimal basis. Each matrix element represents the absolute deviation from the FCI reference value. The sv2RDM (DQG) reconstruction exhibits uniformly low and smoothly distributed errors, consistent with the enforcement of $N$-representability conditions. In contrast, the FCS results display more pronounced and localized deviations, across all elements, further highlighting the statistical noise associated with such stochastic measurement sampling. The visual contrast between the two panels emphasizes that the constrained sv2RDM approach yields systematically more accurate and physically consistent 2-RDMs than the unconstrained FCS method under comparable measurement resources.

Table 8.1 summarizes the Frobenius-norm differences between reconstructed and FCI

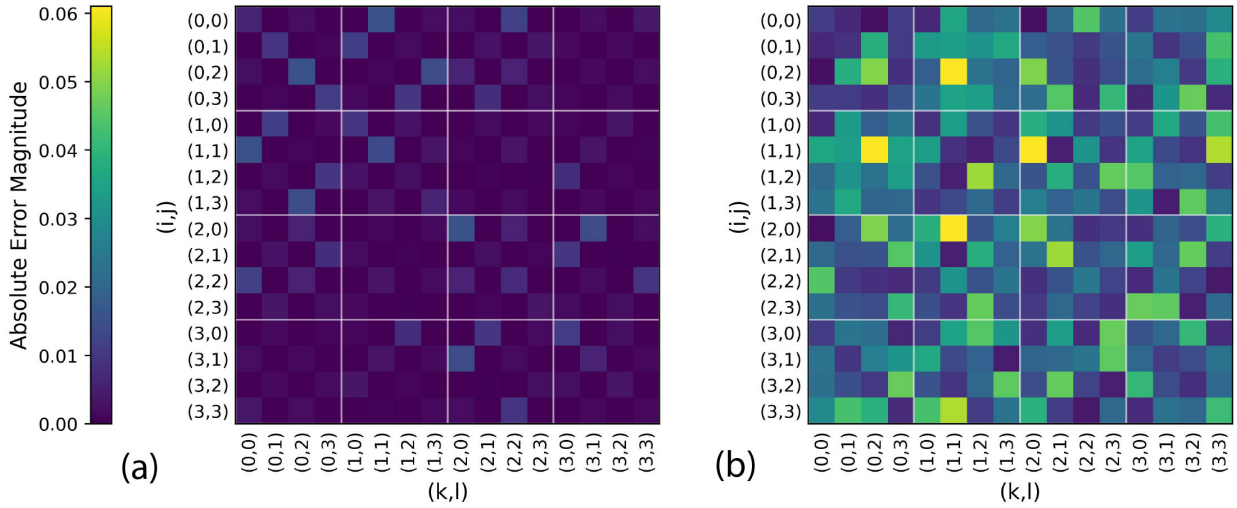


Figure 8.3: Comparison of absolute error matrices for the $H_4$ system in the minimal basis set obtained using the shadow variational 2-RDM (sv2RDM) (a) and Fermionic Classical Shadows (FCS) (b) methods. Each matrix element represents the absolute deviation of the reconstructed 2-RDM from the FCI reference. The color intensity denotes the error magnitude, with brighter regions corresponding to larger deviations from the reference values.

| H chain | Shot Budget | D | DQG | FCS |
|---|---|---|---|---|
| 4 | 16,000 | 0.129 | 0.059 | 0.423 |
| 6 | 36,000 | 0.226 | 0.080 | 0.873 |
| 8 | 160,000 | 0.454 | 0.037 | 0.960 |
| 10 | 300,000 | 0.217 | 0.055 | 1.349 |

Table 8.1: Comparison of Frobenius-norm differences with respect to the FCI 2-RDMs for various H chain lengths with the given total shot budgets when the semidefinite 2-RDM is optimized in the limit where $w \to \infty$ in Eq. 8.11, with partial (D) and all 2-positivity conditions (DQG) included. Shot budgets compared are: 16,000 unitaries/1 shot vs. 16 unitaries/1000 shots for $H_4$, 36,000 unitaries/1 shot vs. 36 unitaries/1000 shots for $H_6$, 160,000 unitaries/1 shot vs. 160 unitaries/1000 shots for $H_8$, and 300,000 unitaries/1 shot vs. 300 unitaries/1000 shots for $H_{10}$.

reference 2-RDMs across hydrogen chains of increasing length using the same total shot budgets. The SDP used in this case has $w \to \infty$ in Eq. 8.11. The results, including only the D condition and the full DQG constraint set, are compared against the FCS protocol. Across all system sizes, imposing $N$-representability conditions systematically reduces the deviation from the reference state, with the greatest improvements observed when all DQG constraints are enforced. The effect becomes more pronounced for larger systems, where unconstrained or partially constrained optimizations show growing discrepancies from the FCS method. These results demonstrate that the inclusion of full 2-positivity conditions provides superior reconstruction fidelity, particularly under limited measurement resources and increasing system complexity.

The inclusion of electronic energy minimization acts as a Hamiltonian-informed regularizer, which is particularly beneficial in molecular ground-state settings, but is not required for the reconstruction itself. In the limit $w \to \infty$, the SDP reconstruction becomes fully independent of the Hamiltonian and may be applied to arbitrary quantum states. In this regime, we find that expectation values such as the electronic energy converge more slowly than norm-based 2-RDM metrics, consistent with the heightened sensitivity of energy observables. Representative equilibrium-point energy benchmarks are provided in Appendix E (Table E.1). Related work by the authors [419] further discusses the $w \to \infty$ limit as a useful setting for correlated purification and error mitigation, including applications beyond ground states such as excited-state reconstruction.

Figure 8.4 presents the simulated potential energy curve of $N_2$ in the cc-pVDZ basis set with a [10,8] active space using complete active space configuration interaction (CASCI), sv2RDM, and FCS methods (Appendix E Sec. A.3 includes v2RDM results). The CASCI results serve as the reference for evaluating the accuracy of the reconstructed energy profiles. The FCS results exhibit noticeable deviations near the equilibrium and bond-stretching region, while the sv2RDM is able to closely reproduce reference results across the full dis-

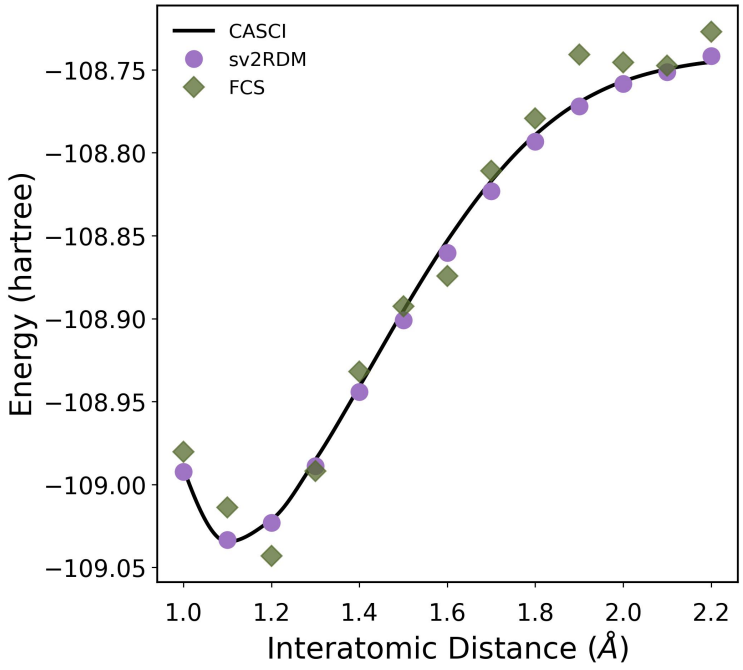


Figure 8.4: Potential energy curve of $N_2$ computed using the cc-pVDZ basis set and a [10,8] active space with complete active space configuration interaction (CASCI), shadow variational 2-RDM (sv2RDM), and Fermionic Classical Shadows (FCS) methods. For sv2RDM and FCS, the total shot budgets used are 100 unitaries $\times$ 1,000 shots and 100,000 unitaries $\times$ 1 shot, respectively.

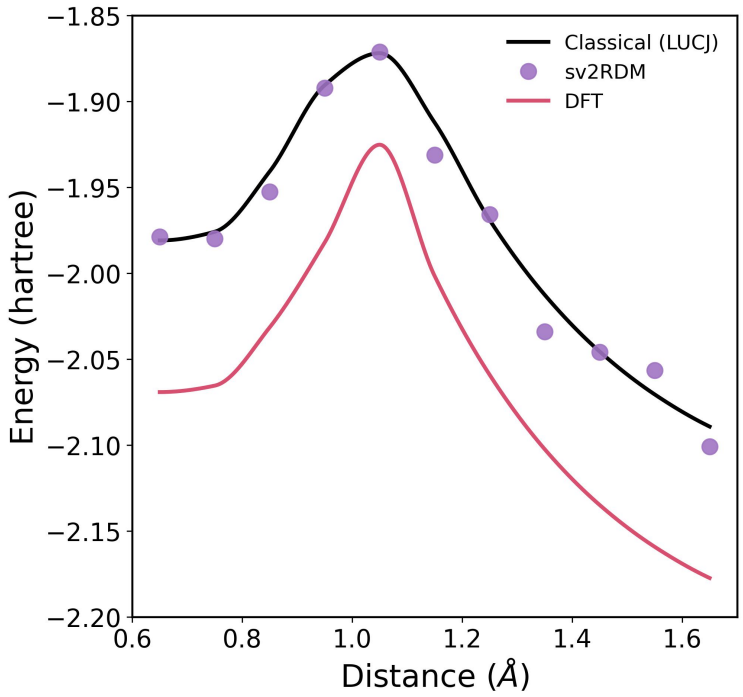


Figure 8.5: Potential energy curve for the $H_4$ rectangle–square–rectangle transition in the minimal basis set, computed using Density Functional Theory (DFT) with the B3LYP functional as a classical baseline, the classically computed Local Unitary Cluster Jastrow (LUCJ) ansatz, and the shadow variational 2-RDM (sv2RDM) method computed using measurements collected on the ibm_fez quantum computer.

sociation range. These comparisons highlight that constrained semidefinite reconstructions provide quantitatively reliable potential energy surfaces even under limited measurement resources, whereas unconstrained fermionic shadow tomography approaches can struggle to maintain accuracy in strongly correlated regimes.

To evaluate the performance of constrained shadow tomography on real quantum hardware, the $H_4$ rectangle–square–rectangle potential energy profile is computed in the minimal basis using both classical and hybrid quantum approaches (Fig. 8.5). Density Functional Theory (DFT) results using the B3LYP functional [425, 426] are shown as the classical baseline, while the sv2RDM calculations are performed using measurements collected on the ibm_fez quantum processor (details can be found in Appendix E Section E.2). The Local Unitary Cluster Jastrow (LUCJ) ansatz [427] is optimized and computed classically, serving

as the initially prepared quantum state and a reference for the sv2RDM calculations. The DFT results fail to reproduce the smooth energy flattening near the square geometry that signals strong static correlation. In contrast, the sv2RDM results recover the correct qualitative features, closely matching the expected multireference character. The sv2RDM energies obtained from the quantum device align well with the LUCJ benchmark within statistical uncertainty, demonstrating that error-mitigated semidefinite constraints can effectively suppress noise-induced artifacts and maintain physical consistency in near-term quantum simulations.

| H chain | sv2RDM | LUCJ | FCI |
|---|---|---|---|
| 4 | 0.011 | 0.034 | 0.068 |
| 6 | 0.013 | 0.062 | 0.101 |
| 8 | 0.024 | 0.061 | 0.133 |
| 10 | 0.065 | 0.084 | 0.166 |

Table 8.2: Comparison of correlation energies with respect to Hartree Fock for various H chain lengths. Measurements for sv2RDM calculations are collected on the ibm_fez quantum device with the following shot budgets: 16 unitaries/10,000 shots for $H_4$, 36 unitaries/10,000 shots for $H_6$, 160 unitaries/10,000 shots for $H_8$, and 300 unitaries/10,000 shots for $H_{10}$. Hartree Fock, LUCJ, and FCI calculations are run classically. All calculations use a minimal basis set.

The scalability of the constrained reconstruction approach is further evaluated by comparing correlation energies for hydrogen chains of increasing length, computed with sv2RDM, FCI, and the LUCJ ansatz in the minimal basis (Table 8.2). sv2RDM energies are obtained from measurement data collected on the ibm_fez quantum processor under fixed total shot budgets scaled with system size, with up to 20 qubits (details can be found in Appendix E Section E.2). Other methods were computed classically. Across all chain lengths, sv2RDM reproduces the qualitative energy trends of the reference LUCJ results, maintaining size-extensive behavior and smooth energy variation. Though deviations from the classical references appear at all system sizes, attributable to the increased noise inherent to hardware sampling, the results highlight that, even with limited quantum resources, enforcing semidef-

inite constraints enables systematically scalable energy predictions for chemical systems.

The results demonstrate that constrained shadow tomography provides a robust and systematically improvable framework for extracting physically meaningful quantities from both simulated and experimental quantum data. The numerical benchmarks employ Gaussian perturbations as a controlled model of finite-shot statistical noise, enabling a clear assessment of the proposed tomography's ability to suppress statistical fluctuations and reduce the number of required measurements. While this noise model does not capture realistic experimental effects, including coherent gate errors, readout bias, and correlated device effects, these are naturally present in the accompanying hardware demonstrations, which show qualitatively similar behavior. This agreement supports the robustness and measurement efficiency of the method beyond idealized shot-noise assumptions.

Across molecular benchmarks, enforcing $N$-representability through the 2-positivity conditions yields stable energy estimates, well-behaved eigenvalue spectra, and accurate two-particle correlations even under modest shot budgets. Comparisons with classical v2RDM, LUCJ, and FCI references confirm that the sv2RDM approach retains quantitative accuracy while remaining resilient to hardware noise and stochastic sampling errors. The constrained shadow tomography is complementary to established quantum error mitigation techniques such as symmetry verification [428] and purification-based post-processing [429], which enforce physical structure at the level of the global state or density matrix. By contrast, the present approach operates directly at the level of fermionic reduced density matrices, enforcing $N$-representability constraints through a convex SDP, and thus provides a noise-model-independent route to suppressing unphysical errors in measured observables. This framework is naturally compatible with other mitigation layers, including correlated purification strategies [419], as well as probabilistic error cancellation methods [214] that rely on explicit noise characterization. These findings establish a consistent foundation for assessing scalability, error mitigation, and resource efficiency in near-term quantum simulations, mo-

tivating a deeper discussion on methodological implications and potential pathways toward chemically accurate hybrid quantum-classical frameworks.

## 8.5 Discussion and Conclusions

The results presented in this work highlight the advantages of incorporating physical constraints into scalable quantum state reconstruction protocols. By embedding $N$-representability directly into the shadow tomography framework, our constrained shadow tomography formulation enables physically consistent and noise-resilient reconstructions of RDMs. The integration of bi-objective semidefinite programming, nuclear-norm regularization, and $N$-representability jointly suppresses measurement-induced errors, yielding accurate and stable estimates under limited shot budgets and realistic noise conditions. Benchmark results for hydrogen chains and the $N_2$ molecule confirm that enforcing physical constraints during reconstruction improves both accuracy and robustness across a range of system sizes and sampling budgets, while remaining compatible with shallow circuits. Beyond quantitative improvements, this approach provides a unified and computationally efficient framework that connects statistical inference, convex optimization, and quantum chemistry post-processing. The demonstrated reduction in measurement requirements and enhanced robustness underscore the potential of constraint-enforced tomography as a key component of hybrid quantum–classical workflows for benchmarking and validating quantum simulations of correlated fermionic systems.

The presented algorithm establishes a practical foundation for advancing quantum state characterization in many-body quantum simulations. Future work may explore the incorporation of additional system symmetries or adaptive weighting strategies to further enhance RDM reconstruction fidelity. As quantum hardware continues to progress, methods that integrate physical insight, optimization principles, and statistical learning will be essential for developing reliable and scalable approaches to quantum state reconstruction. This study

positions constrained shadow tomography as a powerful and generalizable framework for extracting accurate physical insight from limited quantum data, paving the way for robust, physically grounded characterization of complex quantum systems.

## 8.6 Acknowledgments

We thank Nate Earnest-Noble and Jamie Garcia for valuable discussions. D.A.M gratefully acknowledges support from IBM under the IBM-UChicago Quantum Collaboration. I.A. gratefully acknowledges the NSF Graduate Research Fellowship Program under Grant No. 2140001. All data and sample computational script are openly available at: `https://github.com/damazz/ConstrainedShadowTomography.git`. The data supporting this Chapter can be found in Appendix E.

# Part IV

# Many-Body Quantum Order in Mixed-Particle Systems

# CHAPTER 9

# WITNESSING ENTANGLEMENT IN MIXED-PARTICLE QUANTUM SYSTEMS

This chapter is reprinted (adapted) with permissions from *arXiv.2512.17860* **2025**

## 9.1 Chapter Synopsis

Identifying and quantifying entanglement in mixed-particle quantum systems is expected to be highly valuable in the development of hybrid quantum technology platforms. We introduce an entanglement witness that identifies off-diagonal long-range order (ODLRO)—a distinctive form of entanglement—in systems containing both fermionic and bosonic particles. By analyzing the particle–hole reduced density matrices of each subsystem, the approach detects ODLRO independently in both fermionic and bosonic sectors and identifies when long-range order develops across the entire mixed-particle system. The witness also quantifies the magnitude of ODLRO within each particle type, revealing how fermionic and bosonic correlations combine to form the total entanglement of the system, including a bosonic condensation of particle–hole pairs driven by many-body correlations rather than particle statistics. Using the Lipkin–Meshkov–Glick spin model, we show how the transition from ODLRO localized to one particle type to ODLRO shared by both particle types captures the onset of collective entanglement in a mixed-particle environment, providing new insight into systems where fermionic and bosonic correlations coexist.

## 9.2 Introduction

Entanglement, often described as the most non-classical manifestation of quantum mechanics [430–433], plays a major role as a resource enabling various quantum technologies, ranging from quantum computing and cryptography [434–437] to metrology and sens-

ing [2, 155, 175, 438–441]. It not only persists in large many-body systems and at finite temperatures [442] but can also be revealed through macroscopic observables such as heat capacity [443] and magnetic susceptibility [444]. Furthermore, entanglement in many-body systems of bosons and fermions can be indicated through off-diagonal long-range order (ODLRO), a microscopic property that signals quantum coherence on a macroscopic scale [445, 446], and whose onset underlies phenomena such as exciton condensation [130, 323, 366, 447–457], superconductivity [105, 458], and superfluidity [445, 459]. More recently, ODLRO has been shown to serve as an entanglement witness, providing a direct link between macroscopic coherence and many-body entanglement [12, 449, 460]. Real-world quantum materials, however, often involve interacting mixtures of fermions and bosons, where richer many-body behaviors may emerge [461–470]. Such mixed-particle quantum systems—encompassing phonons, photons, and gluons—are pervasive across physics, serving as effective models in condensed-matter and chemical systems [471–474] and forming the natural language of quantum field theory [475]. Yet existing entanglement witnesses, typically based on spin fluctuations [441, 476] or single-particle observables [433, 442], fail to capture the collective coherence that characterizes ODLRO, limiting their ability to identify and quantify many-body order in mixed-particle environments.

In this work, we present a framework for witnessing entanglement in mixed-particle quantum systems by detecting and quantifying ODLRO. The theory shows that the large eigenvalues associated with ODLRO can serve as entanglement witnesses in systems containing both fermions and bosons, allowing the identification of long-range order within each subsystem and revealing when such coherence extends across the mixed-particle system. The witnesses quantify the respective contributions of the fermionic and bosonic sectors and hence provide a vivid picture of how coherence is distributed between particle types as correlations strengthen. They are defined in terms of the large eigenvalues of the fermion and boson blocks of the mixed-particle particle–hole reduced density matrix. Notably, within the

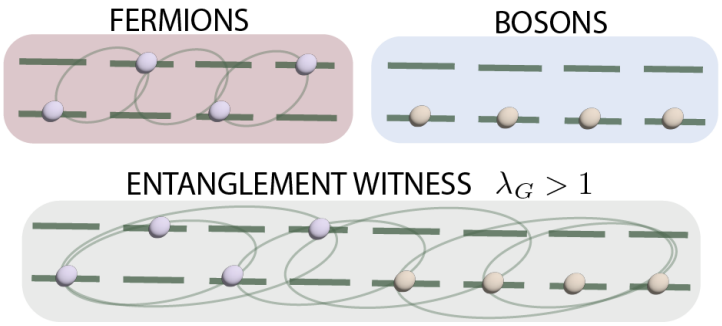


Figure 9.1: Illustration of entanglement witnessing in a mixed fermion-boson system, where the fermionic degrees of freedom are initially strongly correlated. The largest eigenvalue of the fermion and boson blocks of the mixed-particle particle–hole reduced density matrix, $\lambda_G$, captures entanglement arising in the fermionic and bosonic modes, respectively.

boson sector, a large eigenvalue indicates that entanglement can drive a correlated condensation of particle–hole pairs—distinct from the statistics-driven single-particle condensation of conventional Bose–Einstein condensation. We demonstrate these principles using an expanded Lipkin–Meshkov–Glick spin model, showing how the transition from ODLRO in only one particle type to ODLRO in both particle types signals the emergence of collective entanglement spanning the mixed-particle system (refer to Fig. 9.1). This approach establishes a general and scalable route to characterizing entanglement in mixed-particle quantum systems and suggests potential applications in quantum sensing—where entanglement enhances measurement sensitivity—and in quantum communication, where coherence may enable robust information transfer and storage.

## 9.3 Theory

The emergence of ODLRO can be characterized through the appearance of dominant eigenvalues in the system's reduced density matrices (RDMs). For bosonic systems, Penrose and Onsager showed that Bose–Einstein condensation corresponds to an eigenvalue greater than one in the one-boson RDM [446]. Analogously, Yang [445] and Sasaki [477] demonstrated that a large eigenvalue in the particle–particle RDM indicates condensation of fermion pairs

into a single two-particle quantum state, signaling the onset of ODLRO.

Exciton condensation represents a particle–hole analogue of this phenomenon, where below a critical temperature, particle–hole pairs collectively occupy a single excitonic state, resulting in exciton superfluidity [478–480]. Such a phase enables dissipationless energy transfer at elevated temperatures, a long-standing goal in superconductivity research [212, 481–487]. The onset of ODLRO is captured by the particle–hole RDM,

$$ {}^{2}_{a}G^{ij}_{kl} = \langle\psi|\,(\hat{a}^{\dagger}_{i}\hat{a}_{j} - {}^{1}_{a}D^{i}_{j})^{\dagger}(\hat{a}^{\dagger}_{l}\hat{a}_{k} - {}^{1}_{a}D^{l}_{k})\,|\psi\rangle\,, \tag{9.1} $$

where ${}^{1}D$ is the one-particle RDM, $\hat{a}^{\dagger}_{i}$ and $\hat{a}_{i}$ denote the creation and the annihilation operators, and ${}^{2}G \geq 0$ is a positive semidefinite matrix. Here, the index $a \in \{f, b\}$ labels the particle type, with $f$ and $b$ denoting fermionic and bosonic degrees of freedom, respectively.

For pure states, an eigenvalue of the particle-hole RDM exceeding one indicates multiple particle–hole pairs occupying the same excitonic mode, i.e., exciton condensation [366, 447], and cannot arise from independent or separable configurations. As such, it signals collective correlations shared across many particles and serves as an entanglement witness. Here, we propose a mixed-particle model capable of exhibiting simultaneous ODLRO signatures in both fermionic and bosonic sectors. By tracing out either the bosonic or fermionic degrees of freedom in Eq. 9.1, the corresponding fermionic or bosonic subblocks of the particle–hole RDM can be obtained. The largest eigenvalue in each subblock, denoted $\lambda_G$, quantifies the occupancy of the lowest particle–hole mode and, therefore, the extent of ODLRO [366, 447]. For instance, $\lambda_G = 1.5$ indicates the onset of long-range order, while $\lambda_G = 2$ corresponds to two correlated pairs. This eigenvalue-based metric has been successfully applied to quantify ODLRO in a variety of quantum and molecular systems [104, 105, 130, 137, 336, 447, 449, 460]. When particle–hole exchange is allowed between mixed-particle sectors, $\lambda_G$ serves as a unified witness of ODLRO in both fermionic and bosonic degrees of freedom. This framework captures how long-range correlations emerge and redistribute with varying inter-

action strength, offering a systematic means to characterize entanglement and coherence in correlated mixed-particle environments.

The general upper bound on $\lambda_G$ is given by [366, 448]

$$\lambda_G \leq \frac{N(r-N)}{r}, \tag{9.2}$$

where $N$ is the number of particles and $r$ is the rank of the single-particle basis. For a mixed system with $N$ fermions and $N$ bosons occupying $2N$ total levels, this bound becomes

$$\lambda_G \leq \frac{N(2N-N)}{2N} = \frac{N}{2}. \tag{9.3}$$

The maximal large eigenvalue in the particle-hole RDM occurs if the order of the system extends over all particles in the system, hence referred to as long-range order. Because the particle-hole RDM scales linearly with the system size, its largest eigenvalue cannot scale faster than linear in the number of particles. In the thermodynamic limit $N \to \infty$, the presence of ODLRO is therefore characterized by an eigenvalue that remains extensive, i.e., proportional to $N$, rather than remaining of order unity. A similar bound has previously been established for the largest eigenvalue of the two-particle cumulant [448, 458, 460].

## 9.4 Results

The Lipkin–Meshkov–Glick (LMG) model is an exactly solvable framework describing spin-$\frac{1}{2}$ particles in a two-level system, where scattering terms facilitate the excitation and de-excitation of particle pairs between the lower and upper levels [488]. This model has been used extensively to demonstrate fundamental aspects of collective particle behavior [489], illustrate limitations of mean-field approaches [370, 490–492], and has even been implemented on a quantum computer [493]. The LMG quasispin model for $N$ particles contains two energy levels, $\{-\frac{\varepsilon}{2}$ and $\frac{\varepsilon}{2}\}$, each hosting $N$ states that are energetically degenerate. The

second-quantized Hamiltonian is given by

$$\begin{aligned}\mathcal{H}_{\mathrm{LMG}} = \frac{\varepsilon}{2}\sum_{i=1}^{N}\left(\hat{a}_{i+N}^{\dagger}\hat{a}_{i+N} - \hat{a}_{i}^{\dagger}\hat{a}_{i}\right) \\ + \frac{V}{2}\sum_{p,q=1}^{N}\left(\hat{a}_{p}^{\dagger}\hat{a}_{q}^{\dagger}\hat{a}_{q+N}\hat{a}_{p+N} + \mathrm{h.c.}\right),\end{aligned} \tag{9.4}$$

where $V$ is the interaction strength between pairs of scattered particles. Here, the operators $\hat{a}_i$ act on a two-level system with lower and upper orbitals labeled by $i = 1, \ldots, N$ and $i = N+1, \ldots, 2N$, respectively. In the large-$N$ limit, this model exhibits a normal–to–deformed quantum phase transition—corresponding to a change from a symmetry-preserving to a symmetry-broken collective mean-field state—which, while not the focus of the present work, appears as a smooth crossover for the finite system sizes considered here [488]. When $V = 0$, the system behaves as fully non-interacting. As $V$ increases, interactions become more significant, ultimately producing a macroscopically large $\lambda_G$ for strongly interacting systems with large particle number $N$. When the correlation term $V$ is sufficiently larger than the energy term, $\varepsilon$, i.e., in the strong correlation limit, maximum signature of ODLRO, $\lambda_G = \frac{N}{2}$ can be obtained [366].

Since $N$ particles can occupy each level, the LMG model may also be interpreted as a two-level fermionic or bosonic system. The Hamiltonian for each formulation of the model may be obtained by using fermionic or bosonic creation and annihilation operators in Eq. (9.4). The ODLRO signature in each degree of freedom is reflected by a large $\lambda_G$ value in strongly interacting systems.

Here, we propose a model system capable of capturing the development of long-range correlations in fermionic and bosonic degrees of freedom simultaneously. The model keeps the structures of the fermionic and bosonic LMG Hamiltonians, with an additional interaction term, tuned via parameter $V_{fb}$, which allows for a co-occurring particle excitation in one particle type and a particle de-excitation in the other. The proposed Hamiltonian can be

written as:

$$\mathcal{H}_{\text{fb-LMG}} = \frac{\varepsilon_f}{2}\sum_{i=1}^{N}\left(\hat{f}^\dagger_{i+N}\hat{f}_{i+N} - \hat{f}^\dagger_i\hat{f}_i\right) \tag{9.5}$$

$$+\frac{V_f}{2}\sum_{p,q=1}^{N}\left(\hat{f}^\dagger_p\hat{f}^\dagger_q\hat{f}_{q+N}\hat{f}_{p+N} + \text{h.c.}\right) \tag{9.6}$$

$$+\frac{\varepsilon_b}{2}\sum_{i=1}^{N}\left(\hat{b}^\dagger_{i+3N}\hat{b}_{i+3N} - \hat{b}^\dagger_{i+2N}\hat{b}_{i+2N}\right) \tag{9.7}$$

$$+\frac{V_b}{2}\sum_{p,q=1}^{N}\left(\hat{b}^\dagger_{p+2N}\hat{b}^\dagger_{q+2N}\hat{b}_{q+3N}\hat{b}_{p+3N} + \text{h.c.}\right) \tag{9.8}$$

$$+\frac{V_{fb}}{2}\sum_{p,q=1}^{N}\left(\hat{f}^\dagger_{p+N}\hat{f}_p\,\hat{b}^\dagger_{q+3N}\hat{b}_{q+2N} + \text{h.c.}\right) \tag{9.9}$$

Here, the fermionic modes occupy orbitals $1,\ldots,2N$, with lower and upper levels given by $1,\ldots,N$ and $N+1,\ldots,2N$, respectively, while the bosonic modes occupy orbitals $2N+1,\ldots,4N$, with lower and upper levels given by $2N+1,\ldots,3N$ and $3N+1,\ldots,4N$. The parameters $\varepsilon_f/2$ and $\varepsilon_b/2$ denote the single-particle level splittings in the fermionic and bosonic sectors, respectively; $V_f$ and $V_b$ are the corresponding intra-species interaction strengths; and $V_{fb}$ describes the inter-species coupling. The Hamiltonian $\mathcal{H}_{\text{fb-LMG}}$ is homogeneous of degree one in the parameters $(\varepsilon_f, \varepsilon_b, V_f, V_b, V_{fb})$, implying that only their ratios are physically relevant. We, therefore, fix the overall energy scale by setting $\varepsilon_f + \varepsilon_b = 1$, which preserves a symmetric treatment of the fermionic and bosonic sectors.

Since the entanglement witness $\lambda_G$ is independent of particle statistics, evaluating it from the modified particle–hole RDM after tracing out one particle type reveals signatures of ODLRO within that sector, while still accounting for its entanglement with the rest of the system. Thus, a parameter set $\varepsilon_f$, $V_f$, $\varepsilon_b$, $V_b$, $V_{fb}$, defined in Eqs. 9.5– 9.9, directly determines the extent of ODLRO formation in both fermionic and bosonic modes of the mixed-particle quantum system. The interaction parameter $V_{fb}$ allows strong correlations originating in

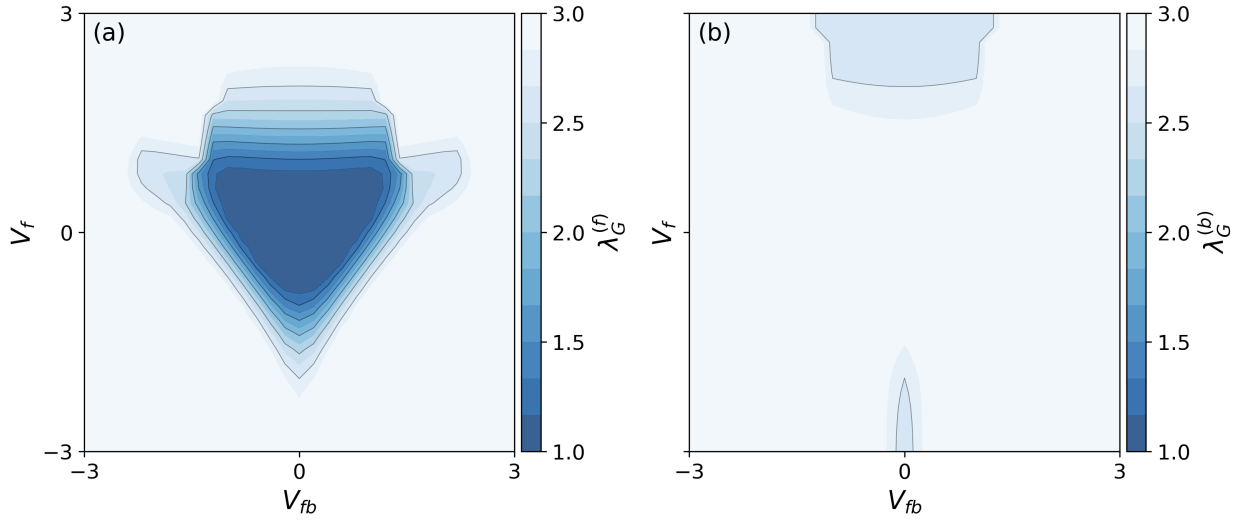


Figure 9.2: Contour plots of the entanglement witness (a) $\lambda_G^{(f)}$ and (b) $\lambda_G^{(b)}$ for the fermionic and bosonic particle sectors $(f)$ and $(b)$, respectively, shown as functions of the fermionic correlation parameter $V_f$ and fermion-boson interaction parameter $V_{fb}$, with $V_b = -2$. The system consists of $N_f = N_b = 6$ particles in 24 orbitals, with $\varepsilon_f = \varepsilon_b$ and $\varepsilon_f + \varepsilon_b = 1$. Lighter regions indicate a stronger entanglement witness signal, reflecting a greater extent of ODLRO within the corresponding particle degrees of freedom.

one particle type to interact with correlations in the other, with $\lambda_G$ providing a quantitative measure of the entanglement established across the mixed-particle system. Importantly, the model can be adapted to capture the interaction of fermions with other bosonic collective excitations in solids (e.g., spin, orbital, charge, etc.) or to capture interactions between two types of bosons (or two types of fermions).

To illustrate how ODLRO, a special case of entanglement, manifests in a mixed-particle system, we first consider a system of 12 particles (6 fermions and 6 bosons) in 24 orbitals. Figure 9.2 shows the entanglement witness $\lambda_G$ for the ground state of the system as a function of the fermionic correlation parameter, $V_f$, and fermion-boson interaction parameter, $V_{fb}$, with all other parameters fixed. Lighter regions indicate stronger ODLRO. Panel (a) shows $\lambda_G^{(f)}$ for the fermionic sector. As $V_f$ increases in magnitude, ODLRO strengthens, reaching its maximum at nonzero values of $V_{fb}$. When $V_{fb} = 0$, fermions remain weakly correlated, except for large $V_f$, and display minimal ODLRO, as indicated by the darker regions in

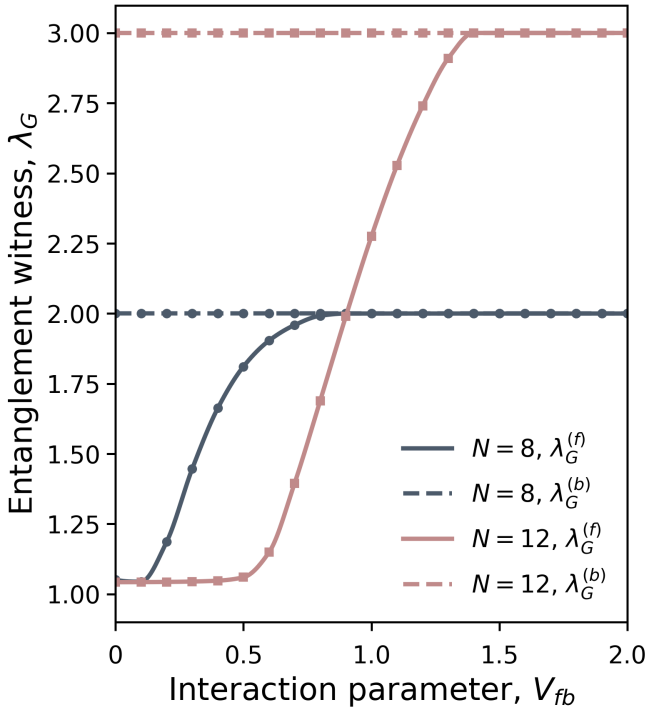


Figure 9.3: Entanglement witnesses $\lambda_G^{(f)}$ (solid lines) and $\lambda_G^{(b)}$ (dashed lines) for fermions and bosons, respectively, in systems with 8 particles—4 fermions and 4 bosons (blue)—and 12 particles—6 fermions and 6 bosons (pink)—as functions of the interaction parameter $V_{fb}$. For both system sizes, $V_f = -0.4$ and $V_b = -2.0$. The overall energy scale is fixed by $\varepsilon_f + \varepsilon_b = 1$, with $\varepsilon_f = \varepsilon_b$. In both systems, the fermions, though initially non-interacting, develop increasing ODLRO with stronger interactions $V_{fb}$.

the plot. Panel (b) shows $\lambda_G^{(b)}$ for the bosonic sector, which lies in the strongly interacting regime, maintaining strong ODLRO across the parameter space. The results establish $\lambda_G$ as an entanglement witness capable of both detecting the presence of long-range correlations within bosonic and fermionic degrees of freedom, and revealing when such coherence extends across the mixed-particle system.

We next consider a scenario where the fermionic sector (f) is initially non-interacting and exhibits no intrinsic ODLRO ($V_f \ll \varepsilon_f$), while the bosonic sector (b) possesses strong internal interactions ($V_b \gg \varepsilon_b$) sufficient to sustain maximal ODLRO, as indicated by $\lambda_G^{(b)}$. Figure 9.3 presents $\lambda_G$ as a function of the interaction parameter $V_{fb}$ between the two particle sectors. With $V_b \gg \varepsilon_b$, bosonic sector retains its ODLRO independently, reaching maximal

$\lambda_G^{(b)}$ values across all $V_{fb}$ (dashed lines in Fig. 9.3). In contrast, the fermionic sector, though initially lacking correlations, progressively develops ODLRO as $V_{fb}$ increases, as reflected in the rising $\lambda_G^{(f)}$ values (solid lines in Fig. 9.3). This behavior shows that $\lambda_G$ can effectively witness the onset of collective entanglement in a subsystem, such as the fermionic degrees of freedom, that is fully driven by the interaction Hamiltonian.

Finally, we illustrate a case where the two particle sectors operate on distinct energy and interaction scales that differ by roughly an order of magnitude, as in the case of electrons and phonons, yet are initially either both uncorrelated or both strongly correlated. Figure 9.4 shows results for the mixed-particle LMG model containing 12 particles (6 electrons and 6 phonons) in 24 orbitals, with an order-of-magnitude energy difference between electronic and vibronic degrees of freedom ($\varepsilon_e/\varepsilon_p \sim 10$). Electron–phonon and electron–photon interactions are important for applications in spintronics [494], catalysis [495, 496], and quantum information processing [497, 498]. Dashed lines correspond to both sectors starting uncorrelated ($\lambda_G = 1$), where maximal ODLRO ($\lambda_G = 3$) appears only at strong interaction strength ($V_{fb} > 0.5$). In contrast, the solid lines represent sectors initially strongly correlated ($\lambda_G \approx 2$), reaching the same maximal $\lambda_G$ at a much lower interaction threshold ($V_{fb} > 0.2$). This contrasting behavior suggests that uncorrelated particle-type environments may require stronger interaction to develop coherent order, whereas initially correlated environments appear more responsive to moderate interaction strengths. Moreover, we also observe for both the correlated and uncorrelated initial conditions that the onset of ODLRO in the phonons lags behind the onset in the electrons. Such results imply that the size of the energy gap influences how coherence emerges and distributes between different degrees of freedom in mixed-particle systems. A related enhancement of excitonic coherence has been observed in $WSe_2/MoS_2$ moiré heterobilayers, where fermion–boson interactions and the joint modulation of electron filling and exciton density have been linked to tunable interlayer exciton emission [499].

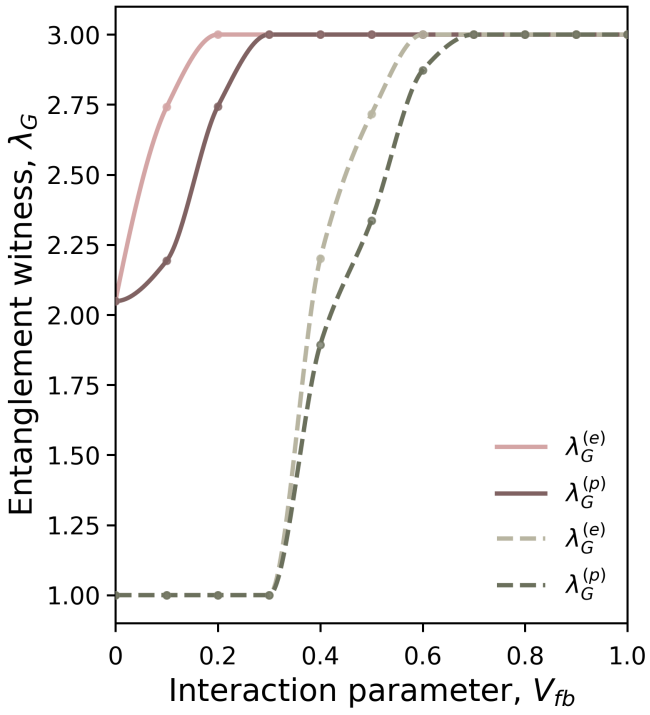


Figure 9.4: Entanglement witness values $\lambda_G^{(e)}$ and $\lambda_G^{(p)}$ for the electron–phonon model system for 12 particles—6 electrons and 6 phonons—in 24 orbitals as functions of interaction parameter $V_{fb}$. Dashed (solid) lines correspond to initially uncorrelated (correlated) environments, reaching $\lambda_G = 3$ only at strong coupling ($V_{fb} \gtrsim 0.5$) and already at moderate coupling ($V_{fb} \gtrsim 0.2$), respectively.

## 9.5 Discussion and Conclusions

Here, we present an entanglement witness for detecting ODLRO in mixed-particle quantum systems. Our results show that the witness successfully quantifies ODLRO—an entanglement-based measure of macroscopic coherence—in systems of up to 12 particles in 24 orbitals, across a broad range of ground-state wavefunctions generated from diverse parameter sets. In addition to its relevance to exciton condensation in mixed-particle systems, the framework has potential applications in quantum memory, computing, and sensing. In memory, the ability to capture and quantify ODLRO may aid in designing local storage devices where spin–photon entanglement in nanophotonic platforms supports scalable quantum repeater networks [500]. In computing, it could inform the development of hybrid fermion–boson architectures such as silicon-based dopant-array analog simulators [501]. In sensing, the framework may provide new insight into how fermionic and bosonic degrees of freedom collectively respond to external magnetic or electric fields [12]—a direction we aim to explore in future work.

The results further show that the proposed entanglement witness reliably captures how ODLRO distributes between fermionic and bosonic particle types as the interaction strength between them is varied. We find that initially uncorrelated particle types require strong interactions between the fermions and bosons to develop long-range order, whereas those with pre-existing correlations exhibit enhanced ODLRO even under moderate interactions. The relative energy scales of the two particle types are also found to influence this behavior. Together, these findings establish the witness as a robust and quantitative tool for characterizing entanglement in mixed-particle quantum systems and highlight the key role of interparticle interactions and energetics in shaping collective quantum behavior. The framework is directly relevant to correlated fermion–boson systems such as polaritons (electrons and photons) and polarons (electrons and phonons), where the transfer and storage of entanglement among electrons, photons, and phonons underlie emerging quantum technologies

in communication, computation, and sensing.

## 9.6 Acknowledgments

D.A.M. gratefully acknowledges the Department of Energy, Office of Basic Energy Sciences, Grant DE-SC0026076. I.A. gratefully acknowledges the NSF Graduate Research Fellowship Program under Grant No. 2140001. All data and analysis scripts are openly available at the following web address: `https://github.com/damazz/Mixed-Particle-Entanglement-Witnesses.git`

# CHAPTER 10

# CONCLUSION

In this thesis, I developed methods based on reduced descriptions of quantum systems to address challenges at the intersection of quantum chemistry and emerging quantum technologies. First, I introduced a method for characterizing interactions between quantum systems and their environments using only limited particle-level information, and demonstrated how this can be leveraged in quantum sensing. Second, I developed techniques that incorporate physical constraints to significantly reduce the measurement requirements of quantum devices, enabling more efficient and scalable molecular simulations. Third, I established a framework for quantifying entanglement in systems with mixed particle types, providing insight into information flow in complex quantum systems and informing the design of quantum communication and hybrid platforms. These approaches were validated across both model systems and realistic molecular applications using classical and quantum computing resources. Together, these contributions demonstrate that reduced representations can serve not only as theoretical, but as practical tools for advancing quantum technologies. By making complex quantum systems more tractable, this work supports progress in molecular simulation, quantum sensing, and quantum computation, with broader implications for chemistry, materials discovery, and emerging quantum devices.

In Chapter 3, we introduced a method, using the one-particle RDM (1-RDM), to detect when many-body quantum systems interact with their environment, demonstrating that deviations from known structural constraints provide a signature of decoherence in superconducting qubit experiments. We showed that even small violations of the constraints imposed by the generalized Pauli exclusion principle provide a direct and experimentally accessible signature of system-environment coupling. Importantly, this illustrated that the onset of openness in a quantum many-body system can be detected only from the knowledge of the 1-RDM, establishing a systematic and practical criterion for diagnosing decoherence.

In Chapter 4, the 1-RDM framework was extended to develop a quantum sensing algorithm in collaboration with experimental ultrafast spectroscopy efforts. Coherence and decoherence in energy transfer served as a model quantum sensing scenario, with the broader objective of assessing quantum sensor performance under realistic conditions. The presented open-system quantum sensing approach uses fermionic correlation and entanglement constraints to probe a noise-assisted relaxation in a multi-qubit system. Ultimately, this work positions the single-particle $N$-representability constraints as a previously unexplored resource for next-generation quantum sensing advancements.

In Chapters 6-8, we presented a semidefinite programming–enhanced quantum tomography algorithm that imposes physical constraints on the two-particle RDM (2-RDM), achieving accurate molecular properties with substantially reduced measurement cost. In Chapters 6 and 7, we developed an enhanced classical shadow tomography method that incorporates 2-RDM $N$-representability conditions to accurately reconstruct target observables, ground- and excited-state energies, and 2-RDMs of hydrogen chains, the $N_2$ dissociation curve, and the photoexcited reaction pathway from *gauche*-1,3-butadiene to bicyclobutane using substantially fewer measurements than unconstrained approaches. Building on this framework, Chapter 8 presented a bi-objective semidefinite programming algorithm for constrained shadow tomography, developed in collaboration with IBM researchers, and designed to reconstruct the 2-RDM from noisy or incomplete shadow data. This method was implemented on IBM's superconducting quantum computers and assessed in terms of measurement requirements with respect to system size, orbital basis dimension, and the choice of $N$-representability conditions. As quantum hardware advances, constrained shadow tomography is expected to enable scalable, physically grounded quantum state reconstruction with broad applications in quantum simulation and molecular property estimation from limited data.

Finally, in Chapter 9, we proposed a witness that identifies off-diagonal long-range order as

a distinctive form of entanglement in systems with both fermionic and bosonic particles. We introduced a coupled fermion–boson Hamiltonian that generalizes the Lipkin-Meshkov-Glick model with an interaction term, enabling correlated excitation processes and the simultaneous emergence of long-range order in fermionic and bosonic degrees of freedom. This establishes a quantitative entanglement witness for mixed-particle systems, with direct relevance to correlated fermion–boson platforms such as polaritons and polarons, understanding collective behavior in mixed-particle platforms, and designing correlated quantum materials and simulators.

Looking forward, the established ensemble of RDM-based quantum resource theories should be extended and improved upon from various perspectives. For example, the experimental verification of generalized Pauli constraint (GPC) violations in open systems opens several promising directions across simulation, sensing, and device characterization. Integrating GPC-based analysis with density-matrix purification may offer a route to efficient simulation of open quantum systems and practical determination of effective bath sizes. At the quantum hardware level, the systematic inward shift of measured 1-RDM eigenvalue spectra within the Pauli polytope suggests a geometry-based signature of noise that can serve as a benchmarking and noise-characterization tool, potentially guiding the development of improved noise mitigation strategies.

Extending this framework to larger multi-qubit systems offers a path toward enhanced quantum sensing at both signal discrimination and post-processing stages. GPC violations can indicate environmental coupling during signal collection, while the evolution of natural-orbital occupations helps distinguish signal from decoherence. Experimentally, these ideas could be incorporated into multi-qubit magnetometry platforms, such as graph-state sensors [502] in solid-state or superconducting systems, where entangled probes already operate under realistic noise, allowing RDM-based diagnostics to run alongside existing Fisher-information–based protocols to identify dominant noise mechanisms and optimal sensing

times.

Beyond these directions, the advances in quantum tomography developed here provide a foundation for continued refinement and broader application of fermionic constraints in the characterization of quantum states on quantum devices. Incorporating additional symmetries and adaptive weighting strategies can further improve RDM reconstruction fidelity, while extending constrained shadow tomography to quantum process tomography offers a scalable route to characterizing dynamical maps. Finally, applying the mixed-particle entanglement witness to probe how coupled fermionic and bosonic degrees of freedom respond to external fields may yield new insight into collective quantum behavior, with implications for hybrid quantum materials, simulators, and sensing technologies.

# APPENDIX A

# SUPPLEMENTAL MATERIAL: CHAPTER 3

This appendix summarizes the technical procedures and supplementary results underlying the analysis in Chapter 3. It includes detailed descriptions of the state preparation algorithms for each considered system, the quantum tomography protocol, and the relevant quantum device specifications. Additional numerical and experimental data are provided to support and extend the findings presented in Chapter 3.

## A.1 State Preparation

The state preparation algorithm used in this work employs unitary rotations of control and target qubits with CNOT gates in between (Fig. A.1). For a four-qubit system, this can be expressed as

$$\begin{aligned}\mathbb{U}_a = U_3(\theta_{10},\phi_{10},\lambda_{10})U_2(\theta_9,\phi_9,\lambda_9)C_2^3\\ U_2(\theta_8,\phi_8,\lambda_8)U_1(\theta_7,\phi_7,\lambda_7)C_1^2\\ U_1(\theta_6,\phi_6,\lambda_6)U_0(\theta_5,\phi_5,\lambda_5)C_0^1\\ U_3(\theta_4,\phi_4,\lambda_4)U_2(\theta_3,\phi_3,\lambda_3)\\ U_1(\theta_2,\phi_2,\lambda_2)U_0(\theta_1,\phi_1,\lambda_1)\end{aligned}$$

where $U_i$ are unitary rotations around three Euler angles ($\theta_{i+1}$, $\phi_{i+1}$, $\lambda_{i+1}$) on qubit $i$. The $U_3$ gates are defined as

$$U_3(\theta,\phi,\lambda) = \begin{bmatrix} \cos\left(\frac{\theta}{2}\right) & -e^{i\lambda}\sin\left(\frac{\theta}{2}\right) \\ e^{i\phi}\sin\left(\frac{\theta}{2}\right) & e^{i\phi+i\lambda}\cos\left(\frac{\theta}{2}\right) \end{bmatrix} \tag{A.1}$$

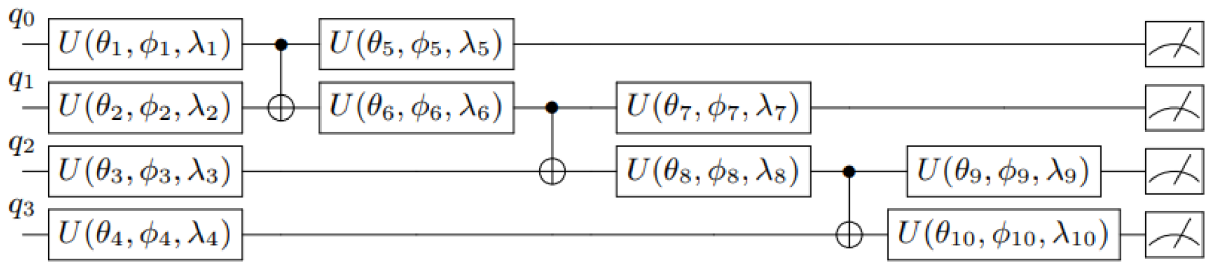


Figure A.1: Quantum circuit used for the state preparation of a four-qubit system. The same logic was used for all state preparations (Figures A.1-A.5).

and the CNOT gates, $C_i^j$ are standard with $i$ control and $j$ target qubits. The same algorithm is applied to all state preparations with additional rotations and CNOT gates added for each extra qubit in the system (see Figs. A.1-A.5). The many unitary rotations allow for a wide range of parameter tuning to span the entirety of the Pauli polytope. Additionally, this algorithm includes some local degrees of freedom [145] and suggests that qubit-ordering dependence may be removed [125]. 2050 measurements of each prepared state were made to ensure statistical robustness of the collected data. The measurements were obtained by simulating each circuit over a range of random angles, $\theta$, $\phi$, and $\lambda$, from $-180°$ to $180°$ used for the single-qubit unitary rotations of qubits, as defined above.

## A.2 Quantum Tomography

To directly measure the eigenvalues of the 1-RDM on a quantum device, we exploit the restriction of the $N$-fermions in $2N$-orbitals system to a system of $N$ qubits, where each qubit is a two-level system sharing an electron. In second quantization the elements of the 1-RDM are given by

$$^1D_j^i = \langle\psi|\, \hat{a}_i^\dagger \hat{a}_j \,|\psi\rangle\,, \tag{A.2}$$

where $\hat{a}_i^\dagger$ creates a particle in the $i$-th orbital and $\hat{a}_j$ annihilates a particle in the $j$-th orbital, where $i$ and $j$ correspond to the same qubit [136]. A one-qubit 1-RDM can be constructed

as follows,

| | $\hat{a}_{p,0}$ | $\hat{a}_{p,1}$ |
|---|---|---|
| $\hat{a}^\dagger_{p,0}$ | $\hat{a}^\dagger_{p,0}\hat{a}_{p,0}$ | $\hat{a}^\dagger_{p,0}\hat{a}_{p,1}$ |
| $\hat{a}^\dagger_{p,1}$ | $\hat{a}^\dagger_{p,1}\hat{a}_{p,0}$ | $\hat{a}^\dagger_{p,1}\hat{a}_{p,1}$ |

for some qubit $p$. In the Pauli basis, these elements can be written as,

$$\hat{a}^\dagger_{p,0}\hat{a}_{p,0} = \begin{pmatrix} 1 & 0 \\ 0 & 0 \end{pmatrix} = \frac{1}{2}(I + Z_p) \tag{A.3}$$

$$\hat{a}^\dagger_{p,0}\hat{a}_{p,1} = \begin{pmatrix} 0 & 1 \\ 0 & 0 \end{pmatrix} = \frac{1}{2}(X_p + iY_p) \tag{A.4}$$

$$\hat{a}^\dagger_{p,1}\hat{a}_{p,0} = \begin{pmatrix} 0 & 0 \\ 1 & 0 \end{pmatrix} = \frac{1}{2}(X_p - iY_p) \tag{A.5}$$

$$\hat{a}^\dagger_{p,1}\hat{a}_{p,1} = \begin{pmatrix} 0 & 0 \\ 0 & 1 \end{pmatrix} = \frac{1}{2}(I - Z_p) \tag{A.6}$$

Since the expectations of the single-qubit Pauli matrices can be directly obtained on a quantum device, it is straightforward to obtain the expectation values of the 1-RDM elements for each state preparation.

## A.3 Quantum Device Specifications

This work utilized superconducting-qubit IBM Quantum devices available online: `ibmq_qasm_simulator`, `ibmq_jakarta`, and a noise model qasm simulator of `ibmq_jakarta` (`qasm_simulator` (`ibmq_jakarta`)). `ibmq_jakarta` is one of the IBM Quantum Falcon processors [138, 146]. The quantum computer is composed of fixed-frequency transmon qubits with coplanar waveguide resonators [147, 148]. For calibration details see Table 1.

## A.4 Additional Data

Table A.1: Calibration data for the IBM quantum computer "Jakarta"

| **Device:** ibmq_jakarta ("Jakarta") | | | | | | | |
|---|---|---|---|---|---|---|---|
| **Calibration Date:** 07/18/22 | | | | | | | |
| **Version:** 1.0.36 | | | | | | | |
| **Gate time (max, ns):** 535.1 | | | | | | | |
| **Qubit:** | 0 | 1 | 2 | 3 | 4 | 5 | 6 |
| *T2 ($\mu s$)* | 50.8 | 28.5 | 24.1 | 34.8 | 83.0 | 51.6 | 23.9 |
| *f (GHz)* | 5.24 | 5.01 | 5.11 | 5.18 | 5.21 | 5.06 | 5.30 |
| *T1 ($\mu s$)* | 104 | 151 | 55.8 | 112 | 112 | 139 | 148 |
| *Gate Error ($10^{-3}$)* | 0.28 | 0.29 | 0.28 | 0.22 | 0.22 | 0.30 | 0.27 |
| *Readout Error ($10^{-3}$)* | 34.0 | 49.4 | 25.1 | 20.8 | 25.3 | 46.6 | 55.1 |
| **Multi-Qubit:** | 0,1 | 1,3 | 1,2 | 3,5 | 4,5 | 5,6 | |
| *Error ($10^{-3}$)* | 7.50 | 8.14 | 11.4 | 7.43 | 9.41 | 6.79 | |

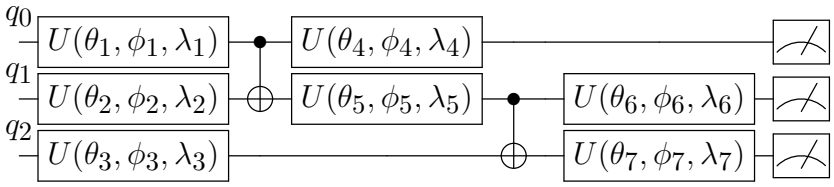


Figure A.2: Quantum circuit used for the state preparation of a three-qubit system.

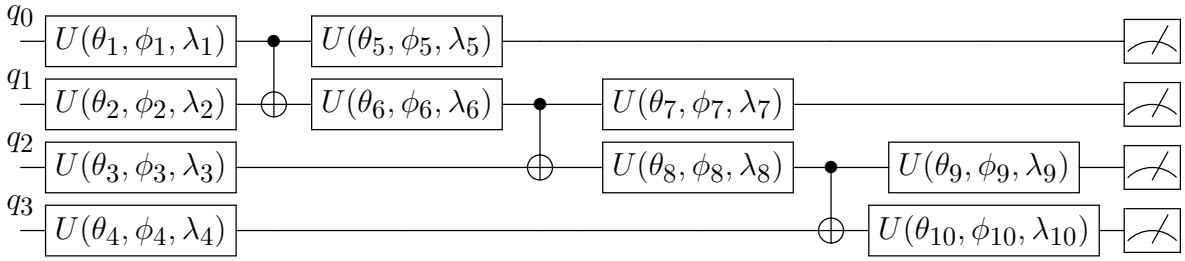


Figure A.3: Quantum circuit used for the state preparation of a four-qubit system.

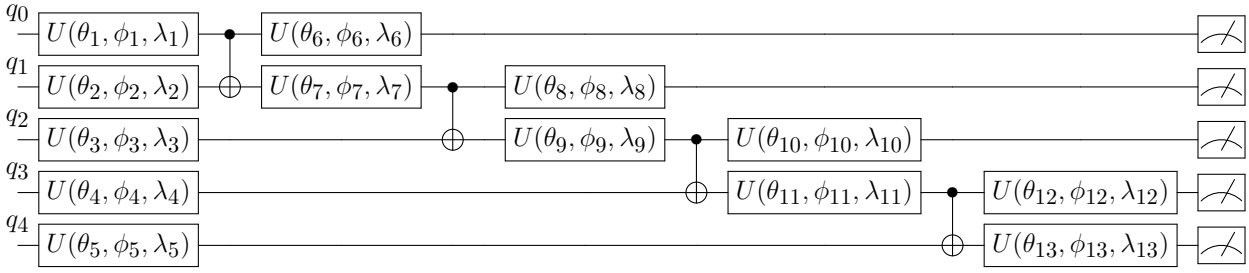


Figure A.4: Quantum circuit used for the state preparation of a five-qubit system.

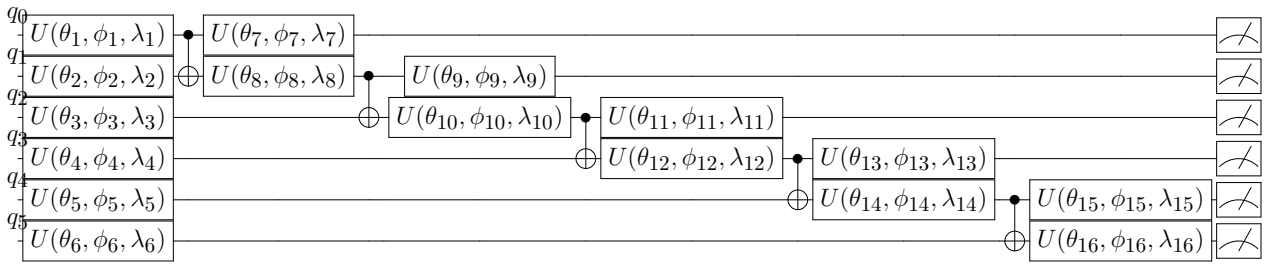


Figure A.5: Quantum circuit used for the state preparation of a six-qubit system.

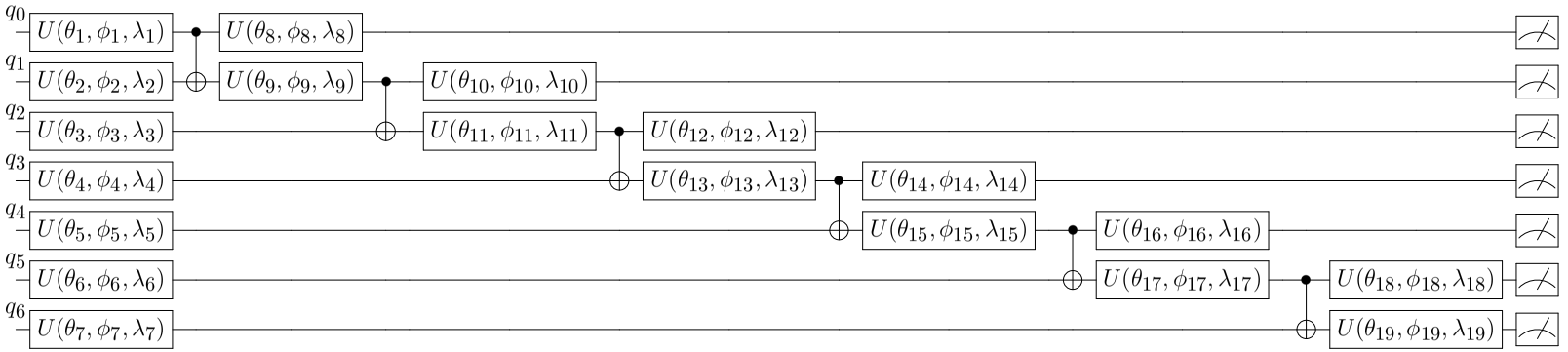


Figure A.6: Quantum circuit used for the state preparation of a seven-qubit system.

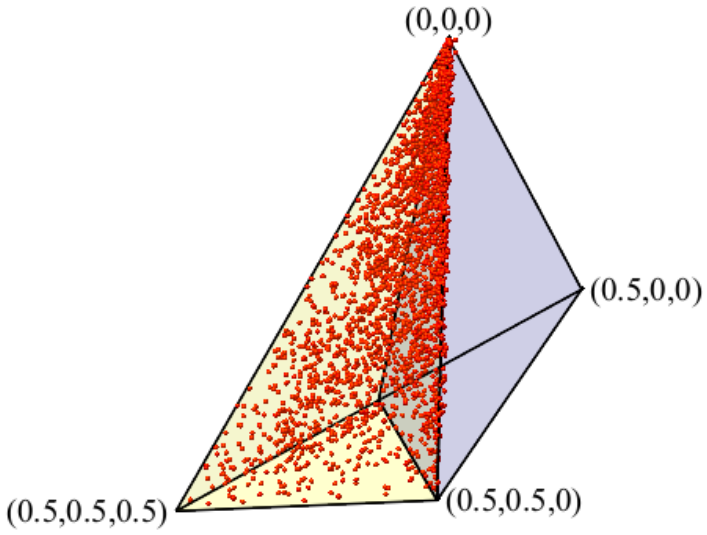


(a)

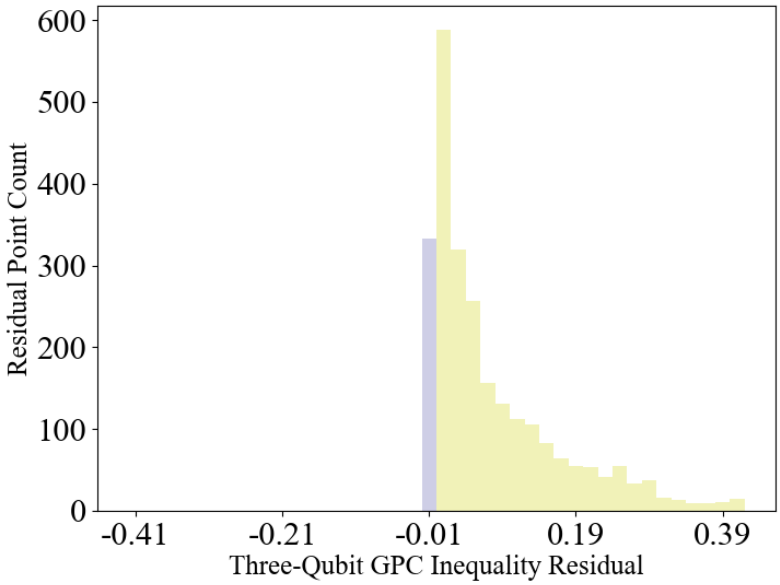


(b)

Figure A.7: (a) Polytope showing eigenvalue triplets measured on the noiseless simulator, ibmq_qasm_simulator for a three-qubit system. A significant number of eigenvalues are pinned to the Borland-Dennis setting but they still remain in the generalized Pauli constraints-defined region of the polytope. (b) Distribution of the generalized Pauli constraints residual for the three-qubit system. The middle blue bar represents residual computed from eigenvalue triplets pinned to the Borland-Dennis edge.

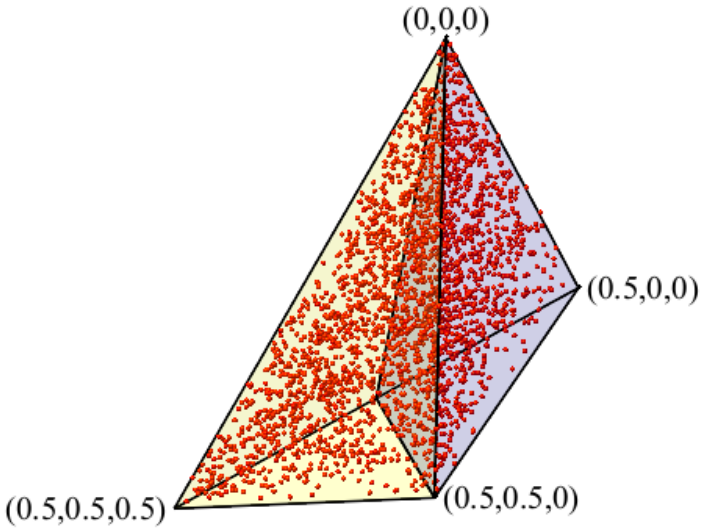


(a)

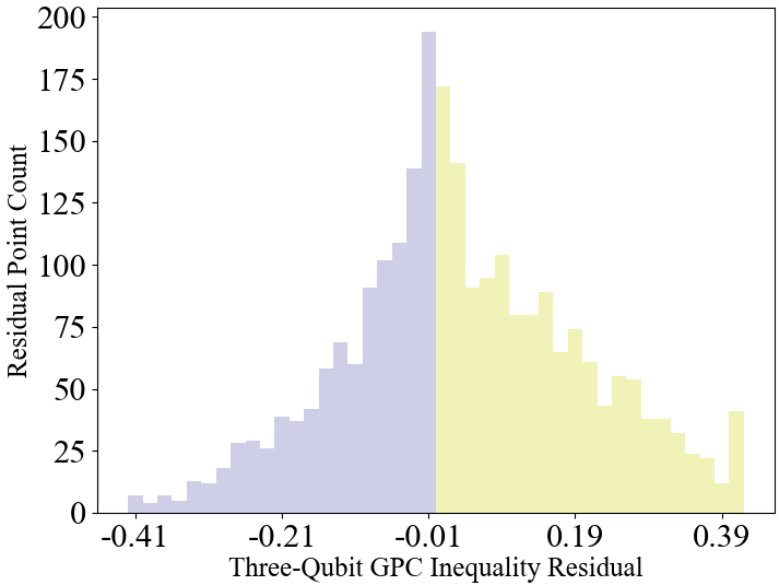


(b)

Figure A.8: (a) Polytope showing eigenvalue triplets measured on the noiseless simulator, ibmq_qasm_simulator for a four-qubit system. A significant portion of the measured points (1089/2500) are in the region defined by ordinary Pauli constraints (blue). (b) Gaussian distribution of the three-qubit inequality residual.

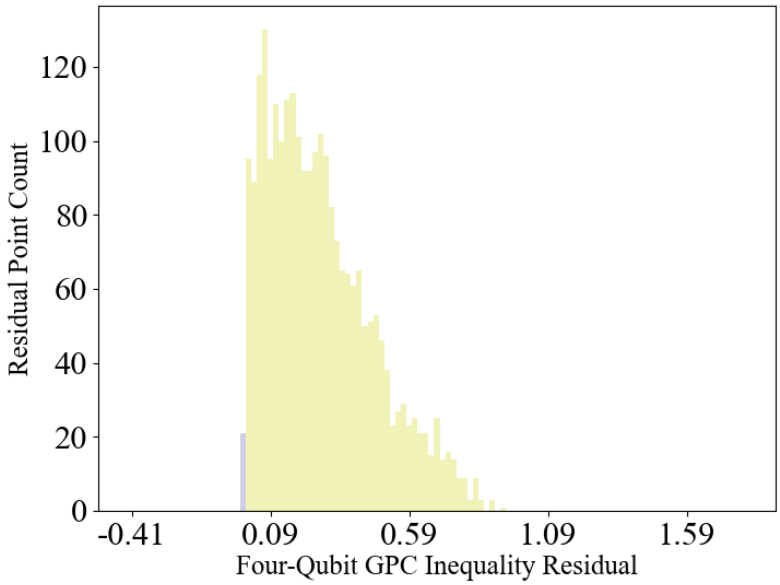


(c)

Figure A.8: (c) Distribution of the four-qubit inequality residual shows insignificant violation of the four-qubit generalized Pauli constraints (21/2500 points).

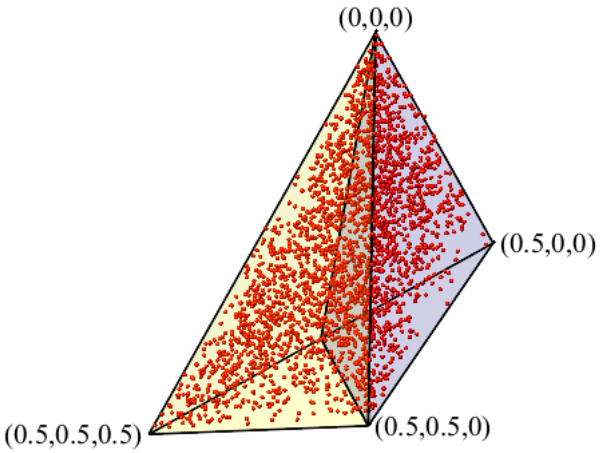


(a)

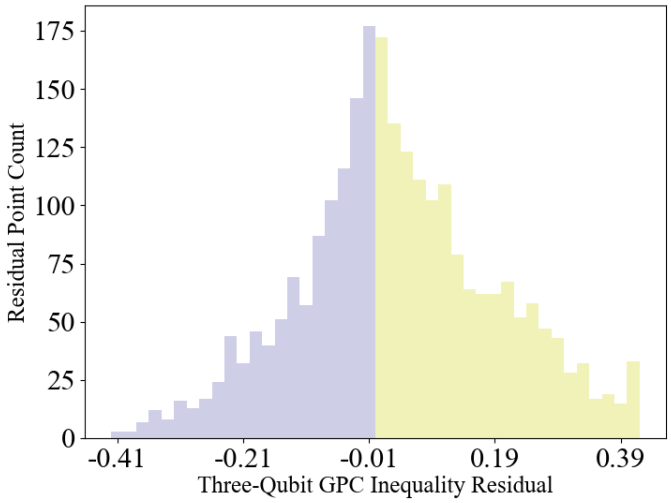


(b)

Figure A.9: (a) Polytope showing eigenvalue triplets measured on the noiseless simulator, ibmq_qasm_simulator for a five-qubit system. Similar to the previous case, a significant portion of the measured points (1070/2500) lies in the blue region (ordinary Pauli constraints) of the polytope. The three-qubit system remains open with addition of another qubit, but access to sets of ensemble one-particle reduced density matrices does not increase any more than what was obtained via addition of a single ancilla qubit. (b) Gaussian distribution of the three-qubit inequality residual shows a similar picture as in the four-qubit system. Most eigenvalue triplets are pinned to the Borland–Dennis setting.

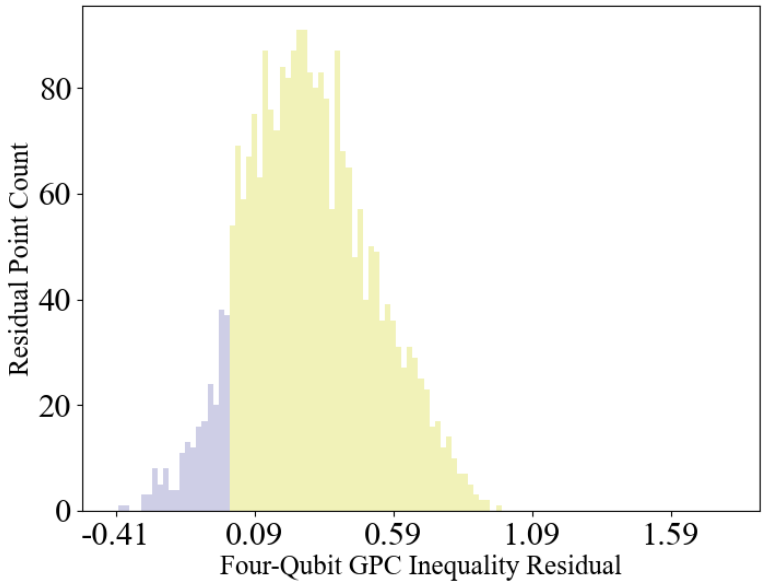


(c)

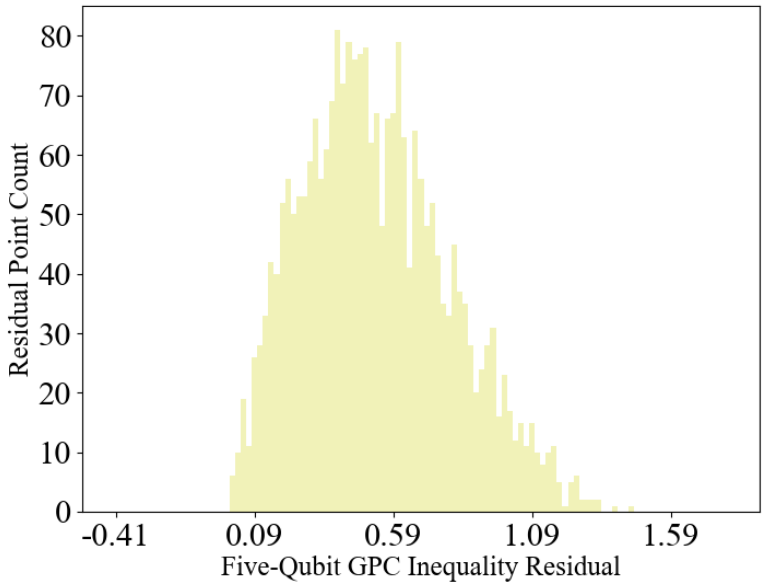


(d)

Figure A.9: (c) Distribution of the four-qubit inequality residual shows noticeable generalized Pauli constraints violation for this five-qubit system (225/2500) but significantly smaller than the three-qubit generalized Pauli constraints violation. (d) Distribution of the five-qubit inequality residual shows no violation of the generalized Pauli constraints.

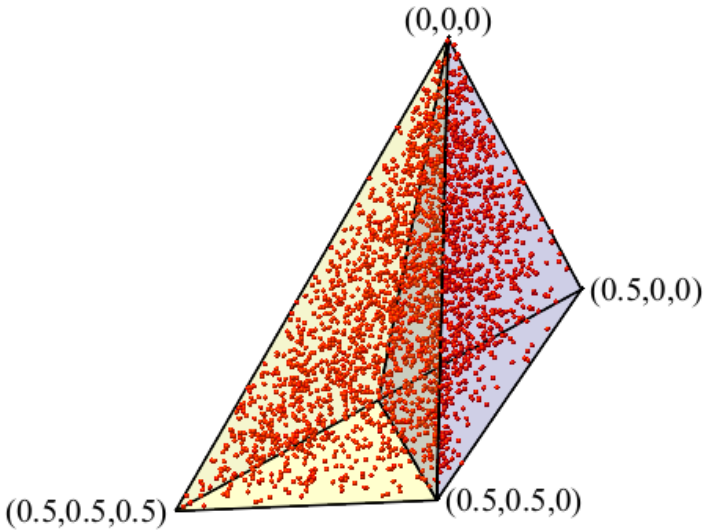


(a)

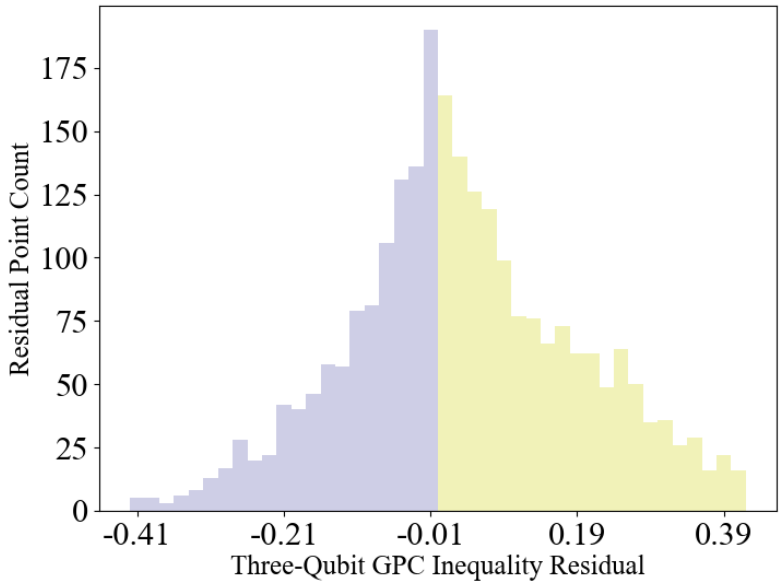


(b)

Figure A.10: (a) Polytope showing eigenvalue triplets measured on the noiseless simulator, ibmq_qasm_simulator for a six-qubit system. There are 1093/2500 points in the blue region of the polytope. (b) Gaussian distribution of the three-qubit inequality residual shows similar behavior as in the previous two cases—most triplets are pinned to the Borland–Dennis edge.

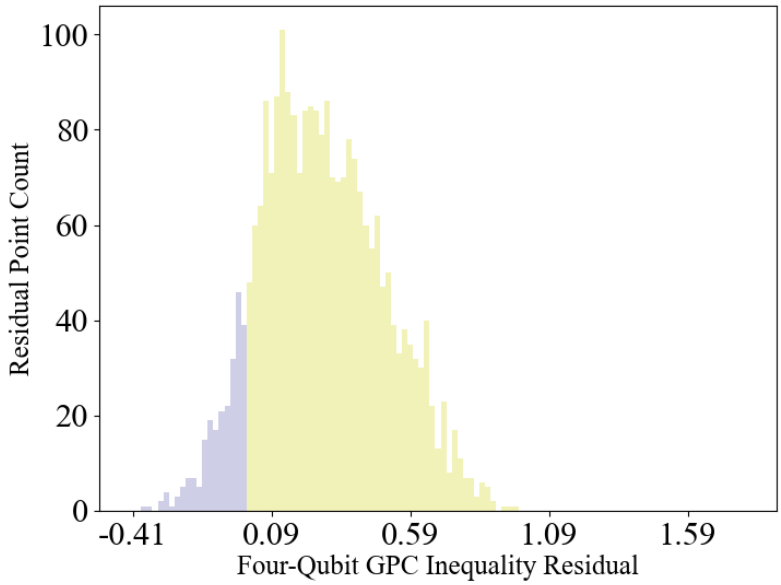


(c)

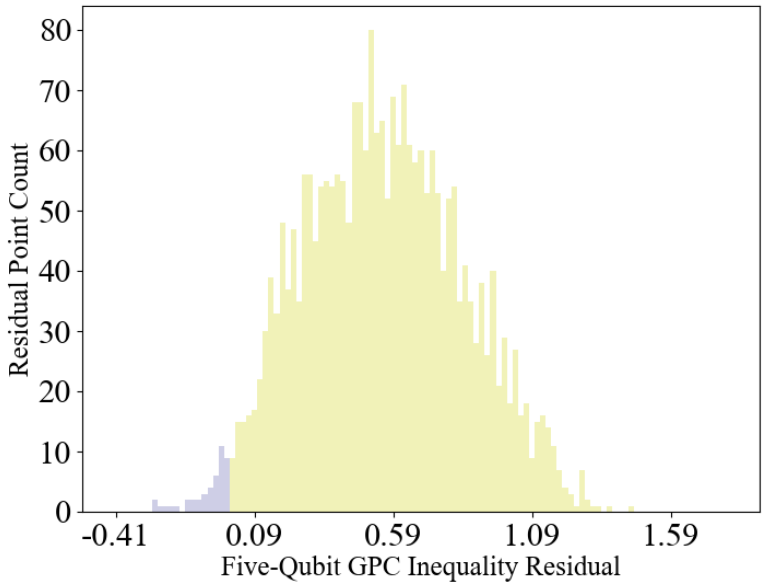


(d)

Figure A.10: (c) Distribution of the four-qubit inequality residual shows noticeable generalized Pauli constraints violation (247/2500 points), similar to the five-qubit system above. (d) Distribution of the five-qubit inequality residual shows some violation of the generalized Pauli constraints (45/2500 points).

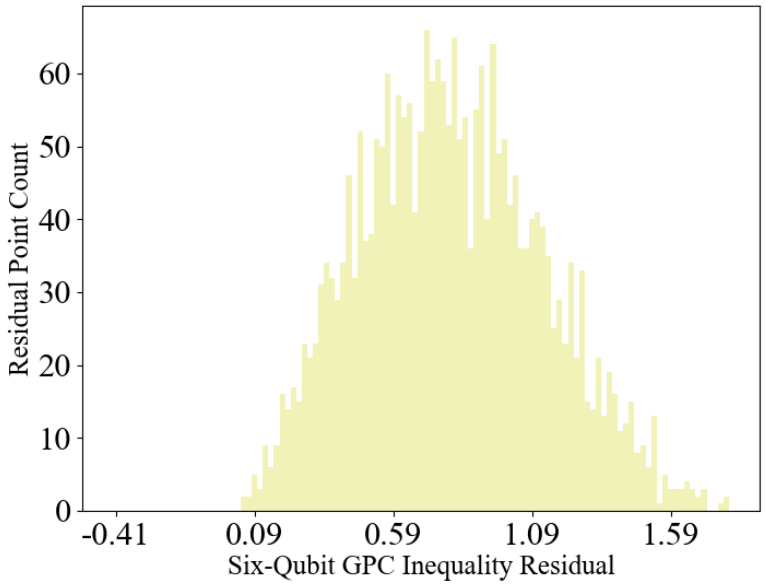


(e)

Figure A.10: (e) Distribution of the six-qubit inequality residual shows no generalized Pauli constraints violation for this six-qubit system.

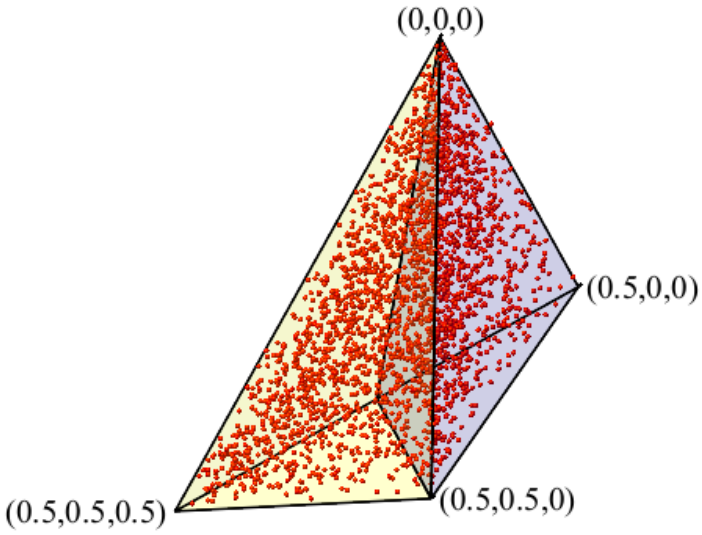


(a)

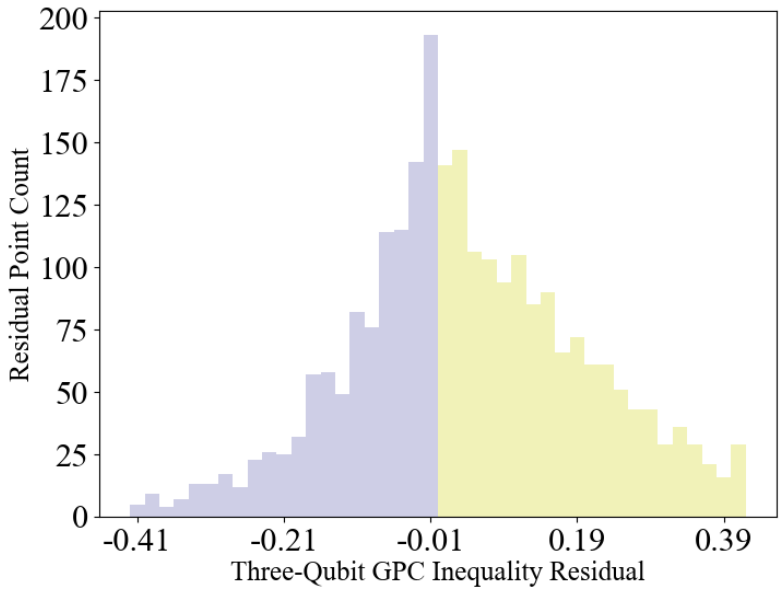


(b)

Figure A.11: (a) Polytope showing eigenvalue triplets measured on the noiseless simulator, ibmq_qasm_simulator for a seven-qubit system. There are 1072/2500 points in the blue region of the polytope. (b) Gaussian distribution of the three-qubit inequality residual shows similar behavior as in the previous three systems.

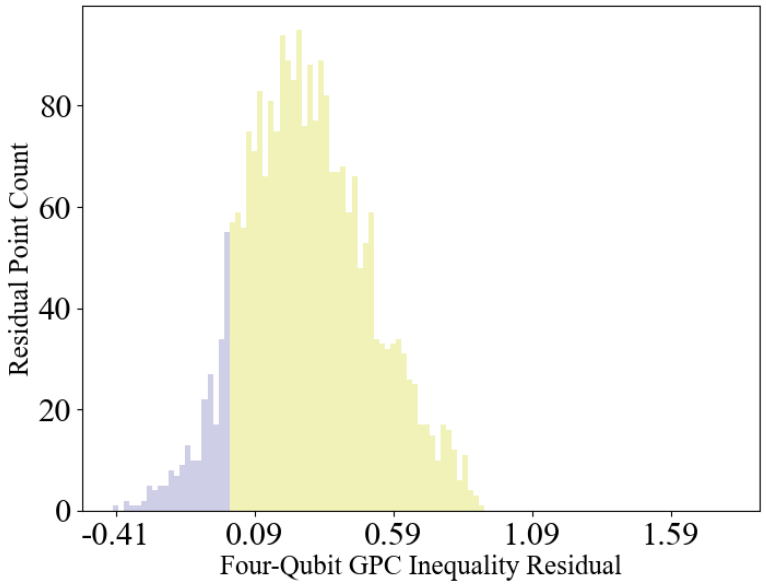


(c)

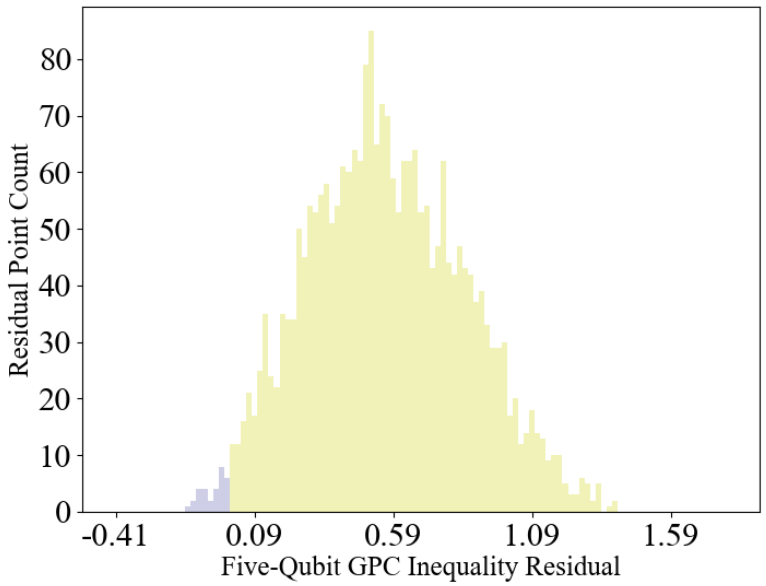


(d)

Figure A.11: (c) Distribution of the four-qubit inequality residual shows noticeable generalized Pauli constraints violation (238/2500 points). (d) Distribution of the five-qubit inequality residual shows some generalized Pauli constraints violation (31/2500 points).

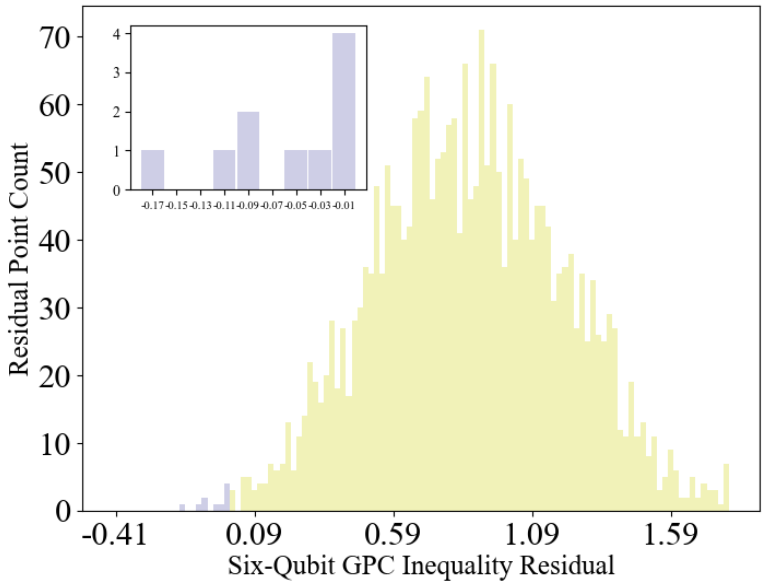


(e)

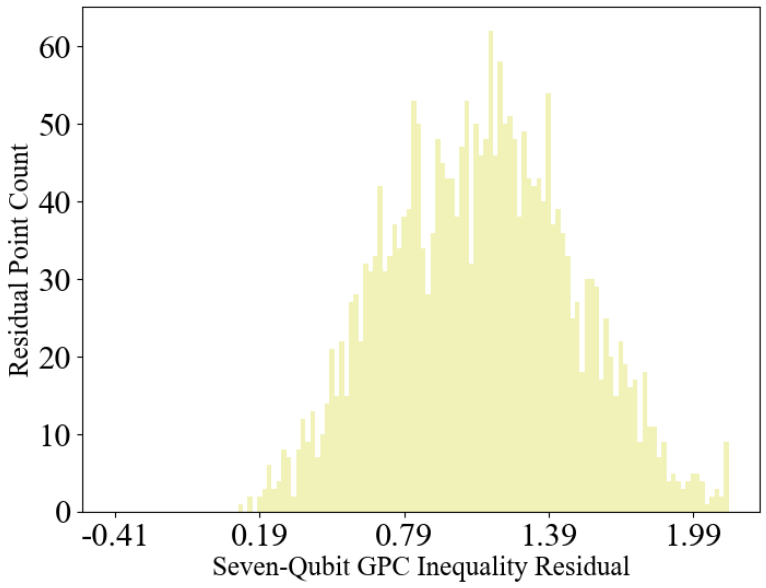


(f)

Figure A.11: (e) Distribution of the six-qubit inequality residual shows very little generalized Pauli constraints violation (10/2500 points). (f) Distribution of the seven-qubit inequality residual shows no violation of the generalized Pauli constraints.

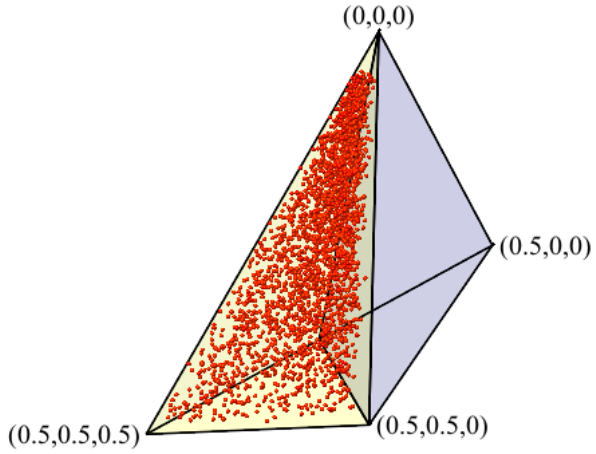


(a)

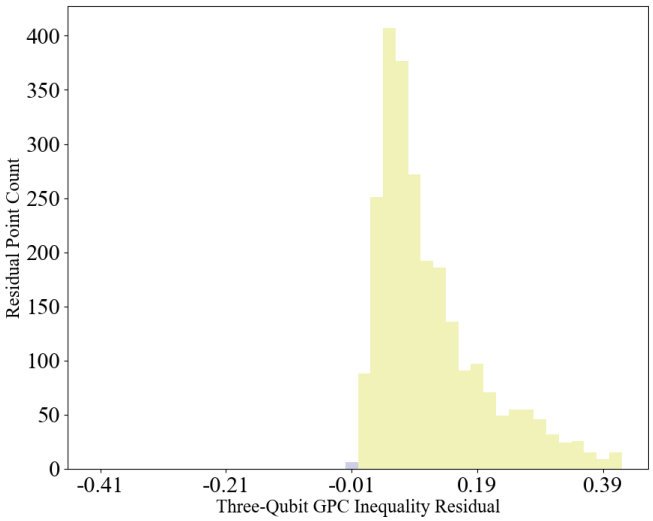


(b)

Figure A.12: (a) Polytope showing eigenvalue triplets measured on the noise model qasm simulator, qasm_simulator(ibmq_jakarta) for a three-qubit system. The simulated noise pulls eigenvalue triplets away from the edge states toward inside of the polytope. There are significantly less points pinned to the Borland-Dennis edge compared to Fig. 1 (a). There are no points in the blue region of the polytope, showing that the generalized Pauli constraintss are not violated in this closed three-qubit system. (b) Distribution of the generalized Pauli constraints residual for the three-qubit system shows no violation of the generalized Pauli constraintss.

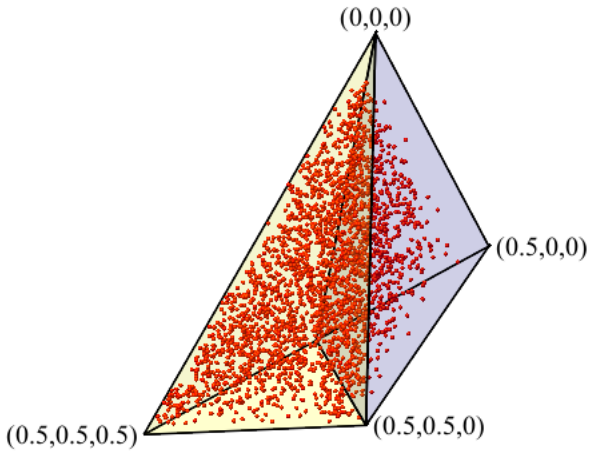


(a)

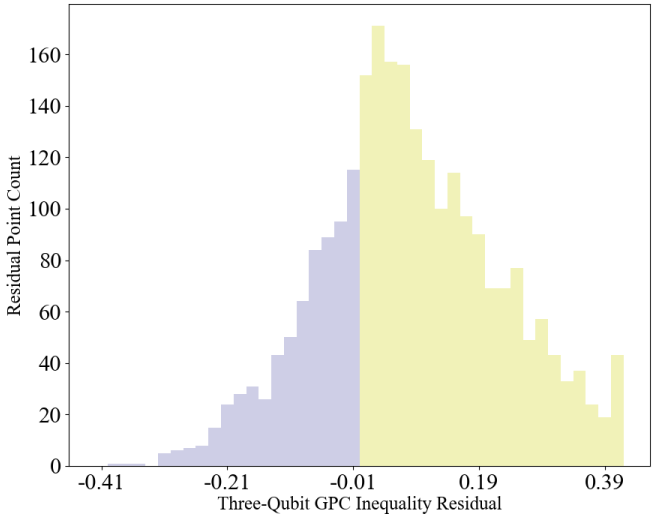


(b)

Figure A.13: (a) Polytope showing eigenvalue triplets measured on the noise model qasm simulator, qasm_simulator(ibmq_jakarta) for a four-qubit system. There are 693/2500 points in the blue region of the polytope, representing the violation of the three-qubit generalized Pauli constraints. This is a significantly lower violation than measured on a noiseless simulator in Fig. 2(a). (b) Distribution of the three-qubit inequality residual shows generalized Pauli constraints violation to a lesser extent than in Fig. 2(b).

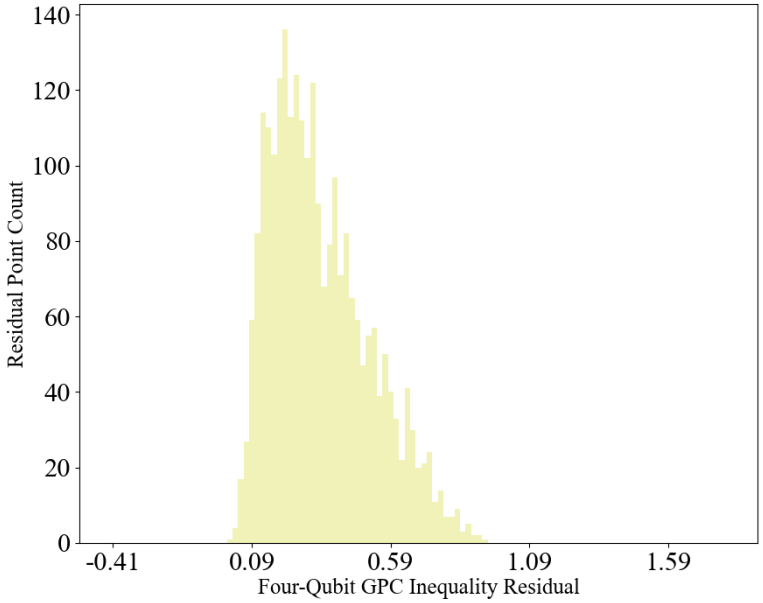


(c)

Figure A.13: (c) Distribution of the four-qubit inequality residual shows no violation of the generalized Pauli constraints.

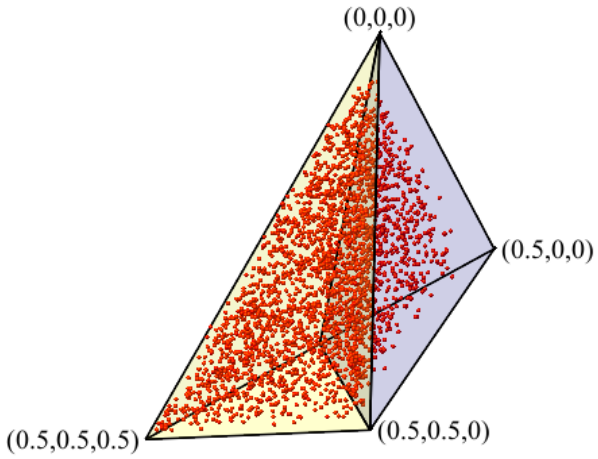


(a)

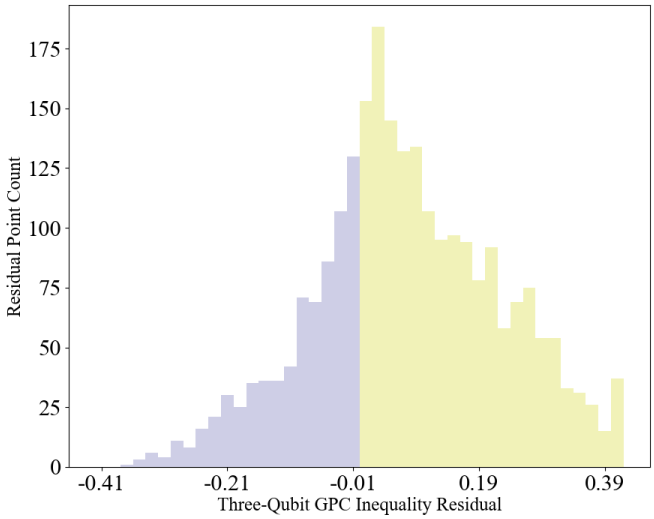


(b)

Figure A.14: (a) Polytope showing eigenvalue triplets measured on the noise model qasm simulator, qasm_simulator(ibmq_jakarta) for a five-qubit system. There are 737/2500 points measured in the blue region of the polytope, which is significantly lower than in Fig. 3(a) but only slightly greater than the violation in the four-qubit system above. (b) Distribution of the three-qubit inequality residual shows similar behavior as described above.

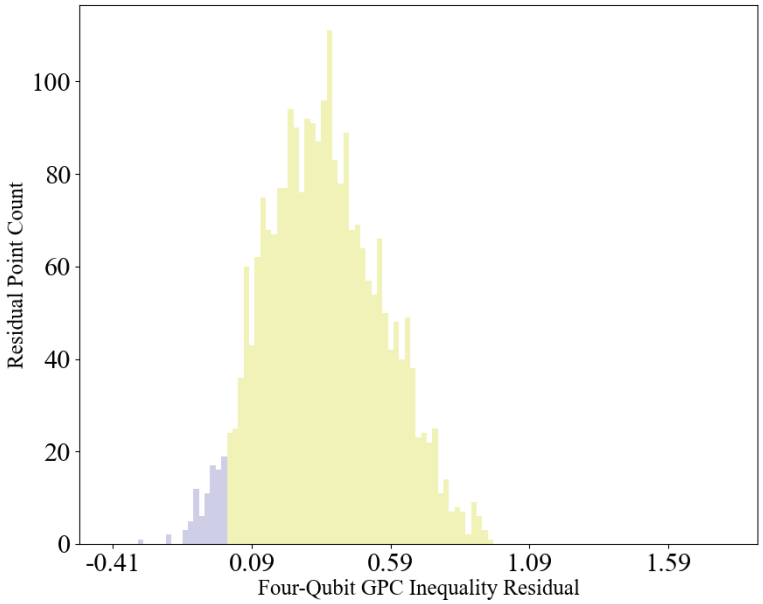


(c)

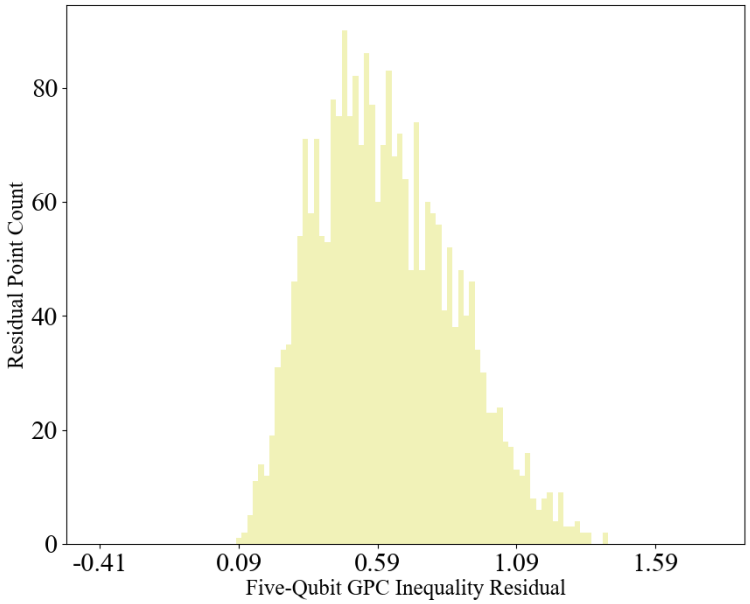


(d)

Figure A.14: (c) Distribution of the four-qubit inequality residual shows some violation of the generalized Pauli constraints (92/2500 points). (d) Distribution of the five-qubit inequality residual shows no violation of the generalized Pauli constraints.

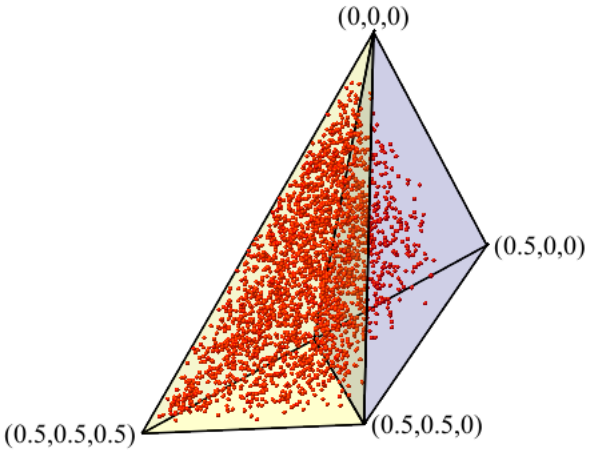


(a)

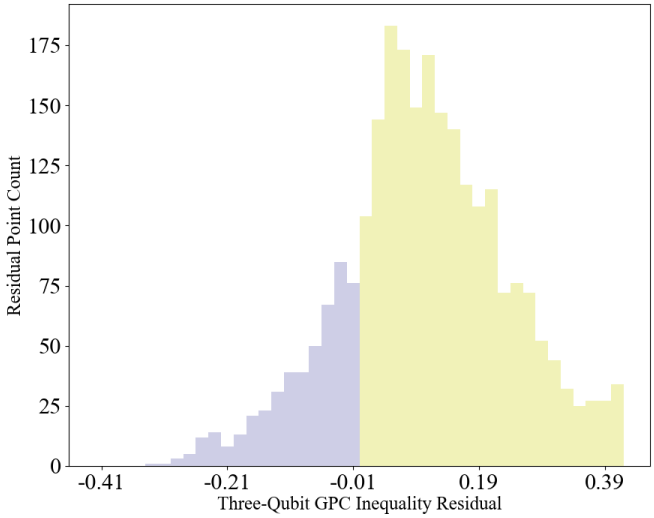


(b)

Figure A.15: (a) Polytope showing eigenvalue triplets measured on the noise model qasm simulator, qasm_simulator(ibmq_jakarta) for a six-qubit system shows a noticeable generalized Pauli constraints violation to a lesser extent than the previous two systems. There are 488/2500 points in the blue region of the polytope. (b) Distribution of the three-qubit inequality residual confirms the behavior in (a).

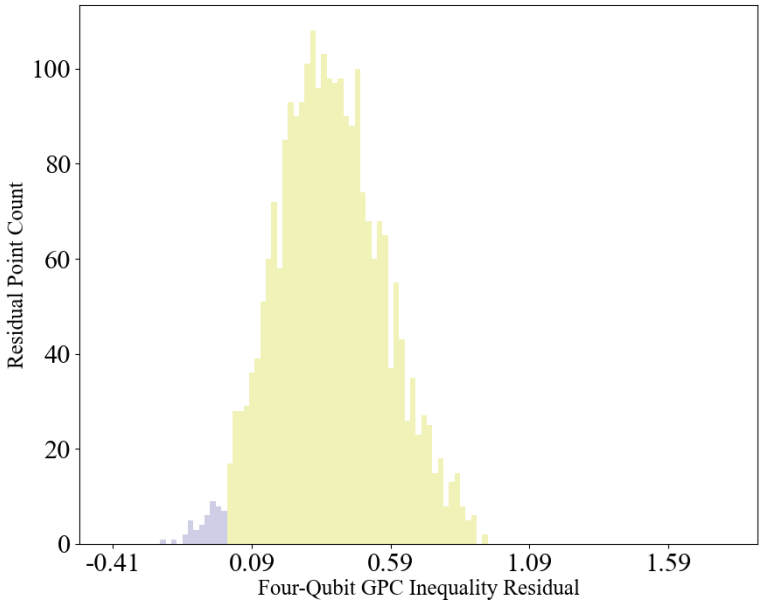


(c)

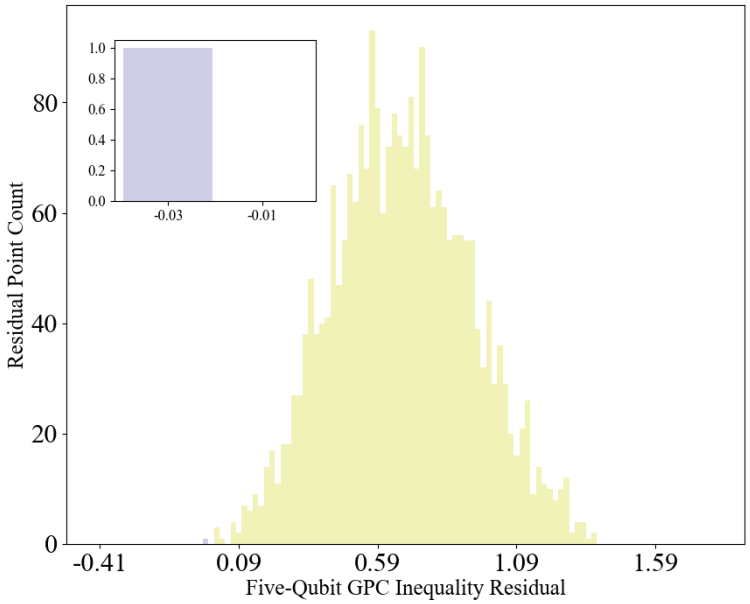


(d)

Figure A.15: (c) Distribution of the four-qubit inequality residual shows some generalized Pauli constraints violation (46/2500). (d) Distribution of the five-qubit inequality residual shows only one point violating the generalized Pauli constraints.

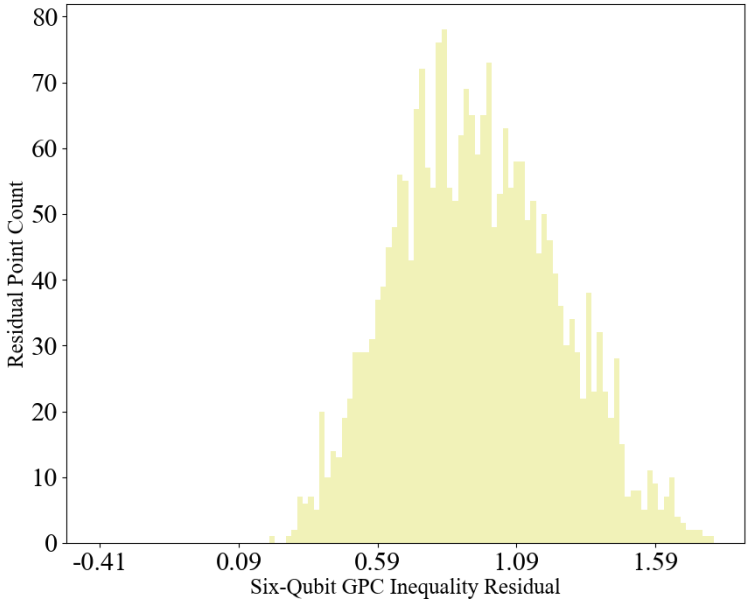


(e)

Figure A.15: (e) Distribution of the six-qubit inequality residual shows no generalized Pauli constraints violation.

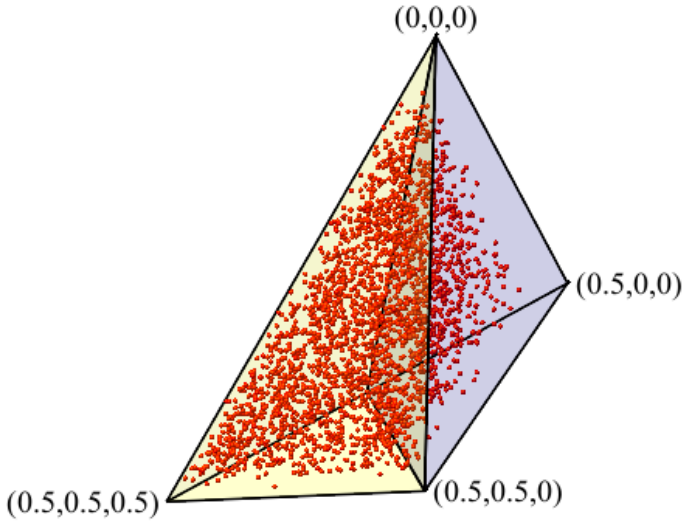


(a)

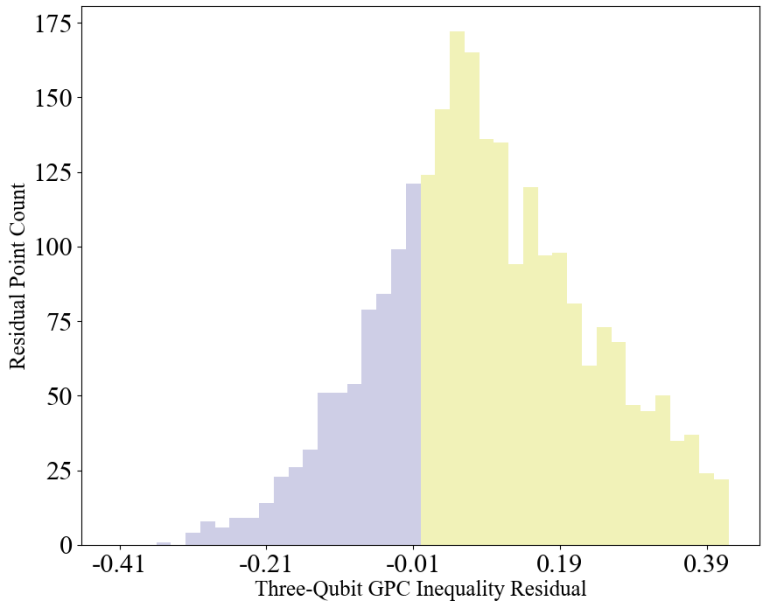


(b)

Figure A.16: (a) Polytope showing eigenvalue triplets measured on the noise model qasm simulator, qasm_simulator(ibmq_jakarta) for a seven-qubit system shows 671/2500 points in the blue region of the polytope. (b) Distribution of the three-qubit inequality residual shows similar behavior to the previous three systems.

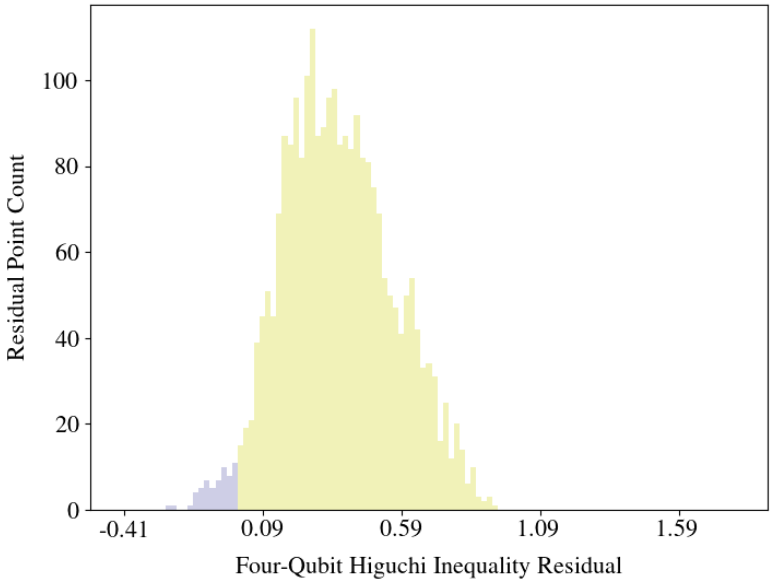


(c)

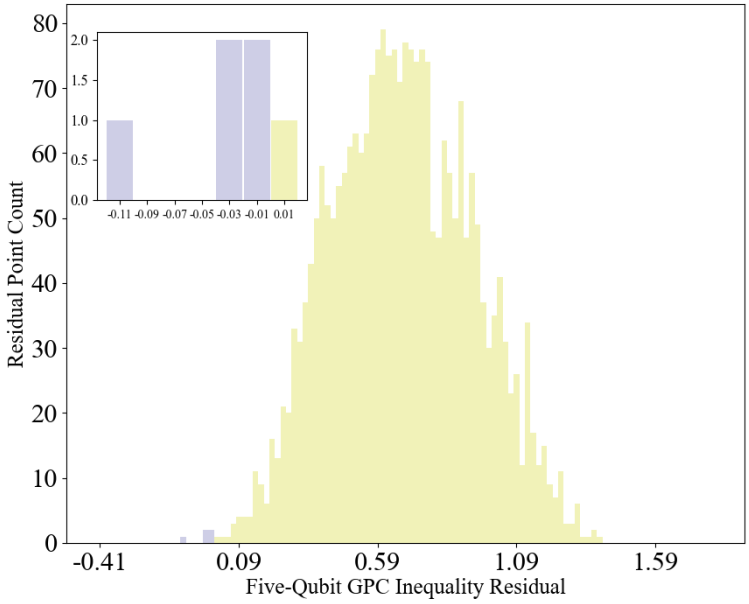


(d)

Figure A.16: (c) Distribution of the four-qubit inequality residual shows some violation of the generalized Pauli constraints (60/2500 points). (d) Distribution of the five-qubit inequality residual shows little violation of the generalized Pauli constraints (5/2500).

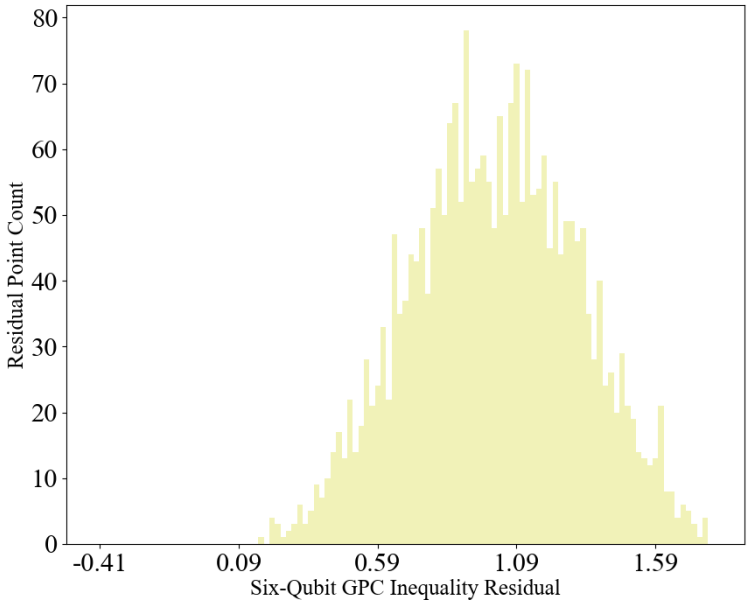


(e)

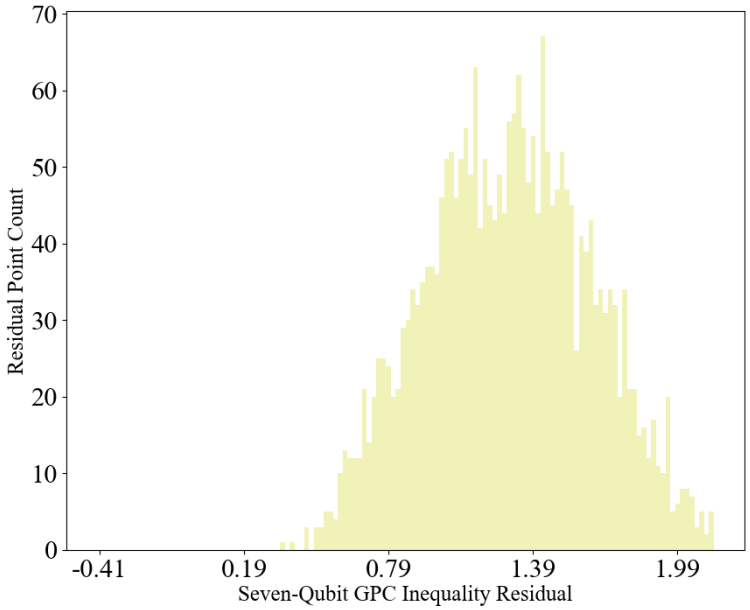


(f)

Figure A.16: (e) Distribution of the six-qubit inequality residual shows no violation of the generalized Pauli constraints. (f) Distribution of the seven-qubit inequality residual shows no generalized Pauli constraints violation.

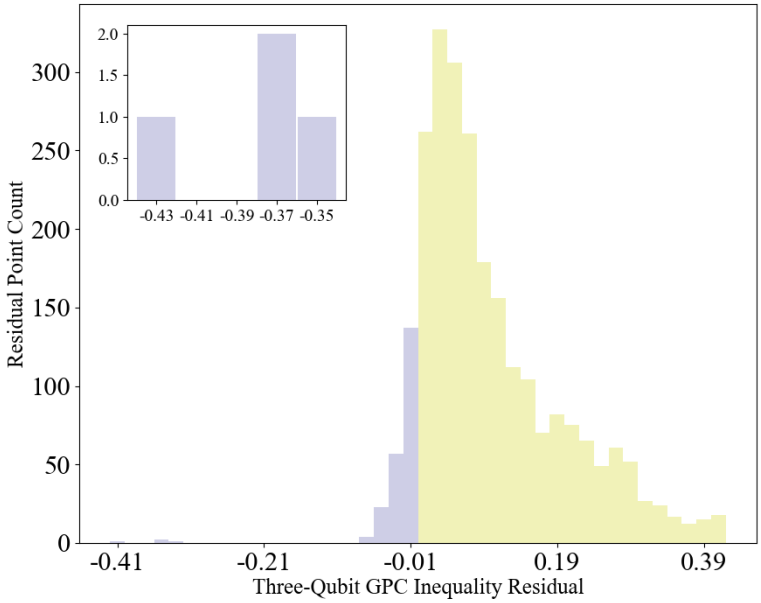


Figure A.17: Distribution of the generalized Pauli constraints residual for the three-qubit system measured on the quantum computer, ibmq_jakarta for a three-qubit system. There are 225/2500 measured points in the blue region of the polytope, defined by the ordinary Pauli constraints, showing some violation of the generalized Pauli constraintss. This is likely an artifact of the noise on this quantum computer at the time of use.

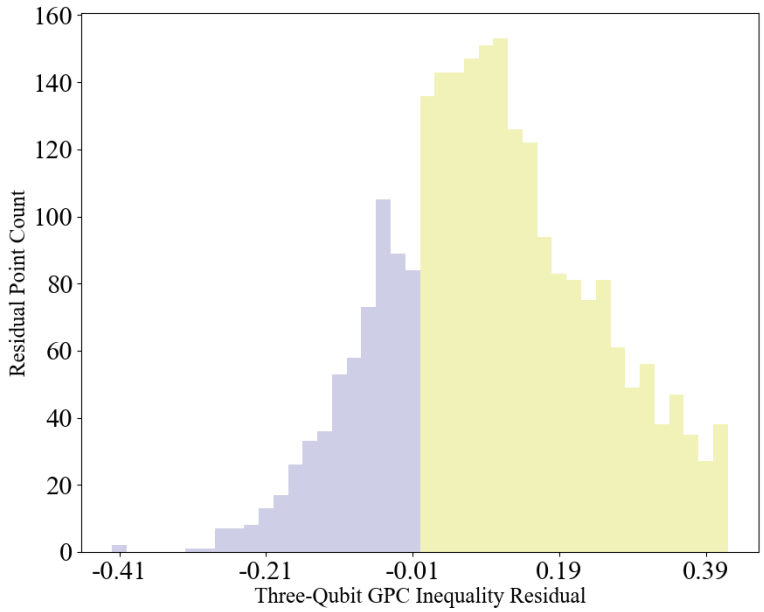


(a)

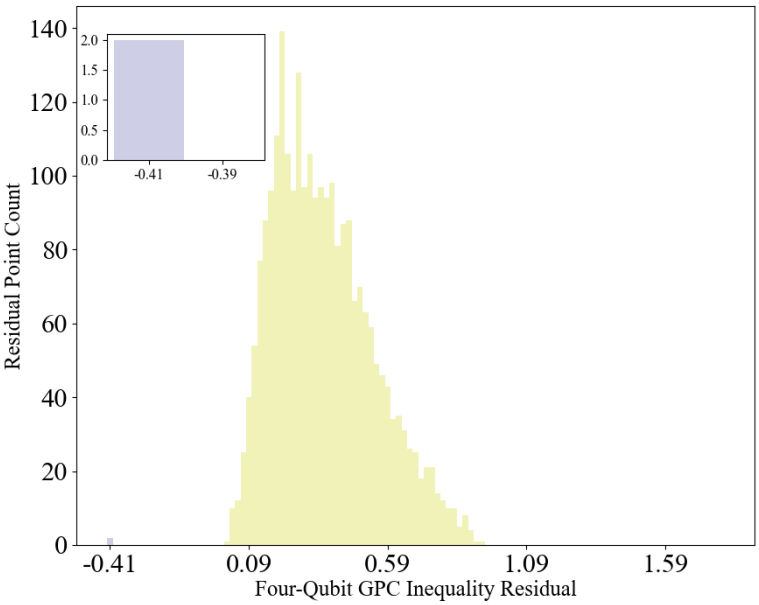


(b)

Figure A.18: (a) Distribution of the three-qubit inequality residual measured on the quantum computer, ibmq_jakarta shows roughly a fourth of the measured points violating the generalized Pauli constraintss. (b) Distribution of the four-qubit inequality residual shows some violation of the generalized Pauli constraintss, which is likely a feature of the device's noise at the time of measurement.

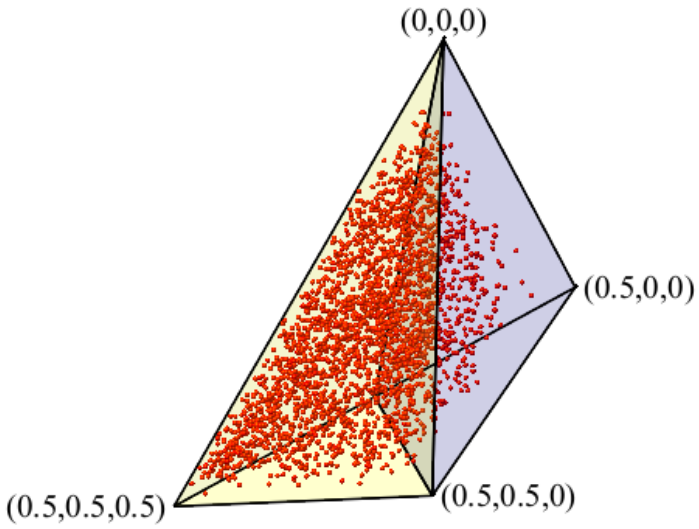


Figure A.19: Polytope showing eigenvalue triplets measured on the quantum computer, ibmq_jakarta, for a five-qubit system. There are 534/2500 points in the blue region of the polytope.

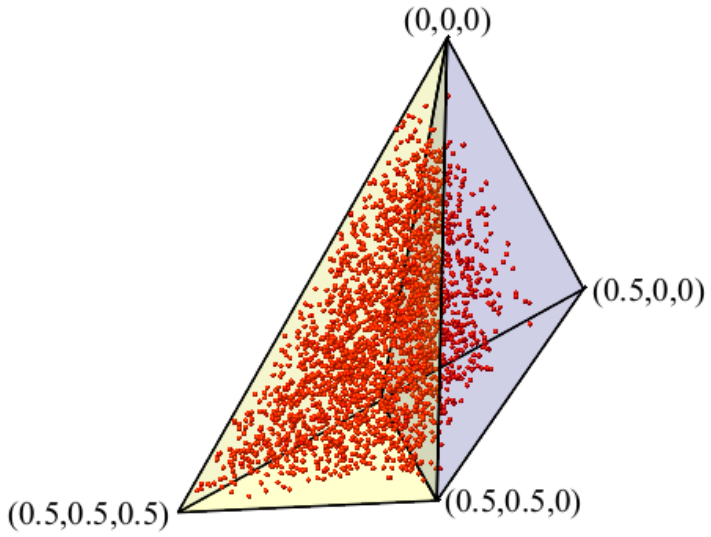


(a)

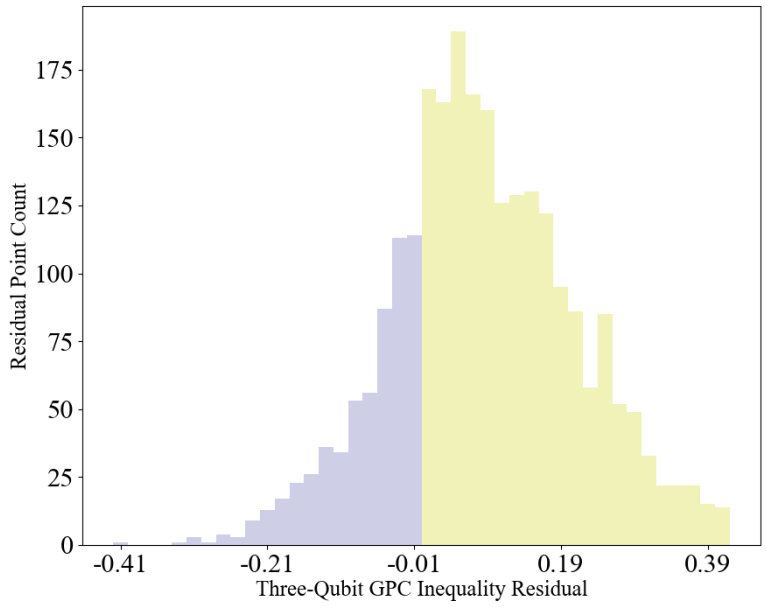


(b)

Figure A.20: (a) Polytope showing eigenvalue triplets measured on the quantum computer, ibmq_jakarta, for a six-qubit system. There are 594/2500 points in the blue region of the polytope. (b) Distribution of the three-qubit inequality residual confirms the polytope behavior in (a).

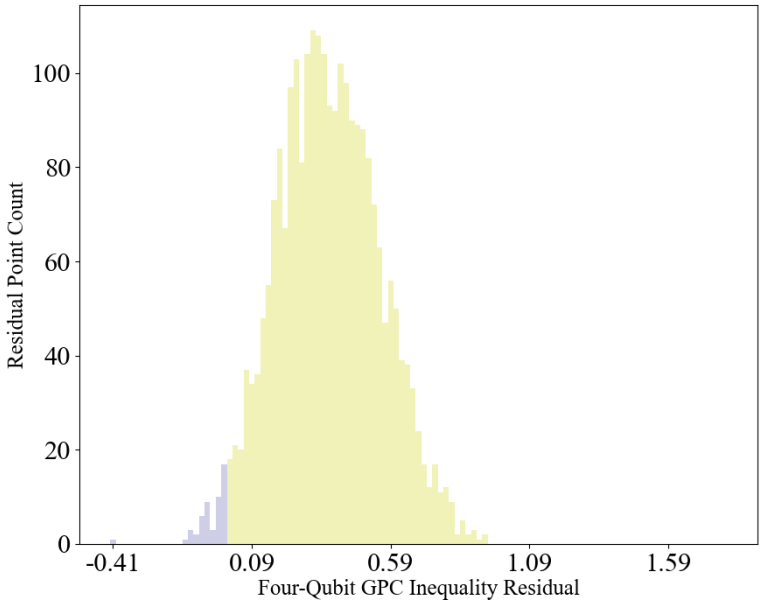


(c)

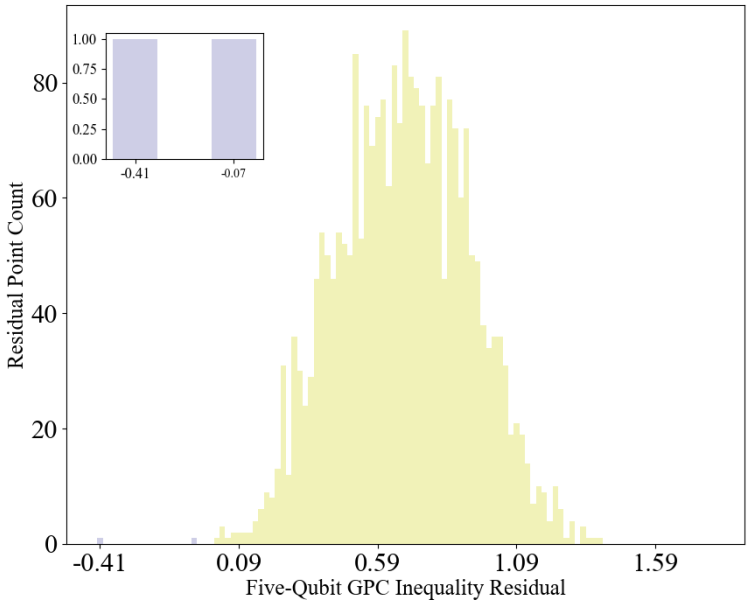


(d)

Figure A.20: (c) Distribution of the four-qubit inequality residual shows some generalized Pauli constraints violation (52/2500 points). (d) Distribution of the five-qubit inequality residual shows very little generalized Pauli constraints violation (2/2500 points).

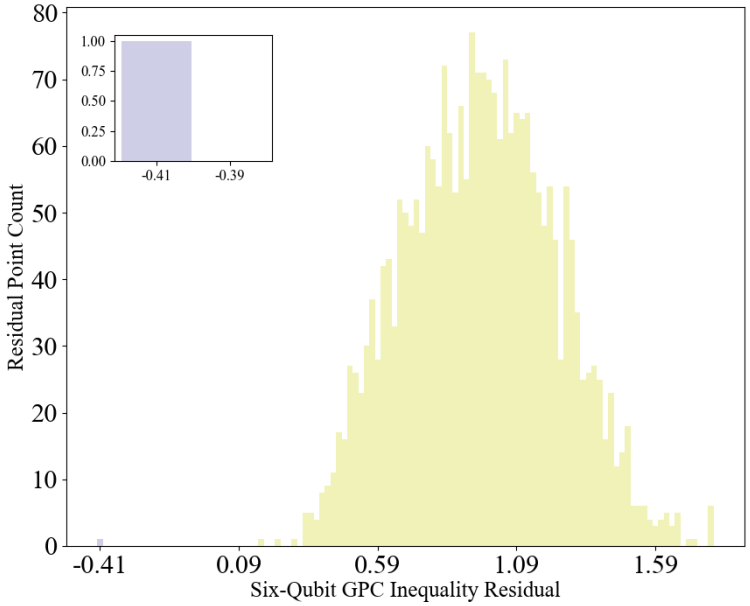


(e)

Figure A.20: (e) Distribution of the six-qubit inequality residual shows one point violating the generalized Pauli constraints.

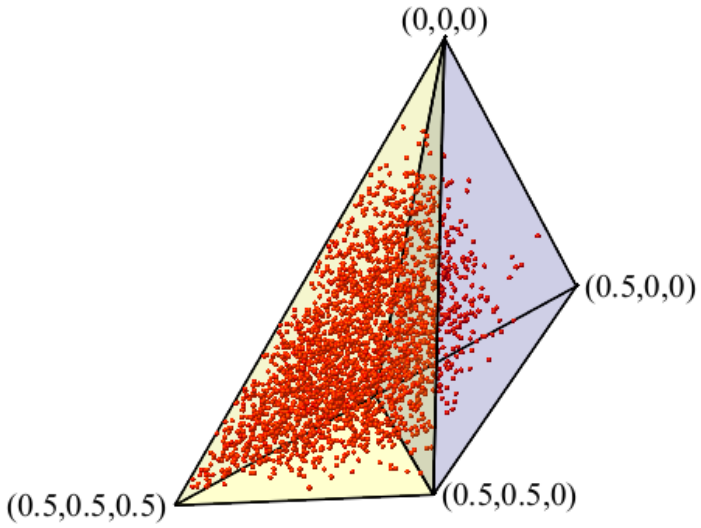


(a)

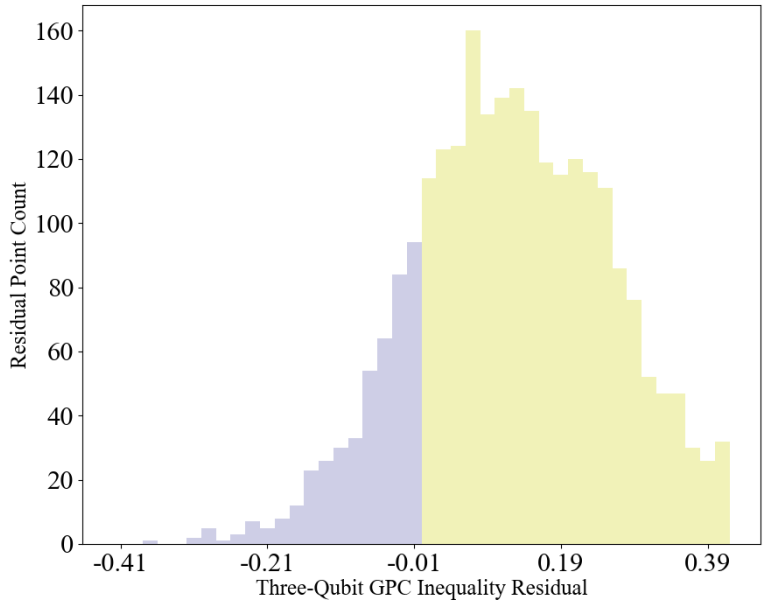


(b)

Figure A.21: (a) Polytope showing eigenvalue triplets measured on the quantum computer, ibmq_jakarta, for a seven-qubit system. There are 452/2500 points in the blue region of the polytope. (b) Distribution of the three-qubit inequality residual confirms the polytope behavior in (a).

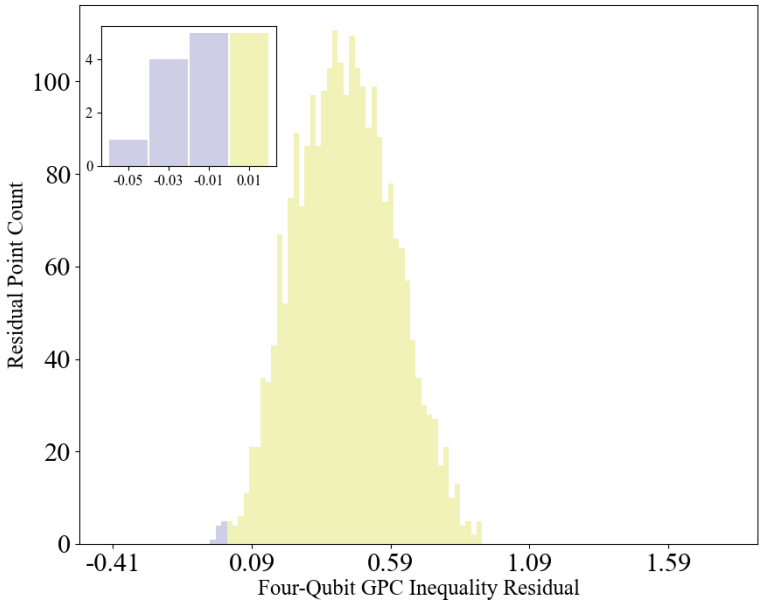


(c)

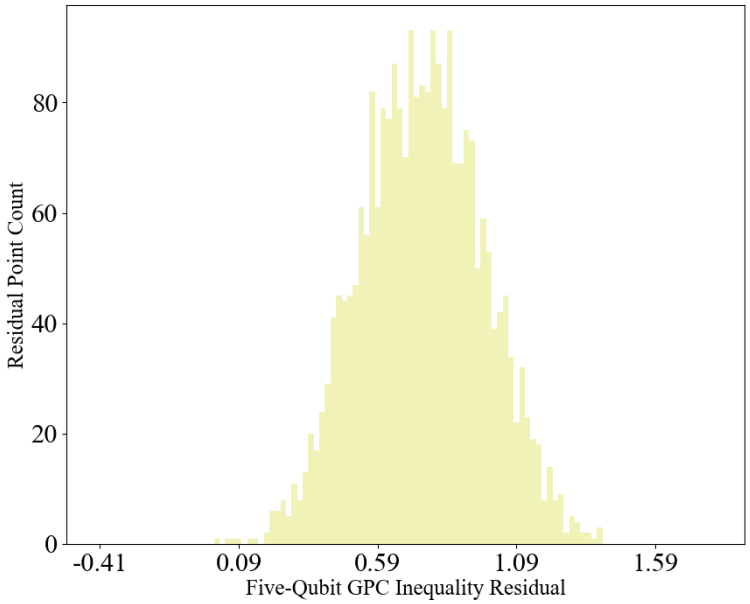


(d)

Figure A.21: (c) Distribution of the four-qubit inequality residual shows little generalized Pauli constraints violation (10/2500 points). (d) Distribution of the five-qubit inequality residual shows no generalized Pauli constraints violation.

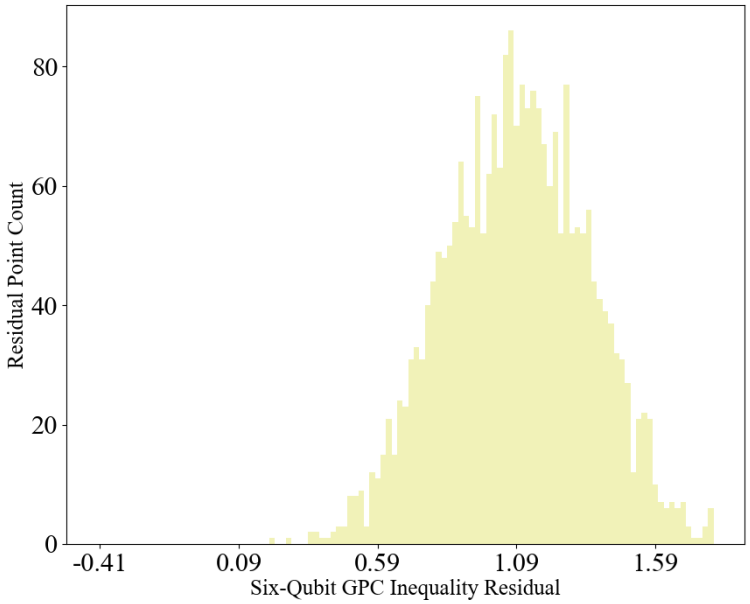


(e)

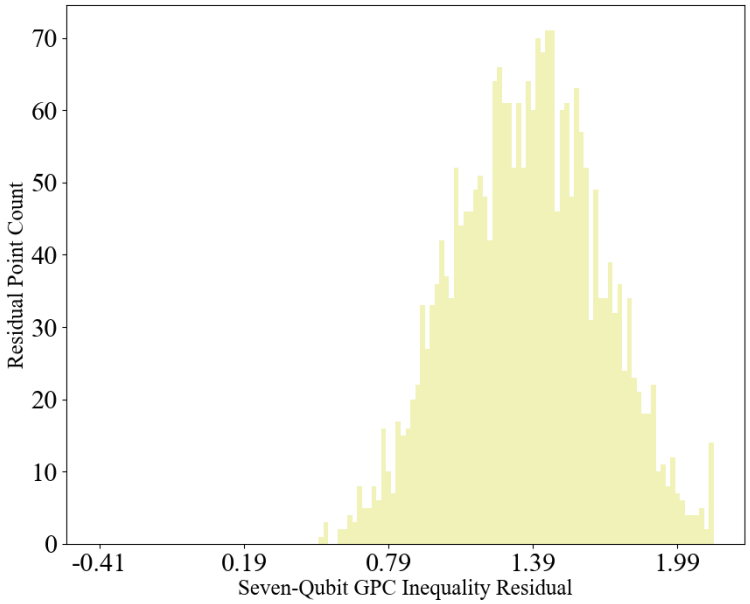


(f)

Figure A.21: (e) Distribution of the six-qubit inequality residual shows no generalized Pauli constraints violation. (f) Distribution of the seven-qubit inequality residual shows no generalized Pauli constraints violation.

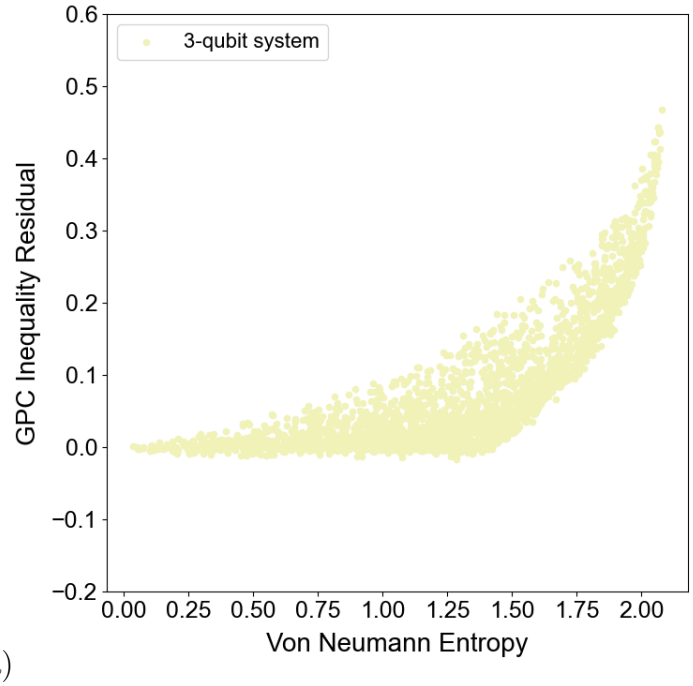


(a)

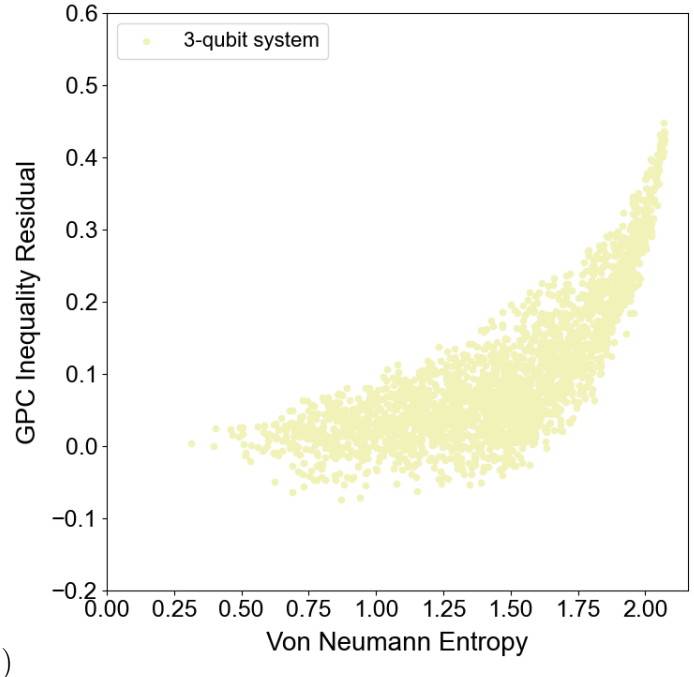


(b)

Figure A.22: Generalized Pauli constraints inequality residual plotted as a function of the von Neumann entropy for the occupation measurements collected on (a) simulator and (b) quantum computer for the three-qubit system.

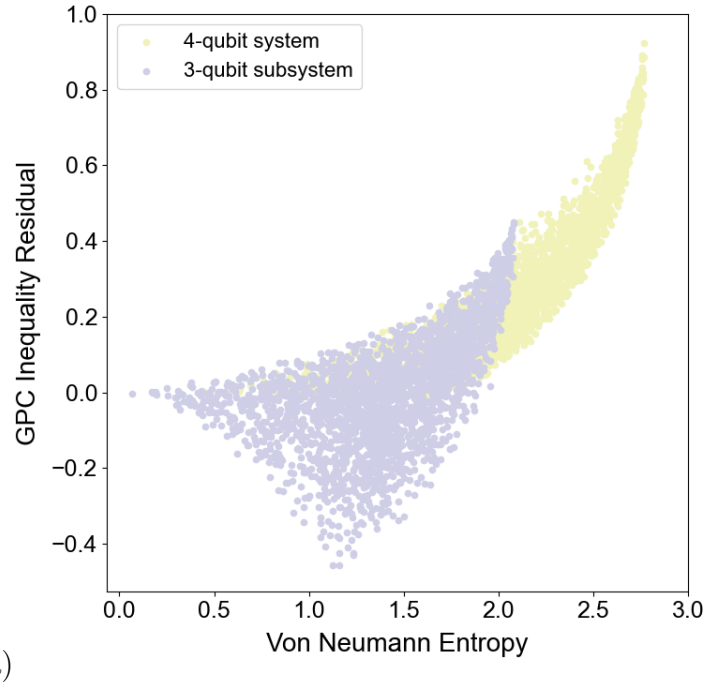


(a)

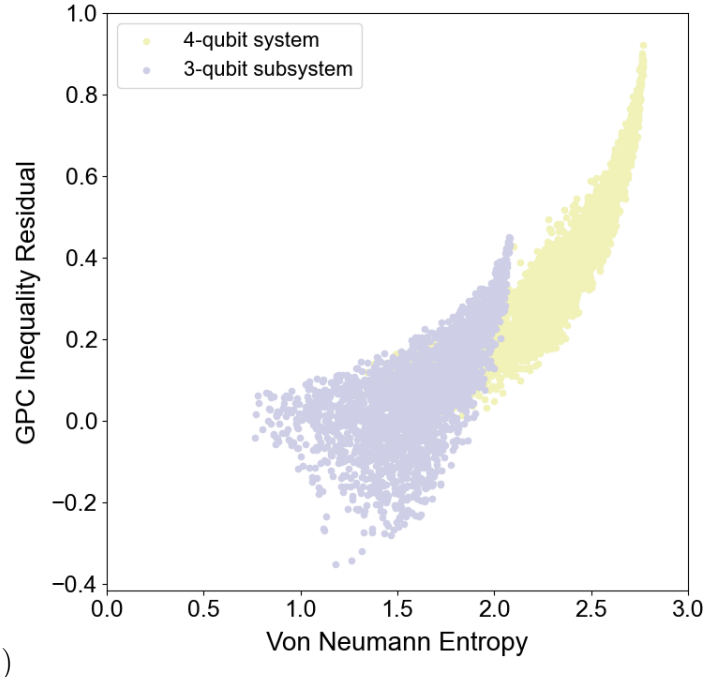


(b)

Figure A.23: Generalized Pauli constraints inequality residual plotted as a function of the von Neumann entropy for the occupation measurements collected on (a) simulator and (b) quantum computer for the four-qubit system.

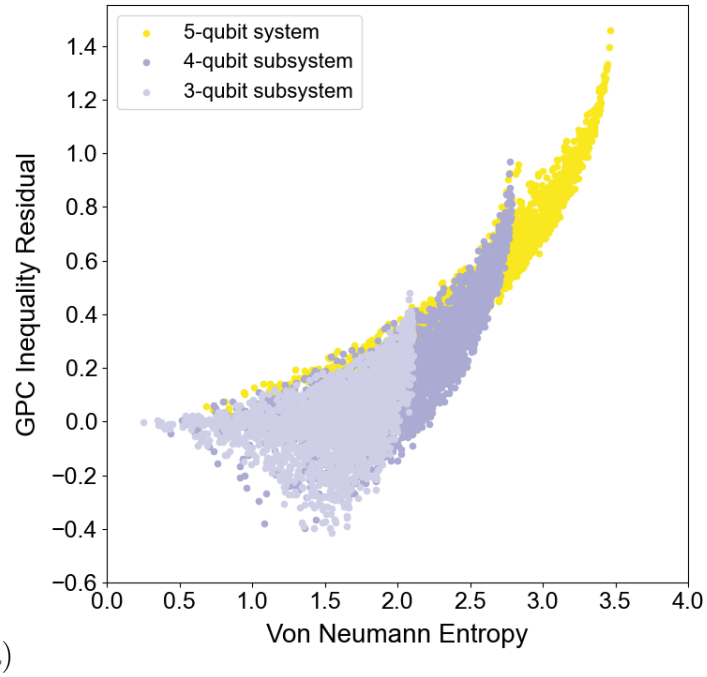


(a)

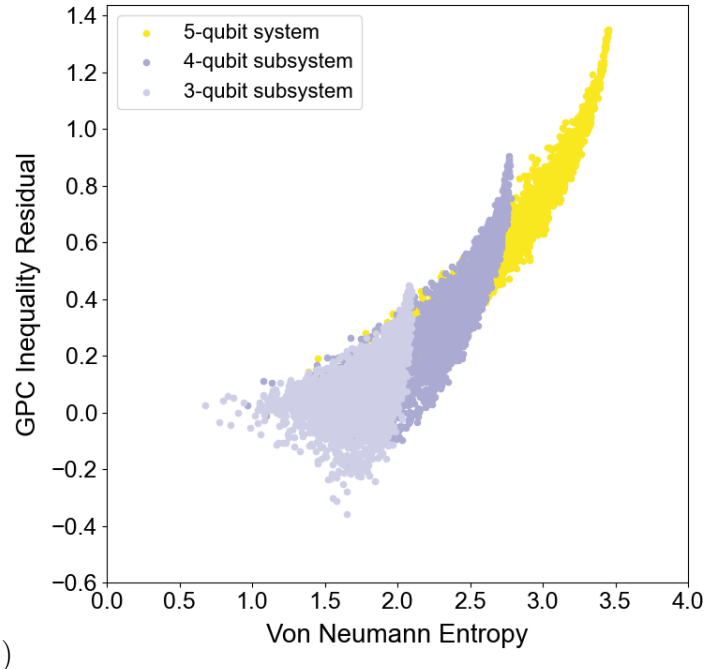


(b)

Figure A.24: Generalized Pauli constraints inequality residual plotted as a function of the von Neumann entropy for the occupation measurements collected on (a) simulator and (b) quantum computer for the five-qubit system.

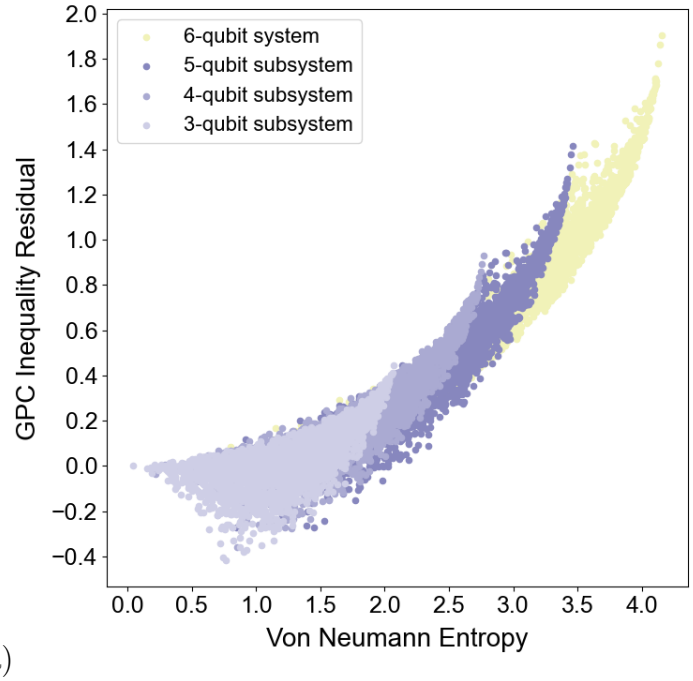


(a)

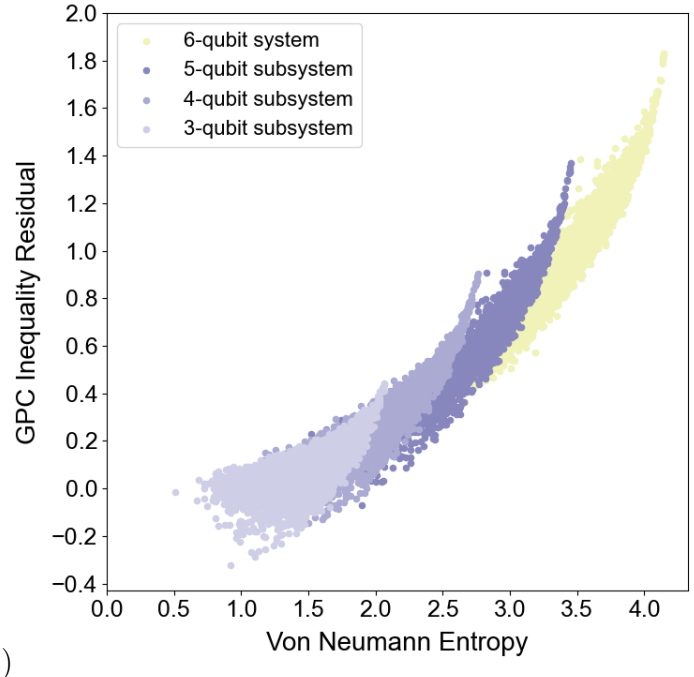


(b)

Figure A.25: Generalized Pauli constraints inequality residual plotted as a function of the von Neumann entropy for the occupation measurements collected on (a) simulator and (b) quantum computer for the six-qubit system.

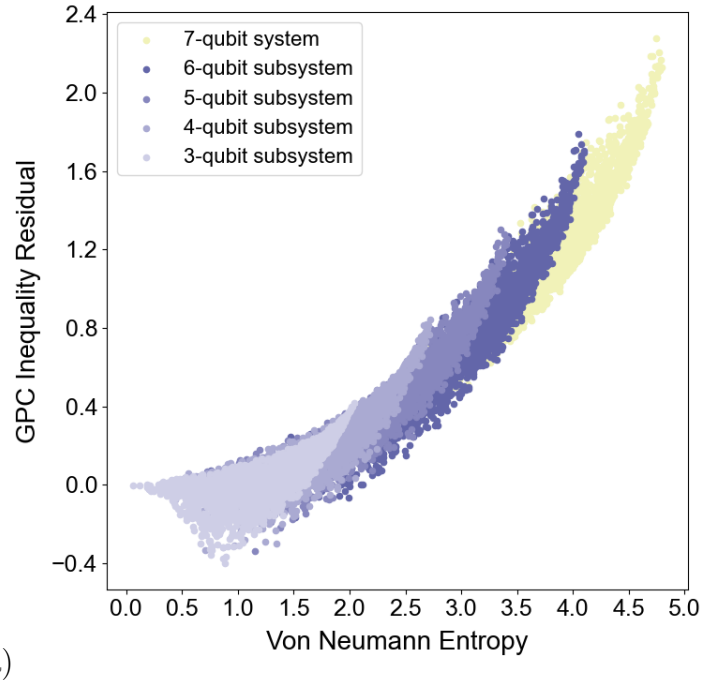


(a)

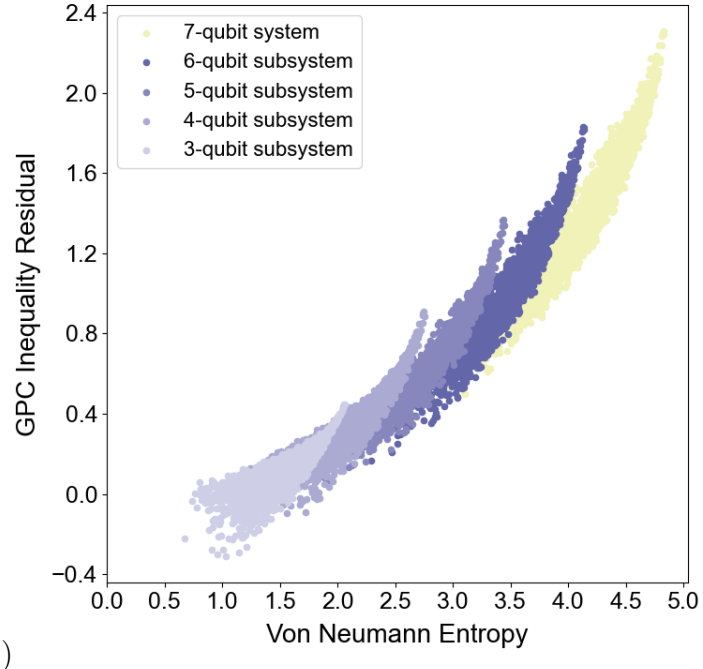


(b)

Figure A.26: Generalized Pauli constraints inequality residual plotted as a function of the von Neumann entropy for the occupation measurements collected on (a) simulator and (b) quantum computer for the seven-qubit system.

# APPENDIX B

# SUPPLEMENTAL MATERIAL: CHAPTER 4

This appendix provides the theoretical background, derivations, and computational details underlying the results presented in Chapter 4. It includes details of the system Hamiltonian and the derivation of the initial density matrix from experimental data, occupations of excited-state orbitals of the three-qubit subsystems considered in the main text, the Fenna-Matthews-Olson complex population dynamics in the excitonic basis, and the effect of dephasing on the Pauli polytope dynamics.

## B.1 Chemical Dynamics

The time evolution of the 8-exciton density matrix is governed by the Lindblad equation (Eq. 4.7), where D is the density matrix,

$$D = \sum_{k,l} \rho_l^k \left|\psi_k\right\rangle \left\langle\psi_l\right|, \tag{B.1}$$

$\rho_l^k$ are the elements of $D$ in the basis set of wavefunctions $\psi_k$, representing an excitation on the $k$th chromophore, and $\hat{L}$ is the Lindblad operator, which accounts for interactions of the 8 chromophores with the environment. The Lindblad operator is taken as a sum of three operators that describe dephasing, dissipation, and loss to the energy sink,

$$\hat{L}_{deph}(D) = \alpha \sum_k 2 \left\langle k\right| D \left|k\right\rangle \left|k\right\rangle \left\langle k\right| - \{\left|k\right\rangle \left\langle k\right|, D\} \tag{B.2}$$

$$\hat{L}_{diss}(D) = \beta \sum_k 2 \left\langle k\right| D \left|k\right\rangle \left|g\right\rangle \left\langle g\right| - \{\left|k\right\rangle \left\langle k\right|, D\} \tag{B.3}$$

$$\hat{L}_{sink}(D) = 2\gamma \left\langle 3\right| D \left|3\right\rangle \left|s\right\rangle \left\langle s\right| - \gamma\{\left|3\right\rangle \left\langle 3\right|, D\}. \tag{B.4}$$

The $|g\rangle$ denotes the state in which each of the chromophores is in its ground state, the $|k\rangle$ represents each excited state having a single excitation on one of the chromophores, the $|s\rangle$ denotes the energy sink, and $|3\rangle$ indicates the excited state of the third chromophore multiplied by the ground states of the other 7 chromophores.

The rate parameters in the Lindblad operators for dephasing ($\alpha$), dissipation ($\beta$), and the sink ($\gamma$) are chosen to be $1.52 \times 10^{-4}$ a.u. ($33.4\,\mathrm{cm}^{-1}$), $7.26 \times 10^{-5}$ a.u. ($15.9\,\mathrm{cm}^{-1}$), and $1.21 \times 10^{-8}$ a.u. ($0.00266\,\mathrm{cm}^{-1}$), respectively, which is consistent with the definitions employed in Ref. [203]. In this model, dissipation transfers energy from the chromophores into the environment and dephasing increases decoherence within the chromophore system. The "sink" captures the energy from the third chromophore that would be transferred to the reaction center. This feature was not present in the experimental setting, so this parameter is set to zero in the present model. Further analysis on the effect of dephasing on the presented results is described in the Section 1.5.5. The Lindbladian operators are Markovian in time and the addition of non-Markovian terms is not expected to qualitatively change the results of this work. More details on the model used in this work can be found in Refs. [119, 503, 504].

## B.2 Derivation of the Initial Density Matrix from Experimental Data

### *B.2.1 Construction of Excitonic Transition Dipoles*

To obtain realistic FMO site populations at the time of initialization, we calculated the 8×8 density matrix of the FMO complex right after coherent optical excitation of the ground state (Eq. B.5), as seen in the ultrafast two-dimensional electronic spectroscopy experiments reported in the study by Higgins et al. [189]. The optical excitations correspond to the $Q_y$ transition of each of the eight bacteriochlorophyll-a chromophores. The site transition dipole moments (TDMs) are, therefore, approximated to be the vectors joining two diago-

nal nitrogen atoms at the center of each of the chlorin moieties of the chromophores. The relevant nitrogen atom coordinates were obtained from the crystal structure of the FMO complex [505]. It is necessary to project these site TDMs in the exciton basis before incorporating the experimental conditions of Ref. [189], since time-domain spectroscopy resolves dynamics in excitonic energy levels, and not in the spatial sites. For this, we obtain the site-to-exciton unitary transformation matrix by diagonalizing the Hamiltonian in the site basis (Eq. B.6) with energies expressed in $\text{cm}^{-1}$ as in Ref. [202].

### *B.2.2 Optical Pulse Interactions With Excitonic Transition Dipole Moments*

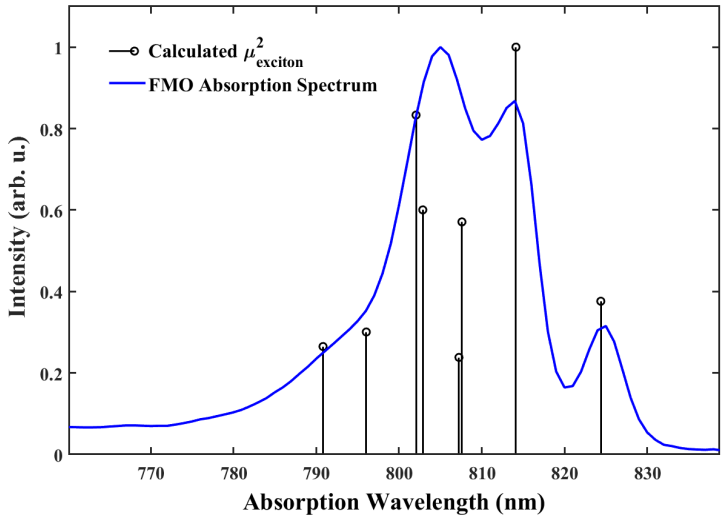


Figure B.1: The calculated excitonic transition dipole moment squared (black) is in good agreement with the linear absorption spectrum (blue).

An excited electronic population is created after the interaction with two optical pulses. In other words, the realistic qubits were initialized in the ultrafast spectroscopy experiment through the quantum system's interaction with two electromagnetic perturbations. We denote the $i$-th excitonic state as $|e_i\rangle$, $i = 1, 2, ..., 8$. After exciting with two optical pulses, carrying energies of all eight excitonic transitions, the ground state population, $|g\rangle\langle g|$, can be excited into an $i$-th excitonic population state, $|e_i\rangle\langle e_i|$, or into a a coherence between the $i$-th

and $j$-th states, $|e_i\rangle\langle e_j|$, considering all the unique double-sided Feynman pathways. Since each light-matter interaction entails a perturbation term of $-\mu \cdot E$, where $E$ is the electric field of the perturbative radiation, the elements of the density matrix, $\rho$, can be written as

$$\rho_{ij} = \mu_i \mu_j E_i E_j \cos\theta_{ij}$$

The perturbative electric field magnitudes at different energies ($E_i$) were obtained from the laser spectrum of the ultrafast spectroscopy experiment in Ref. [189]. $\theta_{ij}$ is the angle between the $i$-th and $j$-th TDM vectors. The term $\cos\theta_{ij}$ comes from the dipole orientational averaging that arises due to the TDMs being able to assume any configuration in three-dimensional space, since the experiments were conducted in the condensed phase [506]. $\mu_i^2$ is plotted in Fig. B.1 showing good agreement with the linear absorption spectrum of the $Q_y$ excitonic transitions of the FMO complex. The initialized density matrix is thus,

$$
D = \begin{pmatrix}
0.091685 & 0.002176199 & 0.066362109 & 0.028780581 & -0.10200601 & 0.078137346 & -0.027569155 & -0.005531506 \\
 & 0.322040254 & -0.174559029 & 0.101588016 & -0.111162506 & -0.031343411 & -0.032443933 & -0.01127451 \\
 & & 0.144900733 & -0.037710647 & -0.017513904 & 0.066606204 & -0.002317347 & 0.001564286 \\
 & & & 0.062229502 & -0.04568451 & 0.066426282 & -0.020214378 & -0.00182618 \\
 & & & & 0.169527856 & -0.02623231 & 0.03989638 & 0.01313672 \\
 & & & & & 0.196813726 & -0.024091979 & 0.004683091 \\
 & & & & & & 0.011546785 & 0.002511428 \\
 & & & & & & & 0.001255918
\end{pmatrix}
\tag{B.5}
$$

$$\hat{H}_{\text{site}} = \begin{pmatrix} 12461.0 & -87.0 & 4.2 & -5.2 & 5.5 & -14.0 & -6.1 & 21.0 \\ & 12486.0 & 28.0 & 6.9 & 1.5 & 8.7 & 4.5 & 4.2 \\ & & 12151.0 & -54.0 & -0.2 & -7.6 & 1.2 & 0.6 \\ & & & 12316.0 & -62.0 & -16.0 & -51.0 & -1.3 \\ & & & & 12458.0 & 60.0 & 1.7 & 3.3 \\ & & & & & 12614.0 & 29.0 & -7.9 \\ & & & & & & 12368.0 & -9.3 \\ & & & & & & & 12460.0 \end{pmatrix} \tag{B.6}$$

## B.3 Occupations of the Excited-State Orbitals Over Time

Three smallest eigenvalues for each of the qubits in the considered three-qubit subsystems over time are the populations of the excited-state orbitals during the relaxation process. The columns denote different chromophore subsystems.

Table B.1: Qubit 1 populations over time in the specified chromophore subsystems.

| Time (fs) | 123 | 124 | 125 | 126 | 127 | 128 |
|---|---|---|---|---|---|---|
| 0 | 0.322 | 0.322 | 0.322 | 0.322 | 0.322 | 0.322 |
| 250 | 0.228 | 0.228 | 0.228 | 0.228 | 0.228 | 0.228 |
| 500 | 0.181 | 0.181 | 0.181 | 0.181 | 0.181 | 0.181 |
| 750 | 0.179 | 0.179 | 0.179 | 0.179 | 0.179 | 0.179 |
| 1000 | 0.163 | 0.163 | 0.163 | 0.163 | 0.163 | 0.163 |
| 1250 | 0.153 | 0.153 | 0.153 | 0.153 | 0.153 | 0.153 |
| 1500 | 0.149 | 0.149 | 0.149 | 0.149 | 0.149 | 0.149 |
| 1750 | 0.145 | 0.145 | 0.145 | 0.145 | 0.145 | 0.145 |
| 2000 | 0.142 | 0.142 | 0.142 | 0.142 | 0.142 | 0.142 |
| 3000 | 0.134 | 0.134 | 0.134 | 0.134 | 0.134 | 0.134 |
| 4000 | 0.130 | 0.130 | 0.130 | 0.130 | 0.130 | 0.130 |
| 5000 | 0.128 | 0.128 | 0.128 | 0.128 | 0.128 | 0.128 |
| 10000 | 0.124 | 0.124 | 0.124 | 0.124 | 0.124 | 0.124 |

Table B.2: Qubit 2 populations over time in the specified chromophore subsystems.

| Time (fs) | 123 | 124 | 125 | 126 | 127 | 128 |
|---|---|---|---|---|---|---|
| 0 | 0.145 | 0.092 | 0.170 | 0.197 | 0.092 | 0.092 |
| 250 | 0.158 | 0.158 | 0.158 | 0.158 | 0.158 | 0.158 |
| 500 | 0.175 | 0.175 | 0.175 | 0.175 | 0.175 | 0.175 |
| 750 | 0.163 | 0.163 | 0.163 | 0.163 | 0.163 | 0.163 |
| 1000 | 0.156 | 0.156 | 0.156 | 0.156 | 0.156 | 0.156 |
| 1250 | 0.153 | 0.153 | 0.153 | 0.153 | 0.153 | 0.153 |
| 1500 | 0.147 | 0.147 | 0.147 | 0.147 | 0.147 | 0.147 |
| 1750 | 0.144 | 0.144 | 0.144 | 0.144 | 0.144 | 0.144 |
| 2000 | 0.141 | 0.141 | 0.141 | 0.141 | 0.141 | 0.141 |
| 3000 | 0.134 | 0.134 | 0.134 | 0.134 | 0.134 | 0.134 |
| 4000 | 0.130 | 0.130 | 0.130 | 0.130 | 0.130 | 0.130 |
| 5000 | 0.127 | 0.127 | 0.127 | 0.127 | 0.127 | 0.127 |
| 10000 | 0.124 | 0.124 | 0.124 | 0.124 | 0.124 | 0.124 |

Table B.3: Qubit 3 populations over time in the specified chromophore subsystems.

| Time (fs) | 123 | 124 | 125 | 126 | 127 | 128 |
|---|---|---|---|---|---|---|
| 0 | 0.092 | 0.062 | 0.092 | 0.092 | 0.012 | 0.001 |
| 250 | 0.129 | 0.089 | 0.133 | 0.132 | 0.070 | 0.062 |
| 500 | 0.115 | 0.101 | 0.118 | 0.137 | 0.089 | 0.083 |
| 750 | 0.116 | 0.105 | 0.116 | 0.132 | 0.093 | 0.096 |
| 1000 | 0.114 | 0.108 | 0.115 | 0.126 | 0.104 | 0.114 |
| 1250 | 0.114 | 0.111 | 0.117 | 0.123 | 0.108 | 0.121 |
| 1500 | 0.114 | 0.113 | 0.117 | 0.122 | 0.111 | 0.125 |
| 1750 | 0.115 | 0.114 | 0.119 | 0.122 | 0.113 | 0.127 |
| 2000 | 0.115 | 0.116 | 0.119 | 0.122 | 0.115 | 0.128 |
| 3000 | 0.118 | 0.119 | 0.121 | 0.122 | 0.119 | 0.129 |
| 4000 | 0.120 | 0.121 | 0.123 | 0.123 | 0.121 | 0.128 |
| 5000 | 0.122 | 0.122 | 0.123 | 0.123 | 0.122 | 0.126 |
| 10000 | 0.124 | 0.124 | 0.124 | 0.124 | 0.124 | 0.124 |

## B.4 Fenna-Matthews-Olson Complex Population Dynamics

To obtain the exciton populations, the diagonal elements of the density matrix, $D$, are constructed from orthogonal transformation operators as follows,

$$p_i = V_i^T D_{site} V_i,$$

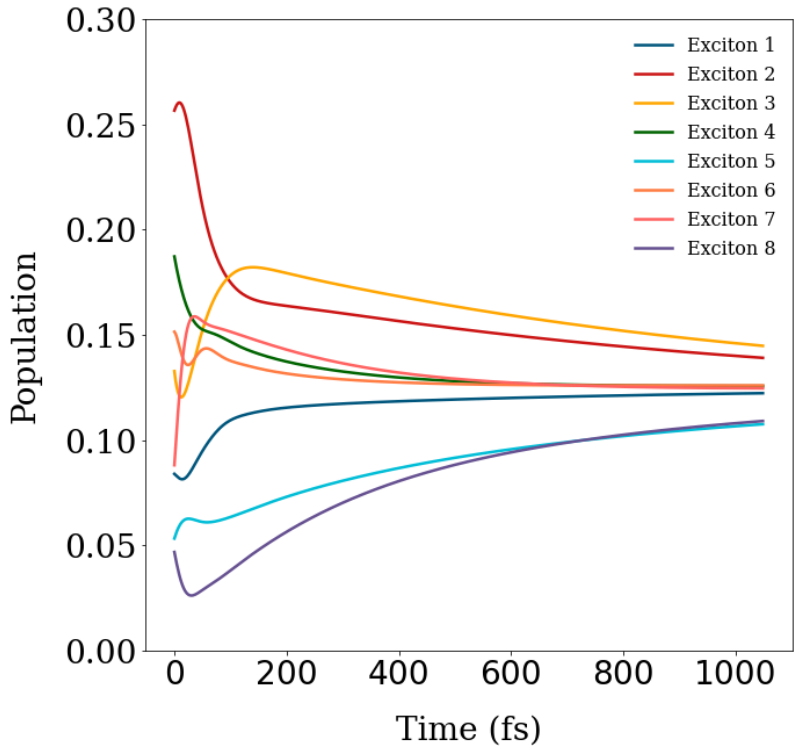


Figure B.2: Exciton populations of the FMO complex for the first 1 ps of the energy transfer process.

where $p_i$ is the population of $i^{th}$ exciton and $V_i$ is the $i^{th}$ eigenvector of the defined Hamiltonian, $\hat{H}$. The Fenna-Matthews-Olson (FMO) complex population dynamics, in the exciton basis, for the first 1 ps of the energy transfer process is shown in Fig. B.2. Note that $\hat{H}$ and $D_{site}$ are not diagonal in this case; therefore, the initial conditions in Fig. B.2 and Fig. 4.2 differ slightly.

## B.5 The Effect of Dephasing on the Pauli Polytope Dynamics

In Figs. B.2 and B.3, the dephasing parameter is increased to 100.2 cm$^{-1}$, which is three times greater than the parameter consistent with definitions in Ref. [203] used in the main text. This was done to, first, obtain a smooth exciton dynamics, since oscillations are dephasing-driven, and second, to illustrate that our main conclusions hold even for the case of high dephasing. In Fig. B.3, the time evolution produces an expanded set of 1-RDMs in

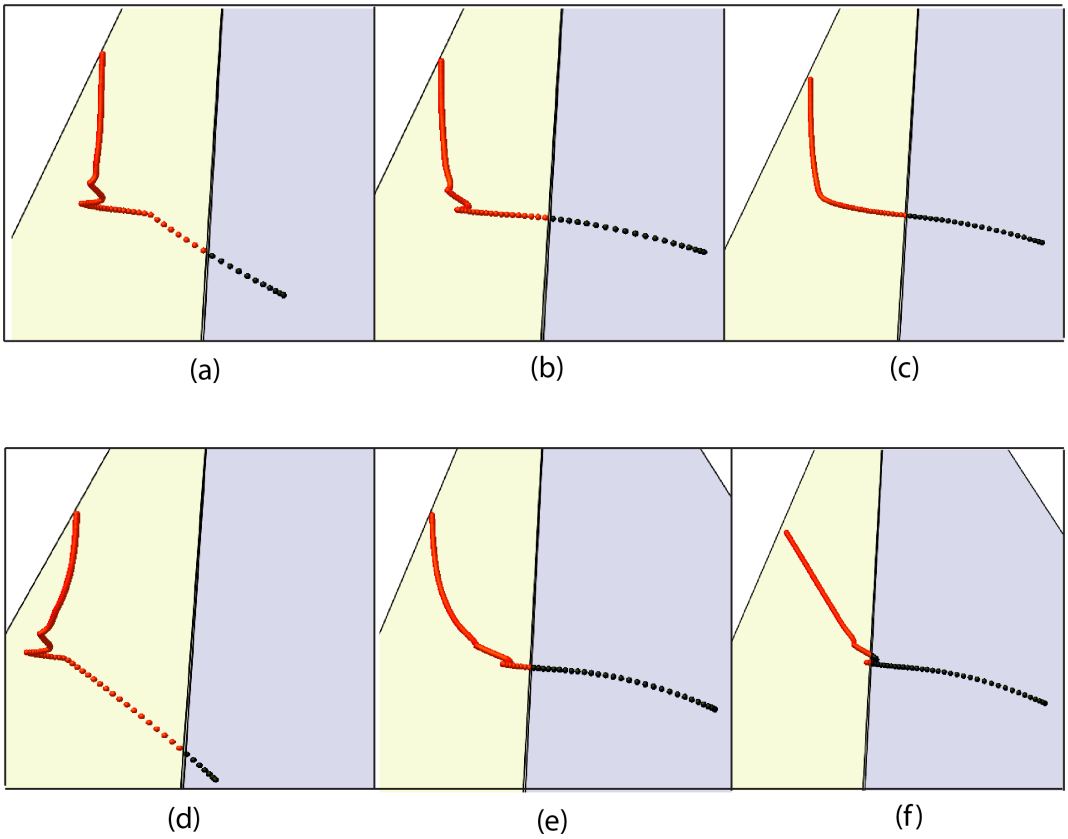


Figure B.3: Temporal trajectories of different 3-qubit subsystems of the FMO complex for the first 2 ps of the energy transfer process from the experimentally derived density matrix, with the dephasing parameter set to 100.2 $cm^{-1}$. The figures differ in the choice of one of the three qubits/chromophores in the subsystem: (a) 123, (b) 124, (c) 125, (d) 126, (e) 127, (f) 128 where, for example, 123 denotes chromophores 1, 2, and 3.

each scenario, violating the GPCs initially, and then converges to the classical limit at longer times, as is the case with lower dephasing character. Varying only one qubit shows enhanced measurements of the relaxation processes of the remaining qubits in the system even in the high presence of dephasing, demonstrating robustness of our qualitative conclusions to the choice of simulation parameters used in the main text.

# APPENDIX C

# SUPPLEMENTAL MATERIAL: CHAPTER 6

This appendix contains additional numerical data for longer hydrogen chains. These results extend the analysis presented in Chapter 6 and provide further support for the observed trends and conclusions.

## C.1 Additional Data

Table C.1: The Euclidean norm of the absolute error of the 2-RDM computed via sv2RDM and FCI with DQG conditions and the total energy (Hartree) for $H_5$ at 1.00 Å separation of H atoms, as a function of the number of shadows. The FCI energy is -2.65451697 Hartree and the v2RDM energy is -2.66447993 Hartree. The trace of the 2-RDM is set to one.

| Shadow number | sv2RDM energy (Hartree) | Euclidean norm |
|---|---|---|
| 1 | -2.66290104 | 0.04112581 |
| 3 | -2.66041116 | 0.02141652 |
| 5 | -2.65724632 | 0.00748939 |
| 7 | -2.65599787 | 0.00487635 |
| 9 | -2.65570427 | 0.00295221 |
| 11 | -2.65535044 | 0.00148801 |
| 13 | -2.65486205 | 0.00136300 |
| 15 | -2.65466665 | 0.00065789 |
| 17 | -2.65451697 | 0.00019911 |

Table C.2: The Euclidean norm of the absolute error of the 2-RDM computed via sv2RDM and FCI with DQG conditions and the total energy (Hartree) for $H_6$ at 1.00 Å separation of H atoms, as a function of the number of shadows. The FCI energy is -3.23606628 Hartree and the v2RDM energy is -3.24407931 Hartree. The trace of the 2-RDM is set to one.

| Shadow number | sv2RDM energy (Hartree) | Euclidean norm |
|---|---|---|
| 1 | -3.24311939 | 0.03707779 |
| 3 | -3.24209910 | 0.02764575 |
| 5 | -3.2410106 | 0.02265639 |
| 7 | -3.23959706 | 0.00588822 |
| 9 | -3.23853874 | 0.00342319 |
| 11 | -3.23801925 | 0.00220432 |
| 13 | -3.23711953 | 0.00197898 |
| 15 | -3.23695956 | 0.00155529 |
| 17 | -3.23698907 | 0.00142037 |
| 19 | -3.23654421 | 0.00108701 |
| 21 | -3.23657486 | 0.00103899 |
| 23 | -3.23621790 | 0.00098648 |
| 25 | -3.23608306 | 0.00102677 |
| 27 | -3.23606628 | 0.00053637 |

Table C.3: The Euclidean norm of the absolute error of the 2-RDM computed via sv2RDM and FCI with DQG conditions and the total energy (Hartree) for $H_7$ at 1.00 Å separation of H atoms, as a function of the number of shadows. The FCI energy is -3.73548753 Hartree and the v2RDM energy is -3.75371421 Hartree. The trace of the 2-RDM is set to one.

| Shadow number | sv2RDM energy (Hartree) | Euclidean norm |
|---|---|---|
| 1 | -3.75281205 | 0.05182792 |
| 3 | -3.75091323 | 0.03994524 |
| 5 | -3.74936700 | 0.03327169 |
| 7 | -3.74692069 | 0.03388806 |
| 9 | -3.74567433 | 0.03626628 |
| 11 | -3.74287558 | 0.01733036 |
| 13 | -3.74238856 | 0.01180265 |
| 15 | -3.74049734 | 0.00635232 |
| 17 | -3.73878198 | 0.00321046 |
| 19 | -3.73833913 | 0.00390605 |
| 21 | -3.73805165 | 0.00377233 |
| 23 | -3.73763877 | 0.00242160 |
| 25 | -3.73758537 | 0.00169237 |
| 27 | -3.73696228 | 0.00179318 |
| 29 | -3.73657142 | 0.00229616 |
| 31 | -3.73651338 | 0.00215099 |
| 33 | -3.73608461 | 0.00194354 |
| 35 | -3.73589811 | 0.00278908 |
| 37 | -3.73552761 | 0.00094593 |
| 39 | -3.73548753 | 0.00087722 |

Table C.4: The Euclidean norm of the absolute error of the 2-RDM computed via sv2RDM and FCI with DQG conditions and the total energy (Hartree) for $H_8$ at 1.00 Å separation of H atoms, as a function of the number of shadows. The FCI energy is -4.30757160 Hartree and the v2RDM energy is -4.32291185 Hartree. The trace of the 2-RDM is set to one.

| Shadow number | sv2RDM energy (Hartree) | Euclidean norm |
|---|---|---|
| 1 | -4.32215060 | 0.04800580 |
| 3 | -4.32091467 | 0.03894779 |
| 5 | -4.32005110 | 0.03874101 |
| 7 | -4.31909665 | 0.03042557 |
| 9 | -4.31794120 | 0.02706046 |
| 11 | -4.31727535 | 0.01668232 |
| 13 | -4.31613371 | 0.01631687 |
| 15 | -4.31452050 | 0.01425402 |
| 17 | -4.31392850 | 0.00914502 |
| 19 | -4.31370491 | 0.00545305 |
| 21 | -4.31201186 | 0.00558218 |
| 23 | -4.31194606 | 0.00820932 |
| 25 | -4.31079046 | 0.00416006 |
| 27 | -4.30974452 | 0.00243050 |
| 29 | -4.30956950 | 0.00275149 |
| 31 | -4.30946945 | 0.00181368 |
| 33 | -4.30945765 | 0.00233200 |
| 35 | -4.30934339 | 0.00164151 |
| 37 | -4.30913381 | 0.07192697 |
| 39 | -4.30892749 | 0.00140248 |
| 41 | -4.30869830 | 0.00134430 |
| 43 | -4.30842589 | 0.00129142 |
| 45 | -4.30820226 | 0.00156066 |
| 47 | -4.30794389 | 0.00117327 |
| 49 | -4.30758121 | 0.00088410 |
| 51 | -4.30757166 | 0.00063863 |
| 53 | -4.30757159 | 0.00064255 |

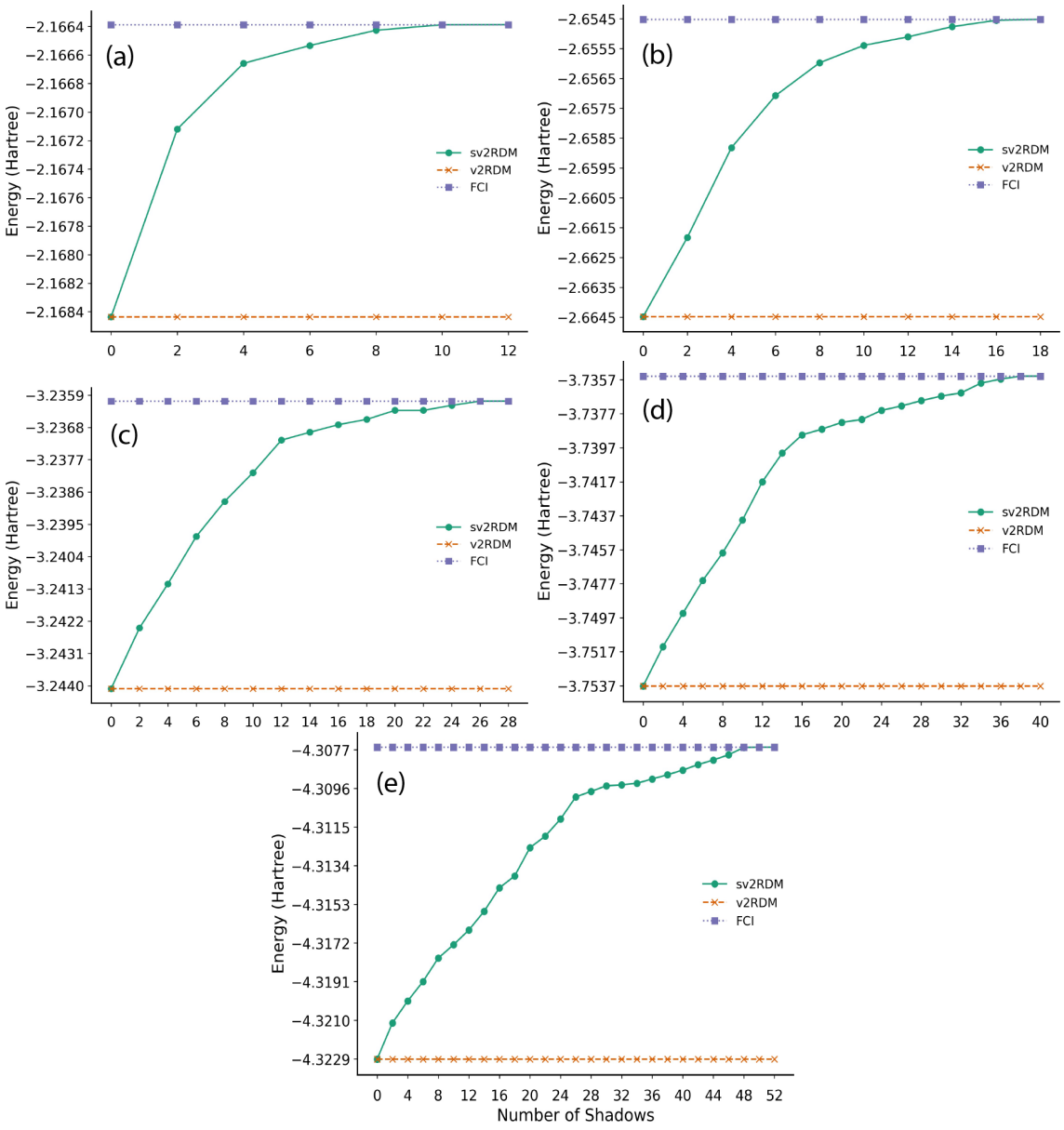


Figure C.1: Total ground state energy (Hartree) of (a) $H_4$, (b) $H_5$, (c) $H_6$, (d) $H_7$, and (e) $H_8$ with equally spaced H atoms, as a function of the number of shadows. By default, v2RDM and sv2RDM include D, Q, and G conditions. The sv2RDM energy converges *exactly* to the FCI energy in the noiseless environment.

# APPENDIX D

# SUPPLEMENTAL MATERIAL: CHAPTER 7

This appendix describes the generation of Haar random unitary matrices in the shadow tomography protocol and provides Cartesian coordinates of optimized geometries of systems along the *gauche*-1,3-butadiene to bicyclobutane reaction pathway analyzed in Chapter 7.

## D.1 Haar Random Unitary Matrices

To generate a random unitary matrix, we first sample the entries from a standard normal distribution with a mean of 0 and variance of 1. We then use the Gram-Schmidt decomposition to orthonormalize the columns of this random matrix. In random matrix theory, a matrix with independent identically distributed Gaussian entries whose columns have been orthonormalized via the Gram-Schmidt process is known to be Haar-distributed [507–509].

## D.2 Cartesian Coordinates of $S_0$ Optimized Geometries

Table D.1: Optimized *gauche*-1,3-butadiene (GBUT) geometry

| Atom | X | Y | Z |
|---|---|---|---|
| C | 1.485202 | 0.410778 | 0.591518 |
| C | 0.784142 | -0.421845 | -0.227685 |
| C | -0.657797 | -0.257762 | -0.608085 |
| C | -1.624724 | 0.293301 | 0.177535 |
| H | 1.037681 | 1.295652 | 1.026702 |
| H | 2.523236 | 0.212914 | 0.824857 |
| H | 1.297233 | -1.270069 | -0.668612 |
| H | -0.935661 | -0.633869 | -1.587117 |
| H | -1.415202 | 0.647289 | 1.179256 |
| H | -2.642322 | 0.384764 | -0.179176 |

Table D.2: Optimized bicyclobutane (BIBUT) geometry

| Atom | X | Y | Z |
|---|---|---|---|
| C | 1.048735 | 0.520858 | 0.237587 |
| C | 0.249728 | -0.766669 | 0.093647 |
| C | -0.181733 | 0.492278 | -0.657964 |
| C | -1.143071 | -0.190138 | 0.304849 |
| H | 2.010714 | 0.552059 | -0.262346 |
| H | 1.007192 | 1.067267 | 1.176613 |
| H | 0.543803 | -1.712983 | -0.326078 |
| H | -0.258061 | 0.626844 | -1.722964 |
| H | -1.377868 | 0.293564 | 1.249819 |
| H | -1.966416 | -0.738091 | -0.140291 |

Table D.3: Optimized disrotatory transition state (TSD) geometry

| Atom | X | Y | Z |
|---|---|---|---|
| C | 1.586439 | -0.156899 | -0.199816 |
| C | -0.820739 | 0.803153 | -0.277155 |
| C | 0.251491 | 0.051542 | 0.475874 |
| C | -1.003710 | -0.678988 | -0.096540 |
| H | 2.486131 | 0.194913 | 0.287410 |
| H | 1.611181 | -0.276946 | -1.275325 |
| H | -1.435076 | 1.636679 | 0.028909 |
| H | 0.283392 | 0.176973 | 1.552527 |
| H | -1.748428 | -1.023159 | 0.612070 |
| H | -0.852439 | -1.324169 | -0.954433 |

Table D.4: Optimized conical intersection (CI) geometry

| Atom | X | Y | Z |
|---|---|---|---|
| C | -0.302985 | -0.137479 | -0.097989 |
| H | 0.285497 | -0.391586 | 0.773003 |
| H | 0.299503 | 0.263434 | -0.899354 |
| C | -1.412927 | -1.008868 | -0.477173 |
| H | -1.82046 | -1.730136 | 0.212719 |
| C | -1.576138 | 0.604010 | 0.183379 |
| H | -1.943193 | 0.596798 | 1.193331 |
| C | -2.152692 | 1.514365 | -0.734461 |
| H | -1.774451 | 1.595952 | -1.735504 |
| H | -3.060043 | 2.036545 | -0.498178 |

# APPENDIX E

# SUPPLEMENTAL MATERIAL: CHAPTER 8

This appendix contains details on the numerical simulation performed in Chapter 8, a derivation of the Fermionic Classical Shadows method, quantum hardware details, and supporting data for hydrogen chains.

## E.1 Numerical Simulation Details

### *E.1.1 Shadow Variational Two-Particle Reduced Density Matrix (sv2RDM) Method*

To simulate measurement uncertainty, we generate noisy two-particle reduced density matrices (2-RDMs) by adding element-wise Gaussian perturbations to the full configuration interaction (FCI) 2-RDMs, where each noise term models the statistical fluctuations arising from finite-shot quantum measurements. Specifically, the variance of the noise for each matrix element is taken as

$$\sigma = \sqrt{\frac{p(1-p)}{N_{shots}}}. \tag{E.1}$$

This expression follows from the binomial variance of repeated independent measurements (Bernoulli trials), where the success probability $p$ reflects the likelihood of finding electrons in particular spin orbitals. In quantum systems, such probabilities originate from the one-particle reduced density matrix (1-RDM), whose eigenvalues (natural orbital occupations) encode the marginal probabilities of electron occupation in each orbital. In Slater determinants (mean-field wavefunctions), these occupations are exactly 0 or 1. However, in correlated many-electron states, the occupations lie in the interval [0,1], introducing measurement uncertainty when estimating these probabilities from finite samples. Repeated projective measurements of such orbitals yield sample frequencies with binomial statistics,

which, in the large-shot limit, converge to Gaussian distributions under the Central Limit Theorem. By modeling each matrix element of the 2-RDM as an effective outcome derived from such orbital occupations, we apply Gaussian-distributed noise consistent with these binomial variances.

For each measurement setting $i$, the spin-free 1- and 2-RDMs were obtained as described above and subsequently spin-adapted to yield the singlet and triplet components. Corresponding antisymmetric and symmetric unitary transformations were used to generate transformed operator bases. To generate a random unitary matrix, we first sample the entries from a standard normal distribution with a mean of 0 and variance of 1. We then use the Gram-Schmidt decomposition to orthonormalize the columns of this random matrix. In random matrix theory, a matrix with independent identically distributed Gaussian entries whose columns have been orthonormalized via the Gram-Schmidt process is known to be Haar-distributed [507–509]. For each setting, linear constraints were accumulated across all unitaries to define the global feasible shadow constraint set. The correlated 2-RDM was obtained by solving the semidefinite program given in Eq. 9 in the manuscript with $w = 1$, using the Maple Quantum Chemistry Package. The recovered energy was computed as

$$E = E_{\text{nuc}} + E_{\text{elec}} - \sum_i w_i \text{Tr}(\mathbf{E}_i), \tag{E.2}$$

where $E_{\text{nuc}}$ is the nuclear energy, $E_{\text{elec}}$ is the electronic energy, $\mathbf{E}_i$ is a positive semidefinite slack error matrix, and $w_i$ is a regularization parameter introduced in Eq. 8 in the manuscript. Final energies were averaged across all iterations.

### *E.1.2 Fermionic Classical Shadows (FCS)*

We briefly outline the derivation of the particle number-conserving Fermionic Classical Shadows (FCS) protocol as presented in Ref. [236].

A single-particle basis rotation acting on the $\eta$-particle sector of Fock space is defined as

$$U_\eta(u) \doteq e^{\sum_{p,q=1}^{n} [\ln(u)]_{pq} a_p^\dagger a_q}, \tag{E.3}$$

where $u \in \mathbb{C}^{n\times n}$ is Haar-random. Measuring in this rotated basis yields projectors $\Pi_z = |\vec{z}\rangle\langle\vec{z}|$ sampled with probability $\langle\psi|U_\eta^\dagger(u)\Pi_z U_\eta(u)|\psi\rangle$. The corresponding shadow estimator is

$$\hat{\rho}_{u,\vec{z}} \doteq \mathcal{M}_{\mathcal{U}}^{-1}\Big[U_\eta^\dagger(u)|\vec{z}\rangle\langle\vec{z}|U_\eta(u)\Big]. \tag{E.4}$$

For each occupation vector $|\vec{z}\rangle$, we introduce a permutation unitary $U(v_z)$ such that $U(v_z)|[\eta]\rangle = |\vec{z}\rangle$, where $|[\eta]\rangle$ is a vector representing the occupation vector in the permuted basis, allowing us to express

$$\hat{\rho}_{u,\vec{z}} = \mathcal{M}_{\mathcal{U}}^{-1}\Big[U_\eta^\dagger(u)U_\eta(v_z)|[\eta]\rangle\langle[\eta]|U_\eta^\dagger(v_z)U_\eta(u)\Big]. \tag{E.5}$$

Using the homomorphism property of fermionic rotations, $U_\eta^\dagger(u)U_\eta(v_z) = U_\eta^\dagger(v_z^\dagger u)$, this simplifies to

$$\hat{\rho}_{u,\vec{z}} = U_\eta^\dagger(v_z^\dagger u)\,\mathcal{M}_{\mathcal{U}}^{-1}[|[\eta]\rangle\langle[\eta]|]\,U_\eta(v_z^\dagger u). \tag{E.6}$$

To obtain reduced quantities, consider the $k$-body reduced density matrix (k-RDM)

$$D = \sum_{\vec{p},\vec{q}\in\mathcal{S}_{n,k}} d_{\vec{p},\vec{q}} D_{\vec{q}}^{\vec{p}}, \quad D_{\vec{q}}^{\vec{p}} \doteq a_{p_1}^\dagger \cdots a_{p_k}^\dagger a_{q_k}\cdots a_{q_1}. \tag{E.7}$$

Expectation values can then be evaluated as

$$\langle D_{\vec{q}}^{\vec{p}}\rangle = \mathrm{Tr}\Big(D_{\vec{q}}^{\vec{p}} U_\eta^\dagger(v_z^\dagger u)\mathcal{M}_{\mathcal{U}}^{-1}[|[\eta]\rangle\langle[\eta]|]\,U_\eta(v_z^\dagger u)\Big), \tag{E.8}$$

which can be efficiently expressed in the $k$-particle subspace as

$$\langle \hat{D}_{\vec{q}}^{\vec{p}}\rangle = \langle\vec{q}|U_k^\dagger(v_z^\dagger u)E_{\eta,k}U_k(v_z^\dagger u)|\vec{p}\rangle, \tag{E.9}$$

where

$$E_{\eta,k} = \sum_{\vec{r}\in\mathcal{S}_{n,k}} |\vec{r}\rangle\langle\vec{r}| \, \frac{\binom{\eta-s'}{k-s'}\binom{n-\eta+s'}{s'}}{(-1)^{k+s'}\binom{k}{s'}}, \qquad s' = |\vec{r}\cap[\eta]|, \tag{E.10}$$

with average variance

$$\mathcal{V} \leq \binom{\eta}{k}\left(1-\frac{\eta-k}{n}\right)^k \frac{1+n}{1+n-k}. \tag{E.11}$$

Each configuration $|\vec{r}\rangle$ corresponds to a term in the $k$-RDM, providing a compact and computationally tractable formulation of fermionic shadow estimation.

In practice, the unitary $U_\eta(u)$ defined in Eq. E.3 cannot be evaluated explicitly for large systems on a classical computer, as it acts on a Hilbert space of dimension $\binom{n}{\eta}$, which scales exponentially with $\eta$. Instead, we compute the generator

$$K = \sum_{p,q=1}^{n} [\ln(u)]_{pq} a_p^\dagger a_q, \tag{E.12}$$

and implement the transformation via a Pauli-sum evolution $e^K|\psi\rangle$. This approach enables the efficient evaluation of $U_\eta(u)$ within variational or simulation frameworks such as Jordan–Wigner representations.

For a fixed, small $k$, $U_k(u)$ is of manageable size, allowing classical evaluation. From Eq. (20) of Ref. [236],

$$U_\eta(u)|\vec{z}\rangle = \bigwedge_{k=1}^{\eta} |u_{z_k}\rangle = \sum_{\vec{p}\in\mathcal{S}_{n,\eta}} \det\left[u_{\vec{p}\vec{z}}\right] |\vec{p}\rangle, \tag{E.13}$$

which leads to

$$[U_k(u)]_{\vec{p},\vec{q}} = \det\left(u_{\vec{p},\vec{q}}\right), \tag{E.14}$$

where $u_{\vec{p},\vec{q}}$ denotes the submatrix of $u$ formed by the corresponding indices. The permutation matrix $U(v_z)$ satisfying $U(v_z)|[\eta]\rangle = |\vec{z}\rangle$ can be computed classically. In the single-particle case (1-spin-orbital basis), this reduces to $U(v_z) = v_z$. The matrix product $v_z^\dagger u$ is computed

directly, forming the argument for subsequent $U_\eta$ and $U_k$ constructions. The operator

$$E_{\eta,k} \doteq \sum_{\vec{r}\in\mathcal{S}_{n,k}} |\vec{r}\rangle\langle\vec{r}| \, \frac{\binom{\eta-s'}{k-s'}\binom{n-\eta+s'}{s'}}{(-1)^{k+s'}\binom{k}{s'}}, \qquad s' = |\vec{r}\cap[\eta]|\,, \tag{E.15}$$

is diagonal in the computational basis and can be evaluated efficiently using classical post-processing.

## E.2 Quantum Hardware Details

All quantum circuits used for data collection were implemented using the Qiskit [146] package and the ffsim [424] library on IBM's 156-qubit superconducting processor ibm_fez.

### *E.2.1 $H_4$ Rectangle-Square-Rectangle Transition*

The data collection details here correspond to Fig. 5 in the manuscript. The compiled circuits consisted primarily of single-qubit $\mathrm{R}_Z(\theta)$ and $\mathrm{S}_X$ rotations, interleaved with two-qubit controlled-$Z$ entangling gates arranged according to the molecular connectivity pattern. The action was confined to nine device qubits, $(q_{123}, q_{124}, q_{136}, q_{143}, q_{144}, q_{145}, q_{146}, q_{147}, q_{148})$, with projective measurements on eight of these ($q_{144}$ idle at readout). The effective circuit depth was $d_{\mathrm{DAG}} \approx 90$ layers. 20 iterations of 16 different unitary bases, each with 10,000 shots, were used.

### *E.2.2 Linear Hydrogen Chains*

The data collection details here correspond to Table II in the manuscript. The compiled circuits consisted primarily of single-qubit $\mathrm{R}_Z(\theta)$ and $\mathrm{S}_X$ rotations, interleaved with two-qubit controlled-$Z$ entangling gates. For $\mathrm{H}_4$, the action was confined to nine device qubits, $(q_{123}, q_{124}, q_{136}, q_{137}, q_{143}, q_{144}, q_{145}, q_{146}, q_{147})$, with projective measurements on eight of

these ($q_{144}$ idle at readout). The effective circuit depth was $d_{\mathrm{DAG}} \approx 100$ layers. 16 different unitary bases, each with 10,000 shots, were used.

For $H_6$, the action was confined to 14 device qubits,
$(q_{122}, q_{123}, q_{124}, q_{125}, q_{126}, q_{127}, q_{136}, q_{137}, q_{142}, q_{143}, q_{144}, q_{145}, q_{146}, q_{147})$, with projective measurements on 12 of these ($q_{136}, q_{137}$ idle at readout). The effective circuit depth was $d_{\mathrm{DAG}} \approx 160$ layers. 36 different unitary bases, each with 10,000 shots, were used.

For $H_8$, the action was confined to 18 device qubits,
$(q_{120}, q_{121}, q_{122}, q_{123}, q_{124}, q_{125}, q_{126}, q_{127}, q_{136}, q_{137}, q_{140}, q_{141}, q_{142}, q_{143}, q_{144}, q_{145}, q_{146}, q_{147})$, with projective measurements on 16 of these ($q_{136}, q_{137}$ idle at readout). The effective circuit depth was $d_{\mathrm{DAG}} \approx 200$ layers. 160 different unitary bases, each with 10,000 shots, were used.

For $H_{10}$, the action was confined to 23 device qubits,
$(q_{97}, q_{105}, q_{106}, q_{107}, q_{108}, q_{109}, q_{110}, q_{117}, q_{118}, q_{123}, q_{124}, q_{125}, q_{126}, q_{127}, q_{128}, q_{129}, q_{136}, q_{137}, q_{143}, q_{144}, q_{145}, q_{146}, q_{147})$, with projective measurements on 20 of these ($q_{108}, q_{126}, q_{144}$ idle at readout). The effective circuit depth was $d_{\mathrm{DAG}} \approx 250$ layers. 300 different unitary bases, each with 10,000 shots, were used.

### *E.2.3 2-RDM Reconstruction and Post-Processing*

Upon measurement, the obtained bitstrings were post-processed to reconstruct RDMs used in the subsequent semidefinite programming (SDP) procedure. Each measurement outcome was represented as a 64-bit integer, which was unpacked into a binary vector $\mathbf{b} \in \{0,1\}^{2n_{\mathrm{spatial}}}$ corresponding to occupations of the spin orbitals $\{i\alpha, i\beta\}$. Spin occupations were then summed to obtain spatial occupations. From these data, the diagonal elements of the spatial 1- and 2-RDMs were computed as statistical averages over all measurement shots. The diagonal elements of the 1-RDM were given by

$$ {}^1D_i^i = \langle n_i \rangle, \tag{E.16}$$

representing the mean occupation of each spatial orbital. The diagonal block of the spatial 2-RDM was obtained directly from pairwise orbital co-occupations,

$$ {}^2D^{ij}_{ij} = \langle n_i n_j \rangle, \tag{E.17}$$

which captures the joint probability that orbitals $i$ and $j$ are simultaneously occupied across all measured bitstrings. These averaged RDM elements were then assembled into matrix and tensor forms and expressed in Maple format for compatibility with subsequent SDP reconstruction and energy evaluation routines in Maple's Quantum Chemistry Package [422, 423].

Each random unitary basis for each point along the potential energy curve was subsequently validated by comparing its corresponding reconstructed 2-RDM against the FCI reference 2-RDM. While FCI was used as the reference in this instance, any method capable of providing a reliable 2-RDM may be used in its place. The deviation was quantified using the Frobenius norm,

$$ \Delta_2 = \left\| {}^2D_{\text{unitary}} - {}^2D_{\text{FCI}} \right\|_2, \tag{E.18}$$

which provides a global measure of the 2-RDM discrepancy. Unitaries yielding $\Delta_2 > 1$ were deemed inconsistent with the target electronic structure and were discarded from further analysis. Along the potential energy curve of $H_4$ (Fig. 5 in the manuscript) ranging from 0.65 to 1.65 Å, the following numbers of unitary bases (out of 16 for each point) were discarded at each geometry: 2, 2, 5, 6, 6, 5, 7, 5, 4, 2, and 3, respectively. For the data on linear hydrogen chains ($H_4$, $H_6$, $H_8$, $H_{10}$), the following numbers of unitary bases (out of 16, 36, 160, and 300, respectively), were discarded: 3, 8, 19, 37.

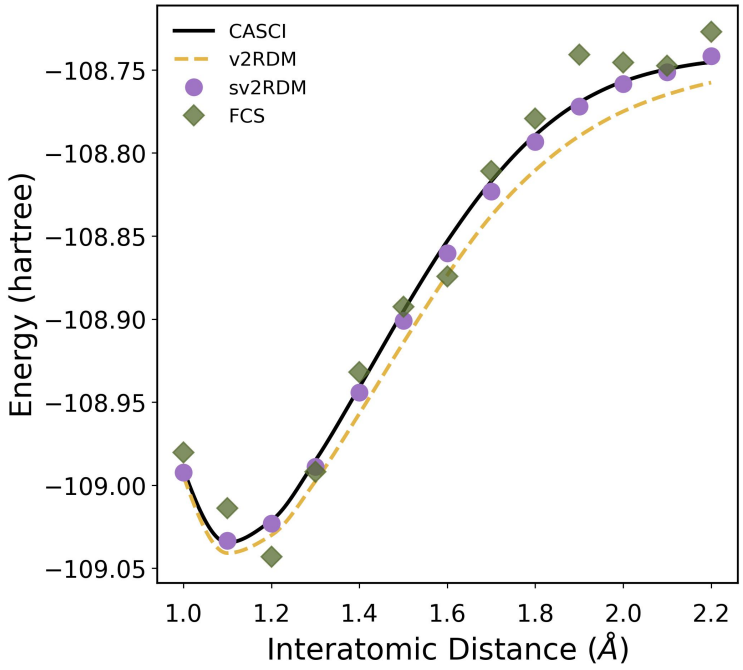


Figure E.1: Potential energy curve of $N_2$ computed using the cc-pVDZ basis set and a [10,8] active space with CASCI, shadow variational 2-RDM (sv2RDM), variational 2-RDM (v2RDM), and Fermionic Classical Shadows (FCS) methods. For sv2RDM and FCS, the total shot budgets used are 100 unitaries × 1,000 shots and 100,000 unitaries × 1 shot, respectively.

## E.3 Additional Data

Figure E.1 supplements Fig. 4 in the manuscript, presenting the simulated potential energy curve of $N_2$ in the cc-pVDZ basis set with a [10,8] active space using complete active space configuration interaction (CASCI), shadow variational 2-RDM (sv2RDM), variational 2-RDM (v2RDM), and fermionic classical shadows (FCS) methods. The CASCI results serve as the reference for evaluating the accuracy of the reconstructed energy profiles. The v2RDM energies are significantly lower than the CACSI reference, by as much as 20 milihartrees at longer distances. In contrast, the sv2RDM method closely reproduces the reference curve across all geometries, demonstrating the constrained shadow approach effectively mitigates the deviations observed with v2RDM.

Figure E.2 supplements Fig. 5 in the manuscript, showing the potential energy curve

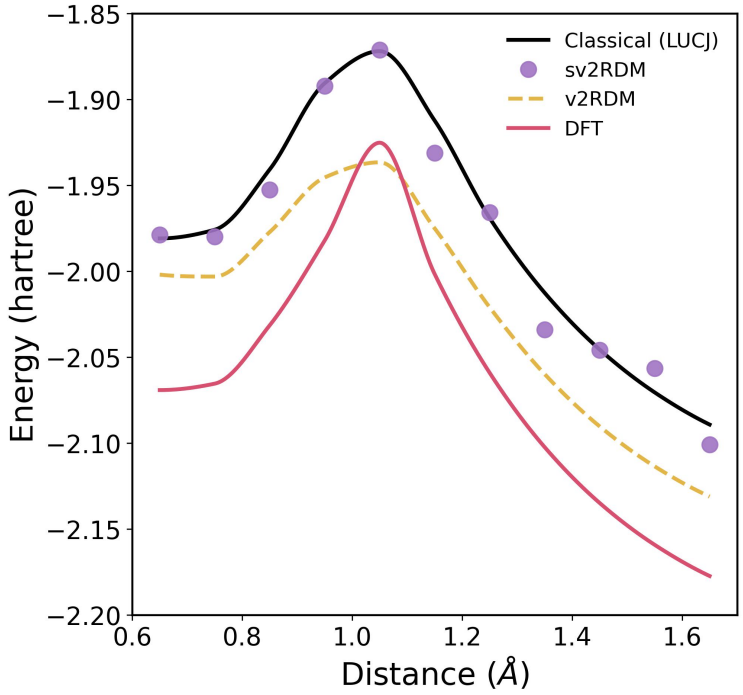


Figure E.2: Potential energy curve for the $H_4$ rectangle–square–rectangle transition in the minimal basis set, computed using Density Functional Theory (DFT) as s classical baseline, the classically computed Local Unitary Cluster Jastrow (LUCJ) ansatz, shadow variational 2-RDM (sv2RDM), and variational 2-RDM (v2RDM) method computed using measurements collected on the ibm_fez quantum computer.

for the $H_4$ rectangle–square–rectangle transition in the minimal basis set, computed using Density Functional Theory (DFT) as a classical baseline, the classically computed Local Unitary Cluster Jastrow (LUCJ) ansatz, variational 2-RDM (v2RDM), and the shadow variational 2-RDM (sv2RDM) methods, where sv2RDM is computed using measurements collected on the ibm_fez quantum computer. The v2RDM curve qualitatively reproduces the expected features of the transition and aligns more closely with the correlated LUCJ profile than the mean-field DFT results. The sv2RDM results, computed using data obtained from a quantum computer, exhibit very close agreement with the LUCJ curve across the full range of geometries, indicating that the constrained shadow reconstruction yields a quantitatively accurate potential energy curve using data collected on a quantum computer.

To illustrate the energetic performance of the reconstruction procedure in the fully state-

| H chain | Shot Budget | D | DQG | FCI |
|---|---|---|---|---|
| 4 | 16,000 | -2.122 | -2.121 | -2.166 |
| 6 | 36,000 | -3.129 | -3.122 | -3.236 |
| 8 | 160,000 | -4.152 | -4.142 | -4.308 |
| 10 | 300,000 | -5.161 | -5.144 | -5.380 |

Table E.1: Comparison of electronic energies (in hartree) for various H chain lengths with the given total shot budgets when the semidefinite 2-RDM is optimized in the limit where $w \to \infty$ in Eq. 11 in the main text, with partial (D) and all 2-positivity conditions (DQG) included. Shot budgets compared are: 16,000 unitaries/1 shot vs. 16 unitaries/1000 shots for $H_4$, 36,000 unitaries/1 shot vs. 36 unitaries/1000 shots for $H_6$, 160,000 unitaries/1 shot vs. 160 unitaries/1000 shots for $H_8$, and 300,000 unitaries/1 shot vs. 300 unitaries/1000 shots for $H_{10}$.

agnostic regime, Table E.1 reports equilibrium electronic energies for linear hydrogen chains obtained from SDP-optimized 2-RDMs in the limit $w \to \infty$, where no Hamiltonian-dependent energy regularization is included in the cost function. In this setting, the reconstruction is driven entirely by measurement data and $N$-representability constraints. As expected, energy expectation values are more sensitive to residual reconstruction errors, leading to deviations from the FCI reference that grow with system size. Nevertheless, this Hamiltonian-independent regime can be practically useful, as discussed in related work by the authors [419], the $w \to \infty$ limit provides a natural setting for correlated purification and error mitigation, and enables reconstruction beyond ground-state assumptions, including excited-state applications.

# REFERENCES


[1] Avdic, I.; Sager-Smith, L. M.; Mazziotti, D. A. Open quantum system violates generalized Pauli constraints on quantum device. *Communications Physics* **2023**, *6*.

[2] Avdic, I.; Sager-Smith, L. M.; Ghosh, I.; Wedig, O. C.; Higgins, J. S.; Engel, G. S.; Mazziotti, D. A. Quantum sensing using multiqubit quantum systems and the Pauli polytope. *Physical Review Research* **2023**, *5*.

[3] Avdic, I.; Mazziotti, D. A. Fewer Measurements from Shadow Tomography with $N$-Representability Conditions. *Phys. Rev. Lett.* **2024**, *132*, 220802.

[4] Avdic, I.; Mazziotti, D. A. Enhanced shadow tomography of molecular excited states via the enforcement of $N$-representability conditions by semidefinite programming. *Phys. Rev. A* **2024**, *110*, 052407.

[5] Avdic, I.; Wang, Y.; Rose, M.; Torres, L. I. P.; Schouten, A. O.; Sung, K. J.; Mazziotti, D. A. Constrained Shadow Tomography for Molecular Simulation on Quantum Devices. 2025; `https://arxiv.org/abs/2511.09717`.

[6] Avdic, I.; Mazziotti, D. A. Witnessing Entanglement in Mixed-Particle Quantum Systems. 2025; `https://arxiv.org/abs/2512.17860`.

[7] Delgado-Granados, L. H.; Krogmeier, T. J.; Sager-Smith, L. M.; Avdic, I.; Hu, Z.; Sajjan, M.; Abbasi, M.; Smart, S. E.; Narang, P.; Kais, S.; Schlimgen, A. W.; Head-Marsden, K.; Mazziotti, D. A. Quantum Algorithms and Applications for Open Quantum Systems. *Chemical Reviews* **2025**, *125*, 1823–1839.

[8] Wang, Y.; Cianci, C.; Avdic, I.; Dutta, R.; Warren, S.; Allen, B.; Vu, N. P.; Santos, L. F.; Batista, V. S.; Mazziotti, D. A. Characterizing Conical Intersections of Nucleobases on Quantum Computers. *Journal of Chemical Theory and Computation* **2025**, *21*, 1213–1221.

[9] Wang, Y.; Avdic, I.; Mazziotti, D. A. Shadow ansatz for the many-fermion wave function in scalable molecular simulations on quantum computing devices. *Physical Review A* **2025**, *112*.

[10] Liebert, J.; Schouten, A. O.; Avdic, I.; Schilling, C.; Mazziotti, D. A. Refining ensemble $N$ -representability of one-body density matrices from partial information. *New Journal of Physics* **2025**, *27*, 124511.

[11] Wang, Y.; Avdic, I.; Rose, M.; Torres, L. I. P.; Schouten, A. O.; Sung, K. J.; Mazziotti, D. A. Correlated Purification for Restoring $N$-Representability in Quantum Simulation. 2025; `https://arxiv.org/abs/2511.10789`.

[12] Torres, L. I. P.; Avdic, I.; Schouten, A. O.; Wedig, O. C.; Engel, G. S.; Mazziotti, D. A. Entanglement witnesses of condensation for enhanced quantum sensing. *arXiv:2511.17749 [quant-ph]* **2025**, `https://arxiv.org/abs/2511.17749`.

[13] Schrödinger, E. An Undulatory Theory of the Mechanics of Atoms and Molecules. *Physical Review* **1926**, *28*, 1049–1070.

[14] Szabo, A.; Ostlund, N. S. *Modern Quantum Chemistry: Introduction to Advanced Electronic Structure Theory*; Dover Publications: New York, 1996.

[15] Cramer, C. J. *Essentials of Computational Chemistry: Theories and Models*; John Wiley & Sons, 2013.

[16] Born, M.; Oppenheimer, R. Zur Quantentheorie der Molekeln. *Annalen der Physik* **1927**, *389*, 457–484.

[17] Tew, D. P.; Klopper, W.; Helgaker, T. Electron correlation: The many-body problem at the heart of chemistry. *Journal of Computational Chemistry* **2007**, *28*, 1307–1320.

[18] Slater, J. C. The Theory of Complex Spectra. *Phys. Rev.* **1929**, *34*, 1293–1322.

[19] Dirac, P. A. M.; Fowler, R. H. On the theory of quantum mechanics. *Proc. R. Soc. Lond. A* **1926**, *112*, 661–677.

[20] Fock, V. Konfigurationsraum und zweite Quantelung. *Zeitschrift fr Physik* **1932**, *75*, 622–647.

[21] Dirac, P. A. M. The quantum theory of the emission and absorption of radiation. *Proceedings of the Royal Society of London. Series A, Containing Papers of a Mathematical and Physical Character* **1927**, *114*, 243–265.

[22] Langel, W. T. Helgaker, P. Jorgensen, J. Olsen, T. Helgaker: Molecular electronic-structure theory: Wiley, New York, 2000. 938 pp (ISBN 0-471-96755-6) US300.00.*Journal of Solid State Electrochemistry***2001**, *6*, 359˘360.

[23] Slater, J. C. Molecular Energy Levels and Valence Bonds. *Physical Review* **1931**, *38*, 1109–1144.

[24] Hartree, D. R. The Wave Mechanics of an Atom with a Non-Coulomb Central Field. Part II. Some Results and Discussion. *Math. Proc. Camb. Philos. Soc.* **1928**, *24*, 111–132.

[25] Fock, V. Self consistent field mit Austausch fü Natrium. *Z. Phys.* **1930**, *62*, 795–805.

[26] Hartree, D. R. The Self-Consistent Field, with Exchange, for Beryllium. *Proceedings of the Royal Society of London. Series A, Mathematical and Physical Sciences* **1935**, *150*, 9–33.

[27] Pople, J. A.; Binkley, J. S.; Seeger, R. Theoretical models incorporating electron correlation. *International Journal of Quantum Chemistry* **2009**, *10*, 1–19.

[28] Čížek, J. On the Correlation Problem in Atomic and Molecular Systems. Calculation of Wavefunction Components in Ursell-Type Expansion Using Quantum-Field Theoretical Methods. *The Journal of Chemical Physics* **1966**, *45*, 4256–4266.

[29] Hampel, C.; Werner, H.-J. Local treatment of electron correlation in coupled cluster theory. *The Journal of Chemical Physics* **1996**, *104*, 6286–6297.

[30] Raghavachari, K.; Anderson, J. B. Electron Correlation Effects in Molecules. *The Journal of Physical Chemistry* **1996**, *100*, 12960–12973.

[31] Balint-Kurti, G. G. Electron Correlation in Small Molecules. *Physics Bulletin* **1978**, *29*, 25–25.

[32] Marti, K. H.; Reiher, M. New electron correlation theories for transition metal chemistry. *Physical Chemistry Chemical Physics* **2011**, *13*, 6750.

[33] Hirao, K. *From Molecules to Molecular Systems*; Springer Japan, 1998; p 11–32.

[34] Hollett, J. W.; Gill, P. M. W. The two faces of static correlation. *The Journal of Chemical Physics* **2011**, *134*.

[35] Bulik, I. W.; Henderson, T. M.; Scuseria, G. E. Can Single-Reference Coupled Cluster Theory Describe Static Correlation? *Journal of Chemical Theory and Computation* **2015**, *11*, 3171–3179.

[36] Piris, M. Global Method for Electron Correlation. *Physical Review Letters* **2017**, *119*.

[37] CREMER, D. Density functional theory: coverage of dynamic and non-dynamic electron correlation effects. *Molecular Physics* **2001**, *99*, 1899–1940.

[38] Coester, F. Bound states of a many-particle system. *Nuclear Physics* **1958**, *7*, 421–424.

[39] Coester, F.; Kümmel, H. Short-range correlations in nuclear wave functions. *Nuclear Physics* **1960**, *17*, 477–485.

[40] Paldus, J.; Čížek, J.; Shavitt, I. Correlation Problems in Atomic and Molecular Systems. IV. Extended Coupled-Pair Many-Electron Theory and Its Application to the $BH_3$ Molecule. *Physical Review A* **1972**, *5*, 50–67.

[41] Bishop, R. F.; Lührmann, K. H. Electron correlations: I. Ground-state results in the high-density regime. *Physical Review B* **1978**, *17*, 3757–3780.

[42] Bartlett, R. J.; Musiał, M. Coupled-cluster theory in quantum chemistry. *Reviews of Modern Physics* **2007**, *79*, 291–352.

[43] Hohenberg, P.; Kohn, W. Inhomogeneous Electron Gas. *Physical Review* **1964**, *136*, B864–B871.

[44] Kohn, W.; Sham, L. J. Self-Consistent Equations Including Exchange and Correlation Effects. *Physical Review* **1965**, *140*, A1133–A1138.

[45] Jones, R. O.; Gunnarsson, O. The density functional formalism, its applications and prospects. *Reviews of Modern Physics* **1989**, *61*, 689–746.

[46] Møller, C.; Plesset, M. S. Note on an Approximation Treatment for Many-Electron Systems. *Physical Review* **1934**, *46*, 618–622.

[47] SHAVITT, I. The history and evolution of configuration interaction. *Molecular Physics* **1998**, *94*, 3–17.

[48] Löwdin, P.-O. Quantum Theory of Many-Particle Systems. *Phys. Rev.* **1955**, *97*, 1474–1489.

[49] Buenker, R. J.; Peyerimhoff, S. D. Individualized configuration selection in CI calculations with subsequent energy extrapolation. *Theoretica Chimica Acta* **1974**, *35*, 33–58.

[50] Buenker, R. J.; Peyerimhoff, S. D.; Butscher, W. Applicability of the multi-reference double-excitation CI (MRD-CI) method to the calculation of electronic wavefunctions and comparison with related techniques. *Molecular Physics* **1978**, *35*, 771–791.

[51] Roos, B. O.; Taylor, P. R.; Sigbahn, P. E. A complete active space SCF method (CASSCF) using a density matrix formulated super-CI approach. *Chemical Physics* **1980**, *48*, 157–173.

[52] Siegbahn, P. E. M.; Almlöf, J.; Heiberg, A.; Roos, B. O. The complete active space SCF (CASSCF) method in a Newton–Raphson formulation with application to the HNO molecule. *The Journal of Chemical Physics* **1981**, *74*, 2384–2396.

[53] Andersson, K.; Malmqvist, P. A.; Roos, B. O.; Sadlej, A. J.; Wolinski, K. Second-order perturbation theory with a CASSCF reference function. *The Journal of Physical Chemistry* **1990**, *94*, 5483–5488.

[54] Andersson, K.; Malmqvist, P.-; Roos, B. O. Second-order perturbation theory with a complete active space self-consistent field reference function. *The Journal of Chemical Physics* **1992**, *96*, 1218–1226.

[55] Angeli, C.; Cimiraglia, R.; Evangelisti, S.; Leininger, T.; Malrieu, J.-P. Introduction of n-electron valence states for multireference perturbation theory. *The Journal of Chemical Physics* **2001**, *114*, 10252–10264.

[56] Angeli, C.; Cimiraglia, R.; Malrieu, J.-P. N-electron valence state perturbation theory: a fast implementation of the strongly contracted variant. *Chemical Physics Letters* **2001**, *350*, 297–305.

[57] David Sherrill, C.; Schaefer, H. F. *Advances in Quantum Chemistry*; Elsevier, 1999; p 143–269.

[58] Chan, G. K.-L.; Head-Gordon, M. Highly correlated calculations with a polynomial cost algorithm: A study of the density matrix renormalization group. *The Journal of Chemical Physics* **2002**, *116*, 4462–4476.

[59] Ghosh, D.; Hachmann, J.; Yanai, T.; Chan, G. K.-L. Orbital optimization in the density matrix renormalization group, with applications to polyenes and -carotene. *The Journal of Chemical Physics* **2008**, *128*.

[60] Chan, G. K.-L.; Sharma, S. The Density Matrix Renormalization Group in Quantum Chemistry. *Annual Review of Physical Chemistry* **2011**, *62*, 465–481.

[61] Lyakh, D. I.; Musiał, M.; Lotrich, V. F.; Bartlett, R. J. Multireference Nature of Chemistry: The Coupled-Cluster View. *Chemical Reviews* **2011**, *112*, 182–243.

[62] Hermes, M. R.; Gagliardi, L. Multiconfigurational Self-Consistent Field Theory with Density Matrix Embedding: The Localized Active Space Self-Consistent Field Method. *Journal of Chemical Theory and Computation* **2019**, *15*, 972–986.

[63] Li Manni, G.; Carlson, R. K.; Luo, S.; Ma, D.; Olsen, J.; Truhlar, D. G.; Gagliardi, L. Multiconfiguration Pair-Density Functional Theory. *Journal of Chemical Theory and Computation* **2014**, *10*, 3669–3680.

[64] *Collected Papers of L.D. Landau*; Elsevier, 1965; p 8–18.

[65] Neumann, J. v. Wahrscheinlichkeitstheoretischer Aufbau der Quantenmechanik. *Nachrichten von der Gesellschaft der Wissenschaften zu Göttingen, Mathematisch-Physikalische Klasse* **1927**, *1927*, 245–272.

[66] Mayer, J. E. Electron Correlation. *Phys. Rev.* **1955**, *100*, 1579–1586.

[67] Coleman, A.; Yukalov, V. *Reduced Density Matrices: Coulson's Challenge*; Lecture Notes in Chemistry; Springer Berlin Heidelberg, 2000.

[68] Mazziotti, D. A. Variational minimization of atomic and molecular ground-state energies via the two-particle reduced density matrix. *Phys. Rev. A* **2002**, *65*, 062511.

[69] Mazziotti, D. A. *Reduced-Density-Matrix Mechanics: With Application to Many-Electron Atoms and Molecule*; Adv. Chem. Phys.: Wiley, New York, 2007; Vol. 134.

[70] Mazziotti, D. A. Two-Electron Reduced Density Matrix as the Basic Variable in Many-Electron Quantum Chemistry and Physics. *Chemical Reviews* **2012**, *112*, 244–262.

[71] Mazziotti, D. A. Pure-N-representability conditions of two-fermion reduced density matrices. *Phys. Rev. A* **2016**, *94*.

[72] Mazziotti, D. A. Large-Scale Semidefinite Programming for Many-Electron Quantum Mechanics. *Phys. Rev. Lett.* **2011**, *106*, 083001.

[73] Cioslowski, J. In *Many-Electron Densities and Reduced Density Matrices*; Cioslowski, J., Ed.; Mathematical and Computational Chemistry; Springer US: Boston, MA, 2000; Vol. 91; pp 399–404.

[74] Nakata, M.; Nakatsuji, H.; Ehara, M.; Fukuda, M.; Nakata, K.; Fujisawa, K. Variational calculations of fermion second-order reduced density matrices by semidefinite programming algorithm. *J. Chem. Phys.* **2001**, *114*, 8282–8292.

[75] Mazziotti, D. A. Realization of Quantum Chemistry without Wave Functions through First-Order Semidefinite Programming. *Phys. Rev. Lett.* **2004**, *93*, 213001.

[76] Zhao, Z.; Braams, B. J.; Fukuda, M.; Overton, M. L.; Percus, J. K. The reduced density matrix method for electronic structure calculations and the role of three-index representability conditions. *J. Chem. Phys.* **2004**, *120*, 2095–2104.

[77] Cancès, E.; Stoltz, G.; Lewin, M. The electronic ground-state energy problem: A new reduced density matrix approach. *J. Chem. Phys.* **2006**, *125*, 064101.

[78] Gidofalvi, G.; Mazziotti, D. A. Active-space two-electron reduced-density-matrix method: Complete active-space calculations without diagonalization of the N-electron Hamiltonian. *J. Chem. Phys.* **2008**, *129*, 134108.

[79] Shenvi, N.; Izmaylov, A. F. Active-Space N-Representability Constraints for Variational Two-Particle Reduced Density Matrix Calculations. *Phys. Rev. Lett.* **2010**, *105*, 213003.

[80] Mazziotti, D. A. Structure of Fermionic Density Matrices: Complete $N$-Representability Conditions. *Phys. Rev. Lett.* **2012**, *108*, 263002.

[81] Verstichel, B.; Aggelen, H. v.; Poelmans, W.; Neck, D. V. Variational Two-Particle Density Matrix Calculation for the Hubbard Model Below Half Filling Using Spin-Adapted Lifting Conditions. *Phys. Rev. Lett.* **2011**, *108*, 213001.

[82] Schlimgen, A. W.; Heaps, C. W.; Mazziotti, D. A. Entangled Electrons Foil Synthesis of Elusive Low-Valent Vanadium Oxo Complex. *J. Phys. Chem. Lett.* **2016**, *7*, 627–631.

[83] Helbig, N.; Tokatly, I. V.; Rubio, A. Physical meaning of the natural orbitals: Analysis of exactly solvable models. *Physical Review A* **2010**, *81*.

[84] Coleman, A. J. Structure of Fermion Density Matrices. *Rev. Mod. Phys.* **1963**, *35*, 668–686.

[85] Tredgold, R. H. Density Matrix and the Many-Body Problem. *Physical Review* **1957**, *105*, 1421–1423.

[86] Pauli, W. The Connection Between Spin and Statistics. *Physical Review* **1940**, *58*, 716–722.

[87] Borland, R. E.; Dennis, K. The conditions on the one-matrix for three-body fermion wavefunctions with one-rank equal to six. *J. Phys. B: At. Mol. Opt. Phys.* **1972**, *5*, 7–15.

[88] Klyachko, A. A. Quantum marginal problem and N-representability. *J. Phys.: Conf. Ser.* **2006**, *36*, 72–86.

[89] Altunbulak, M.; Klyachko, A. The Pauli Principle Revisited. *Commun. Math. Phys.* **2008**, *282*, 287–322.

[90] Mazziotti, D. A.; Erdahl, R. M. Uncertainty relations and reduced density matrices: Mapping many-body quantum mechanics onto four particles. *Phys. Rev. A* **2001**, *63*, 042113.

[91] Garrod, C.; Percus, J. K. Reduction of the $N$-Particle Variational Problem. *J. Math. Phys.* **1964**, *5*, 1756–1776.

[92] Rockafellar, R. T. *Convex Analysis*; Princeton Landmarks in Mathematics and Physics; Princeton University Press: Princeton, NJ, 1970.

[93] Vandenberghe, L.; Boyd, S. Semidefinite Programming. *SIAM Review* **1996**, *38*, 49–95.

[94] Vandenberghe, L., Wolkowicz, H., Saigal, R., Eds. *Handbook of Semidefinite Programming: Theory, Algorithms, and Applications*; International Series in Operations Research & Management Science; Kluwer Academic Publishers: Boston, MA, 2000; Vol. 27.

[95] Nesterov, Y.; Nemirovskii, A.; Ye, Y. *Interior-Point Polynomial Algorithms in Convex Programming*; SIAM Studies in Applied Mathematics; SIAM: Philadelphia, PA, 1994; Vol. 13.

[96] Sturm, J. F. Using SeDuMi 1.02, a MATLAB Toolbox for Optimization over Symmetric Cones. *Optimization Methods and Software* **1999**, *11*, 625–653.

[97] Goemans, M. X.; Williamson, D. P. Improved Approximation Algorithms for Maximum Cut and Satisfiability Problems Using Semidefinite Programming. *Journal of the ACM* **1995**, *42*, 1115–1145.

[98] Society, M. O. Fulkerson Prize 2000: Goemans and Williamson. `https://en.wikipedia.org/wiki/Fulkerson_Prize`, 2000; Awarded for approximation algorithms based on semidefinite programming.

[99] Mazziotti, D. A. First-order semidefinite programming for the direct determination of two-electron reduced density matrices with application to many-electron atoms and molecules. *The Journal of Chemical Physics* **2004**, *121*, 10957–10966.

[100] Erdahl, R. M. Representability. *Int. J. Quantum Chem.* **1978**, *13*, 697–718.

[101] Pelzer, K.; Greenman, L.; Gidofalvi, G.; Mazziotti, D. A. Strong Correlation in Acene Sheets from the Active-Space Variational Two-Electron Reduced Density Matrix Method: Effects of Symmetry and Size. *The Journal of Physical Chemistry A* **2011**, *115*, 5632–5640.

[102] Fosso-Tande, J.; Nguyen, T.-S.; Gidofalvi, G.; DePrince, A. E. Large-Scale Variational Two-Electron Reduced-Density-Matrix-Driven Complete Active Space Self-Consistent Field Methods. *Journal of Chemical Theory and Computation* **2016**, *12*, 2260–2271.

[103] Montgomery, J. M.; Mazziotti, D. A. Strong Electron Correlation in Nitrogenase Cofactor, FeMoco. *The Journal of Physical Chemistry A* **2018**, *122*, 4988–4996.

[104] Schouten, A. O.; Sager, L. M.; Mazziotti, D. A. Exciton Condensation in Molecular-Scale van der Waals Stacks. *J. Phys. Chem. Lett.* **2021**, *12*, 9906–9911.

[105] Sager, L. M.; Mazziotti, D. A. Cooper-pair condensates with nonclassical long-range order on quantum devices. *Phys. Rev. Research* **2022**, *4*, 013003.

[106] Montgomery, J. M.; Alexander, E.; Mazziotti, D. A. Prediction of the Existence of LiCH: A Carbene-like Organometallic Molecule. *The Journal of Physical Chemistry A* **2020**, *124*, 9562–9566.

[107] Smart, S. E.; Scrape, P. G.; Butler, L. J.; Mazziotti, D. A. Using reduced density matrix techniques to capture static and dynamic correlation in the energy landscape for the decomposition of the CH2CH2ONO radical and support a non-IRC pathway. *The Journal of Chemical Physics* **2018**, *149*.

[108] Schlimgen, A. W.; Mazziotti, D. A. Analytical gradients of variational reduced-density-matrix and wavefunction-based methods from an overlap-reweighted semidefinite program. *The Journal of Chemical Physics* **2018**, *149*.

[109] Pauli, W.; In, H. *Uber den Zusammenhang des Abschlusses der Elektronen-gruppen im Atom mit der Komplexstruktur der Spektren*; 1925; Vol. 31.

[110] Heisenber, V. W.; in Kopenhagen *Mehrkrperproblem und Resonanz in der Quantenmechanik*; 1926; Vol. 38.

[111] Schilling, C.; Gross, D.; Christandl, M. Pinning of Fermionic Occupation Numbers. *Phys. Rev. Lett.* **2013**, *110*.

[112] Chakraborty, R.; Mazziotti, D. A. Generalized Pauli conditions on the spectra of one-electron reduced density matrices of atoms and molecules. *Phys. Rev. A* **2014**, *89*.

[113] Theophilou, I.; Lathiotakis, N. N.; Marques, M. A. L.; Helbig, N. Generalized Pauli constraints in reduced density matrix functional theory. *J. Chem. Phys.* **2015**, *142*, 154108.

[114] Benavides-Riveros, C. L.; Gracia-Bondía, J. M.; Springborg, M. Quasipinning and entanglement in the lithium isoelectronic series. *Phys. Rev. A* **2013**, *88*.

[115] Schilling, C. Quasipinning and its relevance for $N$-fermion quantum states. *Phys. Rev. A* **2015**, *91*, 022105.

[116] Schilling, C. Hubbard model: Pinning of occupation numbers and role of symmetries. *Phys. Rev. B* **2015**, *92*, 155149.

[117] Tennie, F.; Vedral, V.; Schilling, C. Influence of the fermionic exchange symmetry beyond Pauli's exclusion principle. *Phys. Rev. A* **2017**, *95*, 022336.

[118] Benavides-Riveros, C. L.; Springborg, M. Quasipinning and selection rules for excitations in atoms and molecules. *Phys. Rev. A* **2015**, *92*, 012512.

[119] Chakraborty, R.; Mazziotti, D. A. Structure of the one-electron reduced density matrix from the generalized Pauli exclusion principle. *Int. J. Quantum Chem.* **2015**, *115*, 1305–1310.

[120] Chakraborty, R.; Mazziotti, D. A. Role of the generalized pauli constraints in the quantum chemistry of excited states. *Int. J. Quantum Chem.* **2016**, *116*, 784–790.

[121] Benavides-Riveros, C. L.; Schilling, C. Natural Extension of Hartree–Fock Through Extremal 1-Fermion Information: Overview and Application to the Lithium Atom. *Zeitschrift für Physikalische Chemie* **2016**, *230*, 703–717.

[122] Davies, E. *Quantum Theory of Open Systems*; Academic Press, 1976.

[123] Breuer, H. P.; Petruccione, F. *The theory of open quantum systems*; Oxford University Press: Great Clarendon Street, 2002.

[124] Chakraborty, R.; Mazziotti, D. A. Sufficient condition for the openness of a many-electron quantum system from the violation of a generalized Pauli exclusion principle. *Phys. Rev. A* **2015**, *91*, 010101.

[125] Smart, S. E.; Schuster, D. I.; Mazziotti, D. A. Experimental data from a quantum computer verifies the generalized Pauli exclusion principle. *Comm. Phys.* **2019**, *2*, 11.

[126] Barends, R. et al. Digital quantum simulation of fermionic models with a superconducting circuit. *Nat. Commun.* **2015**, *6*, 7654.

[127] Ma, R.; Saxberg, B.; Owens, C.; Leung, N.; Lu, Y.; Simon, J.; Schuster, D. I. A dissipatively stabilized Mott insulator of photons. *Nature* **2019**, *566*, 51–57.

[128] Sager, L. M.; Safaei, S.; Mazziotti, D. A. Potential coexistence of exciton and fermion-pair condensations. *Phys. Rev. B* **2020**, *101*, 081107.

[129] Warren, S.; Sager-Smith, L. M.; Mazziotti, D. A. Quantum simulation of quantum phase transitions using the convex geometry of reduced density matrices. *Phys. Rev. A* **2022**, *106*, 012434.

[130] Sager, L. M.; Mazziotti, D. A. Entangled phase of simultaneous fermion and exciton condensations realized. *Phys. Rev. B* **2022**, *105*, L121105.

[131] Smart, S. E.; Hu, Z.; Kais, S.; Mazziotti, D. A. Relaxation of stationary states on a quantum computer yields a unique spectroscopic fingerprint of the computer's noise. *Comm. Phys.* **2022**, *5*, 28.

[132] Mazziotti, D. A.; Smart, S. E.; Mazziotti, A. R. Quantum simulation of molecules without fermionic encoding of the wave function. *New J. Phys.* **2021**, *23*, 113037.

[133] Head-Marsden, K.; Flick, J.; Ciccarino, C. J.; Narang, P. Quantum Information and Algorithms for Correlated Quantum Matter. *Chem. Rev.* **2021**, *121*, 5.

[134] McArdle, S.; Endo, S.; Aspuru-Guzik, A.; Benjamin, S. C.; Yuan, X. Quantum computational chemistry. *Rev. Mod. Phys.* **2020**, *92*, 015003.

[135] Bian, T.; Murphy, D.; Xia, R.; Daskin, A.; Kais, S. Quantum computing methods for electronic states of the water molecule. *Mol. Phys.* **2019**, *117*, 2069–2082.

[136] Aspuru-Guzik, A.; Dutoi, A. D.; Love, P. J.; Head-Gordon, M. Simulated Quantum Computation of Molecular Energies. *Science* **2005**, *309*, 1704–1707.

[137] Sager, L. M.; Smart, S. E.; Mazziotti, D. A. Preparation of an Exciton Condensate of Photons on a 53-Qubit Quantum Computer. *Phys. Rev. Research* **2020**, *2*, 043205.

[138] IBM-Quantum https://quantum-computing.ibm.com/. 2021.

[139] Chakraborty, R.; Mazziotti, D. A. Sparsity of the wavefunction from the generalized Pauli exclusion principle. *J. Chem. Phys.* **2018**, *148*, 054106.

[140] Dür, W.; Vidal, G.; Cirac, J. I. Three qubits can be entangled in two inequivalent ways. *Phys. Rev. A* **2000**, *62*, 062314.

[141] Einstein, A.; Podolsky, B.; Rosen, N. Can Quantum-Mechanical Description of Physical Reality Be Considered Complete? *Phys. Rev.* **1935**, *47*, 777–780.

[142] Greenberger, D. M. In *Compendium of Quantum Physics*; Greenberger, D., Hentschel, K., Weinert, F., Eds.; Springer Berlin Heidelberg: Berlin, Heidelberg, 2009; pp 258–263.

[143] Higuchi, A.; Sudbery, A.; Szulc, J. One-Qubit Reduced States of a Pure Many-Qubit State: Polygon Inequalities. *Phys. Rev. Lett.* **2003**, *90*, 107902.

[144] Hackl, L.; Li, D.; Akopian, N.; Christandl, M. Experimental proposal to probe the extended Pauli principle. 2021.

[145] Sudbery, A. On local invariants of pure three-qubit states. *J. Phys. A: Math. and Gen.* **2001**, *34*, 643–652.

[146] Qiskit contributors Qiskit: An Open-source Framework for Quantum Computing. 2023.

[147] Koch, J.; Yu, T. M.; Gambetta, J.; Houck, A. A.; Schuster, D. I.; Majer, J.; Blais, A.; Devoret, M. H.; Girvin, S. M.; Schoelkopf, R. J.; et. al. Charge-insensitive qubit design derived from the Cooper pair box. *Phys. Rev. A* **2007**, *76*.

[148] Chow, J. M.; Córcoles, A. D.; Gambetta, J. M.; Rigetti, C.; Johnson, B. R.; Smolin, J. A.; Rozen, J. R.; Keefe, G. A.; Rothwell, M. B.; Ketchen, M. B.; et al. Simple All-Microwave Entangling Gate for Fixed-Frequency Superconducting Qubits. *Phys. Rev. Lett.* **2011**, *107*.

[149] Liebert, J.; Castillo, F.; Labbé, J.-P.; Schilling, C. Foundation of One-Particle Reduced Density Matrix Functional Theory for Excited States. *JCTC* **2022**, *18*, 124–140.

[150] von Neumann, J. *Mathematical Foundations of Quantum Mechanics*; Goldstine Printed Materials; Princeton University Press, 1955.

[151] Schlimgen, A. W.; Head-Marsden, K.; Sager-Smith, L. M.; Narang, P.; Mazziotti, D. A. Quantum Simulation of Open Quantum Systems Using Density-Matrix Purification. 2022; `https://arxiv.org/abs/2207.07112`.

[152] Grotti, J. et al. Geodesy and metrology with a transportable optical clock. *Nat. Phys.* **2018**, *14*, 437–441.

[153] Ludlow, A. D.; Boyd, M. M.; Ye, J.; Peik, E.; Schmidt, P. O. Optical atomic clocks. *Rev. Mod. Phys.* **2015**, *87*, 637–701.

[154] Ahmed, Z. et al. Quantum Sensing for High Energy Physics. 2018; `https://arxiv.org/abs/1803.11306`.

[155] Degen, C. L.; Reinhard, F.; Cappellaro, P. Quantum sensing. *Rev. Mod. Phys.* **2017**, *89*, 035002.

[156] Xie, M.; Yu, X.; Rodgers, L. V. H.; Xu, D.; Chi-Durán, I.; Toros, A.; Quack, N.; de Leon, N. P.; Maurer, P. C. Biocompatible surface functionalization architecture for a diamond quantum sensor. *PNAS* **2022**, *119*, e2114186119.

[157] Schirhagl, R.; Chang, K.; Loretz, M.; Degen, C. L. Nitrogen-Vacancy Centers in Diamond: Nanoscale Sensors for Physics and Biology. *Annu. Rev. Phys. Chem.* **2014**, *65*, 83–105, PMID: 24274702.

[158] Barry, J. F.; Schloss, J. M.; Bauch, E.; Turner, M. J.; Hart, C. A.; Pham, L. M.; Walsworth, R. L. Sensitivity optimization for NV-diamond magnetometry. *Rev. Mod. Phys.* **2020**, *92*, 015004.

[159] Raton, B. et al. Nuclear magnetic resonance detection and spectroscopy of single proteins using quantum logic. *Science* **2016**, *351*, 836–842.

[160] Abobeih, M. H.; Randall, J.; Bradley, C. E.; Bartling, H. P.; Bakker, M. A.; Degen, M. J.; Markham, M.; Twitchen, D. J.; Taminiau, T. H. Atomic-scale imaging of a 27-nuclear-spin cluster using a quantum sensor. *Nature* **2019**, *576*, 411–415.

[161] Walker, J. Optical absorption and luminescence in diamond. *Rep. Prog. Phys.* **1979**, *42*, 1605.

[162] Gali, A.; Janzén, E.; Deák, P.; Kresse, G.; Kaxiras, E. Theory of Spin-Conserving Excitation of the $NV^-$ Center in Diamond. *Phys. Rev. Lett.* **2009**, *103*, 186404.

[163] Thiering, G.; Gali, A. Theory of the optical spin-polarization loop of the nitrogen-vacancy center in diamond. *Phys. Rev. B* **2018**, *98*, 085207.

[164] Ádám Gali Ab initio theory of the nitrogen-vacancy center in diamond. *Nanophotonics* **2019**, *8*, 1907–1943.

[165] Mitra, A.; Pham, H. Q.; Pandharkar, R.; Hermes, M. R.; Gagliardi, L. Excited States of Crystalline Point Defects with Multireference Density Matrix Embedding Theory. *J. Phys. Chem. Lett.* **2021**, *12*, 11688–11694.

[166] Jin, Y.; Govoni, M.; Galli, G. Vibrationally resolved optical excitations of the nitrogen-vacancy center in diamond. *npj Comput Mater* **2022**, *8*.

[167] Alkauskas, A.; Buckley, B. B.; Awschalom, D. D.; Van de Walle, C. G. First-principles theory of the luminescence lineshape for the triplet transition in diamond NV centres. *New J. Phys.* **2014**, *16*, 073026.

[168] Tóth, G.; Apellaniz, I. Quantum metrology from a quantum information science perspective. *J. Phys. A Math. Theor.* **2014**, *47*, 39.

[169] Zheng, T.-X.; Li, A.; Rosen, J.; Zhou, S.; Koppenhöfer, M.; Ma, Z.; Chong, F. T.; Clerk, A. A.; Jiang, L.; Maurer, P. C. Preparation of metrological states in dipolar-interacting spin systems. *npj Quantum Information* **2022**, *8*.

[170] Caves, C. M. Quantum-mechanical noise in an interferometer. *Phys. Rev. D* **1981**, *23*, 1693–1708.

[171] Wineland, D. J.; Bollinger, J. J.; Itano, W. M.; Moore, F. L.; Heinzen, D. J. Spin squeezing and reduced quantum noise in spectroscopy. *Phys. Rev. A* **1992**, *46*, R6797–R6800.

[172] Kitagawa, M.; Ueda, M. Squeezed spin states. *Phys. Rev. A* **1993**, *47*, 5138–5143.

[173] Hosten, O.; Engelsen, N. J.; Krishnakumar, R.; Kasevich, M. A. Measurement noise 100 times lower than the quantum-projection limit using entangled atoms. *Nature* **2016**, *529*, 505–508.

[174] Hosten, O.; Krishnakumar, R.; Engelsen, N. J.; Kasevich, M. A. Quantum phase magnification. *Science* **2016**, *352*, 1552–1555.

[175] Giovannetti, V.; Lloyd, S.; MacCone, L. Advances in quantum metrology. *Nat. Photon* **2011**, *5*, 222–229.

[176] Pezzè, L. Entanglement-enhanced sensor networks. *Nature Photonics* **2021**, *15*, 74–76.

[177] Zhang, Z.; Mouradian, S.; Wong, F. N. C.; Shapiro, J. H. Entanglement-Enhanced Sensing in a Lossy and Noisy Environment. *Phys. Rev. Lett.* **2015**, *114*, 110506.

[178] Colombo, S.; Pedrozo-Peñafiel, E.; Vuletić, V. Entanglement-enhanced optical atomic clocks. *Applied Physics Letters* **2022**, *121*, 210502.

[179] Zaiser, S.; Rendler, T.; Jakobi, I.; Wolf, T.; Lee, S.-Y.; Wagner, S.; Bergholm, V.; Schulte-Herbrüggen, T.; Neumann, P.; Wrachtrup, J. Enhancing quantum sensing sensitivity by a quantum memory. *Nature Communications* **2016**, *7*.

[180] Thomas, R. A.; Parniak, M.; Østfeldt, C.; Møller, C. B.; Bærentsen, C.; Tsaturyan, Y.; Schliesser, A.; Appel, J.; Zeuthen, E.; Polzik, E. S. Entanglement between distant macroscopic mechanical and spin systems. *Nature Physics* **2020**, *17*, 228–233.

[181] Wiseman, H. M.; Vaccaro, J. A. Entanglement of Indistinguishable Particles Shared between Two Parties. *Phys. Rev. Lett.* **2003**, *91*, 097902.

[182] Walter, M.; Doran, B.; Gross, D.; Christandl, M. Entanglement Polytopes: Multiparticle Entanglement from Single-Particle Information. *Science* **2013**, *340*, 1205–1208.

[183] Smart, S. E.; Mazziotti, D. A. Quantum-classical hybrid algorithm using an error-mitigating $N$-representability condition to compute the Mott metal-insulator transition. *Phys. Rev. A* **2019**, *100*, 022517.

[184] Gibney, D.; Boyn, J.-N.; Mazziotti, D. A. Toward a Resolution of the Static Correlation Problem in Density Functional Theory from Semidefinite Programming. *J. Phys. Chem. Lett.* **2021**, *12*, 385–391, PMID: 33356286.

[185] Boyn, J.-N.; Mazziotti, D. A. Sparse non-orthogonal wave function expansions from the extension of the generalized Pauli constraints to the two-electron reduced density matrix. *Chem. Phys.* **2019**, *150*, 144102.

[186] Schilling, C.; Altunbulak, M.; Knecht, S.; Lopes, A.; Whitfield, J. D.; Christandl, M.; Gross, D.; Reiher, M. Generalized Pauli constraints in small atoms. *Phys. Rev. A* **2018**, *97*, 052503.

[187] Chakraborty, R.; Mazziotti, D. A. Noise-assisted energy transfer from the dilation of the set of one-electron reduced density matrices. *J. Chem. Phys.* **2017**, *146*, 184101.

[188] Fenna, R. E.; Matthews, B. W. Chlorophyll arrangement in a bacteriochlorophyll protein from Chlorohium limicola. *Nature* **1975**, *258*, 1476–4687.

[189] Higgins, J. S.; Lloyd, L. T.; Sohail, S. H.; Allodi, M. A.; Otto, J. P.; Saer, R. G.; Wood, R. E.; Massey, S. C.; Ting, P.-C.; Blankenship, R. E.; Engel, G. S. Photosynthesis tunes quantum-mechanical mixing of electronic and vibrational states to steer exciton energy transfer. *PNAS* **2021**, *118*, e2018240118.

[190] Blankenship, R. E. Molecular Mechanisms of Photosynthesis. *Q Rev Biol* **2003**, *78*, 234–235.

[191] Engel, G. S.; Calhoun, T. R.; Read, E. L.; Ahn, T.-K.; Mančal, T.; Cheng, Y.-C.; Blankenship, R. E.; Fleming, G. R. Evidence for wavelike energy transfer through quantum coherence in photosynthetic systems. *Nature* **2007**, *446*, 782–786.

[192] Lee, H.; Cheng, Y.-C.; Fleming, G. R. Coherence Dynamics in Photosynthesis: Protein Protection of Excitonic Coherence. *Science* **2007**, *316*, 1462–1465.

[193] Mohseni, M.; Rebentrost, P.; Lloyd, S.; Aspuru-Guzik, A. Environment-assisted quantum walks in photosynthetic energy transfer. *Chem. Phys.* **2008**, *129*, 174106.

[194] Wilkins, D. M.; Dattani, N. S. Why Quantum Coherence Is Not Important in the Fenna–Matthews–Olsen Complex. *JCTC* **2015**, *11*, 3411–3419.

[195] Higgins, J. S.; Allodi, M. A.; Lloyd, L. T.; Otto, J. P.; Sohail, S. H.; Saer, R. G.; Wood, R. E.; Massey, S. C.; Ting, P.-C.; Blankenship, R. E.; Engel, G. S. Redox conditions correlated with vibronic coupling modulate quantum beats in photosynthetic pigment–protein complexes. *PNAS* **2021**, *118*.

[196] Maiuri, M.; Ostroumov, E. E.; Saer, R. G.; Blankenship, R. E.; Scholes, G. D. Coherent wavepackets in the Fenna–Matthews–Olson complex are robust to excitonic-structure perturbations caused by mutagenesis. *Nat. Chem* **2018**, *10*, 177–183.

[197] Häse, F.; Kreisbeck, C.; Aspuru-Guzik, A. Machine learning for quantum dynamics: deep learning of excitation energy transfer properties. *Chem. Sci.* **2017**, *8*, 8419–8426.

[198] Hu, Z.; Head-Marsden, K.; Mazziotti, D. A.; Narang, P.; Kais, S. A general quantum algorithm for open quantum dynamics demonstrated with the Fenna-Matthews-Olson complex. *Quantum* **2022**, *6*, 726.

[199] Chávez-Huerta, M.; Rojas, F. Environment-assisted quantum discord in the chromophores network of light-harvesting complexes. *Quantum Inf. Process.* **2022**, *21*, 1–17.

[200] Gallina, F.; Bruschi, M.; Fresch, B. Strategies to simulate dephasing-assisted quantum transport on digital quantum computers. *New J. Phys.* **2022**, *24*, 023039.

[201] Ullah, A.; Dral, P. O. Predicting the future of excitation energy transfer in light-harvesting complex with artificial intelligence-based quantum dynamics. *Nat. Commun.* **2022**, *13*, 1–8.

[202] Kell, A.; Blankenship, R. E.; Jankowiak, R. Effect of Spectral Density Shapes on the Excitonic Structure and Dynamics of the Fenna–Matthews–Olson Trimer from Chlorobaculum tepidum. *J. Phys. Chem. A* **2016**, *120*, 6146–6154.

[203] Plenio, M. B.; Huelga, S. F. Dephasing-assisted transport: quantum networks and biomolecules. *New J. Phys.* **2008**, *10*, 113019.

[204] Hu, Z.; Xia, R.; Kais, S. A quantum algorithm for evolving open quantum dynamics on quantum computing devices. *Scientific Reports* **2020**, *10*.

[205] Tisler, J.; Reuter, R.; Lämmle, A.; Jelezko, F.; Balasubramanian, G.; Hemmer, P. R.; Reinhard, F.; Wrachtrup, J. Highly Efficient FRET from a Single Nitrogen-Vacancy Center in Nanodiamonds to a Single Organic Molecule. *ACS Nano* **2011**, *5*, 7893–7898, PMID: 21899301.

[206] Pezzagna, S.; Meijer, J. Quantum computer based on color centers in diamond. *Applied Physics Reviews* **2021**, *8*, 011308.

[207] Sager-Smith, L. M.; Mazziotti, D. A. Reducing the Quantum Many-Electron Problem to Two Electrons with Machine Learning. *JACS* **2022**, *144*, 18959–18966.

[208] Feynman, R. Simulating Physics with Computers. *International Journal of Theoretical Physics* **1982**, *2*, 467–488.

[209] Manin, Y. Computable and Non-Computable. *Sovetskoe Radio* **1980**, 128.

[210] Nielsen, M. A.; Chuang, I. L. *Quantum Computation and Quantum Information: 10th Anniversary Edition*; Cambridge University Press, 2011.

[211] Colless, J. I.; Ramasesh, V. V.; Dahlen, D.; Blok, M. S.; Kimchi-Schwartz, M. E.; McClean, J. R.; Carter, J.; de Jong, W. A.; Siddiqi, I. Computation of Molecular Spectra on a Quantum Processor with an Error-Resilient Algorithm. *Phys. Rev. X* **2018**, *8*, 011021.

[212] Li, Y.; Benjamin, S. C. Efficient Variational Quantum Simulator Incorporating Active Error Minimization. *Phys. Rev. X* **2017**, *7*, 021050.

[213] Takeshita, T.; Rubin, N. C.; Jiang, Z.; Lee, E.; Babbush, R.; McClean, J. R. Increasing the Representation Accuracy of Quantum Simulations of Chemistry without Extra Quantum Resources. *Phys. Rev. X* **2020**, *10*, 011004.

[214] Temme, K.; Bravyi, S.; Gambetta, J. M. Error Mitigation for Short-Depth Quantum Circuits. *Phys. Rev. Lett.* **2017**, *119*, 180509.

[215] Kandala, A.; Temme, K.; Córcoles, A. D.; Mezzacapo, A.; Chow, J. M.; Gambetta, J. M. Error mitigation extends the computational reach of a noisy quantum processor. *Nature* **2019**, 049195.

[216] Otten, M.; Gray, S. K. Recovering noise-free quantum observables. *Phys. Rev. A* **2019**, *99*, 012338.

[217] Bonet-Monroig, X.; Sagastizabal, R.; Singh, M.; O'Brien, T. E. Low-cost error mitigation by symmetry verification. *Phys. Rev. A* **2018**, *98*, 062339.

[218] Kitaev, A. Fault-tolerant quantum computation by anyons. *Annals of Physics* **2003**, *303*, 2–30.

[219] Fowler, A. G.; Mariantoni, M.; Martinis, J. M.; Cleland, A. N. Surface codes: Towards practical large-scale quantum computation. *Phys. Rev. A* **2012**, *86*, 032324.

[220] Lanyon, B. P.; Maier, C.; Holzäpfel, M.; Baumgratz, T.; Hempel, C.; Jurcevic, P.; Dhand, I.; Buyskikh, A. S.; Daley, A. J.; Cramer, M.; Plenio, M. B.; Blatt, R.; Roos, C. F. Efficient tomography of a quantum many-body system. *Nat. Phys* **2017**, *13*, 1158–1162.

[221] Yen, T.-C.; Verteletskyi, V.; Izmaylov, A. F. Measuring All Compatible Operators in One Series of Single-Qubit Measurements Using Unitary Transformations. *J Theor Comput Chem.* **2020**, *16*, 2400–2409.

[222] Reagor, M.; others Demonstration of universal parametric entangling gates on a multi-qubit lattice. *Sci. Adv.* **2018**, *4*, eaao3603.

[223] Cramer, M.; Plenio, M. B.; Flammia, S. T.; Somma, R.; Gross, D.; Bartlett, S. D.; Landon-Cardinal, O.; Poulin, D.; Liu, Y.-K. Efficient quantum state tomography. *Nat. Commun* **2010**, *1*, 149.

[224] Rambach, M.; Qaryan, M.; Kewming, M.; Ferrie, C.; White, A. G.; Romero, J. Robust and Efficient High-Dimensional Quantum State Tomography. *Phys. Rev. Lett.* **2021**, *126*, 100402.

[225] Haah, J.; Harrow, A. W.; Ji, Z.; Wu, X.; Yu, N. Sample-Optimal Tomography of Quantum States. *IEEE Trans. Inf. Theory* **2017**, *63*, 5628–5641.

[226] Gupta, R.; Xia, R.; Levine, R. D.; Kais, S. Maximal Entropy Approach for Quantum State Tomography. *PRX Quantum* **2021**, *2*, 010318.

[227] Gupta, R.; Sajjan, M.; Levine, R. D.; Kais, S. Variational approach to quantum state tomography based on maximal entropy formalism. *Phys. Chem. Chem. Phys.* **2022**, *24*, 28870–28877.

[228] Gard, B. T.; Zhu, L.; Barron, G. S.; Mayhall, N. J.; Economou, S. E.; Barnes, E. Efficient symmetry-preserving state preparation circuits for the variational quantum eigensolver algorithm. *Npj Quantum Inf.* **2020**, *6*, 1–9.

[229] Tang, H. L.; Shkolnikov, V.; Barron, G. S.; Grimsley, H. R.; Mayhall, N. J.; Barnes, E.; Economou, S. E. Qubit-ADAPT-VQE: An Adaptive Algorithm for Constructing Hardware-Efficient Ansätze on a Quantum Processor. *PRX Quantum* **2021**, *2*, 020310.

[230] Aaronson, S. Shadow Tomography of Quantum States. *SIAM Journal on Computing* **2020**, *49*, STOC18–368–STOC18–394.

[231] Huang, H.-Y.; Kueng, R.; Preskill, J. Predicting many properties of a quantum system from very few measurements. *Nat. Phys* **2020**, *16*, 1050–1057.

[232] Huang, H.-Y. Learning quantum states from their classical shadows. *Nat. Rev. Phys.* **2022**, *4*, 81–81.

[233] Hu, H.-Y.; Choi, S.; You, Y.-Z. Classical shadow tomography with locally scrambled quantum dynamics. *Phys. Rev. Res.* **2023**, *5*, 023027.

[234] McGinley, M.; Leontica, S.; Garratt, S. J.; Jovanovic, J.; Simon, S. H. Quantifying information scrambling via classical shadow tomography on programmable quantum simulators. *Phys. Rev. A* **2022**, *106*, 012441.

[235] O'Gorman, B. Fermionic tomography and learning. *arXiv* **2022**,

[236] Low, G. H. Classical Shadows of Fermions with Particle Number Symmetry. *arXiv* **2022**,

[237] Fawzi, O.; Kueng, R.; Markham, D.; Oufkir, A. Learning Properties of Quantum States Without the I.I.D. Assumption. *arXiv* **2024**,

[238] Zhao, A.; Rubin, N. C.; Miyake, A. Fermionic Partial Tomography via Classical Shadows. *Phys. Rev. Lett.* **2021**, *127*, 110504.

[239] Peng, L.; Zhang, X.; Chan, G. K.-L. Fermionic reduced density low-rank matrix completion, noise filtering, and measurement reduction in quantum simulations. *arXiv* **2023**,

[240] Hearth, S. N.; Flynn, M. O.; Chandran, A.; Laumann, C. R. Efficient Local Classical Shadow Tomography with Number Conservation. *arXiv* **2023**,

[241] Gyurik, C.; Molteni, R.; Dunjko, V. Limitations of measure-first protocols in quantum machine learning. *arXiv* **2023**,

[242] Jerbi, S.; Gyurik, C.; Marshall, S. C.; Molteni, R.; Dunjko, V. Shadows of quantum machine learning. *arXiv* **2023**,

[243] Struchalin, G. I.; Zagorovskii, Y. A.; Kovlakov, E. V.; Straupe, S. S.; Kulik, S. P. Experimental Estimation of Quantum State Properties from Classical Shadows. *PRX Quantum* **2021**, *2*.

[244] Lewis, L.; Huang, H.-Y.; Tran, V. T.; Lehner, S.; Kueng, R.; Preskill, J. Improved machine learning algorithm for predicting ground state properties. *Nat. Commun.* **2024**, *15*, 895.

[245] Koh, D. E.; Grewal, S. Classical Shadows With Noise. *Quantum* **2022**, *6*, 776.

[246] Ippoliti, M.; Li, Y.; Rakovszky, T.; Khemani, V. Operator Relaxation and the Optimal Depth of Classical Shadows. *Physical Review Letters* **2023**, *130*, 230403.

[247] Nguyen, H. C.; Bönsel, J. L.; Steinberg, J.; Gühne, O. Optimizing Shadow Tomography with Generalized Measurements. *Phys. Rev. Lett.* **2022**, *129*, 220502.

[248] Helsen, J.; Walter, M. Thrifty Shadow Estimation: Reusing Quantum Circuits and Bounding Tails. *Phys. Rev. Lett.* **2023**, *131*, 240602.

[249] Coopmans, L.; Kikuchi, Y.; Benedetti, M. Predicting Gibbs-State Expectation Values with Pure Thermal Shadows. *PRX Quantum* **2023**, *4*, 010305.

[250] Guzman, E. A. R.; Lacroix, D. Restoring symmetries in quantum computing using Classical Shadows. *arXiv* **2023**,

[251] Jnane, H.; Steinberg, J.; Cai, Z.; Nguyen, H. C.; Koczor, B. Quantum Error Mitigated Classical Shadows. *PRX Quantum* **2024**, *5*, 010324.

[252] Wu, B.; Koh, D. E. Error-mitigated fermionic classical shadows on noisy quantum devices. *arXiv* **2023**,

[253] Akhtar, A. A.; Hu, H.-Y.; You, Y.-Z. Scalable and Flexible Classical Shadow Tomography with Tensor Networks. *Quantum* **2023**, *7*, 1026.

[254] Hu, H.-Y.; Gu, A.; Majumder, S.; Ren, H.; Zhang, Y.; Wang, D. S.; You, Y.-Z.; Minev, Z.; Yelin, S. F.; Seif, A. Demonstration of Robust and Efficient Quantum Property Learning with Shallow Shadows. *arXiv* **2024**,

[255] Truger, F.; Barzen, J.; Leymann, F.; Obst, J. Warm-Starting the VQE with Approximate Complex Amplitude Encoding. *arXiv* **2024**,

[256] Caprotti, A.; Morris, J.; Dakić, B. Optimising quantum tomography via shadow inversion. *arXiv* **2024**,

[257] Majsak, J.; McNulty, D.; Oszmaniec, M. A Simple and Efficient Joint Measurement Strategy for Estimating Fermionic Observables and Hamiltonians. *arXiv* **2024**,

[258] Levy, R.; Luo, D.; Clark, B. K. Classical shadows for quantum process tomography on near-term quantum computers. *Phys. Rev. Research* **2024**, *6*, 013029.

[259] Bu, K.; Koh, D. E.; Garcia, R. J.; Jaffe, A. Classical shadows with Pauli-invariant unitary ensembles. *npj Quantum Information* **2024**, *10*, 6.

[260] Becker, S.; Datta, N.; Lami, L.; Rouze, C. Classical Shadow Tomography for Continuous Variables Quantum Systems. *IEEE Trans. Inf.* **2024**, *70*, 3427–3452.

[261] Donoho, D. L. Compressed sensing. *IEEE Trans. Inf. Theory* **2006**, *52*, 1289–1306.

[262] Candès, E. J.; Romberg, J. K.; Tao, T. Stable signal recovery from incomplete and inaccurate measurements. *Commun. Pure Appl. Math.* **2006**, *59*, 1207–1223.

[263] Carrasquilla, J.; Torlai, G.; Melko, R. G.; Aolita, L. Reconstructing quantum states with generative models. *Nat. Mach. Intell* **2019**, *1*, 155–161.

[264] Mukherjee, K.; Schachenmayer, J.; Whitlock, S.; Wüster, S. Quantum network tomography of small Rydberg arrays by machine learning. *Phys. Rev. A* **2025**, *111*, 043319.

[265] Flammia, S. T.; Liu, Y.-K. Direct fidelity estimation from few Pauli measurements. *Phys. Rev. Lett.* **2011**, *106*, 230501.

[266] Zhang, X.; Luo, M.; Wen, Z.; Feng, Q.; Pang, S.; Luo, W.; Zhou, X. Direct fidelity estimation of quantum states using machine learning. *Phys. Rev. Lett.* **2021**, *127*, 130503.

[267] Seshadri, A.; Ringbauer, M.; Spainhour, J.; Blatt, R.; Monz, T.; Becker, S. Versatile fidelity estimation with confidence. *Phys. Rev. Lett.* **2024**, *133*, 020402.

[268] Singh, V.; Gupta, R.; Sajjan, M.; Remacle, F.; Levine, R. D.; Kais, S. Maximal Entropy Formalism and the Restricted Boltzmann Machine. *J. Phys. Chem. A.* **2025**, *129*, 5405–5414.

[269] Zhang, D.-J.; Tong, D. M. Krylov shadow tomography: Efficient estimation of quantum Fisher information. *Phys. Rev. Lett.* **2025**, *134*, 110802.

[270] Castaneda, J.; Wiebe, N. Hamiltonian Learning via Shadow Tomography of Pseudo-Choi States. *Quantum* **2025**, *9*, 1700.

[271] Somma, R. D.; King, R.; Kothari, R.; O'Brien, T. E.; Babbush, R. Shadow Hamiltonian simulation. *Nat. Commun.* **2025**, *16*, 57451.

[272] King, R.; Gosset, D.; Kothari, R.; Babbush, R. Triply efficient shadow tomography. Proceedings of the 2025 Annual ACM-SIAM Symposium on Discrete Algorithms (SODA). 2025; pp 914–946.

[273] Reiher, M.; Wiebe, N.; Svore, K. M.; Wecker, D.; Troyer, M. Elucidating reaction mechanisms on quantum computers. *Proceedings of the National Academy of Sciences* **2017**, *114*, 7555–7560.

[274] Caesura, A.; Cortes, C. L.; Pol, W.; Sim, S.; Steudtner, M.; Anselmetti, G.-L. R.; Degroote, M.; Moll, N.; Santagati, R.; Streif, M.; Tautermann, C. S. Faster Quantum Chemistry Simulations on a Quantum Computer with Improved Tensor Factorization and Active Volume Compilation. *PRX Quantum* **2025**, *6*.

[275] Childs, A. M.; Maslov, D.; Nam, Y.; Ross, N. J.; Su, Y. Toward the first quantum simulation with quantum speedup. *Proceedings of the National Academy of Sciences* **2018**, *115*, 9456–9461.

[276] Bauer, B.; Bravyi, S.; Motta, M.; Chan, G. K.-L. Quantum Algorithms for Quantum Chemistry and Quantum Materials Science. *Chemical Reviews* **2020**, *120*, 12685–12717.

[277] Klippenstein, S. J.; Pande, V. S.; Truhlar, D. G. Chemical Kinetics and Mechanisms of Complex Systems: A Perspective on Recent Theoretical Advances. *Journal of the American Chemical Society* **2014**, *136*, 528–546.

[278] Cao, Y.; Romero, J.; Olson, J. P.; Degroote, M.; Johnson, P. D.; Kieferová, M.; Kivlichan, I. D.; Menke, T.; Peropadre, B.; Sawaya, N. P. D.; Sim, S.; Veis, L.; Aspuru-Guzik, A. Quantum Chemistry in the Age of Quantum Computing. *Chemical Reviews* **2019**, *119*, 10856–10915, PMID: 31469277.

[279] Alexeev, Y. et al. A Perspective on Quantum Computing Applications in Quantum Chemistry Using 25–100 Logical Qubits. *Journal of Chemical Theory and Computation* **2025**, *21*, 11335–11357.

[280] Verma, S.; Mitra, A.; Wang, Q.; D'Cunha, R.; Jangid, B.; Hennefarth, M. R.; Agarawal, V.; Otis, L.; Haldar, S.; Hermes, M. R.; Gagliardi, L. Multireference Embedding and Fragmentation Methods for Classical and Quantum Computers: From Model Systems to Realistic Applications. *Chemical Reviews* **2026**, *126*, 184–203.

[281] Jordan, P.; Wigner, E. Über das Paulische Äquivalenzverbot. *Zeitschrift für Physik* **1928**, *47*, 631–651.

[282] Bravyi, S. B.; Kitaev, A. Y. Fermionic Quantum Computation. *Ann. Phys.* **2002**, *298*, 210–226.

[283] Seeley, J. T.; Richard, M. J.; Love, P. J. The Bravyi-Kitaev transformation for quantum computation of electronic structure. *The Journal of Chemical Physics* **2012**, *137*.

[284] Tranter, A.; Love, P. J.; Mintert, F.; Coveney, P. V. A Comparison of the Bravyi–Kitaev and Jordan–Wigner Transformations for the Quantum Simulation of Quantum Chemistry. *Journal of Chemical Theory and Computation* **2018**, *14*, 5617–5630.

[285] Setia, K.; Whitfield, J. D. Bravyi-Kitaev Superfast simulation of electronic structure on a quantum computer. *The Journal of Chemical Physics* **2018**, *148*.

[286] Abrams, D. S.; Lloyd, S. Simulation of Many-Body Fermi Systems on a Universal Quantum Computer. *Physical Review Letters* **1997**, *79*, 2586–2589.

[287] Abrams, D. S.; Lloyd, S. Quantum Algorithm Providing Exponential Speed Increase for Finding Eigenvalues and Eigenvectors. *Physical Review Letters* **1999**, *83*, 5162–5165.

[288] Sun, J.; Zeng, P.; Gur, T.; Kim, M. S. High-precision and low-depth quantum algorithm design for eigenstate problems. *Science Advances* **2026**, *12*.

[289] Kitaev, A. Y. Quantum measurements and the Abelian Stabilizer Problem. 1995; `https://arxiv.org/abs/quant-ph/9511026`.

[290] Cleve, R.; Ekert, A.; Macchiavello, C.; Mosca, M. Quantum algorithms revisited. *Proceedings of the Royal Society of London. Series A: Mathematical, Physical and Engineering Sciences* **1998**, *454*, 339–354.

[291] Knill, E.; Ortiz, G.; Somma, R. D. Optimal quantum measurements of expectation values of observables. *Physical Review A* **2007**, *75*.

[292] Poulin, D.; Wocjan, P. Sampling from the Thermal Quantum Gibbs State and Evaluating Partition Functions with a Quantum Computer. *Physical Review Letters* **2009**, *103*.

[293] Peruzzo, A.; McClean, J.; Shadbolt, P.; Yung, M.-H.; Zhou, X.-Q.; Love, P. J.; Aspuru-Guzik, A.; O'Brien, J. L. A variational eigenvalue solver on a photonic quantum processor. *Nature Communications* **2014**, *5*.

[294] Lee, J.; Huggins, W. J.; Head-Gordon, M.; Whaley, K. B. Generalized Unitary Coupled Cluster Wave functions for Quantum Computation. *Journal of Chemical Theory and Computation* **2018**, *15*, 311–324.

[295] Hoffmann, M. R.; Simons, J. A unitary multiconfigurational coupled-cluster method: Theory and applications. *The Journal of Chemical Physics* **1988**, *88*, 993–1002.

[296] Kandala, A.; Mezzacapo, A.; Temme, K.; Takita, M.; Brink, M.; Chow, J. M.; Gambetta, J. M. Hardware-efficient variational quantum eigensolver for small molecules and quantum magnets. *Nature* **2017**, *549*, 242–246.

[297] Grimsley, H. R.; Economou, S. E.; Barnes, E.; Mayhall, N. J. An adaptive variational algorithm for exact molecular simulations on a quantum computer. *Nature Communications* **2019**, *10*.

[298] Ryabinkin, I. G.; Lang, R. A.; Genin, S. N.; Izmaylov, A. F. Iterative Qubit Coupled Cluster Approach with Efficient Screening of Generators. *Journal of Chemical Theory and Computation* **2020**, *16*, 1055–1063.

[299] Ryabinkin, I. G.; Yen, T.-C.; Genin, S. N.; Izmaylov, A. F. Qubit Coupled Cluster Method: A Systematic Approach to Quantum Chemistry on a Quantum Computer. *Journal of Chemical Theory and Computation* **2018**, *14*, 6317–6326.

[300] Lloyd, S. Universal Quantum Simulators. *Science* **1996**, *273*, 1073–1078.

[301] O'Malley, P. et al. Scalable Quantum Simulation of Molecular Energies. *Physical Review X* **2016**, *6*.

[302] Childs, A. M.; Su, Y. Nearly Optimal Lattice Simulation by Product Formulas. *Physical Review Letters* **2019**, *123*.

[303] Childs, A. M.; Su, Y.; Tran, M. C.; Wiebe, N.; Zhu, S. Theory of Trotter Error with Commutator Scaling. *Physical Review X* **2021**, *11*.

[304] Babbush, R.; McClean, J.; Wecker, D.; Aspuru-Guzik, A.; Wiebe, N. Chemical basis of Trotter-Suzuki errors in quantum chemistry simulation. *Physical Review A* **2015**, *91*.

[305] Low, G. H.; Chuang, I. L. Hamiltonian Simulation by Qubitization. *Quantum* **2019**, *3*, 163.

[306] Motta, M.; Sun, C.; Tan, A. T. K.; O'Rourke, M. J.; Ye, E.; Minnich, A. J.; Brandão, F. G. S. L.; Chan, G. K.-L. Determining eigenstates and thermal states on a quantum computer using quantum imaginary time evolution. *Nature Physics* **2019**, *16*, 205–210.

[307] Ollitrault, P. J.; Kandala, A.; Chen, C.-F.; Barkoutsos, P. K.; Mezzacapo, A.; Pistoia, M.; Sheldon, S.; Woerner, S.; Gambetta, J. M.; Tavernelli, I. Quantum equation of motion for computing molecular excitation energies on a noisy quantum processor. *Phys. Rev. Res.* **2020**, *2*, 043140.

[308] Temme, K.; Bravyi, S.; Gambetta, J. M. Error Mitigation for Short-Depth Quantum Circuits. *Physical Review Letters* **2017**, *119*.

[309] van den Berg, E.; Minev, Z. K.; Kandala, A.; Temme, K. Probabilistic error cancellation with sparse Pauli–Lindblad models on noisy quantum processors. *Nature Physics* **2023**, *19*, 1116–1121.

[310] Wan, K.; Huggins, W. J.; Lee, J.; Babbush, R. Matchgate Shadows for Fermionic Quantum Simulation. *Communications in Mathematical Physics* **2023**, *404*, 629–700.

[311] Seif, A.; Cian, Z.-P.; Zhou, S.; Chen, S.; Jiang, L. Shadow Distillation: Quantum Error Mitigation with Classical Shadows for Near-Term Quantum Processors. *PRX Quantum* **2023**, *4*, 010303.

[312] Helsen, J.; Ioannou, M.; Kitzinger, J.; Onorati, E.; Werner, A. H.; Eisert, J.; Roth, I. Shadow estimation of gate-set properties from random sequences. *Nature Communications* **2023**, *14*, 5039.

[313] Kunjummen, J.; Tran, M. C.; Carney, D.; Taylor, J. M. Shadow process tomography of quantum channels. *Physical Review A* **2023**, *107*, 042403.

[314] McGinley, M.; Fava, M. Shadow Tomography from Emergent State Designs in Analog Quantum Simulators. *Physical Review Letters* **2023**, *131*, 160601.

[315] Helsen, J.; Walter, M. Thrifty Shadow Estimation: Reusing Quantum Circuits and Bounding Tails. *Physical Review Letters* **2023**, *131*, 240602.

[316] O'Donnell, R.; Wright, J. Efficient quantum tomography. Proceedings of the forty-eighth annual ACM symposium on Theory of Computing. 2016.

[317] Corcoles, A. D.; Kandala, A.; Javadi-Abhari, A.; McClure, D. T.; Cross, A. W.; Temme, K.; Nation, P. D.; Steffen, M.; Gambetta, J. M. Challenges and Opportunities of Near-Term Quantum Computing Systems. *Proceedings of the IEEE* **2020**, *108*, 1338–1352.

[318] Jiang, X.; Wang, K.; Qian, K.; Chen, Z.; Chen, Z.; Lu, L.; Xia, L.; Song, F.; Zhu, S.; Ma, X. Towards the standardization of quantum state verification using optimal strategies. *Npj Quantum Inf.* **2020**, *6*, 90.

[319] Smart, S. E.; Mazziotti, D. A. Quantum Solver of Contracted Eigenvalue Equations for Scalable Molecular Simulations on Quantum Computing Devices. *Phys. Rev. Lett.* **2021**, *126*, 070504.

[320] Benavides-Riveros, C. L.; Chen, L.; Schilling, C.; Mantilla, S.; Pittalis, S. Excitations of Quantum Many-Body Systems via Purified Ensembles: A Unitary-Coupled-Cluster-Based Approach. *Phys. Rev. Lett.* **2022**, *129*, 066401.

[321] Kummer, H. $N$-Representability Problem for Reduced Density Matrices. *J. Math. Phys.* **1967**, *8*, 2063–2081.

[322] Mazziotti, D. A. Variational reduced-density-matrix method using three-particle $N$-representability conditions with application to many-electron molecules. *Phys. Rev. A* **2006**, *74*, 032501.

[323] Mazziotti, D. A. Structure of Fermionic Density Matrices: Complete $N$-Representability Conditions. *Phys. Rev. Lett.* **2012**, *108*, 263002.

[324] Mazziotti, D. A. Quantum Many-Body Theory from a Solution of the $N$-Representability Problem. *Phys. Rev. Lett.* **2023**, *130*, 153001.

[325] Vandenberghe, L.; Boyd, S. Semidefinite Programming. *SIAM Review* **1996**, *38*, 49–95.

[326] Baumgratz, T.; Plenio, M. B. Lower bounds for ground states of condensed matter systems. *New J. Phys.* **2012**, *14*, 023027.

[327] Mazziotti, D. A. Enhanced Constraints for Accurate Lower Bounds on Many-Electron Quantum Energies from Variational Two-Electron Reduced Density Matrix Theory. *Phys. Rev. Lett.* **2016**, *117*, 153001.

[328] Alcoba, D. R.; Torre, A.; Lain, L.; Massaccesi, G. E.; Oña, O. B.; Honoré, E. M.; Poelmans, W.; Neck, D. V.; Bultinck, P.; Baerdemacker, S. D. Direct variational determination of the two-electron reduced density matrix for doubly occupied-configuration-interaction wave functions: The influence of three-index N-representability conditions. *J. Chem. Phys.* **2018**, *148*, 024105.

[329] Mazziotti, D. A. Dual-cone variational calculation of the two-electron reduced density matrix. *Phys. Rev. A* **2020**, *102*, 052819.

[330] Li, R. R.; Liebenthal, M. D.; DePrince, A. E. Challenges for variational reduced-density-matrix theory with three-particle N-representability conditions. *J. Chem. Phys.* **2021**, *155*, 174110.

[331] Piris, M. Global Natural Orbital Functional: Towards the Complete Description of the Electron Correlation. *Phys. Rev. Lett.* **2021**, *127*, 233001.

[332] Knight, M. J.; Quiney, H. M.; Martin, A. M. Reduced density matrix approach to ultracold few-fermion systems in one dimension. *New J. Phys.* **2022**, *24*, 053004.

[333] Boyn, J.-N.; Xie, J.; Anderson, J. S.; Mazziotti, D. A. Entangled Electrons Drive a Non-superexchange Mechanism in a Cobalt Quinoid Dimer Complex. *J. Phys. Chem. Lett.* **2020**, *11*, 4584–4590.

[334] Kawamura, A.; Xie, J.; Boyn, J.-N.; Jesse, K. A.; McNeece, A. J.; Hill, E. A.; Collins, K. A.; Valdez-Moreira, J. A.; Filatov, A. S.; Kurutz, J. W.; Mazziotti, D. A.; Anderson, J. S. Reversible Switching of Organic Diradical Character via Iron-Based Spin-Crossover. *J. Am. Chem. Soc.* **2020**, *142*, 17670–17680.

[335] Xie, J. et al. Intrinsic glassy-metallic transport in an amorphous coordination polymer. *Nature* **2022**, *611*, 479–484.

[336] Schouten, A. O.; Klevens, J. E.; Sager-Smith, L. M.; Xie, J.; Anderson, J. S.; Mazziotti, D. A. Potential for exciton condensation in a highly conductive amorphous polymer. *Phys. Rev. Mat.* **2023**, *7*, 045001.

[337] Haar, A. Der Massbegriff in der Theorie der Kontinuierlichen Gruppen. *The Annals of Mathematics* **1933**, *34*, 147.

[338] Candès, E. J.; Recht, B. Exact Matrix Completion via Convex Optimization. *Found. Comput. Math.* **2009**, *9*, 717.

[339] Cai, J.-F.; Cands, E. J.; Shen, Z. A Singular Value Thresholding Algorithm for Matrix Completion. *SIAM J. Optim.* **2010**, *20*, 1956–1982.

[340] Foley, J. J.; Mazziotti, D. A. Measurement-driven reconstruction of many-particle quantum processes by semidefinite programming with application to photosynthetic light harvesting. *Phys. Rev. A* **2012**, *86*, 012512.

[341] Rubin, N. C.; Babbush, R.; McClean, J. Application of fermionic marginal constraints to hybrid quantum algorithms. *New J. Phys.* **2018**, *20*, 053020.

[342] Smart, S. E.; Mazziotti, D. A. Quantum-classical hybrid algorithm using an error-mitigating N-representability condition to compute the Mott metal-insulator transition. *Phys. Rev. A* **2019**, *100*, 022517.

[343] Smart, S. E.; Boyn, J.-N.; Mazziotti, D. A. Resolving correlated states of benzyne with an error-mitigated contracted quantum eigensolver. *Phys. Rev. A* **2022**, *105*, 022405.

[344] Piskor, T.; Eich, F. G.; Marthaler, M.; Wilhelm, F. K.; Reiner, J.-M. Post-processing noisy quantum computations utilizing $N$-representability constraints. *arXiv* **2023**,

[345] Gidofalvi, G.; Mazziotti, D. A. Spin and symmetry adaptation of the variational two-electron reduced-density-matrix method. *Phys. Rev. A* **2005**, *72*, 052505.

[346] *Maple*; Maplesoft, Waterloo, 2023.

[347] *RDMChem, Quantum Chemistry Package*; Maplesoft, Waterloo, 2023.

[348] Suhai, S. Electron correlation in extended systems: Fourth-order many-body perturbation theory and density-functional methods applied to an infinite chain of hydrogen atoms. *Phys. Rev. B* **1994**, *50*, 14791–14801.

[349] Hehre, W. J.; Stewart, R. F.; Pople, J. A. Self-Consistent Molecular-Orbital Methods. I. Use of Gaussian Expansions of Slater-Type Atomic Orbitals. *Chem. Phys.* **1969**, *51*, 2657–2664.

[350] Dunning, T. H. Gaussian basis sets for use in correlated molecular calculations. I. The atoms boron through neon and hydrogen. *Chem. Phys.* **1989**, *90*, 1007–1023.

[351] Cerullo, G.; Polli, D.; Lanzani, G.; De Silvestri, S.; Hashimoto, H.; Cogdell, R. J. Photosynthetic Light Harvesting by Carotenoids: Detection of an Intermediate Excited State. *Science* **2002**, *298*, 2395–2398.

[352] Cheng, Y.-C.; Fleming, G. R. Dynamics of Light Harvesting in Photosynthesis. *Annual Review of Physical Chemistry* **2009**, *60*, 241–262.

[353] Herbst, J.; Heyne, K.; Diller, R. Femtosecond Infrared Spectroscopy of Bacteriorhodopsin Chromophore Isomerization. *Science* **2002**, *297*, 822–825.

[354] Schultz, T.; Samoylova, E.; Radloff, W.; Hertel, I. V.; Sobolewski, A. L.; Domcke, W. Efficient Deactivation of a Model Base Pair via Excited-State Hydrogen Transfer. *Science* **2004**, *306*, 1765–1768.

[355] Yam, V. W.-W. Using synthesis to steer excited states and their properties and functions. *Nat. Synth.* **2023**, *2*, 94–100.

[356] Hsu, L.-Y.; Jin, B.-Y.; Chen, C.-h.; Peng, S.-M. Reaction: New Insights into Molecular Electronics. *Chem* **2017**, *3*, 378–379.

[357] Lindh, R.; González, L. *Quantum Chemistry and Dynamics of Excited States: Methods and Applications*; John Wiley & Sons, 2020.

[358] Bustard, T. M.; Jaffé, H. H. Excited-State Variational Calculations with Orthogonality Constraint. *J. Chem. Phys.* **1970**, *53*, 534–539.

[359] Glushkov, V. Excitation Energies from a Partially Spin-Restricted Wave Function. *Computing Letters* **2007**, *3*, 65–69.

[360] Tassi, M.; Theophilou, I.; Thanos, S. Hartree–Fock calculation for excited states. *Int. J. Quantum Chem.* **2013**, *113*, 690–693.

[361] Balková, A.; Bartlett, R. J. A multireference coupled-cluster study of the ground state and lowest excited states of cyclobutadiene. *J. Chem. Phys.* **1994**, *101*, 8972–8987.

[362] Parac, M.; Grimme, S. Comparison of Multireference MøllerPlesset Theory and Time-Dependent Methods for the Calculation of Vertical Excitation Energies of Molecules. *J. Phys. Chem. A* **2002**, *106*, 6844–6850.

[363] Mazziotti, D. A. Extraction of electronic excited states from the ground-state two-particle reduced density matrix. *Phys. Rev. A* **2003**, *68*.

[364] Sundstrom, E. J.; Head-Gordon, M. Non-orthogonal configuration interaction for the calculation of multielectron excited states. *J. Chem. Phys.* **2014**, *140*.

[365] Bharti, K.; Cervera-Lierta, A.; Kyaw, T. H.; Haug, T.; Alperin-Lea, S.; Anand, A.; Degroote, M.; Heimonen, H.; Kottmann, J. S.; Menke, T.; Mok, W.-K.; Sim, S.; Kwek, L.-C.; Aspuru-Guzik, A. Noisy intermediate-scale quantum algorithms. *Rev. Mod. Phys.* **2022**, *94*, 015004.

[366] Garrod, C.; Rosina, M. Particle-Hole Matrix: Its Connection with the Symmetries and Collective Features of the Ground State. *J. Math. Phys.* **1969**, *10*, 1855–1861.

[367] Mazziotti, D. A. Significant conditions for the two-electron reduced density matrix from the constructive solution of $N$ representability. *Phys. Rev. A* **2012**, *85*, 062507.

[368] Mazziotti, D. A. Pure-$N$-representability conditions of two-fermion reduced density matrices. *Phys. Rev. A* **2016**, *94*, 032516.

[369] Gidofalvi, G.; Mazziotti, D. A. Computation of quantum phase transitions by reduced-density-matrix mechanics. *Phys. Rev. A* **2006**, *74*.

[370] Mazziotti, D. A. Realization of Quantum Chemistry without Wave Functions through First-Order Semidefinite Programming. *Phys. Rev. Lett.* **2004**, *93*, 213001.

[371] Ceperley, D.; Alder, B. Quantum Monte Carlo. *Science* **1986**, *231*, 555–560.

[372] Higgott, O.; Wang, D.; Brierley, S. Variational Quantum Computation of Excited States. *Quantum* **2019**, *3*, 156.

[373] Nakanishi, K. M.; Mitarai, K.; Fujii, K. Subspace-search variational quantum eigensolver for excited states. *Phys. Rev. Research* **2019**, *1*, 033062.

[374] Wang, Y.; Sager-Smith, L. M.; Mazziotti, D. A. Quantum Simulation of Bosons with the Contracted Quantum Eigensolver. arXiv preprint, 2023; `https://arxiv.org/abs/2307.07088`.

[375] Smart, S. E.; Mazziotti, D. A. Verifiably exact solution of the electronic Schrödinger equation on quantum devices. *Physical Review A* **2024**, *109*.

[376] Sicilia, F.; Blancafort, L.; Bearpark, M. J.; Robb, M. A. Quadratic Description of Conical Intersections: Characterization of Critical Points on the Extended Seam. *J. Phys. Chem. A* **2007**, *111*, 2182–2192.

[377] Snyder, J. W.; Mazziotti, D. A. Photoexcited conversion of gauche-1, 3-butadiene to bicyclobutane via a conical intersection: Energies and reduced density matrices from the anti-Hermitian contracted Schrödinger equation. *J. Chem. Phys.* **2011**, *135*.

[378] Mazziotti, D. A. Energy Barriers in the Conversion of Bicyclobutane to gauche-1, 3-Butadiene from the Anti-Hermitian Contracted Schrödinger Equation. *J. Phys. Chem. A* **2008**, *112*, 13684–13690.

[379] Boyn, J.-N.; Mazziotti, D. A. Elucidating the molecular orbital dependence of the total electronic energy in multireference problems. *J. Chem. Phys.* **2022**, *156*.

[380] Shevlin, P. B.; McKee, M. L. Theoretical investigation of the thermal ring opening of bicyclobutane to butadiene. Evidence for a nonsynchronous process. *J. Am. Chem Soc.* **1988**, *110*, 1666–1671.

[381] Nguyen, K. A.; Gordon, M. S. Isomerization Of Bicyclo[1.1.0]butane to Butadiene. *J. Am. Chem Soc.* **1995**, *117*, 3835–3847.

[382] Kinal, A.; Piecuch, P. Computational Investigation of the Conrotatory and Disrotatory Isomerization Channels of Bicyclo[1.1.0]butane to Buta-1, 3-diene: A Completely Renormalized Coupled-Cluster Study. *J. Phys. Chem. A* **2007**, *111*, 734–742.

[383] Lutz, J. J.; Piecuch, P. Extrapolating potential energy surfaces by scaling electron correlation: Isomerization of bicyclobutane to butadiene. *J. Chem. Phys.* **2008**, *128*.

[384] Craig, D. P. Configurational interaction in molecular orbital theory. A higher approximation in the non-empirical method. *Proc. R Soc. Lond. A Math. Phys. Sci.* **1950**, *200*, 474–486.

[385] Knowles, P.; Handy, N. A new determinant-based full configuration interaction method. *Chem. Phys. Lett.* **1984**, *111*, 315–321.

[386] Rassolov, V. A.; Pople, J. A.; Ratner, M. A.; Windus, T. L. 6-31G* basis set for atoms K through Zn. *J. Chem. Phys.* **1998**, *109*, 1223–1229.

[387] Dick, B.; Haas, Y.; Zilberg, S. Locating conical intersections relevant to photochemical reactions. *Chem. Phys.* **2008**, *347*, 65–77.

[388] Bernardi, F.; Olivucci, M.; Robb, M. A. The role of conical intersections and excited state reaction paths in photochemical pericyclic reactions. *J. Photochem. Photobiol., A* **1997**, *105*, 365–371.

[389] Ostojić, B.; Domcke, W. Ab initio investigation of the potential energy surfaces involved in the photophysics of s-trans-1, 3-butadiene. *Chem. Phys.* **2001**, *269*, 1–10.

[390] Woodward, R. B.; Hoffmann, R. *The Conservation of Orbital Symmetry*; Academic: New York, 1970.

[391] Köuppel, H.; Domcke, W.; Cederbaum, L. S. *Advances in Chemical Physics*; John Wiley & Sons, Ltd, 1984; pp 59–246.

[392] Kunjummen, J.; Tran, M. C.; Carney, D.; Taylor, J. M. Shadow process tomography of quantum channels. *Physical Review A* **2023**, *107*.

[393] Vogel, K.; Risken, H. Determination of quasiprobability distributions in terms of probability distributions for the rotated quadrature phase. *Phys. Rev. A* **1989**, *40*, 2847–2849.

[394] Hradil, Z. Quantum-state estimation. *Phys. Rev. A* **1997**, *55*, R1561–R1564.

[395] James, D. F. V.; Kwiat, P. G.; Munro, W. J.; White, A. G. Measurement of qubits. *Phys. Rev. A* **2001**, *64*, 052312.

[396] Paris, M., Řeháček, J., Eds. *Quantum State Estimation*; Lecture Notes in Physics; Springer: Berlin, Heidelberg, 2004; Vol. 649.

[397] Huggins, W. J.; O'Gorman, B. A.; Rubin, N. C.; Reichman, D. R.; Babbush, R.; Lee, J. Unbiasing fermionic quantum Monte Carlo with a quantum computer. *Nature* **2022**, *603*, 416–420.

[398] Zhao, A.; Miyake, A. Group-theoretic error mitigation enabled by classical shadows and symmetries. *npj Quantum Inf.* **2024**, *10*, 854.

[399] Huang, B.; Chen, Y.-T.; Gupt, B.; Suchara, M.; Tran, A.; McArdle, S.; Galli, G. Evaluating a quantum-classical quantum Monte Carlo algorithm with matchgate shadows. *Phys. Rev. Res.* **2024**, *6*, 043063.

[400] Mazziotti, D. A. Variational minimization of atomic and molecular ground-state energies via the two-particle reduced density matrix. *Phys. Rev. A* **2002**, *65*, 062511.

[401] Mazziotti, D. A. Realization of Quantum Chemistry without Wave Functions through First-Order Semidefinite Programming. *Phys. Rev. Lett.* **2004**, *93*, 213001.

[402] Mazziotti, D. A. Enhanced Constraints for Accurate Lower Bounds on Many-Electron Quantum Energies from Variational Two-Electron Reduced Density Matrix Theory. *Phys. Rev. Lett.* **2016**, *117*, 153001.

[403] Mazziotti, D. A. Dual-cone variational calculation of the two-electron reduced density matrix. *Phys. Rev. A* **2020**, *102*, 052819.

[404] Gao, Q.; Lanzetta, R. A.; Ledwith, P.; Wang, J.; Khalaf, E. Bootstrapping the Quantum Hall Problem. *Phys. Rev. X* **2025**, *15*, 031034.

[405] Schouten, A. O.; Ewing, S.; Mazziotti, D. A. Bootstrapping the Electronic Structure of Quantum Materials. *arXiv* **2025**,

[406] Elben, A.; Yu, J.; Zhu, G.; Hafezi, M.; Pollmann, F.; Zoller, P.; Vermersch, B. Many-body topological invariants from randomized measurements in synthetic quantum matter. *Sci. Adv.* **2020**, *6*, eaz3666.

[407] Elben, A.; Flammia, S. T.; Huang, H.-Y.; Kueng, R.; Preskill, J.; Vermersch, B.; Zoller, P. The randomized measurement toolbox. *Nature Reviews Physics* **2022**, *5*, 9–24.

[408] Jiang, Z.; Kalev, A.; Mruczkiewicz, W.; Neven, H. Optimal fermion-to-qubit mapping via ternary trees with applications to reduced quantum states learning. *Quantum* **2020**, *4*, 276.

[409] O'Brien, T. E.; Senjean, B.; Sagastizabal, R.; Bonet-Monroig, X.; Dutkiewicz, A.; Buda, F.; DiCarlo, L.; Visscher, L. Calculating energy derivatives for quantum chemistry on a quantum computer. *npj Quantum Inf.* **2019**, *5*, 113.

[410] Overy, C.; Booth, G. H.; Blunt, N. S.; Shepherd, J. J.; Cleland, D.; Alavi, A. Unbiased reduced density matrices and electronic properties from full configuration interaction quantum Monte Carlo. *J. Chem. Phys.* **2014**, *141*, 244117.

[411] Gidofalvi, G.; Mazziotti, D. A. Molecular properties from variational reduced-density-matrix theory with three-particle $N$-representability conditions. *J. Chem. Phys.* **2007**, *126*, 024105.

[412] Evans, J. P.; Steuer, R. E. A revised simplex method for linear multiple objective programs. *Math. Program.* **1973**, *5*, 54–72.

[413] Zeleny, M. *Linear Multi-Objective Programming*; Springer-Verlag: New York, NY, 1974.

[414] Foley, J. J.; Mazziotti, D. A. Measurement-driven reconstruction of many-particle quantum processes by semidefinite programming with application to photosynthetic light harvesting. *Phys. Rev. A* **2012**, *86*, 012512.

[415] Kotil, A.; Pelofske, E.; Riedmüller, S.; Egger, D. J.; Eidenbenz, S.; Koch, T.; Woerner, S. Quantum approximate multi-objective optimization. *Nat. Comput. Sci.* **2025**, *5*, 873.

[416] Recht, B.; Fazel, M.; Parrilo, P. A. Guaranteed Minimum-Rank Solutions of Linear Matrix Equations via Nuclear Norm Minimization. *SIAM Review* **2010**, *52*, 471–501.

[417] Beck, C.; D'Andrea, R. Computational study and comparisons of LFT reducibility methods. Proceedings of the 1998 American Control Conference (ACC). 1998; pp 1013–1017, Vol. 2.

[418] Mesbahi, M.; Papavassilopoulos, G. On the rank minimization problem over a positive semidefinite linear matrix inequality. *IEEE Trans. Autom. Control* **1997**, *42*, 239–243.

[419] Wang, Y.; Avdic, I.; Rose, M.; Torres, L. I. P.; Schouten, A. O.; Sung, K. J.; Mazziotti, D. A. Correlated Purification for Restoring $N$-Representability in Quantum Simulation. 2025; `https://arxiv.org/abs/2511.10789`.

[420] Liebert, J.; Castillo, F.; Labbé, J.-P.; Schilling, C. Foundation of One-Particle Reduced Density Matrix Functional Theory for Excited States. *J Theor Comput Chem.* **2021**, *18*, 124–140.

[421] Mazziotti, D. A.; Erdahl, R. M. Uncertainty relations and reduced density matrices: Mapping many-body quantum mechanics onto four particles. *Phys. Rev. A* **2001**, *63*, 042113.

[422] *Maple*; Maplesoft, Waterloo, 2025.

[423] *RDMChem, Quantum Chemistry Package*; Maplesoft, Waterloo, 2025.

[424] The ffsim developers ffsim: Faster simulations of fermionic quantum circuits. `https://github.com/qiskit-community/ffsim`.

[425] Stephens, P. J.; Devlin, F. J.; Chabalowski, C. F.; Frisch, M. J. Ab Initio Calculation of Vibrational Absorption and Circular Dichroism Spectra Using Density Functional Force Fields. *J. Phys. Chem.* **1994**, *98*, 11623–11627.

[426] Becke, A. D. Density-functional thermochemistry. III. The role of exact exchange. *J. Chem. Phys.* **1993**, *98*, 5648–5652.

[427] Motta, M.; Sung, K. J.; Whaley, K. B.; Head-Gordon, M.; Shee, J. Bridging physical intuition and hardware efficiency for correlated electronic states: the local unitary cluster Jastrow ansatz for electronic structure. *Chem. Sci.* **2023**, *14*, 11213–11227.

[428] Sagastizabal, R.; Bonet-Monroig, X.; Singh, M.; others Experimental error mitigation via symmetry verification in a variational quantum eigensolver. *Phys. Rev. A* **2019**, *100*, 010302.

[429] O'Brien, T. E.; Anselmetti, G.; Gkritsis, F.; others Purification-based quantum error mitigation of pair-correlated electron simulations. *Nature Physics* **2023**, *19*, 1787–1792.

[430] Schrödinger, E. Discussion of Probability Relations between Separated Systems. *Math. Proc. Camb. Philos. Soc.* **1935**, *31*, 555–563.

[431] Wootters, W. K. Quantum entanglement as a quantifiable resource. *Philos. Trans. R. Soc. London. Ser. A and Phil. Trans. R. Soc. A.* **1998**, *356*, 1717–1731.

[432] Bell, J. S. *Speakable and Unspeakable in Quantum Mechanics: Collected Papers on Quantum Philosophy*, 2nd ed.; Cambridge University Press: Cambridge, UK, 2004.

[433] Horodecki, R.; Horodecki, P.; Horodecki, M.; Horodecki, K. Quantum entanglement. *Rev. Mod. Phys.* **2009**, *81*, 865–942.

[434] Nielsen, M. A.; Chuang, I. L. *Quantum Computation and Quantum Information: 10th Anniversary Edition*, 10th ed.; Cambridge University Press: USA, 2011.

[435] Jozsa, R.; Linden, N. On the role of entanglement in quantum-computational speed-up. *Proc. R. Soc. Lond., Ser. A, Math. Phys. Eng. Sci.* **2003**, *459*, 2011–2032.

[436] Yin, J. et al. Entanglement-based secure quantum cryptography over 1, 120 kilometres. *Nature* **2020**, *582*, 501–505.

[437] Naik, D. S.; Peterson, C. G.; White, A. G.; Berglund, A. J.; Kwiat, P. G. Entangled State Quantum Cryptography: Eavesdropping on the Ekert Protocol. *Phys. Rev. Lett.* **2000**, *84*, 4733–4736.

[438] Chin, Z. E.; Leibrandt, D. R.; Chuang, I. L. Quantum Entanglement Enables Single-Shot Trajectory Sensing for Weakly Interacting Particles. *Phys. Rev. Lett.* **2025**, *134*, 210802.

[439] Prabhu, S.; Kremenetski, V.; Khan, S. A.; Yanagimoto, R.; McMahon, P. L. Exponential advantage in quantum sensing of correlated parameters. *arXiv:2504.21745 [quant-ph]* **2025**, `https://arxiv.org/abs/2504.21745`.

[440] Demkowicz-Dobrzański, R.; Maccone, L. Using Entanglement Against Noise in Quantum Metrology. *Phys. Rev. Lett.* **2014**, *113*, 250801.

[441] Tóth, G. Multipartite Entanglement and High-Precision Metrology. *Phys. Rev. A* **2012**, *85*, 022322.

[442] Amico, L.; Fazio, R.; Osterloh, A.; Vedral, V. Entanglement in many-body systems. *Rev. Mod. Phys.* **2008**, *80*, 517–576.

[443] Singh, H.; Chakraborty, T.; Das, D.; Jeevan, H. S.; Tokiwa, Y.; Gegenwart, P.; Mitra, C. Experimental quantification of entanglement through heat capacity. *New J. Phys.* **2013**, *15*, 113001.

[444] Wieśniak, M.; Vedral, V.; Brukner, Magnetic susceptibility as a macroscopic entanglement witness. *New J. Phys.* **2005**, *7*, 258–258.

[445] Yang, C. N. Concept of Off-Diagonal Long-Range Order and the Quantum Phases of Liquid He and of Superconductors. *Rev. Mod. Phys.* **1962**, *34*, 694–704.

[446] Penrose, O.; Onsager, L. Bose-Einstein Condensation and Liquid Helium. *Phys. Rev.* **1956**, *104*, 576–584.

[447] Safaei, S.; Mazziotti, D. A. Quantum signature of exciton condensation. *Phys. Rev. B* **2018**, *98*, 045122.

[448] Schouten, A. O.; Sager-Smith, L. M.; Mazziotti, D. A. Large cumulant eigenvalue as a signature of exciton condensation. *Phys. Rev. B* **2022**, *105*, 245151.

[449] Schouten, A. O.; Sager-Smith, L. M.; Mazziotti, D. A. Exciton-Condensate-Like Amplification of Energy Transport in Light Harvesting. *PRX Energy* **2023**, *2*.

[450] Adolphs, J.; Renger, T. How Proteins Trigger Excitation Energy Transfer in the FMO Complex of Green Sulfur Bacteria. *Biophys. J.* **2006**, *91*, 2778–2797.

[451] Schouten, A. O.; Mazziotti, D. A. Exciton-Condensate-Like Energy Transport in Light-Harvesting Complex 2. *PRX Energy* **2025**, *4*.

[452] Payne Torres, L. I.; Schouten, A. O.; Mazziotti, D. A. Lifetime of Strongly Correlated States on Near-Term Quantum Computers. *J. Phys. Chem. A* **2024**, *128*, 7269–7276.

[453] Dijkstra, A. G.; Beige, A. Efficient long-distance energy transport in molecular systems through adiabatic passage. *J. Chem. Phys.* **2019**, *151*.

[454] Mattioni, A.; Caycedo-Soler, F.; Huelga, S. F.; Plenio, M. B. Design Principles for Long-Range Energy Transfer at Room Temperature. *PRX* **2021**, *11*.

[455] Giannini, S.; Peng, W.-T.; Cupellini, L.; Padula, D.; Carof, A.; Blumberger, J. Exciton transport in molecular organic semiconductors boosted by transient quantum delocalization. *Nat. Commun.* **2022**, *13*.

[456] Mueller, T.; Malic, E. Exciton physics and device application of two-dimensional transition metal dichalcogenide semiconductors. *npj 2D Mater. Appl.* **2018**, *2*.

[457] High, A. A.; Leonard, J. R.; Hammack, A. T.; Fogler, M. M.; Butov, L. V.; Kavokin, A. V.; Campman, K. L.; Gossard, A. C. Spontaneous coherence in a cold exciton gas. *Nature* **2012**, *483*, 584–588.

[458] Raeber, A.; Mazziotti, D. A. Large eigenvalue of the cumulant part of the two-electron reduced density matrix as a measure of off-diagonal long-range order. *Physical Review A* **2015**, *92*, 052502.

[459] Ma, E. S.; Song, Z. Superconducting state generated dynamically from distant pair source and drain. *New J. Phys.* **2024**, *26*, 023030.

[460] Liu, T.; Xu, L.; Liu, J.; Wang, Y. Entanglement Witness for Indistinguishable Electrons Using Solid-State Spectroscopy. *Phys. Rev. X* **2025**, *15*.

[461] Warren, S.; Wang, Y.; Benavides-Riveros, C. L.; Mazziotti, D. A. Exact Ansatz of Fermion-Boson Systems for a Quantum Device. *Phys. Rev. Lett.* **2024**, *133*.

[462] Warren, S.; Wang, Y.; Benavides-Riveros, C. L.; Mazziotti, D. A. Quantum algorithm for polaritonic chemistry based on an exact ansatz. *Quantum Sci. Technol.* **2025**, *10*, 02LT02.

[463] Macridin, A.; Spentzouris, P.; Amundson, J.; Harnik, R. Digital quantum computation of fermion-boson interacting systems. *Phys. Rev. A* **2018**, *98*.

[464] Lamata, L.; Mezzacapo, A.; Casanova, J.; Solano, E. Efficient quantum simulation of fermionic and bosonic models in trapped ions. *EPJ Quantum Technol.* **2014**, *1*.

[465] Casanova, J.; Lamata, L.; Egusquiza, I. L.; Gerritsma, R.; Roos, C. F.; García-Ripoll, J. J.; Solano, E. Quantum Simulation of Quantum Field Theories in Trapped Ions. *Phys. Rev. Lett.* **2011**, *107*.

[466] Barry, J. F.; Schloss, J. M.; Bauch, E.; Turner, M. J.; Hart, C. A.; Pham, L. M.; Walsworth, R. L. Sensitivity optimization for NV-diamond magnetometry. *Rev. Mod. Phys.* **2020**, *92*.

[467] Pang, X.-L.; Yang, A.-L.; Dou, J.-P.; Li, H.; Zhang, C.-N.; Poem, E.; Saunders, D. J.; Tang, H.; Nunn, J.; Walmsley, I. A.; Jin, X.-M. A hybrid quantum memory–enabled network at room temperature. *Sci. Adv.* **2020**, *6*.

[468] Jiang, L.; Hodges, J. S.; Maze, J. R.; Maurer, P.; Taylor, J. M.; Cory, D. G.; Hemmer, P. R.; Walsworth, R. L.; Yacoby, A.; Zibrov, A. S.; Lukin, M. D. Repetitive Readout of a Single Electronic Spin via Quantum Logic with Nuclear Spin Ancillae. *Science* **2009**, *326*, 267–272.

[469] Udvarhelyi, P.; Thiering, G.; Londero, E.; Gali, A. Ab initio theory of the $N_2V$ defect in diamond for quantum memory implementation. *Phys. Rev. B* **2017**, *96*, 155211.

[470] Schouten, A. O.; Ewing, S.; Mazziotti, D. A. Two-electron reduced density matrix method for the electronic structure of correlated materials. *Physical Review B* **2025**, *112*.

[471] Holstein, T. Studies of polaron motion. *Ann. Phys.* **1959**, *8*, 325–342.

[472] Berger, E.; Valášek, P.; von der Linden, W. Two-dimensional Hubbard-Holstein model. *Phys. Rev. B* **1995**, *52*, 4806–4814.

[473] Engelsberg, S.; Schrieffer, J. R. Coupled Electron-Phonon System. *Phys. Rev.* **1963**, *131*, 993–1008.

[474] Melnikov, D. V.; Fowler, W. B. Electron-phonon interaction in a spherical quantum dot with finite potential barriers: The Fröhlich Hamiltonian. *Phys. Rev. B* **2001**, *64*.

[475] Fradkin, E.; Schaposnik, F. A. The fermion-boson mapping in three-dimensional quantum field theory. *Phys. Lett. B* **1994**, *338*, 253–258.

[476] Hyllus, P.; Laskowski, W.; Krischek, R.; Schwemmer, C.; Wieczorek, W.; Weinfurter, H.; Pezzé, L.; Smerzi, A. Fisher Information and Multiparticle Entanglement. *Phys. Rev. A* **2012**, *85*, 022321.

[477] Sasaki, F. Eigenvalues of Fermion Density Matrices. *Physical Review* **1965**, *138*, B1338–B1342.

[478] Keldysh, L. V. Coherent states of excitons. *Physics-Uspekhi* **2017**, *60*, 1180–1186.

[479] Fil, D. V.; Shevchenko, S. I. Electron-hole Superconductivity (Review). *Low Temp. Phys.* **2018**, *44*, 867–909.

[480] Payne Torres, L. I.; Schouten, A. O.; Sager-Smith, L. M.; Mazziotti, D. A. A Molecular Perspective of Exciton Condensation from Particle-Hole Reduced Density Matrices. *J. Phys. Chem. Lett.* **2025**, *16*, 1352–1366.

[481] Eisenstein, J. P.; MacDonald, A. H. Bose-Einstein condensation of excitons in bilayer electron systems. *Nature* **2004**, *432*, 691–694.

[482] Butov, L. Exciton condensation in coupled quantum wells. *Solid State Commun.* **2003**, *127*, 89–98.

[483] Kasprzak, J.; Richard, M.; Kundermann, S.; Baas, A.; Jeambrun, P.; Keeling, J. M. J.; Marchetti, F. M.; Szymańska, M. H.; André, R.; Staehli, J. L.; Savona, V.; Littlewood, P. B.; Deveaud, B.; Dang, L. S. Bose–Einstein condensation of exciton polaritons. *Nature* **2006**, *443*, 409–414.

[484] Min, H.; Bistritzer, R.; Su, J.-J.; MacDonald, A. H. Room-temperature superfluidity in graphene bilayers. *Physical Review B* **2008**, *78*.

[485] Liu, X.; Watanabe, K.; Taniguchi, T.; Halperin, B. I.; Kim, P. Quantum Hall drag of exciton condensate in graphene. *Nature Physics* **2017**, *13*, 746–750.

[486] Ma, L.; Nguyen, P. X.; Wang, Z.; Zeng, Y.; Watanabe, K.; Taniguchi, T.; MacDonald, A. H.; Mak, K. F.; Shan, J. Strongly correlated excitonic insulator in atomic double layers. *Nature* **2021**, *598*, 585–589.

[487] Gao, Q.; Chan, Y.-h.; Wang, Y.; Zhang, H.; Jinxu, P.; Cui, S.; Yang, Y.; Liu, Z.; Shen, D.; Sun, Z.; Jiang, J.; Chiang, T. C.; Chen, P. Evidence of high-temperature exciton condensation in a two-dimensional semimetal. *Nature Communications* **2023**, *14*.

[488] Lipkin, H. J.; Meshkov, N.; Glick, A. J. Validity of many-body approximation methods for a solvable model: (I.) Exact solutions and perturbation theory. *Nuclear Physics A* **1965**, *62*, 188–198.

[489] Schouten, A. O.; Sager-Smith, L. M.; Mazziotti, D. A. Computation of exciton binding energies in exciton condensation. *Phys. Rev. B* **2024**, *110*.

[490] Mazziotti, D. A. Contracted Schrödinger equation: Determining quantum energies and two-particle density matrices without wave functions. *Phys. Rev. A* **1998**, *57*, 4219–4234.

[491] Pérez, R.; Cambiaggio, M. C.; Vary, J. P. texpansion and the Lipkin model. *Phys. Rev. C* **1988**, *37*, 2194–2198.

[492] Stein, J. Unitary flow of the bosonized large-NLipkin model. *J. Phys. G Nucl. Part. Phys.* **2000**, *26*, 377–385.

[493] Cervia, M. J.; Balantekin, A. B.; Coppersmith, S. N.; Johnson, C. W.; Love, P. J.; Poole, C.; Robbins, K.; Saffman, M. Lipkin model on a quantum computer. *Phys. Rev. C* **2021**, *104*.

[494] Thomas, A.; George, J.; Shalabney, A.; Dryzhakov, M.; Varma, S. J.; Moran, J.; Chervy, T.; Zhong, X.; Devaux, E.; Genet, C.; Hutchison, J. A.; Ebbesen, T. W. Ground-State Chemical Reactivity under Vibrational Coupling to the Vacuum Electromagnetic Field. *Angew. Chem. Int. Ed.* **2016**, *55*, 11462–11466.

[495] Campos-Gonzalez-Angulo, J. A.; Ribeiro, R. F.; Yuen-Zhou, J. Resonant catalysis of thermally activated chemical reactions with vibrational polaritons. *Nat. Commun.* **2019**, *10*.

[496] Kéna-Cohen, S.; Yuen-Zhou, J. Polariton Chemistry: Action in the Dark. *ACS Cent. Sci.* **2019**, *5*, 386–388.

[497] Jahnke, K. D.; Sipahigil, A.; Binder, J. M.; Doherty, M. W.; Metsch, M.; Rogers, L. J.; Manson, N. B.; Lukin, M. D.; Jelezko, F. Electron–phonon processes of the silicon-vacancy centre in diamond. *New J. Phys.* **2015**, *17*, 043011.

[498] Ladd, T. D.; Jelezko, F.; Laflamme, R.; Nakamura, Y.; Monroe, C.; O'Brien, J. L. Quantum computers. *Nature* **2010**, *464*, 45–53.

[499] Tan, Q.; Rasmita, A.; Zhang, Z.; Dai, X.; He, R.; Cai, X.; Watanabe, K.; Taniguchi, T.; Cai, H.; Gao, W.-b. Enhanced coherence from correlated states in WSe2/MoS2 moiré heterobilayer. *Nat. Commun.* **2025**, *16*.

[500] Bhaskar, M. K.; Riedinger, R.; Machielse, B.; Levonian, D. S.; Nguyen, C. T.; Knall, E. N.; Park, H.; Englund, D.; Lončar, M.; Sukachev, D. D.; Lukin, M. D. Experimental demonstration of memory-enhanced quantum communication. *Nature* **2020**, *580*, 60–64.

[501] Rad, A.; Schuckert, A.; Crane, E.; Nambiar, G.; Fei, F.; Wyrick, J.; Silver, R. M.; Hafezi, M.; Davoudi, Z.; Gullans, M. J. Analog Quantum Simulator of a Quantum Field Theory with Fermion-Spin Systems in Silicon. 2024; `https://arxiv.org/abs/2407.03419`.

[502] Nguyen, P. T.; Le, T. K.; Nguyen, H. Q.; Ho, L. B. Harnessing graph state resources for robust quantum magnetometry under noise. *Scientific Reports* **2024**, *14*.

[503] Mazziotti, D. A. Effect of strong electron correlation on the efficiency of photosynthetic light harvesting. *J. Chem. Phys.* **2012**, *137*, 074117.

[504] Skochdopole, N.; Mazziotti, D. A. Functional Subsystems and Quantum Redundancy in Photosynthetic Light Harvesting. *J. Phys. Chem. Lett* **2011**, *2*, 25.

[505] Tronrud, D.; Camara-Artigas, A.; Blankenship, R.; Allen, J. Crystal structure of the Fenna-Matthews-Olson Protein from Chlorobaculum Tepidum. 2009; `https://doi.org/10.2210/pdb3eni/pdb`.

[506] Hamm, P.; Zanni, M. *Concepts and Methods of 2D Infrared Spectroscopy*; Cambridge University Press, 2011.

[507] Diaconis, P. Patterns in Eigenvalues: The 70th Josiah Willard Gibbs Lecture. *Bulletin of the American Mathematical Society* **2003**, *40*, 155–178, Article electronically published on February 12, 2003.

[508] Mezzadri, F. How to generate random matrices from the classical compact groups. *arXiv* **2006**,

[509] Maplesoft Generating random unitary matrices. `https://www.mapleprimes.com/questions/227248-Generating-Random-Unitary-Matrices`, n.d.; [Online forum post].